AFRL-SR-BL-TR-99-

1999

. 0223

REPORT DOCUMENTATION PAGE

OMB No. 0704-0188

Public reporting burden for this collection of information is estimated to average 1 hour per response, including the time reviewing instructions, searching data sources, gathering and maintaining the data needed, and completing and reviewing the collection of information. Send comments regarding burden estimate or any other aspect of this collection of information, including suggestions for reducing this burden to Washington Headquarters Service, Directorate for Information Operations and Reports, 1215 Jefferson Davis Highway, Suite 1204, Arlington, VA 22202-4302, and to the Office of Management and Budget, Paperwork Reduction Project (0704-0188) Washington, DC 20503.

PLEASE DO NOT RETURN YOUR FORM TO THE ABOVE ADDRESS.

1. REPORT DATE (DD-MM-YYYY)	2. REPORT DATE	3. DATES COVERED (From - To)
31-07-99		May 1, 1996 – April 30, 1999

4. TITLE AND SUBTITLE	5a. CONTRACT NUMBER
Shear Flow Control using Synthetic Jet Fluidic Actuator Technology	
	5b. GRANT NUMBER F49620-96-1-0194
	5c. PROGRAM ELEMENT NUMBER

6. AUTHOR(S)	5d. PROJECT NUMBER 2307/BS
Glezer, A.	**5e. TASK NUMBER**
	5f. WORK UNIT NUMBER

7. PERFORMING ORGANIZATION NAME(S) AND ADDRESS(ES)	8. PERFORMING ORGANIZATION REPORT NUMBER
Georgia Tech Research Corporation Georgia Institute of Technology CRB -24 Atlanta, GA 30332-0420	

9. SPONSORING/MONITORING AGENCY NAME(S) AND ADDRESS(ES)	10. SPONSOR/MONITOR'S ACRONYM(S)
AFOSR/PKA 110 Duncan Av. B115 Bolling AFB, DC 20332-8080	
	11. SPONSORING/MONITORING AGENCY REPORT NUMBER

12. DISTRIBUTION AVAILABILITY STATEMENT

unlimited

13. SUPPLEMENTARY NOTES

19990927 042

14. ABSTRACT

This research outlined in this report focuses on a novel approach to manipulation and control of shear flows using surface fluidic actuators based on synthetic jet technology. Synthetic jets are zero-mass-flux in nature and are synthesized from the working fluid in the flow system in which they are embedded. Although there is no net mass injection, the jets enable momentum transfer into the flow system to be controlled. Thus the interaction of a synthetic jet with an embedding flow near the flow surface results in formation of closed recirculating regions and in an apparent modification of the surface shape. These attributes enable synthetic-jet control systems to effect significant global modification of embedding flows on scales that are one to two orders of magnitude larger than the characteristic length scale of the jets. While conventional excitation methods have been limited to frequency bands tailored to the linear receptivity mechanisms of a given flow, fluidic actuation facilitates exploitation of nonlinear mechanisms for amplification of disturbances in a very broad frequency band. The present report discusses the flow physics of synthetic jets and the application of fluidic technology based on synthetic jets for dynamic control of jet vectoring and the modification of the aerodynamic performance of lifting surfaces.

15. SUBJECT TERMS

16. SECURITY CLASSIFICATION OF:			17. LIMITATION OF ABSTRACT	18. NUMBER OF PAGES	19a. NAME OF RESPONSIBLE PERSON Ari Glezer
a. REPORT	b. ABSTRACT	c. THIS PAGE			
u	u	u	u	135	**19b. TELEPONE NUMBER** (include area code) 404-894-3266

SHEAR FLOW CONTROL
USING
SYNTHETIC JET FLUIDIC ACTUATOR TECHNOLOGY

Final Technical Report
AFOSR Grant F49620-96-100194

submitted by

Ari Glezer
Woodruff School of Mechanical Engineering
Georgia Institute of Technology

OVERVIEW

The research outlined in this report focuses on a novel approach to manipulation and control of shear flows using surface fluidic actuators based on synthetic jet technology. Synthetic jets are zero-mass-flux in nature and are synthesized from the working fluid in the flow system in which they are embedded. Although there is no net mass injection, the jets enable momentum transfer into the flow system to be controlled. Thus, the interaction of a synthetic jet with an embedding flow near the flow surface results in formation of closed recirculating regions and in an apparent modification of the surface shape. These attributes enable synthetic-jet control systems to effect significant global modification of embedding flows on scales that are one to two orders of magnitude larger than the characteristic length scale of the jets. While conventional excitation methods have been limited to frequency bands tailored to the linear receptivity mechanisms of a given flow, fluidic actuation facilitates exploitation of nonlinear mechanisms for amplification of disturbances in a very broad frequency band.

The present report discusses the flow physics of synthetic jets and the application of fluidic technology based on synthetic jets for dynamic control of jet vectoring and the modification of the aerodynamic performance of lifting surfaces and bluff bodies. The flow physics of synthetic jets is described in Section I. The interaction between adjacent synthetic jets is discussed in Section II. Vectoring of conventional jets using synthetic jet actuators is discussed in Section III. Aerodynamic flow control of an unconventional airfoil is discussed in Section IV. Finally, Section V describes experiments on the modification of the aerodynamic characteristic of bluff bodies (a circular cylinder).

I. SYNTHETIC JETS

I.1 Introduction

The concept of synthesizing a turbulent shear flow by controlled coalescence of its rudimentary coherent vortical structures (e.g., turbulent spots in a transitional boundary layer or vortex rings in a round jet) was proposed by Coles in the early seventies and was later tested in a flat plate boundary layer experiment (Savas and Coles, 1985). While in the boundary layer experiments of Savas and Coles, turbulent spots were triggered by hairpin vortices induced by the periodic protrusion of a spanwise array of small pins into the flow, in the present work, synthetic jets are engendered by the interaction of discrete vortical structures which are formed by time-periodic ejection of fluid out of an orifice at the flow boundary. Unlike conventional continuous jets (e.g., Gutmark and Wygnanski, 1976, 2D jet) or pulsed jets (e.g. Bremhorst and Hollis, 1990, axisymmetric jet) a unique feature of synthetic jets is that they are formed from the working fluid of the flow system in which they are deployed and thus transfer linear momentum to the flow system without net mass injection across the system boundary. Thus, the interaction of synthetic jets with an external flow can lead to the formation of closed recirculation flow regions and consequently to an apparent modification of the flow boundary (Smith and Glezer, 1997, Amitay, Honohan, Trautman and Glezer, 1997). This attribute enables synthetic jets to effect significant global modifications of the base flow on scales that are one to two orders of magnitude larger than the characteristic length scales of the jets themselves.

It has been known for some time that streaming motions can be induced in fluids without mass addition by the transmission of sound (often referred to as acoustic streaming) or by oscillating the boundary of a quiescent medium. In a review of streaming motions induced by acoustic waves Lighthill (1978) noted that acoustic streaming results from the dissipation of acoustic energy or the attenuation of the transmitted sound. Such attenuation can occur either within the body of the fluid (i.e., away from solid surfaces) at very high frequencies (e.g., Meissner, 1926), or due to viscous effects near a solid boundary (Andres and Ingard, 1953). Streaming motions associated with oscillating solid boundaries have been the subject of a number of investigations, most notably time-harmonic oscillations of a cylinder normal to its axis (e.g., Stuart, 1966, Davidson and Riley, 1972, Riley and Wibrow, 1995) leading to streaming velocities on the order of 1 cm/s in water at a nominal frequency of 45 Hz.

Jet flows without net mass addition can be produced by an oscillatory flow having a zero (time-averaged) mean velocity through an orifice provided that the amplitude of oscillations is large enough to induce flow separation at the orifice and the time-periodic rollup of a train of vortices. Ingard and Labate (1950) used standing waves in an acoustically driven circular tube to induce an oscillating velocity field in the vicinity of an orifice plate placed near a pressure node and observed the formation of jets from trains of vortex rings on both sides of the orifice with no net mass flux. More recently, Lebedeva (1980) created a round jet with velocities of up to 10 m/s, by transmitting high amplitude sound waves (150 dB) through an orifice placed at the end of a tube. In a related investigation, Mednikov and Novitskii (1975) reported the formation of a jet without net mass flux and average streaming velocities of up to 17 m/s by inducing a low frequency (10-100 Hz) oscillatory velocity field with a mechanical piston.

The evolution of a submerged round turbulent water jet that is formed without an orifice by an oscillating diaphragm flush-mounted on a flat plate was recently investigated by James, Jacobs, and Glezer, 1996. The jet which was produced normal to and at the center of the diaphragm, was comprised entirely of radially entrained fluid, and was formed only when a small cluster of cavitation bubbles appeared near the center of the diaphragm during each oscillation cycle. The authors conjectured that the time-periodic formation of these bubbles displaces vorticity from the actuator's boundary layer, and leads to the formation of vortex puffs (in the parlance of Kovasznay, Fujita and Lee, 1973) that coalesce to synthesize a turbulent jet. Laser Doppler

velocity measurements showed that the time averaged jet is similar to a conventional turbulent round jet in that both its width and the inverse of its centerline velocity increase linearly with the distance from the actuator.

In the present implementation, plane (or round) turbulent jets having finite streamwise momentum are synthesized normal to an orifice in a flat plate by a train of vortex pairs (or vortex rings). The vortices are formed at the edge of an actuator orifice without net mass injection by the motion of a diaphragm in a sealed cavity. Because the characteristic dimensions of the jet scale with the characteristic dimension of the orifice, it is possible to synthesize jets over a broad range of length scales. The present work focuses on the evolution of a nominally two-dimensional (aspect ratio 150) synthetic jet.

I.2 Apparatus and Measurements

In the work reported here, the synthetic jet is formed in air at a rectangular orifice measuring 0.5×75mm flush mounted in a flat plate measuring 30×38cm as shown schematically in Figures I.1a and b. The exit plane of the jet is instrumented with a linear array of 17 static pressure ports equally spaced along $z/h = 0$ between $y/h = 6.3$ and 39, and connected to a Scannivalve pressure switch. The exit plane geometry can be altered by the addition of a "step" to one side (Figure I.1c), which restricts the entrainment flow from the stepped side of the synthetic jet. When a step is added, the origin of the x-axis remains at position of the non-stepped side. The jet is created by the motion of four piezoelectric disks mounted in the walls of the synthetic jet cavity. The cavity is designed to resonate near the resonance of the piezoelectric disks (nominally 1000Hz). The amplitude of the piezoelectric disks is controlled by varying the amplitude of the sinusoidal driving voltage that is applied to them. The pumping motion of the disks results in a nominally time-harmonic streamwise velocity $u_0(t)$ with amplitude u_{max} and zero mean inside the orifice.

As for axisymmetric vortex rings (e.g., Didden, 1979 and Glezer, 1988), each vortex pair may be characterized by two primary dimensionless parameters based on a simple "slug" model: i) the dimensionless "stroke" length L_0/h ($L_0 = \int_0^\tau u_0(t)dt$ where $\tau = T/2$ is the time of discharge or half the period of the diaphragm motion), and ii) a Reynolds number based on the impulse per unit width (i.e., the momentum associated with the discharge per unit width) $\mathrm{Re}_{I_0} = I_0/\mu h$ ($I_0 = \rho h \int_0^\tau u_0^2(t)dt$, ρ and μ are is the fluid density and viscosity, respectively). When these vortices are generated time-periodically to synthesize a jet, additional formation parameters include the formation frequency and the duty cycle, both of which are fixed in the present experiments. Under these conditions (and for a fixed orifice width), the formation parameters of the jet depend only on the amplitude of the diaphragm motion and cannot be varied independently. In the present experiments $5.3 < L_0/h < 25$ and $1400 < I_0/\mu h < 30,000$. The corresponding Reynolds number of the synthetic jet, Re_{U_0} (based on the orifice width h and the average orifice velocity $U_0 = L_0/T$) varies between 104 and 489.

Cross-stream distributions of the streamwise and cross-stream velocity components are measured at a number of streamwise and spanwise stations ($0 < x/h < 177$ and $80 < z/h < 80$) using hot wire anemometry. The single-sensor probe was used primarily in the near field of the jet and the two sensor probe was used for $x/h > 10$ (where cross-stream distributions of the mean streamwise velocity measured with both probe types are virtually identical). The hot wire probes are traversed using a three-axis computer-controlled traversing mechanism and are calibrated in the primary jet. A laboratory computer system equipped with a 12 bit 100 kHz A/D board dedicated to experiment control and data acquisition.

x

a

y

Piezoelectric
Driver

Metal Disk

b

h=0.5mm

z

75mm

y

c

x

y

S

h
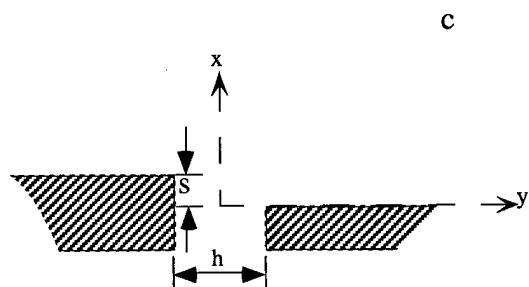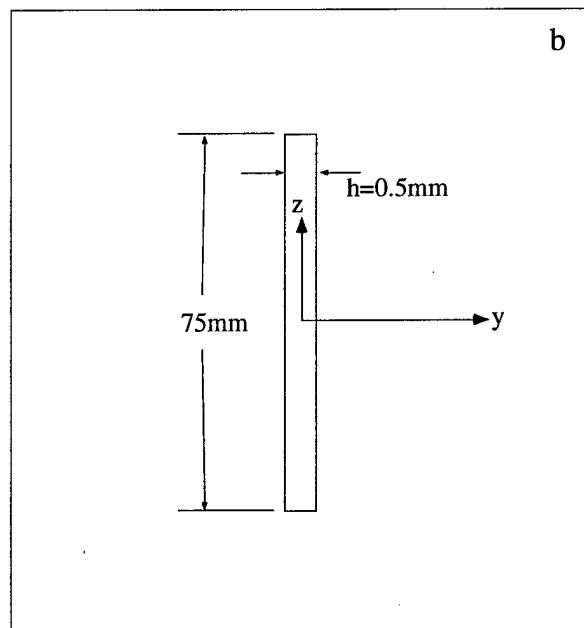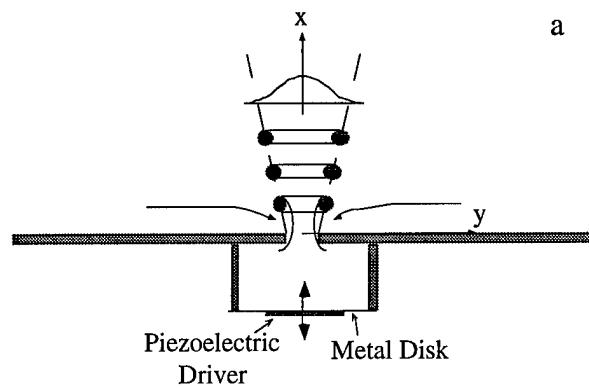
Figure I.1. Schematic of synthetic jet (a) x-y plane (b) y-z plane (c) synthetic jet with stepped orifice.

I.3 Results

A schlieren image of the ensuing two-dimensional jet used in this study is shown in Figure I.2. For the purpose of the schlieren visualization, the air inside the actuator's cavity is slightly heated using a thin-film surface heater that is internally mounted on one of the cavity walls. The schlieren view is in the x-y plane and extends approximately through x = 70h. The motion is recorded at standard video rate using a CCD camera having an exposure time of 100 μsec. The image shows a vortex pair that is formed near the orifice, and a turbulent jet farther downstream. Although this image does not show the motion of the ambient air that is drawn towards the cavity along the surface of the flat plate, such motion is evident in the streamline plot in Figure I.11. The evolution of the synthetic jet can be divided into two distinct domains. Near the jet exit plane, the flow is dominated by the time-periodic formation and advection of discrete vortex pairs, which ultimately undergo transition to turbulence, slow down and lose their coherence. The transition process is followed by the emergence of a fully developed turbulent jet, which is similar in some respects to a conventional 2-D jet.

I.3.1 Near-Field Formation and Evolution

The formation of a synthetic jet at Re_{U_0} = 383 and Re_{I_0} = 18,000 (referred to below as the "nominal case") is shown in a sequence of digitized video schlieren images (Figure I.3) that are each taken phase-locked to the actuator driving signal at 27 equal time intervals (33.8 μsec apart) during the forcing period beginning with the forward motion of the actuator diaphragm (t/T = 0) which results in the ejection of fluid from the jet cavity. (The coordinate system is shown for reference in the image corresponding to t/T = 0.481 which is repeated on the bottom right hand side.) It should be noted that while the images in Figure I.3 are phase-locked to the actuator's driving signal, the video frame rate is a sub-multiple of the forcing frequency, and thus successive images do not show the *same* vortex pair.

The front end of the fluid slug that is ejected out of the orifice and leads to the formation of the vortex pair is apparent on the left at time t/T = 0.11. Some traces of the previous vortex pair are still discernible near x/h = 11 and the emerging turbulent jet is visible farther downstream. In subsequent images (0.15 < t/T < 0.41), the new vortex pair continues its rollup as it is advected downstream while the previous vortex pair becomes indistinguishable from the background flow (and, as discussed further below, it is no longer phase locked to the excitation signal). The new vortex pair and the remainder of the ejected fluid behind it appear to be laminar after the rollup process is completed and while the vortex core is advected through x/h = 8.5 (t/T = 0.407).

The cores of the vortex pairs begin to exhibit small-scale motions and undergo transition to turbulence around t/T = 0.5 which, as shown in Figure I.8 below, is accompanied by a reduction in their advection velocity. The transition process begins with the onset and rapid amplification of a spanwise instability of each (primary) vortex that leads to the formation of nominally spanwise-periodic counter-rotating streamwise vortex pairs that are wrapped around the cores of the primary vortices and ultimately lead to a cellular breakup of their cores (as shown in the spanwise view in Figure I.4). The formation of these streamwise vortices and the small-scale transition of the primary vortices is shown in a sequence of phase-locked smoke visualization images taken in the x-z plane y = 0 using a laser sheet. In order to maintain smoke concentration that is adequate for spanwise visualization, the jet frequency was lowered to 360 Hz and, as a result, the advection velocity of the vortex pairs is reduced to approximately one tenth the advection velocity for the nominal case. The images in Figures IV.3a-d show a spanwise section of the jet that is approximately 30h wide (about z = 0) and are captured at t/T = 0.5, 0.625, 0.75, and 0.875, respectively. Figure I.4a shows a new spanwise vortex on the left and the previous vortex, which is in the final stages of the transition process. The image clearly shows the formation of spanwise-regular rib-like secondary vortical structures about the core of the primary vortex on the left with an average spanwise spacing of 2.5h. As the primary vortex is advected downstream (Figures I.4b, t/T = 0.625 and 4c, t/T = 0.75), the secondary vortical structures intensify and shortly thereafter appear to lead to a cellular breakdown of the

4

core of the primary vortex (Figure I.4d, t/T = 0.875). As is evident from the image of the downstream primary vortex in Figure I.4a, the cellular segments apparently continue to break down to smaller and smaller scales until the primary vortex loses its identity (e.g., on the right hand side of Figure I.4d). Similar secondary vortex tubes that are wrapped around the core of an isolated vortex ring appear during the final stages of its transition following an azimuthal instability of the vortex core (Didden, 1977, Schneider, 1980), and were also observed in a turbulent vortex ring (Glezer, 1988, Glezer & Coles, 1990). The appearance of counter-rotating pairs of streamwise vortices around the cores of the spanwise (primary) vortices in plane shear layers (e.g., Bernal & Roshko, 1986, Nygaard & Glezer, 1991) and wakes (e.g., Roberts, 1985, Williamson, 1991) marks the appearance of small scale motion within the cores of the primary vortices and the onset of mixing transition.

The schlieren images for t/T > 0.444 in Figure I.3 suggest that similar to a vortex ring (Glezer, 1988), the onset of small-scale transition appears to take place near the front stagnation point of the primary vortex where the strain rates are high. Based on the schlieren visualization, the transition process seems to proceed towards the rear of the vortex, and ultimately progresses through the fluid stem behind it. In Figure I.3 for 0.67 < t/T < 1.07, the entire vortex pair appears to be turbulent and its celerity, or propagation velocity, is diminished as it merges into the ensuing turbulent jet. An important feature of this sequence of images is that unlike vortex pairs in that form near the edges of the potential core of conventional 2-D jets, consecutive vortex pairs in the present jet do not coalesce or undergo pairing and (as shown in Figures I.22 below) there are no sub-harmonic components in power spectra of the streamwise velocity.

Time series of the streamwise velocity component are measured along the centerline of the jet (y = 0) using a single sensor hot wire probe. The sensor is operated at low overheat ratio (1.2) to minimize heat transfer to the jet orifice, and the measured velocity is corrected for changes in the room temperature. These data are taken phase-locked to the actuator signal (1140 Hz, T = 0.877msec) at 88 equal time intervals per cycle (i.e., 10 μsec apart) for 1200 cycles. Figure I.5 shows a sequence of phase-averaged velocity traces $<u(t/T; x)>/U_0$ measured in the domains 0 < x/h < 5 (at five equally-spaced positions, marked with closed symbols), and 5 < x/h < 25 (at nine equally-spaced positions, marked with open symbols) for the nominal case. Near the jet orifice, the velocity traces are rectified by the hot wire sensor when the velocity reverses its direction at mid-cycle. Thus, for x/h ≤ 3.0, the velocity during the suction part of the cycle is inverted to reflect the correct flow direction, and data are not plotted where the magnitude of the velocity is below the low end of the calibration range of the sensor (i.e., within the gaps around zero).

The phase-averaged centerline velocity near the exit plane of the orifice reflects the momentary fluid ejection as well as the rollup and ultimately the advection of the vortex pair during the discharge period, and the flow toward the orifice behind the advected vortex pair during the suction period. At the center of the orifice (x/h = 0), the two halves of the velocity cycle are virtually identical and the time-averaged velocity and the net mass flux are indeed zero. The local velocity extreme at t/T = 0.08 and 0.58, mark the symmetrical rollup and advection of a vortex pair at the upstream and downstream sides of the orifice during both the ejection and suction parts of the cycle (symmetric rollup on both sides of a circular orifice was also reported by Ingard and Labate (1950). The rollup of the vortex pair proceeds as it is advected downstream and the velocity peak induced by its passage at a given streamwise position increases in magnitude, while the magnitude of the velocity minimum associated with the suction decreases. These changes are accompanied by an increase in the mean (time-averaged) velocity. It appears that at x/h = 4, the vortex pair is fully formed and the suction cycle no longer affects the phase-averaged velocity. Similar to the streamwise velocity measured along the axis of a vortex ring (Glezer and Coles, 1990), the centerline velocity reflects the passage of the cores of a vortex pair where the peak corresponds to the center of the cores. As demonstrated in Figure I.5 (3.9 < x/h < 9.8), the magnitude of the induced velocity peak on the centerline

5

decreases monotonically as the vortex is advected downstream, ostensibly as a result of the transition to turbulence (cf. Figure I.3) and loss of vorticity to the wake which are also accompanied by reduction in phase coherence. Figure I.5 (x/h > 3.0) also shows that in addition to the time-dependent velocity induced by the passage of the vortex pair, the mean velocity at a given streamwise position includes a time-invariant offset component $u_{os}(x) = \min(<u(t/T; x)>)$ (as marked in Figure I.5) which increases with downstream distance. The evolution of u_{os} is discussed further in connection with Figure I.9 below.

As the magnitude of the velocity that is induced by the passage of the vortex pair diminishes farther downstream, it becomes evident that the centerline velocity of the emerging synthetic jet has a low-level time-periodic component at the frequency of the actuator and its higher harmonics. Figures I.6a-c show phase averaged time traces (with the local time-averaged velocity removed) at x/h = 15.7, 17.7, and 19.7. While at x/h = 15.7 (Figure I.6a), the velocity increase associated with the passage of the vortex pair is still detectable during the first half of the cycle, at x/h = 19.7 (Figure I.6c), the velocity distributions during each of the two halves of the cycle are virtually identical. As shown in Figure I.23 below, although the magnitude of the spectral component at the actuator frequency decreases with downstream distance, it is nevertheless detectable throughout the present domain of measurements (x/h < 180). That the phase of this spectral component relative to the actuator motion does not change appreciably with downstream distance suggests that it is induced by the oscillating pressure field which is associated with the pumping of the jet fluid in and out of the cavity.

The time t_p at which the (phase-averaged) velocity peak on the jet centerline is measured during the passage of the vortex pair at a given measurement station, allows for the determination of the streamwise position of its core. Figure I.7a shows the mean trajectories of a family of vortex pairs that are produced with increasing total impulse (i.e., $1,400 < I_0/\mu h < 30,000$) at a fixed actuator frequency. (Time is measured from the beginning of the forward motion of the actuator or the beginning of the ejection period). It is striking that regardless of the magnitude of the impulse, the resulting trajectories are quite similar and are comprised of three distinct domains that are characterized by changes in slope (or celerity). In Figure I.7b, the same data are plotted in dimensionless form where the streamwise trajectory of each pair is normalized by the corresponding "stroke" length L_0, and the reasonable collapse of the data suggests that the trajectories of the vortex pairs indeed scale with L_0. In the domain $x/L_0 < 40$, $U_c \approx U_0$ and, as can be shown from these data, it increases approximately like $(I_0)^{1/3}$. The vortex pair begins to slow down at $t_p/T \approx 0.6$ and $x/L_0 \approx 45$ which is where it begins to undergo transition to turbulence as suggested by flow visualization (cf. Figure I.3). Finally, at $t_p/T \approx 1$, the vortex pair begins to move faster until it loses its phase coherence and becomes part of the ensuing jet. Note also, that regardless of the total impulse, no vortex pairs are still phase-locked to the actuator signal much beyond t/T > 1.3.

The celerity $U_c(x,t)$ of the vortex pair is determined by taking the time derivative of its trajectory. The variation of the celerity (normalized by the characteristic ejection velocity U_0) with t/T for the family of vortex pairs in Figures I.7a and b is shown in Figure I.8. For 0.25 < t/T < 0.5, the vortex pairs are nominally laminar and the celerity decreases like $(t/T)^{-0.5}$ (a straight line segment m = -0.5 is shown for reference). As noted in connection with Figures I.3 and I.4 above, the transition to turbulence of the vortex pair starts approximately at the beginning of the suction cycle of the actuator and thus may be triggered by the reversal of the streamwise velocity near the exit plane. Following transition (0.5 < t/T < 0.8), the celerity decreases like $[(t/T)^{-2}]$ which is faster than for the laminar vortex pair and considerably faster than for an isolated turbulent vortex pair (for which $U_c \propto t^{0.5}$). The celerity reaches a minimum at t/T $\approx$ 0.8 and then increases again like $(t/T)^2$ until the vortex pair becomes indistinguishable from the jet flow and its fluid effectively moves with the mean flow of the jet.
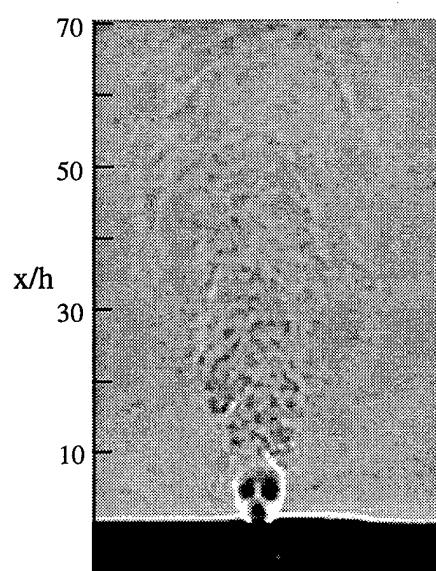
Figure I.2. Schlieren image of rectangular synthetic jet. Re_{U_o}=380, f=1000Hz, h=0.508mm.
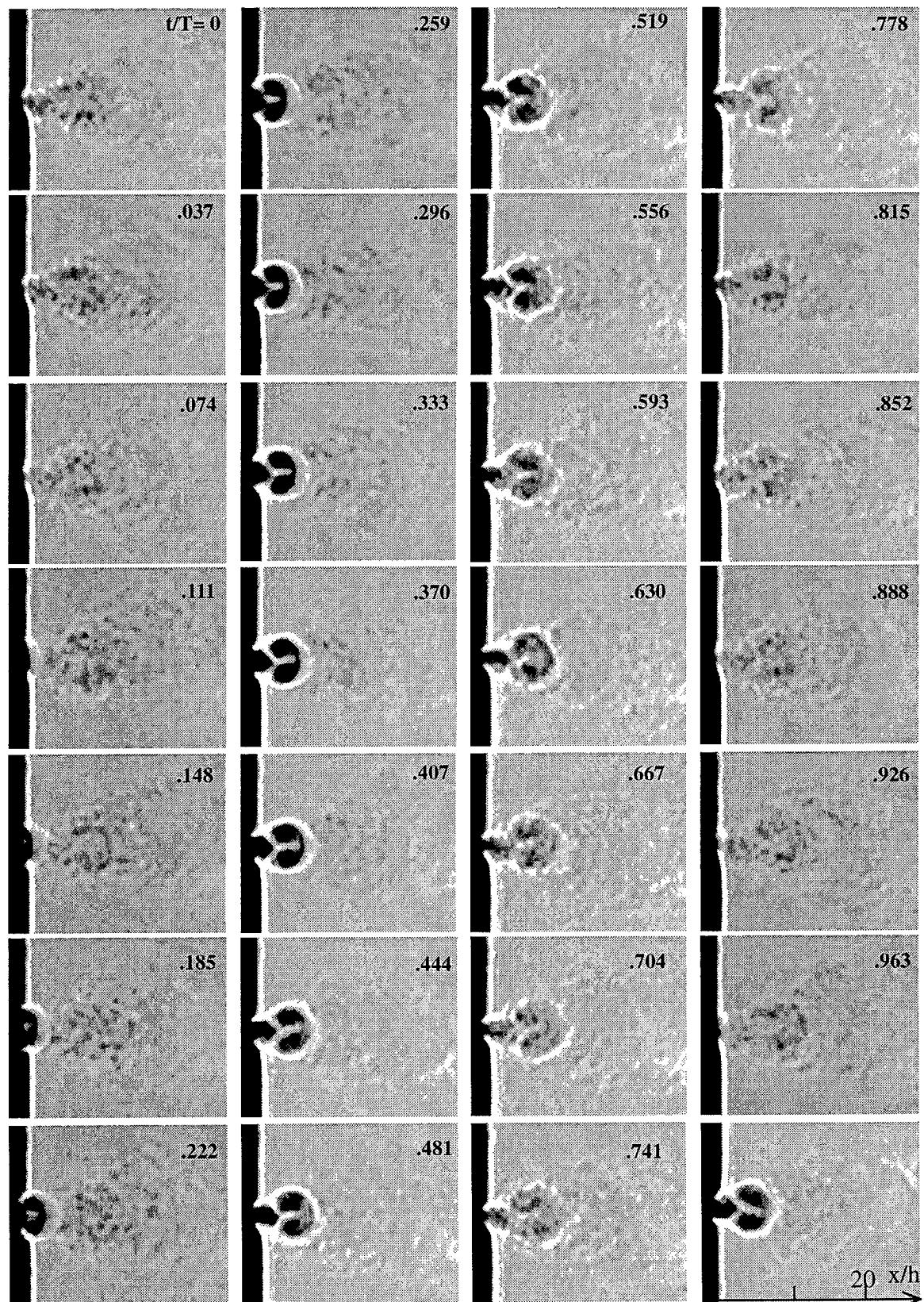
Figure I.3. Phase-locked schlieren images of the synthetic jet in the x-y plane taken at 27 equal intervals during the actuator cycle. The forward and backward motions of the diaphragm from the rest position begin at t/T=0 and t/T=0.5 respectively. (Re_{U_o}=383,f=1120Hz).
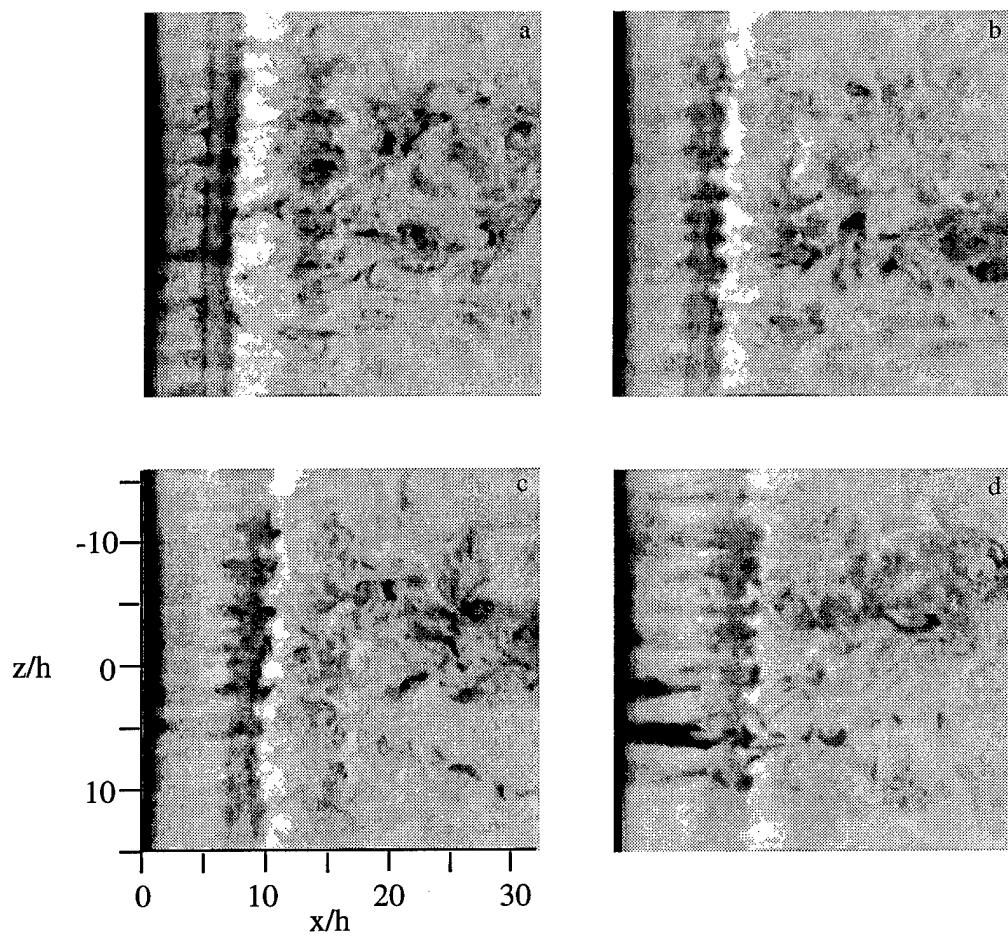
Figure I.4. Phase-locked smoke visualization images of the synthetic jet (f = 360Hz) in the x-z plane taken at equal time intervals (T/8).
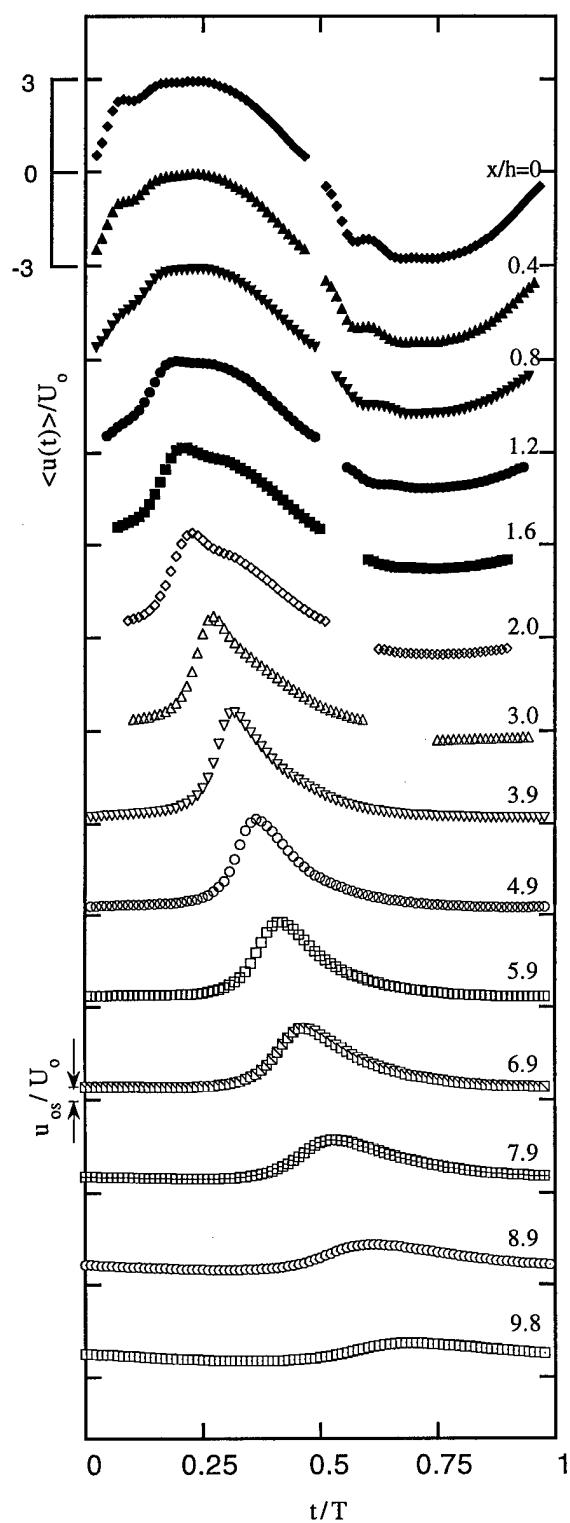
Figure I.5. Phase-averaged centerline velocity during one cycle of the actuator: x/h = 0 (◆), 0.4 (▲), 0.8 (▼), 1.2 (●), 1.6 (■), 2.0 (◇), 3.0 (△), 3.9 (▽), 4.9 (○), 5.9 (□), 6.9 (◨), 7.9 (⊞), 8.9 (⊙), 9.8 (⊡). Re_{U_o}=383.
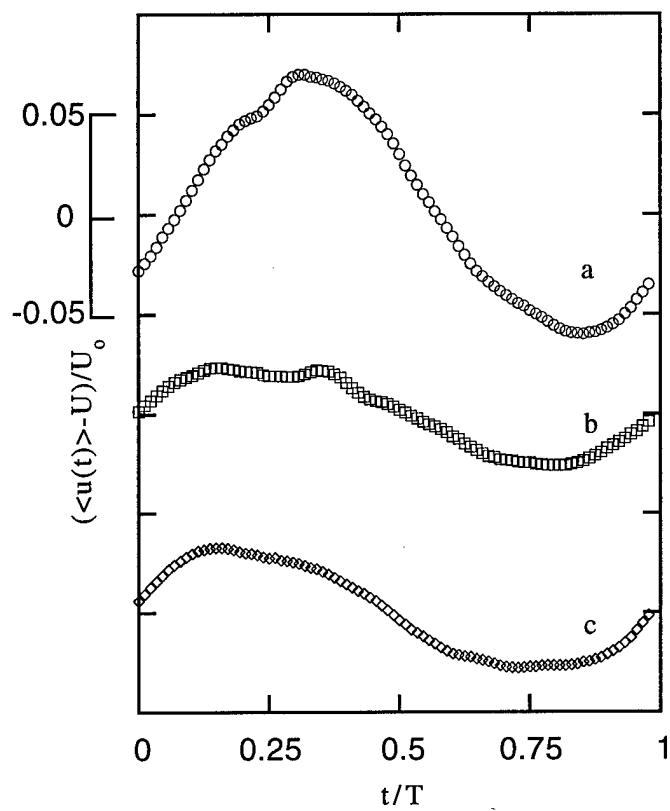
Figure I.6. Phase-averaged centerline velocity during one cycle of the actuator: x/h=15.7 (a, ○), 17.7 (b, □), 19.7 (c, ◇).
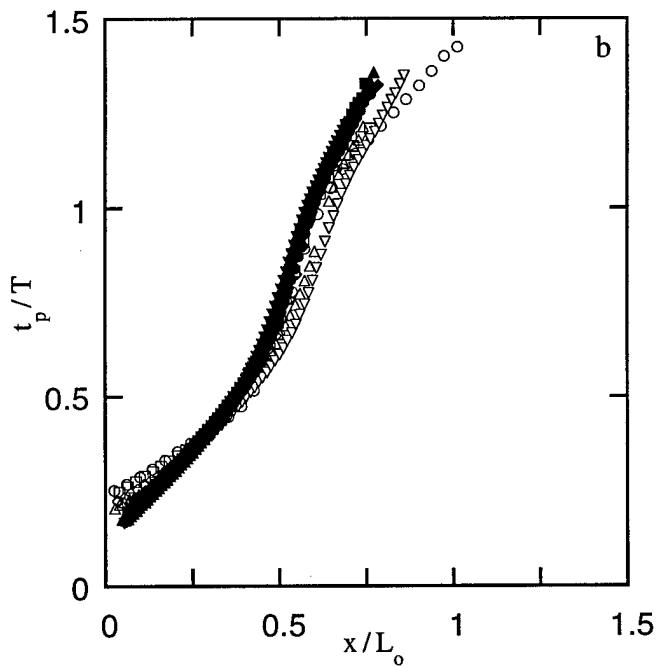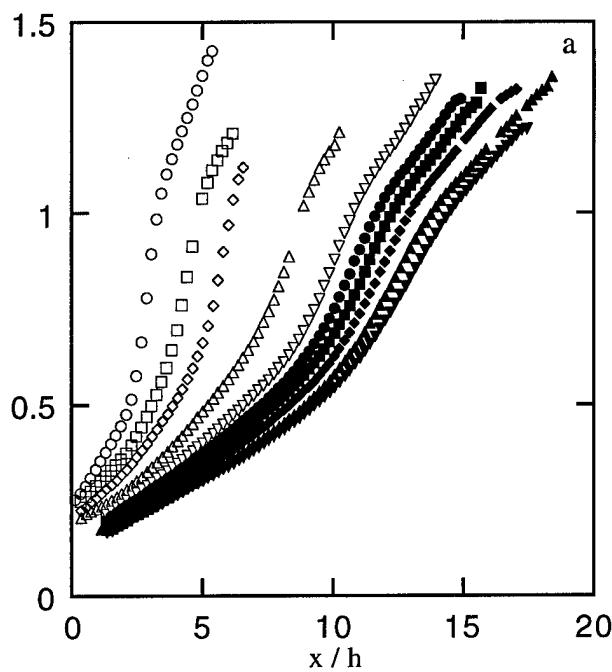
Figure I.7. Vortex pair trajectories a) global normalization, b) individual normalization: $Re_I = 1396$ (o), 3171 (□), 4967 (◇), 9072 (△), 12552 (▽), 18124 (●), 20761 (■), 22282 (◆), 27025 (▲), 29654 (▼).
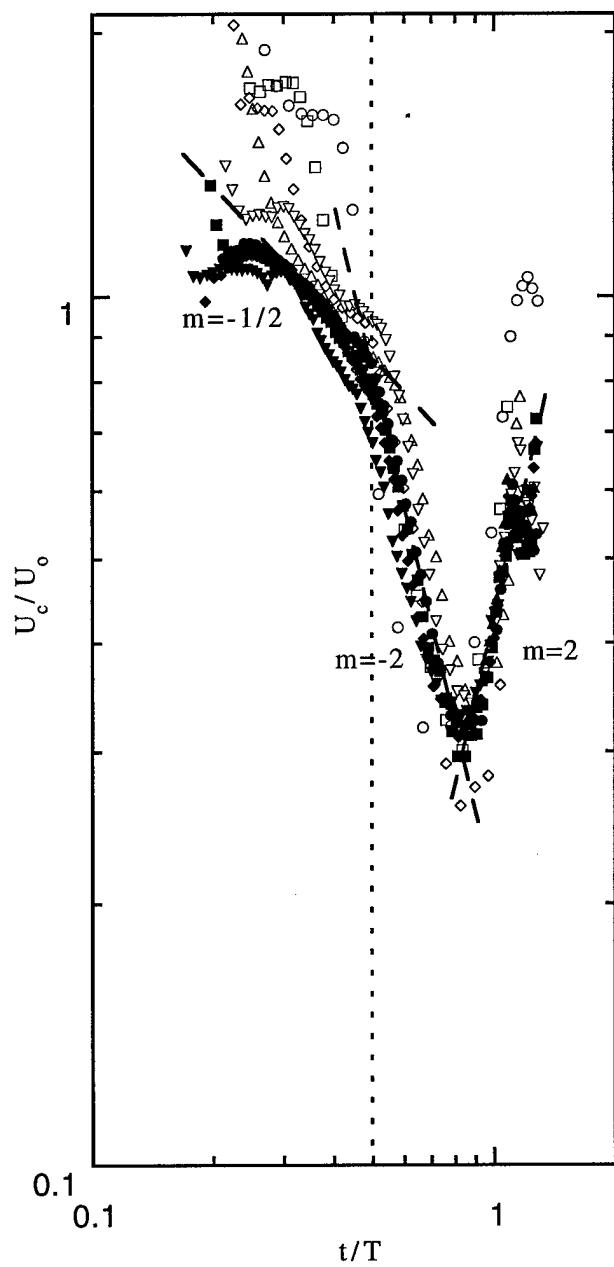
Figure I.8. Variation of vortex pair celerity $U_c(x,t)$ with time (symbols as in Figure IV.6).

The streamwise dependence of the offset velocity u_{os} (cf. Figure I.5), which may be thought of as the time-invariant velocity of fluid that is entrained into the jet in part as a result of the suction at the orifice is shown in Figure I.9a for different impulse levels. It is remarkable that (except for the lowest I_o) regardless of the impulse, u_{os} of all vortex pairs initially increases along the *same* curve before it reaches a maximum value which depends on and increases with the initial impulse. Past the maximum, for a given impulse level, u_{os} begins to decrease with streamwise distance ostensibly as a result of the cross-stream spreading of the jet. Finally, for $x/h > 20$, u_{os} is equal to U_{cl}, which, as is shown in Figure I.15, decreases like $x^{-0.58}$. The same data are plotted in dimensionless form in Figure I.9b which shows a reasonable collapse with the possible exception of the vortex pair that is formed at the lowest impulse level. The streamwise dependence of the celerity, offset velocity and the mean velocity for the nominal case is shown in Figure I.10. It is interesting to note that when the vortex pair undergoes transition to turbulence around $x/h = 7$, the streamwise rate of decay of the centerline velocity and the celerity increases substantially. The celerity and the offset velocity change again at $x/h \approx 10$ and ultimately merge with the mean velocity at $x/h > 20$.

The flow in the near field of an isolated synthetic jet may be thought of as induced by a temporally alternating (during each actuation cycle) source- and sink-like flow element that is coincident with the jet orifice. The strength of the source and sink flows varies approximately like the displacement of the actuator disk during the ejection and suction strokes, respectively. An important feature of the flow field is the formation of stagnation or saddle points on the jet centerline downstream of the orifice during the suction stroke. The presence of the stagnation point is evident in a map of the streamlines that are obtained from phase-averaged PIV measurements of the velocity field during the peak of the suction stroke for synthetic jets at two different frequencies (Figure I.11a-b). The stream function increment between adjacent streamlines corresponds to $0.25Q_o$, where $Q_o = hU_o$. In the higher frequency case ($f = 1100$Hz, $Re_{U_o} = 300$, Figure I.11a), the stagnation point forms closer to the exit plane than in the low frequency case ($f = 600$Hz, $Re_{U_o} = 300$, Figure I.11b). The stagnation streamline separates between the flow associated with the ejection stroke of the actuator (i.e, away from the exit plane) and the flow associated with the suction stroke (i.e., towards the jet orifice). The presence of the stagnation point indicates that unlike a continuous sink flow, the flow towards the orifice during the suction stroke of the actuator is restricted to the flow tube bounded by the stagnation streamline and the exit plane of the jet. It is this feature that allows the synthetic jet to selectively entrain fluid in the presence of a cross flow, and enables deflection or vectoring of an adjacent jet.

The symmetry of the flow towards the orifice about the jet centerline during the suction stroke can be effectively manipulated by extending one of the edges of the synthetic jets' orifice in the downstream direction. This is accomplished by placing a small "step" at the jet exit plane as shown schematically in Figure III.1c. The presence of the step restricts the suction flow from that side and therefore leads to an increase in the flow through the opposite side of the jet orifice. The effect of the step is demonstrated in a map of phase-locked streamlines (Figure I.12) for a synthetic jet operating in a quiescent environment. The step is placed on the left side of the orifice and extends 0.6h downstream. This small change in the geometry results in an imbalance in the suction flow where 75% of the fluid that enters the actuator cavity comes from the right, while in the absence of a step, 50% of the entrained flow comes from either side. This imbalance is manifest by the disparate pressure distribution along the surface on either side of the orifice.

14
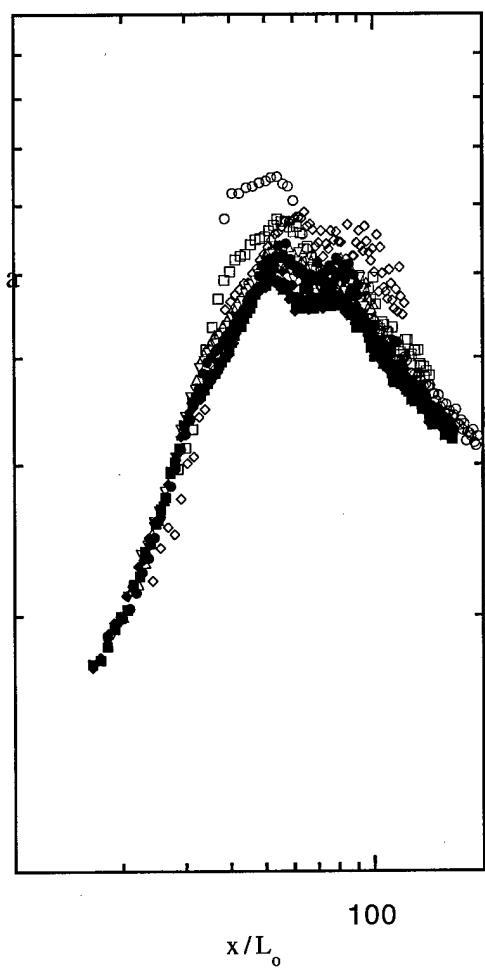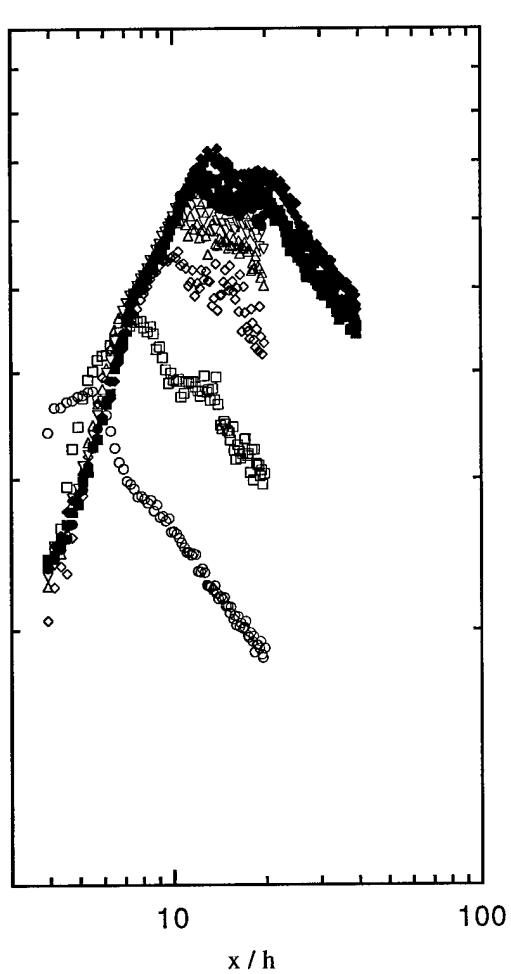
Figure I.9. Offset velocity u_{os}. a) dimensional variables, b) normalized variables: Re_I = 4967 (O), 9072 (□), 12552 (◇), 18124 (△), 20761 (▽), 22282 (●), 27025 (■), 29654 (◆).
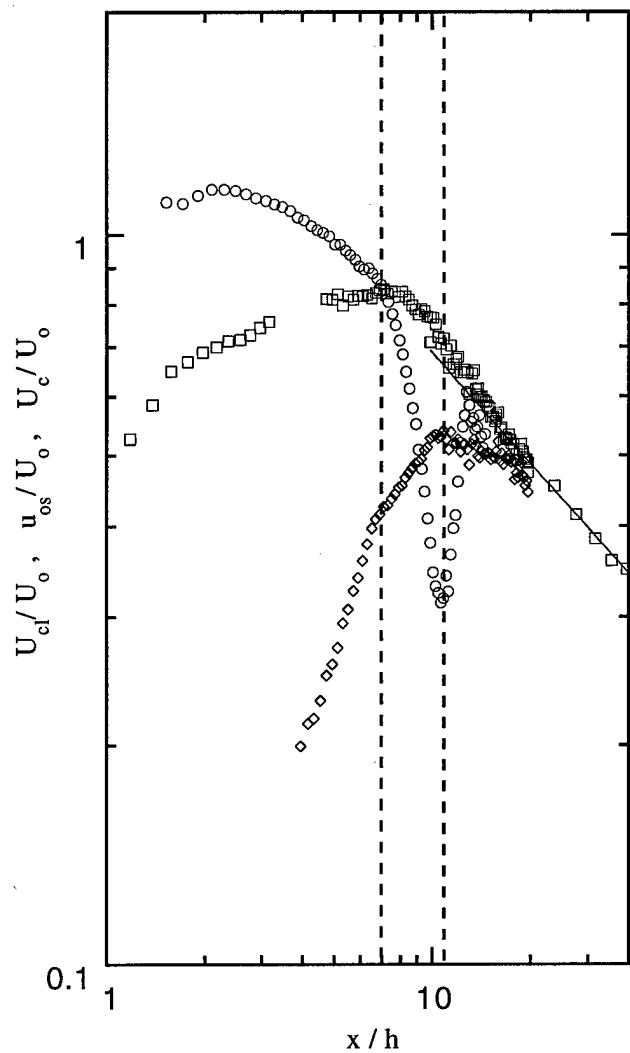
Figure I.10. Mean centerline velocity (□), celerity (O) and offset velocity (◇) for the nominal case Re_{I_o} =18124 (Re_{U_o}=383).
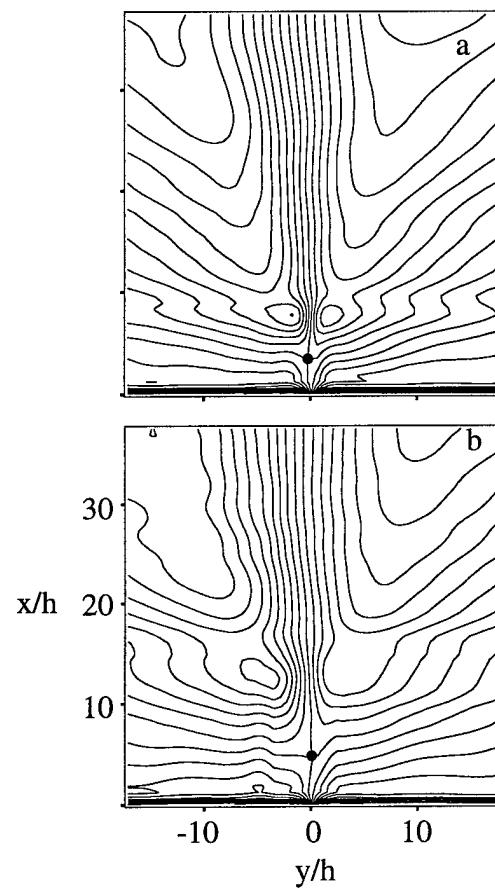
Figure I.11. Phase locked streamlines of rectangular synthetic jet at t/T=0.5, Re_{U_o}=300 (a) 1120Hz (b) 600Hz.
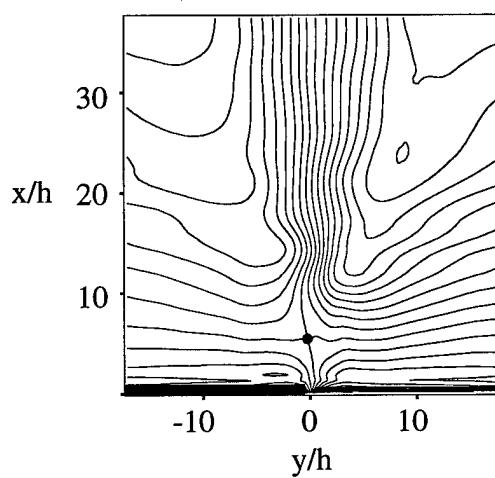
Figure I.12. Phase locked streamlines of rectangular synthetic jet with a 0.6h step (left side) at t/T=0.5, Re_{U_o}=300, f= 600Hz.

The asymmetry in the flow from either side of the actuator may be explained by considering time traces of the streamwise velocity component on the jet centerline with a step, and without at the exit plane and at x/h = 1.5 (Figure I.13a and b). The step height is 1.5h. The velocity time traces in both cases are identical, indicating that the step does not affect the development of the jet on the centerline. The flow at the exit plane is time harmonic with zero mean (Figure I.13a). In the presence of a step, the flow approaching on the opposite side is readily drawn into the jet orifice during the suction stroke. However, the flow toward the orifice on the opposite side encounters weaker suction as manifested by the duration and magnitude of the reversed flow (Figure I.13b) compared with the corresponding velocity trace at the exit plane.

I.3.2 The Mean Flow

Cross-stream distributions of the time-averaged streamwise (U) and cross stream (V) velocity components along with the corresponding rms velocity fluctuations u', v', and u'v' of the nominal case are plotted in Figures I.14 (a-e) in the usual similarity coordinates of conventional 2-D jets (the cross stream coordinate is normalized with the local jet width b(x) based on $U_{cl}/2$). These data are measured at a 11 streamwise stations between x/h = 9.8 and 78.7 and, at least within this streamwise domain, collapse reasonably well despite the fact that the jet is formed by time-harmonic motion. The mean cross stream velocity component (Figure I.14b) is nominally antisymmetric about the jet centerline and its normalized magnitude is similar to that corresponding to conventional jets (Krothapalli, et al., 1981). The normalized distributions of the rms velocity fluctuations u' (Figure I.14c), v' (Figure I.14d) and of u'v' (Figure I.14d) are also very similar to and have approximately the same magnitudes as corresponding distributions in conventional jets (Gutmark and Wygnanski, 1976, Krothapalli et al., 1981, Everitt and Robins, 1978, Bradbury, 1965).

The cross-stream distribution of u' (Figure I.14c) exhibits two distinct peaks on both sides of the centerline (where u' $\approx$ 0.25U_{cl}) which coincide with the peaks of the cross stream velocity components. In conventional jets, u' and v' typically increase rapidly downstream of the potential core and, where the flow becomes fully developed, their magnitudes are normally between 0.2 and 0.3U_{cl} (Gutmark and Wygnanski, 1976, Krothapalli et al., 1981, Bradbury, 1965) and increase with decreasing Reynolds number (based on the jet height) (Bradbury, 1965). In contrast to conventional plane jets which become fully developed at x/h > 40 (e.g., Gutmark and Wygnanski, 1976), the mean flow of the synthetic jet appears to become fully developed considerably closer to the jet exit plane (x/h > 10).

The streamwise variation of the mean velocity and rms velocity fluctuations along the jet centerline for 9.8 < x/h < 177 are shown in Figure I.15. For x/h < 80, U decreases like $x^{-0.58}$ and u' decreases like $x^{-0.5}$, while for conventional 2-D fully developed turbulent jets, both U and u' decrease like $x^{-0.5}$. Note also, that for x/h > 80, the rate of streamwise decay of the centerline velocity diminishes to $x^{-0.25}$ ostensibly due to three-dimensional effects associated with the streamwise decrease in the aspect ratio of the jet cross section in the y-z plane (cf. Figure I.21 below). It is interesting to note that u' appears to be unaffected by these changes and continues to decrease like $x^{-0.5}$. Figure I.15 also shows that for 10 < x/h < 80, the jet width b(x) (based on $U_{cl}/2$) in the cross stream plane z = 0 increases like $x^{0.88}$ while in conventional 2-D jets, b $\propto$ x. The streamwise rate of increase of the jet width at x/h = 30 is 0.194 and is almost twice the corresponding streamwise increase in the width of conventional 2-D jets at Reynolds numbers on the order of 10^4 (which varies between 0.09 to 0.12) (Gutmark and Wygnanski, 1976, Krothapalli et al., 1981, Heskestad, 1965). Note also that the linear fit $b^{1.136} \propto$ x yields a virtual origin for the nominal case of $x_o \approx$ -4h which is comparable to what was measured by Gutmark and Wygnanski (1976) (-2.5h) and Krothapalli et al. (1981) (-2h) in conventional 2-D jets. Gutmark and Ho (1983) suggested that the disparity in streamwise spreading rates of 2-D jets in earlier investigations could be attributed to the spontaneous emergence of different instability modes of the jet shear layers. Thus, because the synthetic jet is formed by a train of 2-D vortex

pairs which do not interact (or pair) it is expected that at least near the exit plane, the cross stream spreading of the synthetic jet would be limited.

When the motion of the diaphragm is time-harmonic (and for a fixed orifice width), the formation parameters of the jet depend only on the amplitude of the actuator signal, and cannot be varied independently. Figures I.8 and I.9b demonstrate that the celerity and offset velocity of the vortex pairs, respectively, scale with the average orifice velocity and thus with the amplitude of the actuator signal. The effect of the amplitude on the global properties of the ensuing jet is demonstrated by considering the dependence of the centerline velocity (normalized by U_0, Figure I.16) on x/h. These data show that the existence of three distinct streamwise domains corresponding to the formation of the vortex pairs, their laminar advection and transition to turbulence, and finally the emergence of the turbulent jet. In the first domain $x/h < 2$, the jet centerline velocity increases rapidly to a level which scales with the average orifice velocity (which depends on the formation amplitude). In the second domain, the streamwise rate of increase of the centerline velocity is much smaller (although not zero). Farther downstream (nominally $x/h \approx 10$) the centerline velocity begins to decay with streamwise distance (within the third domain). As noted in Near Field Evolution section, the streamwise decay of the centerline velocity begins at $t/T = 0.5$, and thus the corresponding streamwise locations increase linearly with the formation amplitude (or the slug length L_0). Note that all the data within the third domain ultimately collapse onto a single curve given by $x^{0.58}$ (c.f. Figure I.15) which is also shown for reference.

The streamwise variation of integral quantities such as the jet volume flow rate and its streamwise momentum flux are assessed using a least squares fit of the hyperbolic cosine function $U_f = U_{cl}\cosh^{-2}(\eta y)$ (where η is a parameter of the fit) to cross stream distributions of the streamwise velocity. The quality of the fit at $x/h = 20$ is demonstrated in Figure I.17. Similarity arguments for conventional 2-D turbulent jets suggest that the volume flow rate per unit width i.e., $Q = \int_{-\infty}^{\infty} U dy$ increases like $x^{0.5}$. However, Figure I.18 shows that, at least within the domain of the present measurements, the normalized volume flow rate Q/Q_0 (where $Q_0 = U_0 h$) increases only like $x^{0.33}$. Nevertheless, despite the lower streamwise increase in volume flow rate compared to conventional jets, the net entrained volume flow rate of the synthetic jet within the domain $x/h < 10$ is $4Q_0$ which results from strong entrainment along the flat plate towards the jet orifice. Substantial entrainment is also maintained farther downstream and the net entrained volume flow rate within the domain $10 < x/h < 80$ is also $4Q_0$. The normalized volume flow rate in a conventional 2-D jet (computed from velocity measurements of Heskestad(1965) at $Re_h = 3.4 \cdot 10^4$) is also plotted for comparison in Figure I.18 (open symbols) and shows that although $Q \propto x^{0.5}$ for $x/h > 60$, it is considerably smaller than the volume flow rate of the synthetic jet indicating lower entrainment in the near field.

The invariance of the time-averaged momentum flux per unit width, i.e., $J = \rho \int_{-\infty}^{\infty} (U^2 + u'^2) dy$ in a conventional 2-D jet, is tacitly connected with the assumption that the static pressure within the jet is also streamwise invariant. The strong flow induced towards the actuator during the suction cycle indicates that the mean static pressure near the exit plane is lower than the ambient pressure. This is evident in measurements of the static pressure on the exit plane along $z = 0$ at different Reynolds numbers. The static pressure ports are equally spaced (2.3h apart), and unfortunately, owing to structural constraints, it is not possible to achieve better resolution near the jet orifice. The resulting pressure coefficient (normalized by ρU_0^2) in Figure I.19 shows that the mean static pressure near the jet orifice is lower than the ambient pressure and is consistent with the steady suction of ambient fluid towards the jet orifice as is evident in Figure I.11. Figure I.19 also shows for reference a line segment, which represents the radial decrease of the static pressure in the flow field of a 2-D potential sink (i.e., $p \propto r^{-2}$). These measurements

suggest the existence of an adverse streamwise pressure gradient near the jet orifice and consequently a streamwise decrease in the momentum flux of the synthetic jet. The streamwise variation of the momentum flux per unit width normalized by the average momentum flux of the ejected fluid is shown in Figure I.20. The closed symbols correspond to integration of the (fitted) hyperbolic cosine profiles (which near the jet exit plane yields a value near unity), while the open symbols are based on integral limits of half the centerline velocity (i.e., $-b < y < b$). The data set represented by open symbols is effectively based on measured velocity (rather than the fitted curve) and is included for reference. For a conventional self-similar flow, both curves should be streamwise invariant. However, the momentum flux of the synthetic jet decreases monotonically with streamwise distance. The decrease is further complicated by the spanwise nonuniformities in the jet cross section and the streamwise decrease in its aspect ratio as shown in Figure I.21. A single measurement taken at $x/h = 78.7$, suggests that far enough downstream ($x/h > 100$), the momentum flux asymptotes to a constant value around 0.55.

As noted by Kotsovinos and Angelidis (1991), the streamwise variation of the time-averaged momentum flux in plane (or axisymmetric) jets depends critically on the pressure field, and on the geometry of the jet. Based on data published by other investigators since 1957, these authors assert that in conventional jets emanating normal to a plane surface the momentum flux decreases with downstream distance. Variation in the streamwise rate of decrease among the different data sets results in momentum flux at $x/h = 80$ that is between 75% and 85% of the level at the exit plane (at $x/h = 0$).

The streamwise variation of the jet cross section in the y-z plane can be assessed from contours of the mean streamwise velocity at $x/h = 19.6$, 39.4, and 78.7 shown in Figures I.21a-c respectively (contours start at 1 m/s and the contour increment is 0.5 m/s). These plots indicate that the aspect ratio of the jet cross section (based on contour level of 1 m/sec) decreases from approximately 6 at $x/h = 19.6$ to 3 at $x/h = 78.7$. While near the exit plane ($x/h = 19.6$, Figure I.21a) the jet appears to be reasonably spanwise uniform, farther downstream, ($x/h = 39.4$, Figure I.21b) the cross-stream width of the jet near its spanwise edges is larger than at the mid span. At $z/h = \pm 55$, the streamwise velocity has local spanwise maximae, and the normalized momentum flux in these x-y planes is 1.16 compared to 0.58 at $z/h = 0$ which may be associated with the streamwise decrease in the jet aspect ratio. At $x/h = 78.7$, the centerline velocity is relatively low (2.8 m/sec) and the cross section of the jet appears to be slightly rotated about its centerline. Similar saddle-like distributions of the streamwise velocity were also observed in conventional high aspect ratio rectangular jets (Krothapalli et al., 1981, van der Hegge Zijnen, 1958).

Additional insight into the evolution of the synthetic jet may be gained from spectra of the streamwise velocity. Power spectra of the jet centerline velocity measured at $x/h = 5.9$, 9.8, 19.7, 98.4, and 177.2, are shown in Figures I.22a-e, respectively (each of the curves in Figures I.22b-e are successively displaced by seven decades, and the power spectrum at $x/h = 5.9$ is replotted for reference using a shaded curve). Near the jet exit plane (Figure I.22a), the spectrum is dominated by the formation frequency of the vortex pairs and its higher harmonics (although hot-wire rectification of velocity traces within this domain clearly contributes to the spectral contents at the higher harmonics), while the spectral distribution below the fundamental frequency is virtually featureless. The harmonics of the formation frequency are rapidly attenuated with downstream distance and by $x/h = 9.8$, only four harmonics are present. Concomitantly, there is also a significant increase in the magnitude of the spectral band below the formation frequency which is indicative of the decay of the vortex pairs and the development of the jet flow. However, with the exception of a weak band of spectral components centered around 10 Hz, which disappears by $x/h = 98$, the spectral band below the formation frequency remains featureless throughout the present domain of measurements and shows no evidence of sub-harmonics of the formation frequency.

20
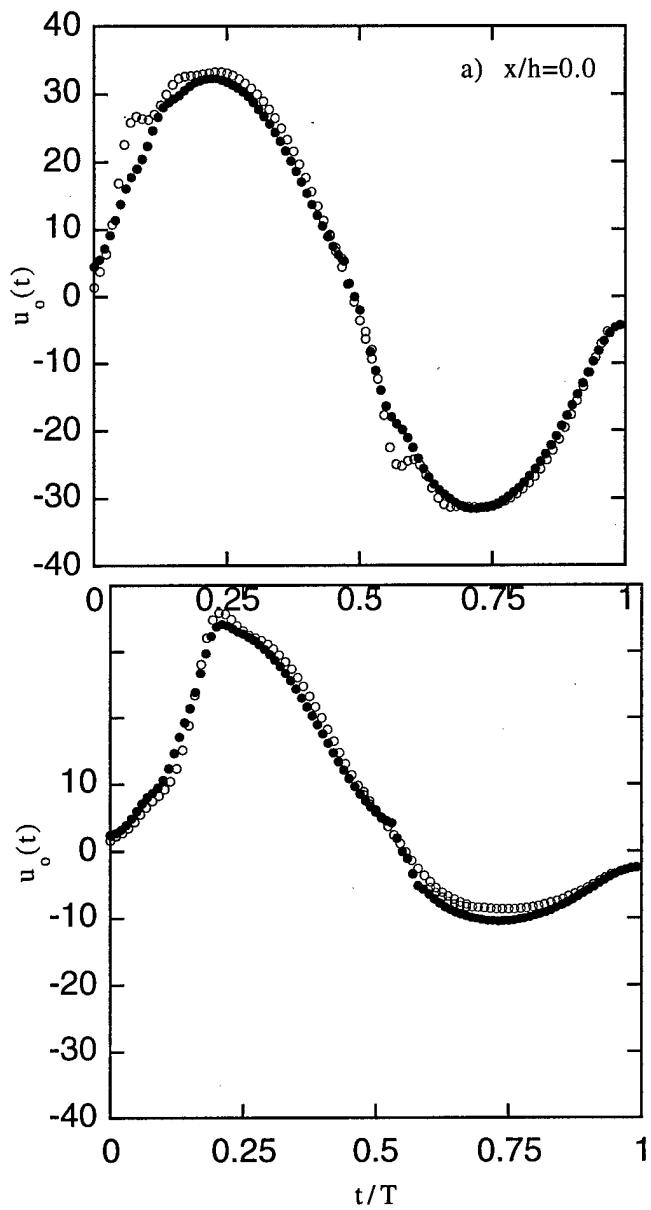
Figure I.13. Phase locked velocity on centerline of the synthetic jet at (a) x/h=0 and
(b) x/h=1.5. Open symbols are synthetic jet without a step. Close symbols are synthetic
jet with s=1.5h step.
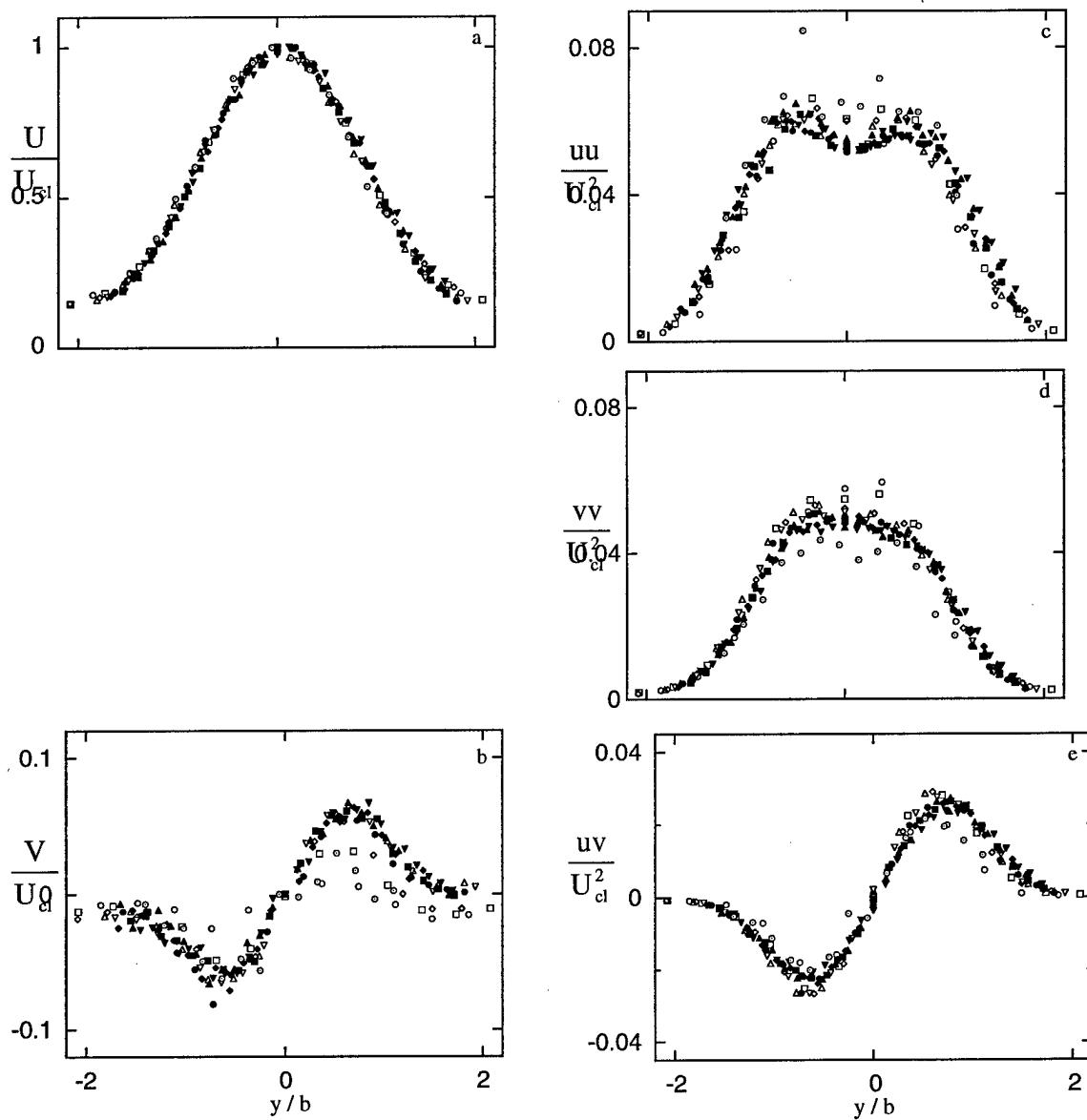
Figure I.14₂ Cross-stream distributions of: U/U_{cl} (a), V/U_{cl} (b), $u'u'/U^2_{cl}$ (c), $v'v'/U^2_{cl}$ (d), and $u'v'/U^2_{cl}$ (e), at x/h= 9.8 (O), 11.8 (□), 13.8 (◇), 15.7 (△), 19.7 (▽), 23.6 (●), 27.6 (■), 31.5 (◆), 35.4 (▲), 39.4 (▼), and 78.7(⊙). Re_{U_o}=383.
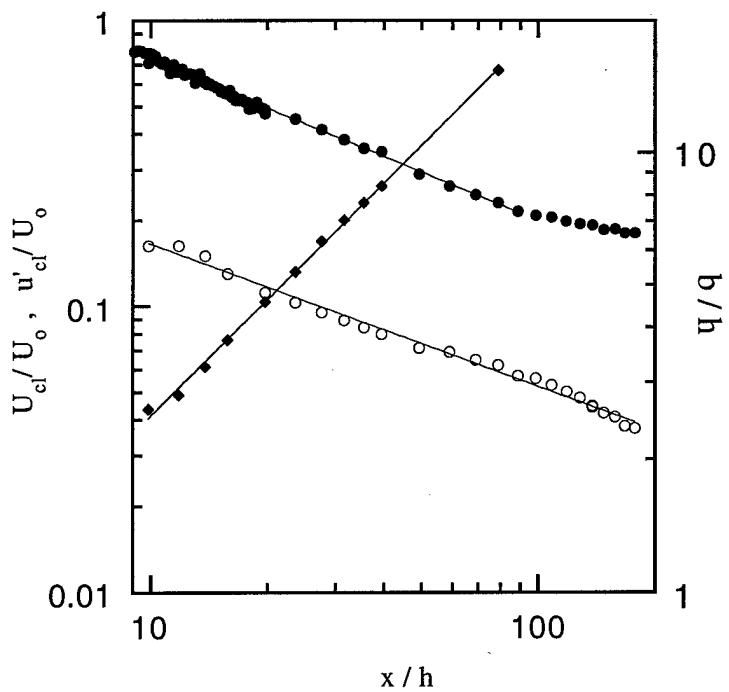
Figure I.15. Streamwise variation of: U (●), u' (O), and b (◆). $Re_{U_0} = 383$.
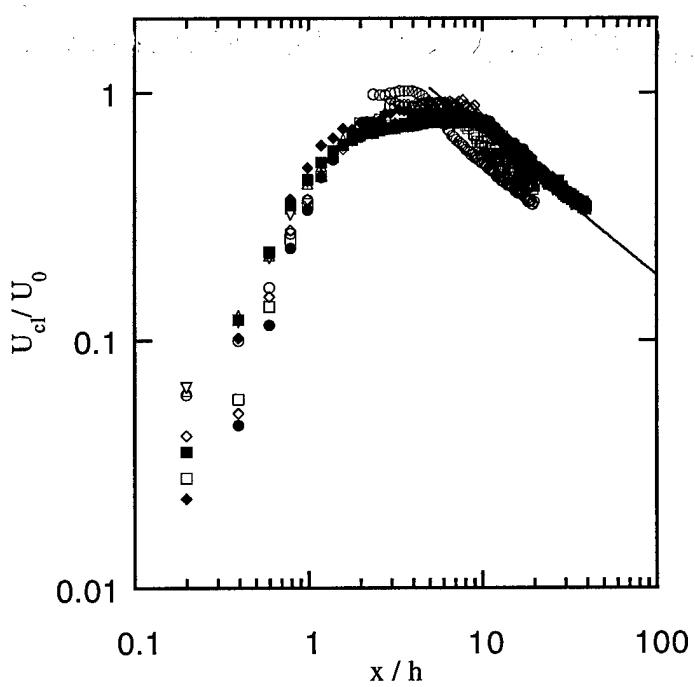
Figure I.16. Variation of centerline velocity $U_{cl}(x,t)$ with axial distance (symbols as in Figure I.7).
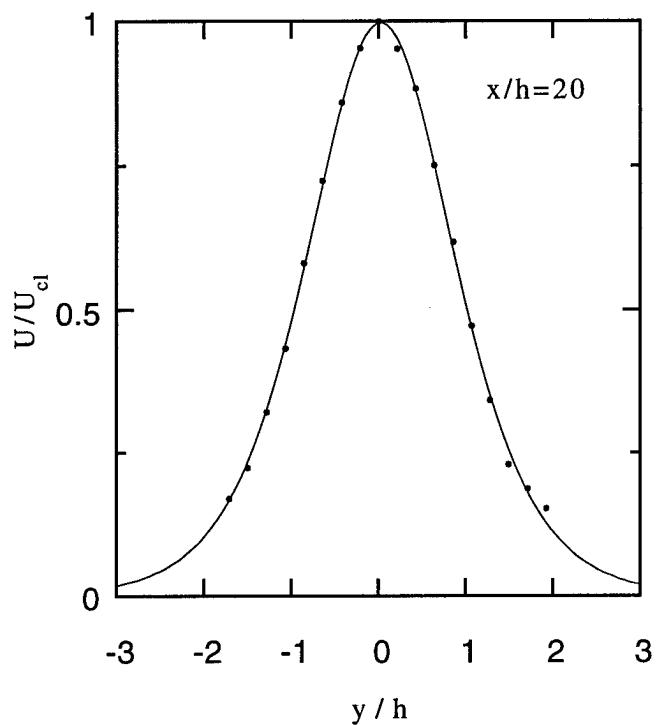
Figure I.17. Least-squares fit of a cross stream distribution of the mean streamwise velocity at x/h = 20 to a hyperbolic cosine function.
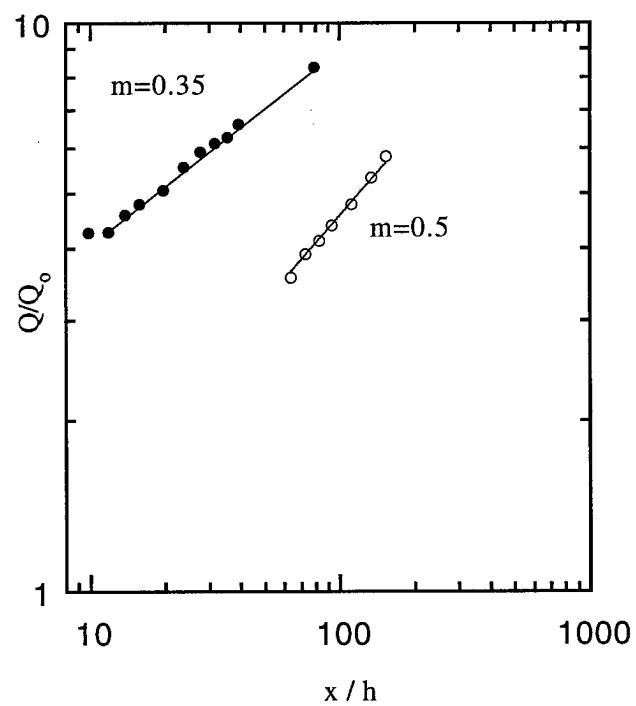
Figure I.18. Streamwise variation of the volume flow rate. The straight line segment denotes $Q \propto x^{0.5}$ (for self-similar 2-D jet).
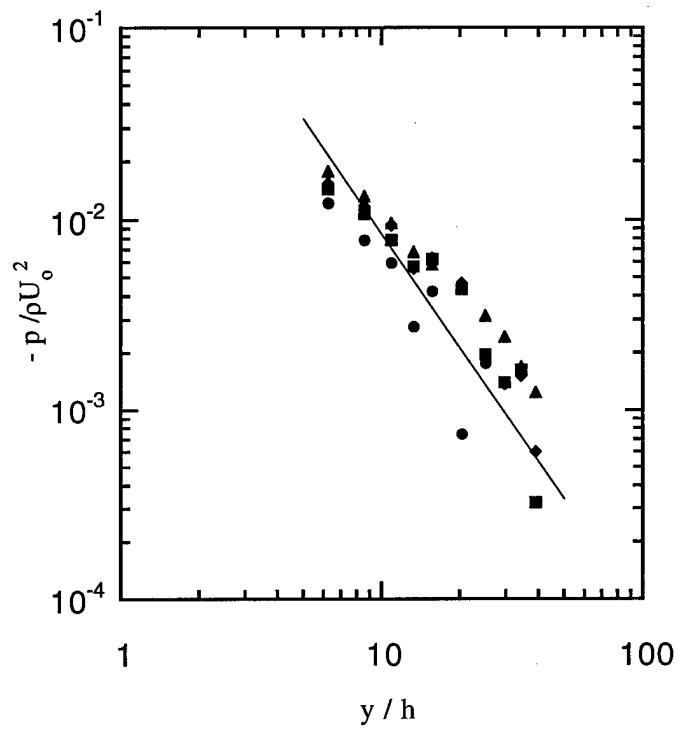
Figure I.19. Distributions of the pressure coefficient at the exit plane: $Re_{U_o}= 270$ (●), 383 (■), 424 (◆), and 489 (▲).
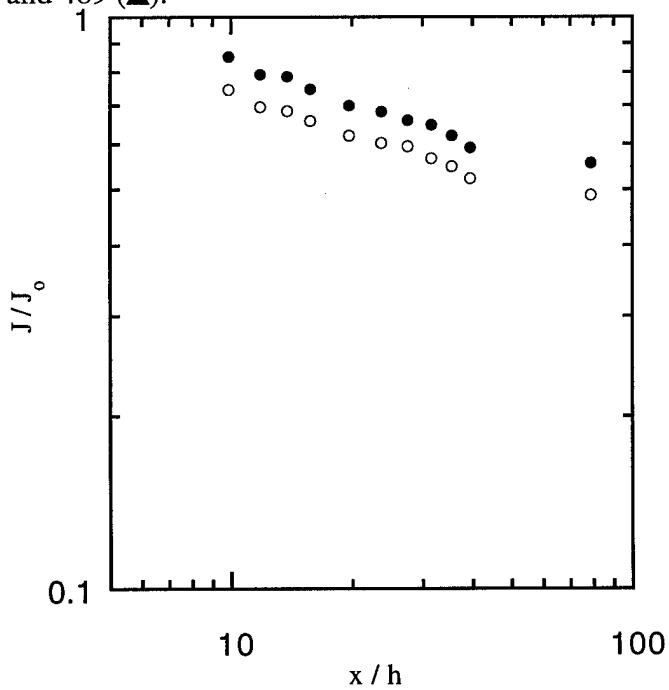

Figure I.20. Streamwise variation of the jet momentum flux based on fitted cos hyperbolic distribution, and on the velocity data for $-b < y < b$. $Re_{U_o}=383$.
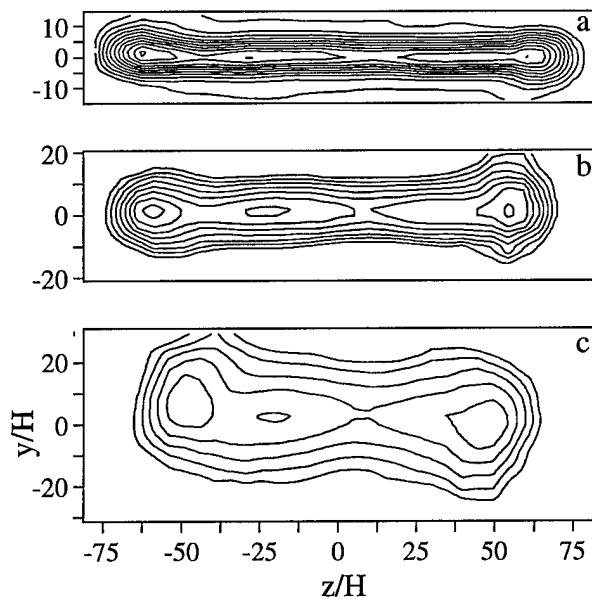
Figure I.21. Contour maps of the streamwise velocity in the y-z planes x/h = 19.7 (a), 39.4 (b), and 78.7 (c). The first contour is 1 m/s and contour increment is 0.5 m/s. Re_{U_o}=383.
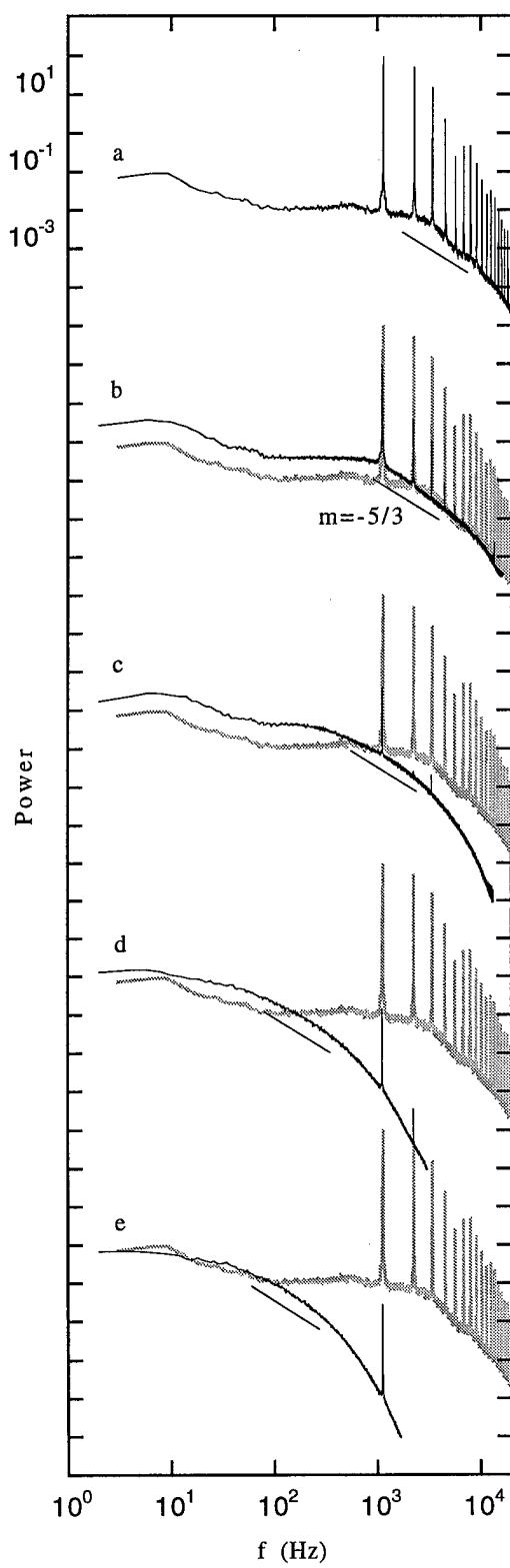
Figure I.22. Power spectra of the centerline velocity (each curve is successively displaced 7 decades): x/h = 5.9 (a), 9.8 (b), 19.7 (c), 98.4 (d), 177 (e). Re_{U_o}=383.

A striking feature of the velocity spectra in Figures I.22b-e is the rapid streamwise attenuation of virtually all spectral components indicating strong dissipation within the synthetic jet and a reduction in the total turbulent kinetic energy. The spectral decay is initially more prominent at frequencies that are above the formation frequency of the jet (Figures I.22a and b) while, as noted above, there is a concomitant increase in the magnitude of the spectral band below the formation frequency. Thus, it is conjectured that following the time-harmonic formation of discrete vortex pairs, energy is transferred from these primary ("large scale") eddies, which coalesce to form the jet, to the mean flow and also cascades down to smaller scales at which dissipation ultimately takes place. Farther downstream (Figures I.22c-e), the low frequency components of the jet are continuously attenuated and by x/h = 177 (Figure I.22e), the nominal magnitude of the band f < 100 Hz is comparable to the corresponding band near the jet exit plane suggesting energy transfer to the smaller scale. At the same time, the "roll-over" frequency (at which the low-frequency end of the spectrum begins to undergo a change in slope), moves towards lower frequencies (in Figure I.22c, the roll-over frequency is below the formation frequency). The spectral distributions in Figures I.22c-e also include a relatively narrow frequency band having a slope of approximately -5/3 suggesting the existence of an inertial sub-range which is limited by the low Reynolds number of the flow. It is noteworthy that because the characteristic local (centerline) velocity decreases with downstream distance, the spectral peak at the formation frequency actually shifts towards higher wave numbers where the dissipation ultimately takes place (e.g., Figure I.22e).

As mentioned in the discussion on the synthetic jet formation above, a notable feature of the synthetic jet is the absence of pairing interactions between the vortex pairs that form the jet and consequently the absence of sub-harmonic frequencies in spectra of the streamwise velocity component in Figure I.22. The phase-locked schlieren images in Figure I.3 indicate that the primary vortex pairs undergo transition and breakdown to smaller eddies and that the jet is ultimately formed by the coalescence of clusters of such smaller eddies. The breakdown of the spanwise vortex pair is alluded to by an abrupt and rapid decrease (around x/h = 10) in the magnitude of the spectral component at the forcing frequency, a_{fo} (Figure I.23). A line of slope -2, which would correspond to the $1/r^2$ decay associated with sound waves, is added for reference. This change is also apparent in the gray-scale raster plot of the auto correlation function $\rho(\tau,x)$ of the centerline velocity shown in Figure I.24. For (a fixed) large x, $\rho(\tau) > 0$ ($\rho(0,x) = 1$) and decays monotonically to zero for large τ as in other fully developed turbulent flows. However, as a result of the coherent vortex motion near the exit plane, the auto correlation is nominally time-harmonic with a zero cycle average (negative grayscale values are marked with contours). As x increases, ρ becomes gradually non-negative and although fluctuations at the forcing frequency are still apparent, their amplitude is considerably diminished indicating loss of coherence of the vortical structures. The streamwise domain where ρ becomes non-negative, coincides with the abrupt decrease in the amplitude of the spectral peak of the formation frequency (Figure I.23).

Finally, the spanwise correlation function R_{11} is measured along the z-axis at a number of streamwise stations using two single-element hot wire probes Δz apart (one of the sensors is located on the jet centerline). A contour plot of $R_{11}(x,\Delta z)$, (Figure I.25) shows that for x/h < 6, the jet is nearly spanwise-uniform (the highest contour level is 0.8) but that as a result of the transition process, R_{11} decreases rapidly with streamwise distance and at x/h ≈ 12 the spanwise coherence is almost lost. It is conjectured that similar to thin isolated vortex rings (in the experiments of Sturtevant as shown in Van Dyke, 1982), the instability of the vortex pair cores is quickly amplified because the high length to core diameter ratio (approximately 50). However, the spanwise correlation does not exhibit spanwise variations at the wavelength of the vortex core instability (e.g., Figure I.4) which indicates (as confirmed separately by flow visualization) that the instability is not locked to spanwise disturbances upstream of the jet orifice. The distortion of R_{11} near the edge of the jet suggests that the primary vortices bend in the streamwise direction. This distortion presumably occurs as a result of a local interaction

28
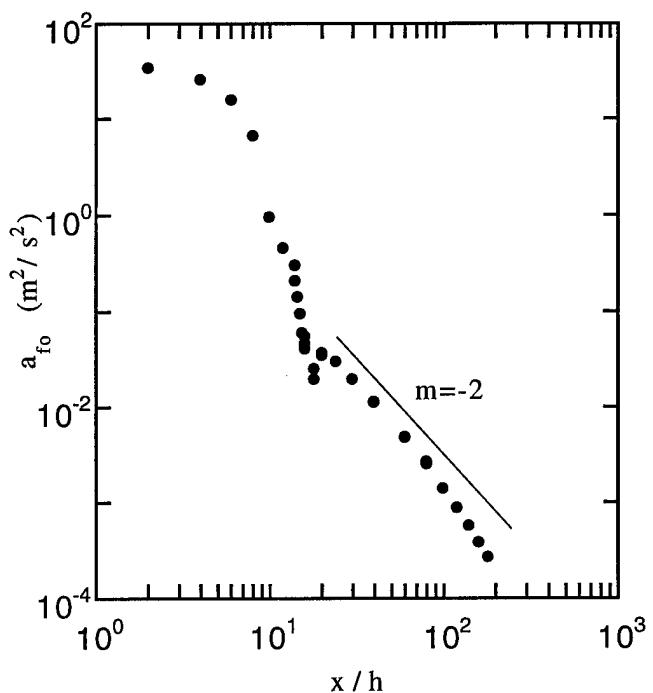
Figure I.23. Streamwise variation of the magnitude of the spectral component at the forcing frequency. Re_{U_o}=383.
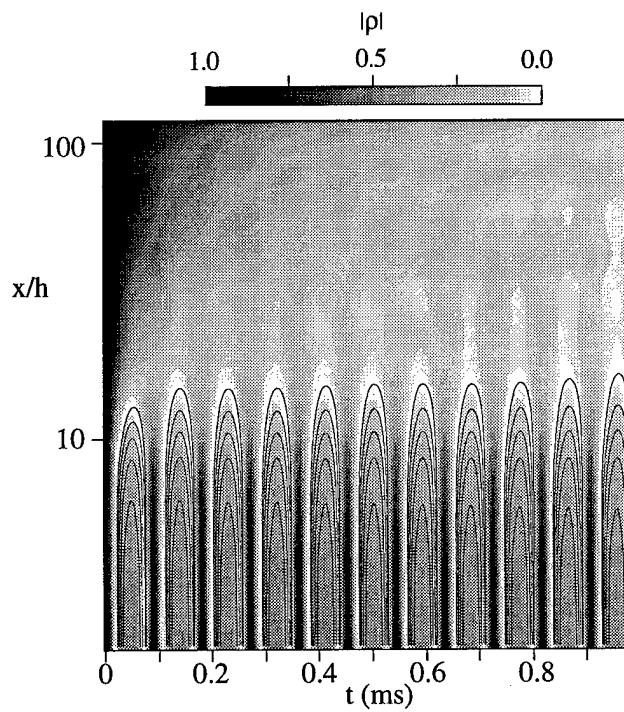

Figure I.24. Gray-scale raster plot of the autocorrelation function of the streamwise velocity $\rho(x,\tau)$. Negative levels are marked with contours (contour increment 0.1). Re_{U_o}=383.
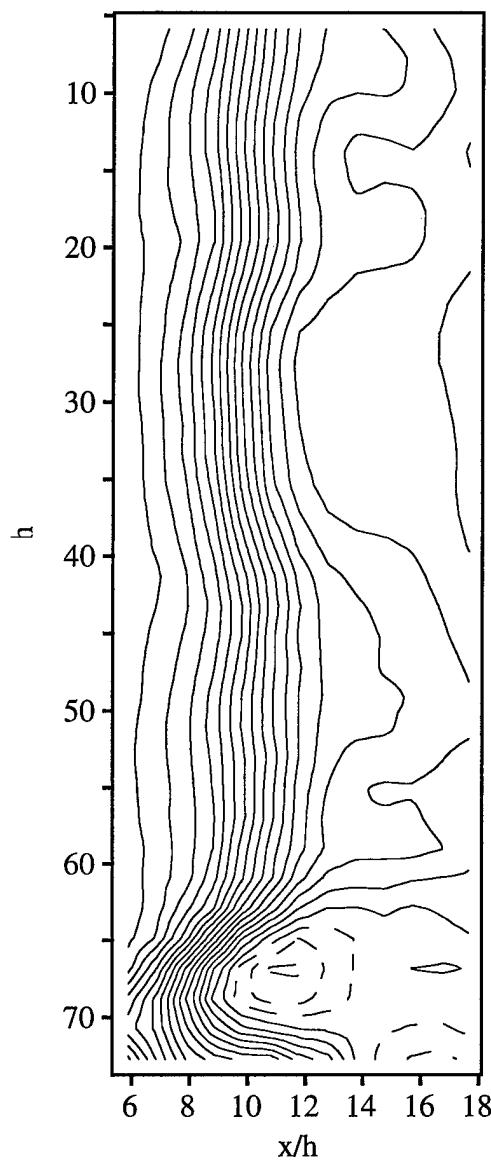
Figure I.25. Contour map of the spanwise correlation function of the streamwise velocity component $R_{11}(x,\Delta z)$. The lowest and highest contour levels are 0.8 and -0.15, respectively and the contour increment is 0.05. Re_{U_o}=383.

between the vortex pair and the vortex segment that forms along the short side of the jet orifice similar to the streamwise distortion of elliptic vortex rings in the cross stream view along their minor axes (e.g., Gutmark and Ho, 1983). Such a streamwise distortion is consistent with negative values of R_{11} near the edge of the jet and before the spanwise breakdown of the primary vortices takes place.

I.4 Conclusion

A high aspect ratio rectangular air jet is synthesized by the time-harmonic formation and subsequent interactions of a train of counter-rotating vortex pairs. Each pair is formed at the edge of an orifice of an otherwise sealed cavity by the motion of a flexible diaphragm that is mounted on one of the cavity walls and is driven at resonance. Even though the net mass flux out of the cavity during each cycle of the diaphragm motion is zero, the mass and hydrodynamic impulse of the ejected fluid are non-zero. The flow separates at the sharp edges of the orifice and the resulting vortex sheet rolls into a vortex pair which is advected away from the orifice under its own self-induced velocity. When the diaphragm begins to retract from the cavity, the vortex pair is already sufficiently removed and is thus relatively unaffected by the motion of the ambient fluid that is drawn into the cavity.

The evolution of the synthetic jet near its exit plane is dominated by the time-periodic formation and advection of these vortex pairs, which ultimately undergo transition to turbulence, slow down and lose their coherence. Schlieren visualization shows that despite the relatively high formation frequency of the jet, successive vortex pairs do not pair and the spectral band below the formation frequency in velocity spectra remains relatively featureless throughout the present domain of measurements. The passage of the vortex pairs is manifested by a strong time time-periodic component of the streamwise velocity which diminishes rapidly with downstream distance until the vortex pairs are no longer phase-locked to the excitation signal and become indistinguishable from the background flow. Spanwise flow visualization shows the appearance rib-like secondary vortical structures that are wrapped around the cores of the primary (spanwise) vortices which lead to the formation of spanwise-periodic cellular structure within the cores of the vortices and ultimately to their small scale breakdown.

The mean trajectories of vortex pairs at a given formation frequency scale with the "stroke" length L_0 regardless of the magnitude of the formation impulse and are comprised of three distinct domains that are characterized by changes in the vortex pair celerity. Following the formation process, the vortex pairs are advected at almost constant speed which scales approximately with $(I_o)^{1/3}$. After the transition to turbulence ($0.5 < t/T < 0.8$), the celerity decreases as $(t/T)^{-2}$ which is considerably faster than for an isolated turbulent vortex pair ($U_c \propto t^{-0.5}$). The celerity reaches a minimum at $t/T \approx 0.8$ and then increases again like $(t/T)^2$ until the vortex pair becomes indistinguishable from the jet flow ($x/h > 12$) and effectively moves with the mean flow of the jet. While the celerity of the vortex pairs decreases monotonically in the domain $x/h < 10$, the mean (centerline) velocity of the jet increases until it reaches a local maximum at $x/h \approx 7$ and then begins to decay monotonically.

The synthetic jet is similar to conventional 2-D turbulent jets in that cross-stream distributions of the time-averaged streamwise and cross stream velocity components and the corresponding rms velocity fluctuations u' and v' and the correlation u'v' appear to collapse when plotted in the usual similarity coordinates for conventional 2-D jets. However, compared to conventional 2-D jets, the streamwise decrease of the mean centerline velocity of the synthetic jet is somewhat higher ($x^{-0.58}$ vs. $x^{-0.5}$ for 2D jets). Also, the width of the synthetic jet b(x) (based on $U_{cl}/2$) increases like $x^{0.88}$ (for conventional 2-D jets, $b \propto x$), and its volume flow rate Q(x) increases like $x^{0.33}$ (for conventional 2-D jets $Q \propto x^{0.5}$). Despite the lower streamwise increase of b(x) and Q(x) of the synthetic jet, db/dx is almost twice the value measured for conventional 2-D jets at much higher Reynolds numbers (of order 10^4). Furthermore, even though dQ/dx is smaller than in

conventional jets, the net entrained volume flow rate of the synthetic jet within the present domain is nearly $4Q_0$ and substantially larger than for conventional 2-D jets.

This departure from conventional self similarity is associated with a streamwise decrease in the jet's momentum flux. While for conventional self-similar 2-D jets the momentum flux is presumably an invariant of the motion, the momentum flux of synthetic jets decreases with streamwise distance as a result of an adverse streamwise pressure gradient near the jet orifice that is associated with the suction cycle of the actuator and an induced mean static pressure which is lower than the ambient.

Finally, a striking feature of the velocity spectra of the synthetic jet is the rapid streamwise attenuation of virtually all spectral components indicating strong dissipation within the jet and reduction in the total turbulent kinetic energy. Following the time-harmonic formation of the discrete vortex pairs, energy is transferred from these primary ("large scale") eddies which coalesce to form the jet both to the mean flow and to smaller scales at which dissipation ultimately takes place. Ultimately, the spectral components within the (low) frequency band below the formation frequency begins to decay and the energy is transferred primarily to the smaller scales. Because the characteristic local (centerline) velocity decreases with downstream distance, the spectral peak at the formation frequency continuously shifts towards higher wave numbers where the dissipation ultimately takes place.

II. INTERACTION OF ADJACENT SYNTHETIC JETS

II.1 Introduction
The number of papers reporting continuous jet-jet interaction is rather limited (e.g. LePera and Vandsburger, 1997). The interaction of two adjacent rectangular synthetic jets at varying phase results in very unique effects, which may be attributed in part to the interaction of the generated vortex pairs. Lee & Reynolds (1985) demonstrated that small changes in the azimuthal formation of successive vortex rings in a circular jet can lead to changes in their trajectories and consequently to substantial changes in the far field structure of the jet (which the authors refer to as "bifurcation" or "blooming").

II.2 Apparatus and Measurements
The experiments are performed inside of a sealed glass enclosure measuring 86cm (x direction) by 61cm (y direction) by 41cm (z direction). The jet generator in the present investigation is comprised of two adjacent cavities that are each driven independently by piezoelectric disks. A pair of parallel rectangular jets is formed when the cavities and orifices are separated by a common partition along the long dimension of the orifices as shown schematically in Figure II.1. The width of each orifice is h = 0.508mm, the partition is 2.3h thick, and the orifice plate is 2.5h thick. Each orifice is 75mm long. Measurements of a single synthetic jet are conducted using the same hardware with the right orifice sealed. Each cavity is instrumented with a pressure transducer having a range of 1psid and a frequency response of 100kHz.

In order to determine the dependence of U_0 on the cavity pressure, the jet actuators are calibrated by placing a hot-wire sensor at the center of the orifice, and simultaneously measuring the instantaneous velocity and cavity pressure phase locked to the driving signal as shown for a single 2-D jet is shown in Figure II.2 (the rectification of the velocity traces is removed). For the purposes of this calibration, it is assumed that the velocity profile in the orifice is uniform. The calibration curves (Re_{U_0} versus cavity rms pressure) for the two sides of the actuator are shown in Figure II.3. Although the calibration does not depend on the drivers, it is very sensitive to frequency, as well as changes in the pressure on the jet exit plane and orifice geometry. In particular, when the jets are operated side by side, each orifice velocity varies with that of the other, as well as the phase angle between the two driving signals. Thus, the required input to generate identical $u_0(t)$ at all phases was determined prior to the experiments.
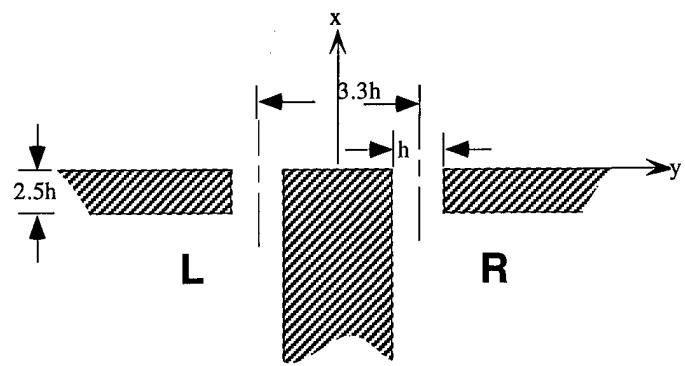
Figure II.1. Schematic diagram of 2-D adjacent jet generator.
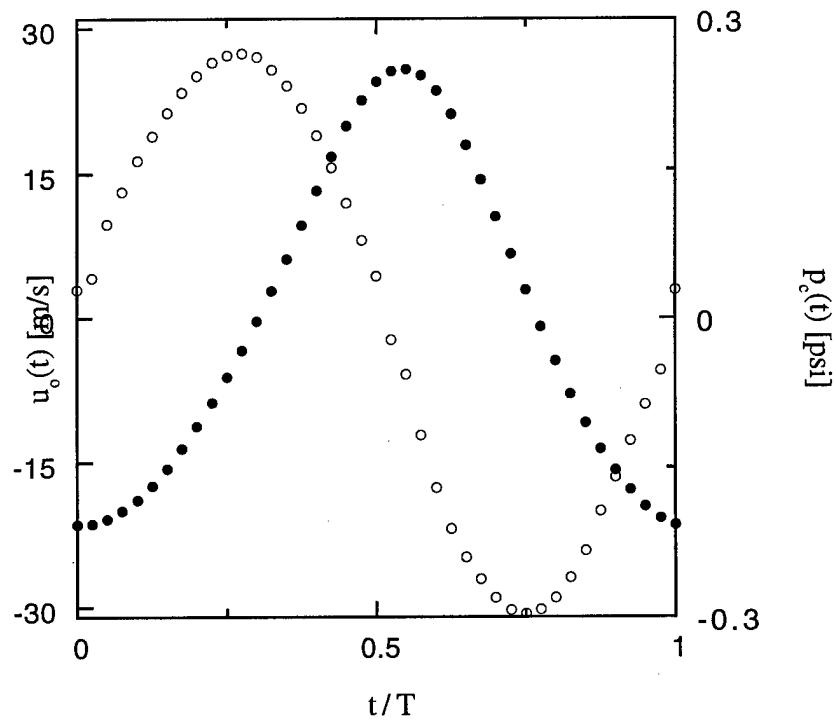
FigureII.2. Phase-averaged orifice velocity (o), and cavity pressure (●).

Figure II.3. Adjacent synthetic jet calibration data.

II.3 Results

The strong entrainment of ambient fluid that is induced by a zero mass flux jet near the orifice can be exploited for dynamic vectoring of the jet. Smith and Glezer, 1998 showed that when two high aspect ratio jets are placed side by side, so that they are parallel along the spanwise dimension of their orifices, the resultant jet can be effectively manipulated by varying the amplitude or the relative phase of the driving waveforms and thus modifying the formation and evolution of the vortex pairs of the adjacent jets. Figures II.4a-c show schlieren images of adjacent jets and demonstrates the effect of phase variation between two driving signals that have the same frequency and amplitude. The relative phase between the two waveforms is shown to the right of each image. When the two jets are in phase (Figure II.4a), the inner vortices of each vortex pair cancel each other resulting in a single, wider synthetic jet. When one of the jets is leading in phase (Figure II.4b), its vortex pair is formed first during the outward stroke of the excitation cycle while the neighboring actuator is still going through its suction stroke. The interaction between the adjacent vortex pairs (which are no longer horizontally aligned) and the effect of the suction from the neighboring actuator alters the vortex pair trajectories and the merged jet is vectored towards the actuator that is leading in phase (e.g., Figure II.4b for $\theta = 70°$). When the phase angle is $\theta = 130°$ (Figure II.4c), the merged jet becomes attached to the exit plane. The details of this interaction are one of the primary topics of the present investigation.

This section describes an investigation of the velocity field near the exit plane of an adjacent pair of rectangular synthetic jets that are operated at the same frequency (600Hz) and Reynolds number ($Re_{Uo} = 300$), but with driving signals which vary in phase. The measured domain is 37.3h square bounded by the orifice plate and centered in y on the jet partition.

Streamline maps of the mean flow of a single jet operated at 600Hz and 1100 Hz and of the adjacent jets operating at 600Hz are shown in Figures II.5a-c respectively. The contour increments are 0.223 Q_o, where Q_o is the mean orifice flow rate based on U_o. These data show only minor differences between the streamline maps of the single jet when it is operated at 1100 and 600Hz, and it appears that within the measurement domain, the flow rate and width of the jets are the same. It is noteworthy, however, that as a result of the orifice asymmetry, the single jet is slightly vectored to the left (i.e. away from the cavity partition). Similarly, when the right hand side jet is operated by itself, it is vectored to the right.

When the adjacent jets are operated simultaneously, the streamline maps demonstrate that the combined flow has a larger volume flux than the individual jets and that the entrainment of ambient fluid toward the jet orifice is stronger, as is evidenced by the angle of the streamlines on either side of the jet column. The cross section of the combined jet increases rapidly near $x/h = 10$.

Contour maps of phase-averaged spanwise vorticity measured at four equally spaced dimensionless time intervals ($t^* = t/T$) during the actuator period are shown in Figure II.6 for a single jet operating at 1100 Hz (a), and 600 Hz(b) and for the adjacent jets at 600Hz(c). Contour levels begin at $\omega^* = 0.071$ and the contour increments are $\omega^* = 0.142$, with one additional contour at $\square^* \pm 0.057$ indicating of the jet boundaries. Dashed lines indicate negative values. At t^* = 0.055, the vortex sheet in each shear layer at the orifice is beginning to roll into a vortex pair (2 pairs in case c). In each case, the remnants of the vortex generated during the previous stroke are visible farther downstream. At the peak of the blowing stroke ($t^* = 0.278$, Figure II.6.2), the new pair is almost fully formed. As shown above, the celerity (speed of the vortex cores) scales with the stroke length. Although in Figures II.6a and 6b the jet Reynolds numbers are the same, the ratio of the stroke lengths is equal to the inverse of the ratio of the actuation frequencies (at $Re_{Uo} = 300$, $L_o/h = 29$ for f = 600Hz and 16 for f = 1100 Hz). Therefore, the vortex pair travels farther downstream when the driving frequency is lower. It is also noted

that at the low frequency, there is more vorticity in the wake of each vortex, suggesting that the vortex is advected downstream before the rollup of the vortex sheet is completed (when the total circulation generated by the stroke exceeds the maximum that each vortex of the pair can contain before it pinches off and propagates downstream (Gharib et al., 1998). For all three cases, the suction stroke is accompanied by the presence of boundary layers on the surface of the exit plane at $0.528 < t^* < 1$ (Figure II.6 a-c.2-4).

The vorticity contours of the adjacent jets show four distinct vortices of alternating sign (Figure II.6.c.1). The two inner pair are stretched and apparently canceled by $t^* = 0.528$, leaving a single, larger pair. This pair has a lower celerity than the pair formed by the single jet at 600 Hz, but persists farther downstream. The evolution of this vortex pair is discussed in more detail below. Note also that the vorticity levels within the surface boundary layers are considerably higher than for the single jet, indicating a stronger flow along the wall of the exit plane.

The streamwise variation of the centerline velocity for these three cases is shown in Figure II.7. For the adjacent jets, the streamwise coordinate is normalized by 2h. When the velocity is scaled with the average orifice velocity for a single jet (U_o) the data collapse well in the far field, suggesting similarity.

Far-field similarity is also inferred from the plot of the jet width (Figure II.8). Here, the width b is the cross-stream location where the streamwise velocity is half of the corresponding centerline velocity (b for the adjacent jets is normalized by 2h). These data show reasonable collapse, although the width of the single jet does seem to depend on frequency.

The volume flow rate of the jet pair, Q^* ($Q^* = Q / Q_o$ for a single jet or $Q / 2Q_o$ for adjacent jets), is substantially larger than the corresponding flow rate of the single jet (Figure II.9). The flow rate of the single jet is invariant with frequency, and increases linearly with downstream distance through $\hat{x} = 25$, where it appears to undergo a slight change in slope. The streamwise increase in Q^* of the adjacent jets is two times higher in the near field ($\hat{x} < 6$) than for the single jet. Farther downstream ($10 < \hat{x} < 15$), dQ^* / dx^* for the adjacent jets is similar a single jet (0.16 for that adjacent jets and 0.13 for the single jet). It appears that the increased entrainment when the adjacent jet are operating is a result of the vortex dynamics within this domain. When the vortex interactions are completed ($\hat{x} > 6$) the entrainment rate remains relatively unchanged.

The variation of the streamwise momentum flux with downstream distance is plotted in Figure II.10 (the flux of the adjacent pair is normalized by twice the momentum flux of a single jet). In the far field, the momentum flux in all three cases decays to approximately the same level, which is lower than the far field level for a single jet for which $Re_{U_o} = 383$ jet (shown for reference) by an amount which scales linearly with the Reynolds numbers.

The trajectories of the vortex cores are determined by locating the coordinates of vorticity extremae (positive and negative) at each point in time, and are shown in Figure II.11. During the first half of the blowing stroke ($0.0 < t/T < 0.25$), the trajectory is similar for all three cases, which suggests that the interaction between adjacent vortex pairs in the adjacent jets is probably not very significant. These plots also indicate that the vortices in the adjacent jets are strongly affected by the suction flow (more so than in the single jet) and, as a result, experience stronger deceleration. It appears that the proximity of the vortices generated by the adjacent synthetic jets to the jet orifices and the stronger suction leads to a stronger deceleration of the vortices due to the suction stroke.
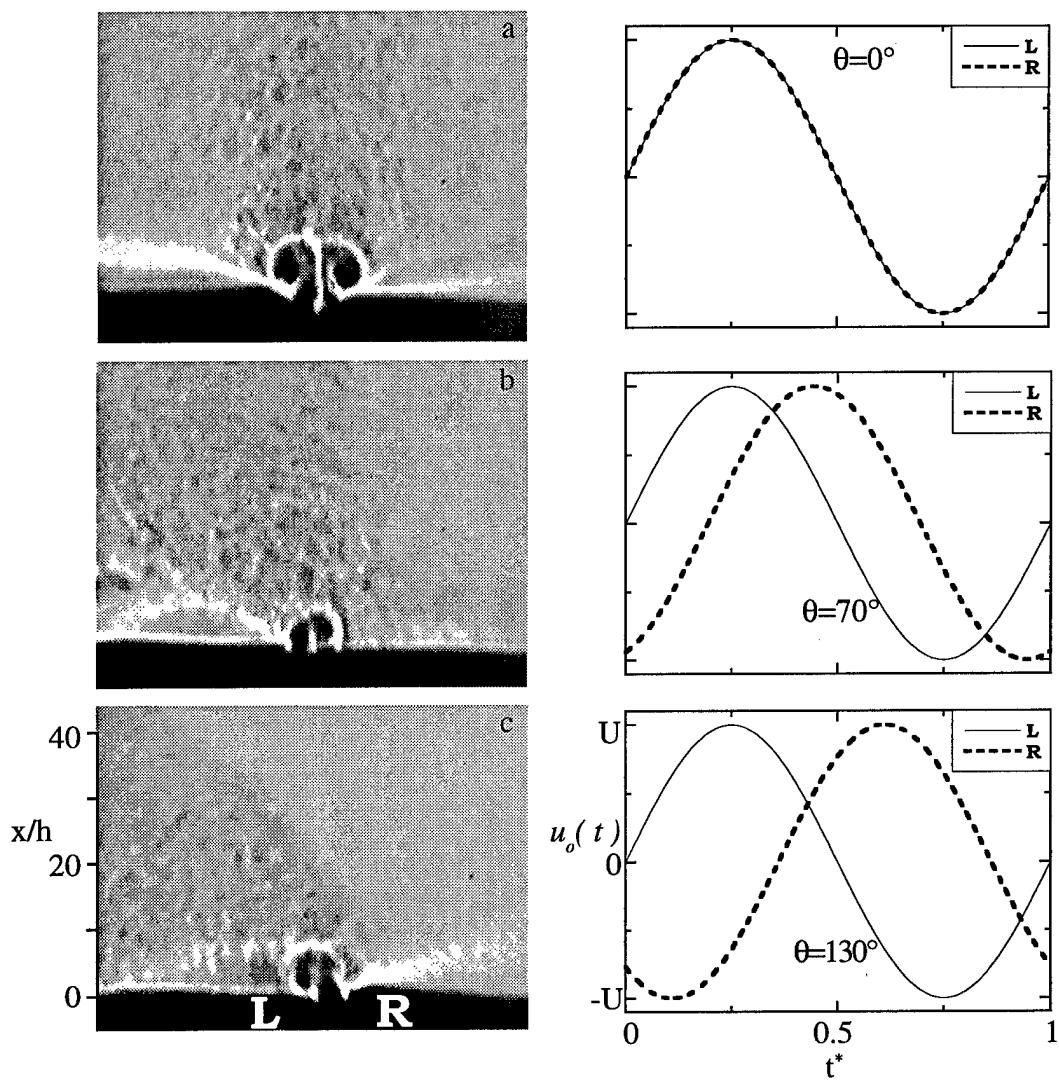
Figure II.4. Schlieren visualization of adjacent synthetic jets in the (x,y) plane for Re=300, f=600Hz. (a) θ=0°, (b) θ=60°, (c) θ=130°.
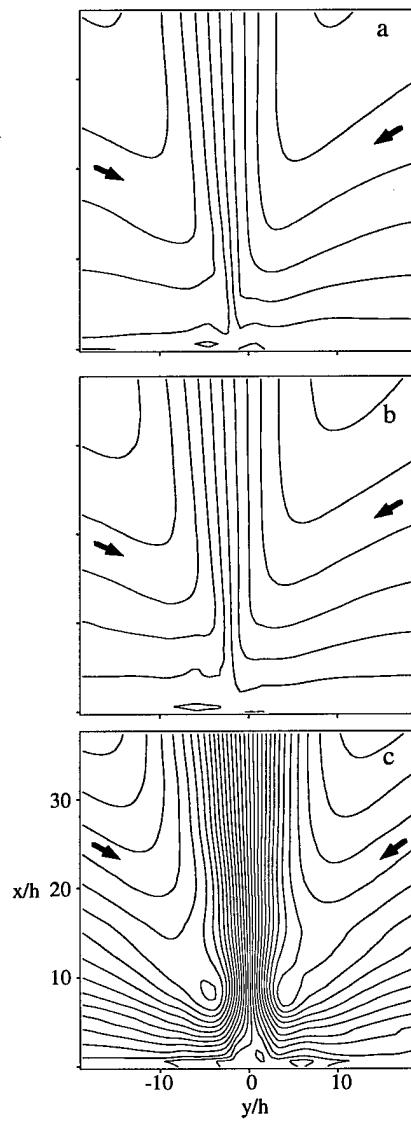
Figure II.5. Contour maps of the streamfunction of the mean flow for Re=300. Contour increment is 0.223 Q_o. (a) single jet at 1100Hz, (b) single jet at 600Hz, and (c) adjacent jets at 600Hz.
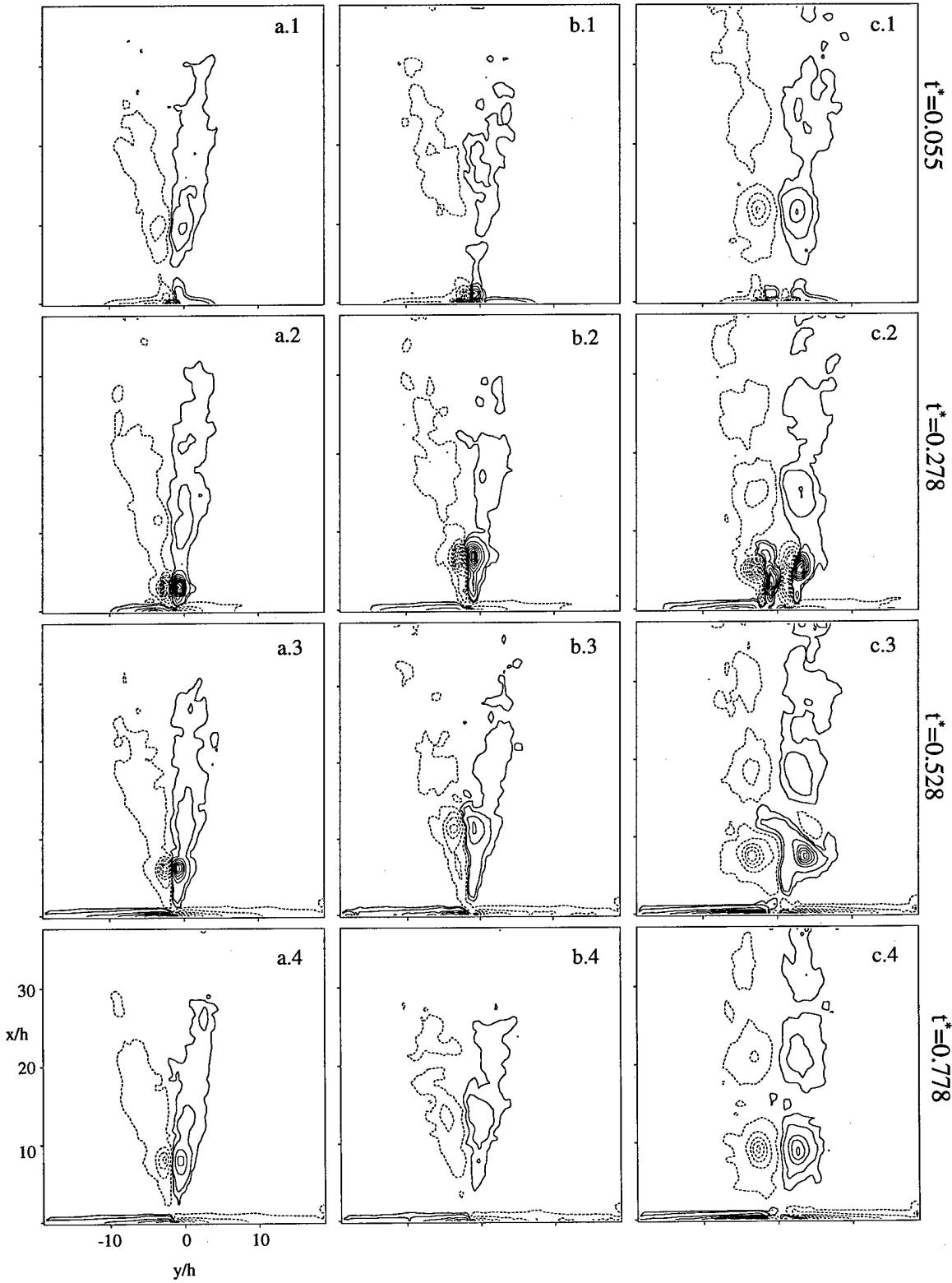
Figure II.6. Contours maps of the phase averaged spanwise vorticity, ω^*_z. Contour levels begin at $\omega^*_z = \pm 0.057$, the next level is ± 0.071, and thereafter the contour increments are ± 0.0142 (a) single jet at 1100Hz, (b) single jet at 600Hz, and (c) adjacent jets at 600Hz.
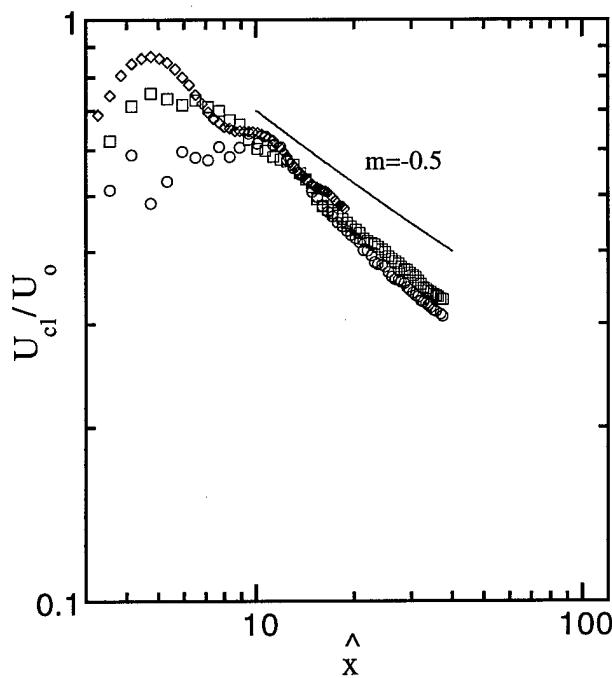
Figure II.7. Streamwise variation of U_{cl}, (□) single jet at 1100Hz, (o) single jet at 600Hz, and (◇) adjacent jets at 600Hz.
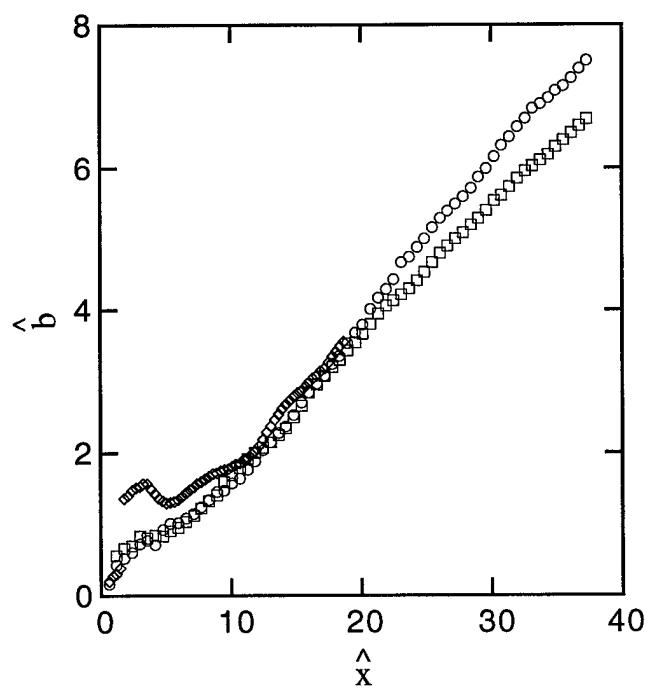
Figure II.8. Streamwise variation of jet width, (□) single jet at 1100Hz, (o) single jet at 600Hz, and (◇) adjacent jets at 600Hz.

When two adjacent synthetic jets are driven such that there is a phase difference between the two driving signals, the combined jet vectors toward the actuator that is leading in phase (cf. Figure II.4). Although a given excitation input results in a given orifice velocity $u_o(t)$ of the individual jets, when the adjacent jets are operated in concert, $u_o(t)$ varies with phase angle, ostensibly as a result of variation in the pressure field outside the jet cavities. Thus, in the present investigations, the Reynolds numbers of the adjacent jets are set at $Re_{U_o} = 300$, and the amplitude of the cavity pressure fluctuations required to maintain a fixed Reynolds number over the entire range of phase angles is determined iteratively at each phase angle by adjusting the input signal amplitudes until $Re_{U_o} = 300$ in each orifice, and noting the pressure fluctuation amplitudes in both cavities.

The vectoring is shown in streamline maps in the x-y plane at midspan where the adjacent synthetic jets are operating at increasing phase angles (Figure II.12). The contour increments are $0.223\ Q_o$. The actuator on the left, (L) is leading the actuator on the right (R), by phase angle θ.

At $\theta = 0°$ (Figure II.12a), the combined jet is symmetric, and the entrained flow that originates along y/h = ±18 (i.e. at the left and right edges of the measurement domain) is directed toward the exit plane. Streamlines beginning at x/h < 20 bend sharply toward the exit plane, while farther downstream, the angle of the entrainment flow is nearly perpendicular to the jet axis and resembles a typical jet.

When the phase angle is increased to 10°(Figure II.12b), the combined jet begins to vector to the left. The entrained flow becomes asymmetric and appears to be stronger on the left. At 30° (Figure II.12d), there is increased flow from the left (18 streamlines enter from the left side of the domain as compared with 14 from each side at $\theta = 0°$), while the flow from the right is reduced by a similar amount. A similar trend continues through $\theta = 60°$ (Figure II.12g).

At $\theta = 70°$ (Figure II.12h), the increased vector angle results in a smaller region from which to entrain fluid, while the flow rate through this region is larger than at lower phase angles, resulting in what appears in the mean to be a closed recirculation region. Examination of the individual velocity field realizations shows this is to be an unstable phenomenon at this phase angle, and the associated velocity fluctuations are large. When the phase angle is increased further, the bubble becomes trapped between the jet and the exit plane, and the jet is attached to the left hand side of the exit plane (Figure II.12i). The jet is considerably weaker in this state compared to the unattached cases ($\theta < 80°$), since a significant part of the jet is recirculating. As the phase angle exceeds 90° (Figure II.12k), the recirculation bubble becomes smaller, and the flow rate of the jet increases. The flow rate of the vectored jet begins to decrease again when $\theta > 120°$ because some of the fluid ejected from the right hand side actuator is sucked into the left-hand side actuator. At $\theta = 180°$ (not shown), most of the ejected fluid from each actuator is sucked into the adjacent actuator and very little flow is generated in the field.

In what follows, we use the notation defined in the sketch in Figure I.13. Each actuator (L and R) produces counter-rotating vortex pairs denoted L-L+ and R-R+. These pairs merge in most cases to a single vortex pair M-M+. The corresponding maps of vorticity measured phase-locked to the excitation waveform are plotted in Figure II.14. Contour levels begin at $\omega^* = \pm 0.071$, and the contour increments are $\omega^* = \pm 0.142$. An additional contour at $\omega^* = \pm 0.057$ is added to indicate the jet boundaries.

Figure II.14a shows that for $\theta = 0°$, four vortices of equal strength and alternating sign are formed near the exit plane, while the combined pair from the last cycle (M-M+) is visible near x/h = 7 and remnants of the pair created 2 cycles before are visible at x/h = 12. When the phase angle is increased to 10°, L-L+ is slightly ahead of R-R+. However, M-M+ is tilted to the left.

41

Figures II.14 c-g show that M-M+ becomes more diffuse as the phase angle increases. There is also an increased tendency for the initial vortices of the same sign to merge rather than to cancel. When θ exceeds 60°, the vortex pairs from the adjacent actuators are merged to a single pair such that the positive vorticity concentration is on the left-hand side (Figures II.14f-h). The axis of the merged pair (normal to the line that connects their centers) is tilted at the nominal vectoring angle of the combined jet. At the same time, a significant part of the combined jet forms a closed recirculation bubble. This recirculation is evidenced by the presence of positive vorticity within the boundary layer on the left-hand side surface that appears to be strongest in Figure II.14h (when the recirculation of the mean flow is strongest). The absence of significant vorticity concentration within the boundary layer on the right hand side surface suggests that the entrainment velocity there is considerably smaller. When θ > 90°, the separation between the vortices is sufficient that they do not merge, and the recirculation bubble, which is apparent from the presence of a positive vorticity patch on the left surface becomes weaker and ultimately disappears around θ = 110°. The jet is completely attached to the surface and the vortex pairs appear to simply follow the trajectory of the mean flow. It is interesting to note that for θ = 130°, the negative vorticity concentration near the wall is considerably stronger that the positive vorticity concentration, ostensibly because it is reinforced by the mean flow. The three domains of θ that characterized the vectored jet: free vectoring (θ ≤ 70°), attached flow with recirculation (80° < θ < 100°) and attached flow without recirculation (θ ≥ 110°) are now investigated in detail using phase averaged vorticity distributions.

Figure II.15 shows a sequence of phase-averaged vorticity plots in the x-y plane for θ = 0° at equally spaced time increments within the excitation waveform beginning at $t^* = 0.083$ and incrementing by 1/36. The contour levels begin at $\omega^* = \pm 0.071$ and contour increments are 0.142. The vortices L-L+ and R-R+ form simultaneously, and for $t^* < 0.166$, all four vortices are of similar size. The cross-section of the vortices L+ and R- vortices appear to stretch in the streamwise direction and by $t^* = 0.277$ (Figure II.15h), they each begin to wrap around the vortices L- and R+, which aids in the mixing of the vorticity contained in L+ and R- by $t^* = 0.361$ (Figure II.15k). Of particular interest is the vorticity contained within the boundary layers due to the induced flow along the walls. This vorticity begins to evolve at $t^* > 0.194$ as a result of the flow induced by the vortex pairs, and later on is enhanced by the suction flow that begins at $t^* = 0.25$. At the end of the suction cycle and before a new pair is formed, the vorticity within the wall boundary layer appears to be negligible.

When θ = 60° (Figure II.16), L is leading in phase and hence L-L+ emerges before R-R+. It is clear that L- is weaker than L+. Presumably, the reason for this imbalance is the suction that is still effected by R. As a result, L-L+ begins to tilt to the right, and by the time R-R+ appears ($t^* = 1/4$, Figure II.16g), L-L+ has convected significantly to the right. The suction stroke of the L begins at $t^* = 1/4$, and is evidenced by the boundary layer vorticity present on the left side of the exit plane. The suction induced by L leads to the formation of a stronger R- so that R-R+ is beginning to tilt to the left. Similar sign vortices within the left and right pairs merge into a single vortex pair, M-M+, (Figure II.16n), and the resultant pair advects to the left along the centerline of the vectored jet. The left tilt of the merged pair is probably aided by the suction flow into L.

Figure II.17 is a similar sequence for θ = 80°. The previous pair, M-M+, is located at x/h = 5 and y/h = 6 at $t^* = 0.06$, and the line connecting the vortex centers is nearly vertical. Although the jet is now attached to the exit plane, the imbalance between the strength of the vortices L-L+ is the same as for 60□, and L-L+ tilts to the right as shown in Figure II.17c. The reason for the radical difference in the vectoring angle of the mean combined jet is the vortex dynamics that result in a vertical resultant pair. Shortly after emerging, L- is weakened, (perhaps by the presence of vorticity of the opposite sign in the boundary layer), L+ catches up with and overtakes L- near the time when the blowing cycle of R begins (Figure II.17j). The vortex pairs merge as before, resulting in a nearly vertical pair M-M+, where the vorticity within M- is much more concentrated than in M+, and therefore M-M+ continues to rotate and is advected to the left.
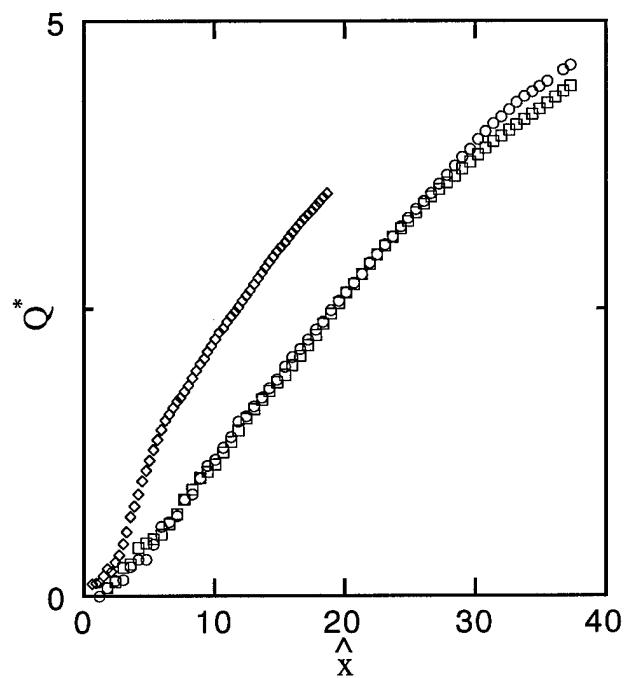
Figure II.9. Streamwise variation of volume flow rate, (□) single jet at 1100Hz, (○) single jet at 600Hz, and (◇) adjacent jets at 600Hz.
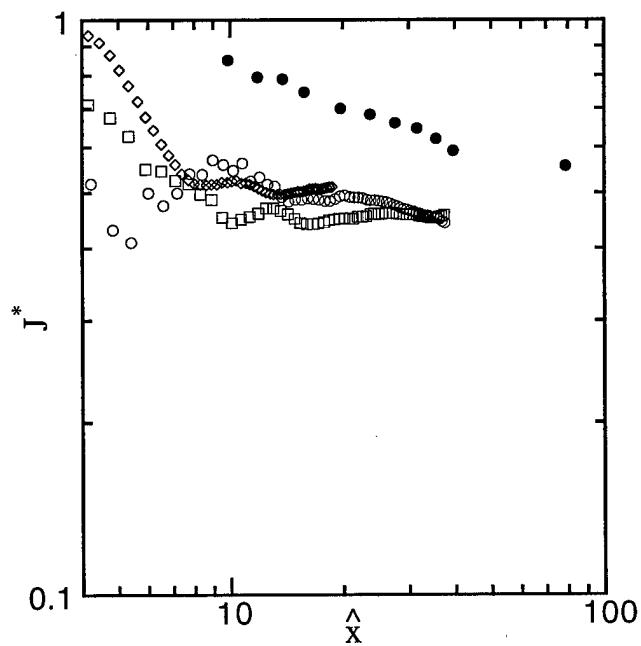
Figure II.10. Streamwise variation of momentum flux, (□) single jet at 1100Hz, (○) single jet at 600Hz, and (◇) adjacent jets at 600Hz. Data from Figure I.20 for Re=383, f=1120 (●).
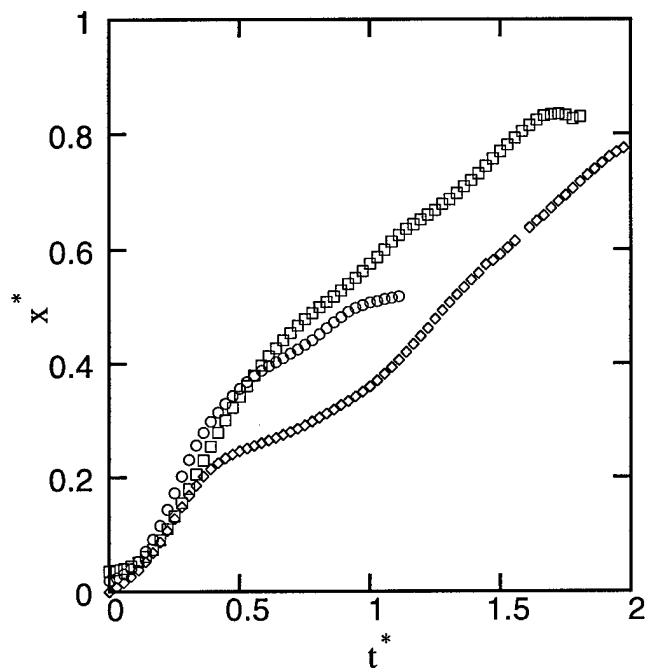
Figure II.11. Vortex pair trajectory, (□) single jet at 1100Hz, (○) single jet at 600Hz, and (◇) adjacent jets at 600Hz.
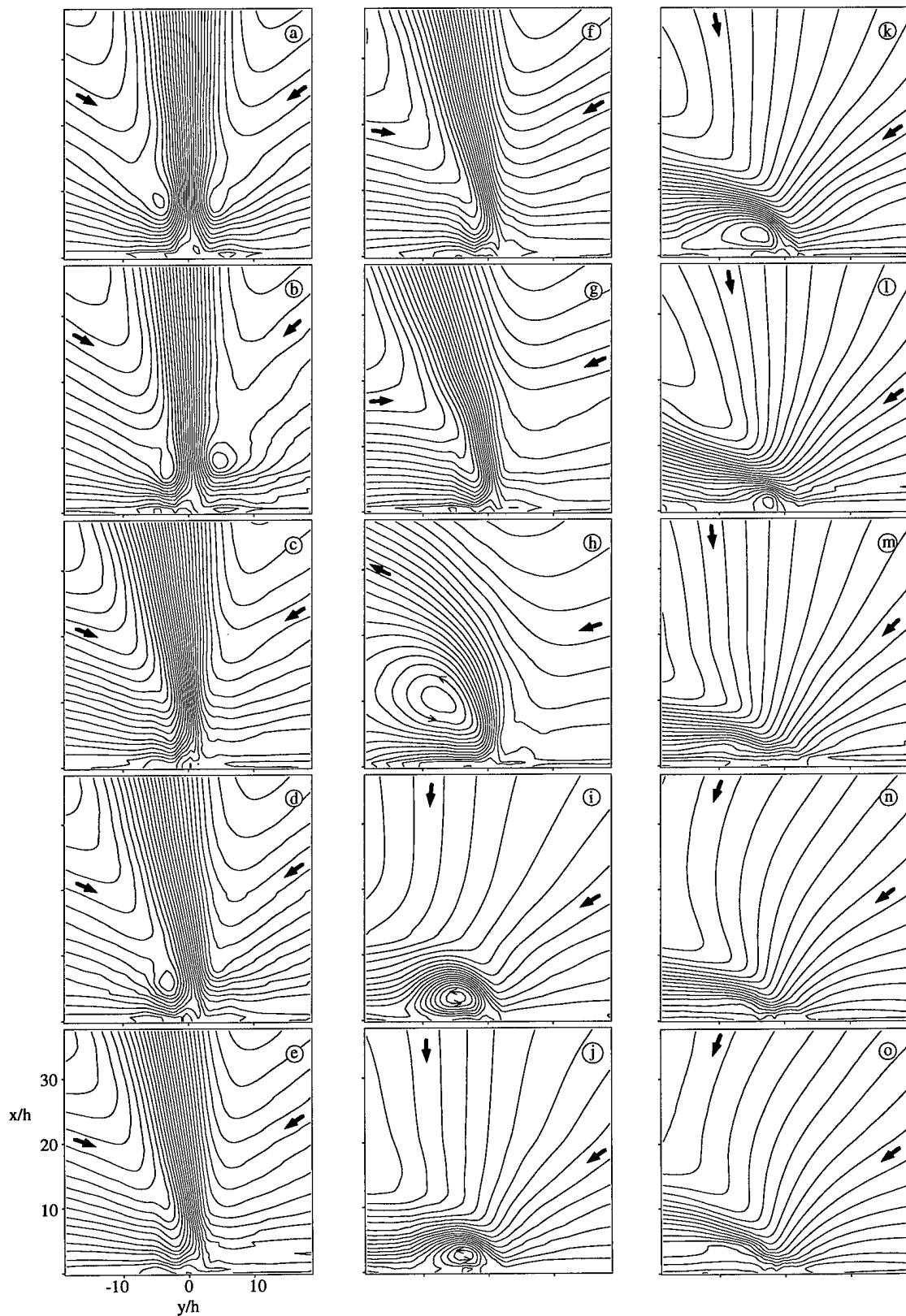
Figure II.12. Contour maps of the streamfunction of the mean flow for adjacent jets. Contour increment is 0.223 Q_o. (a) $\theta=0°$, (b) $\theta=10°$, (c) $\theta=20°$, (d) $\theta=30°$, (e) $\theta=40°$, (f) $\theta=50°$, (g) $\theta=60°$, (h) $\theta=70°$, (i) $\theta=80°$, (j) $\theta=90°$, (k) $\theta=100°$, (l) $\theta=110°$, (m) $\theta=130°$, (n) $\theta=150°$, and (o) $\theta=170°$.
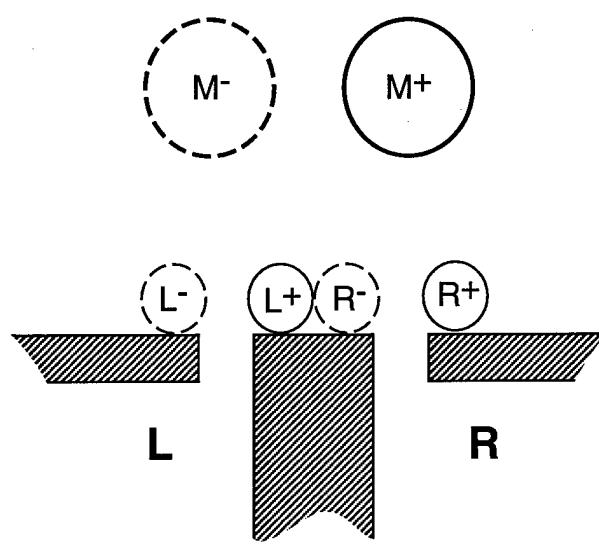
Figure II.13. Schematic diagram of vortices generated by adjacent synthetic jets.
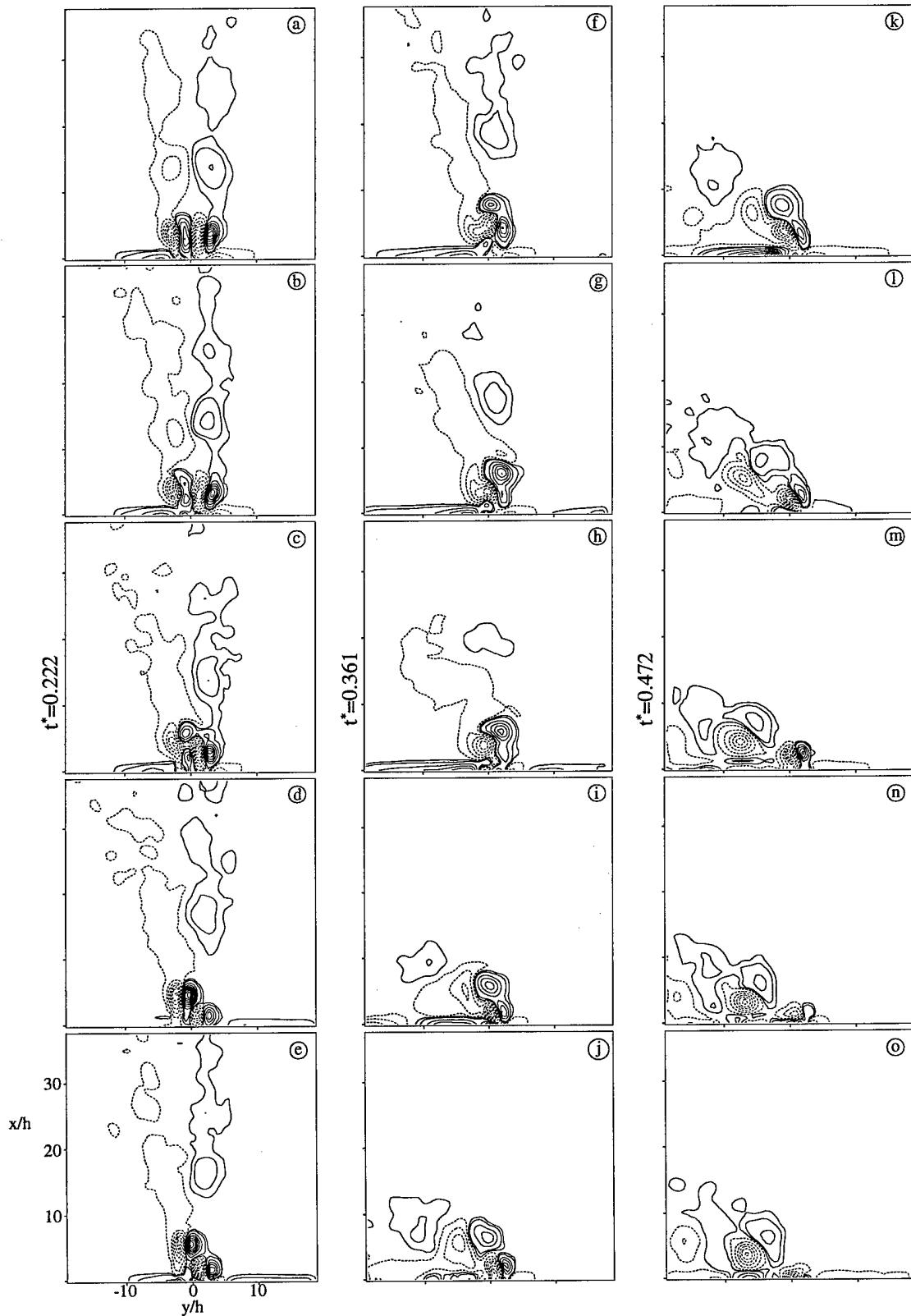
Figure II.14. Contours maps of the phase averaged spanwise vorticity, ω^*_z. Contour increments are the same as Figure II.6. (a) $\theta=0°$, (b) $\theta=10°$, (c) $\theta=20°$, (d) $\theta=30°$, (e) $\theta=40°$, (f) $\theta=50°$, (g) $\theta=60°$, (h) $\theta=70°$, (i) $\theta=80°$, (j) $\theta=90°$, (k) $\theta=100°$, (l) $\theta=110°$, (m) $\theta=130°$, (n) $\theta=150°$, and (o) $\theta=170°$.
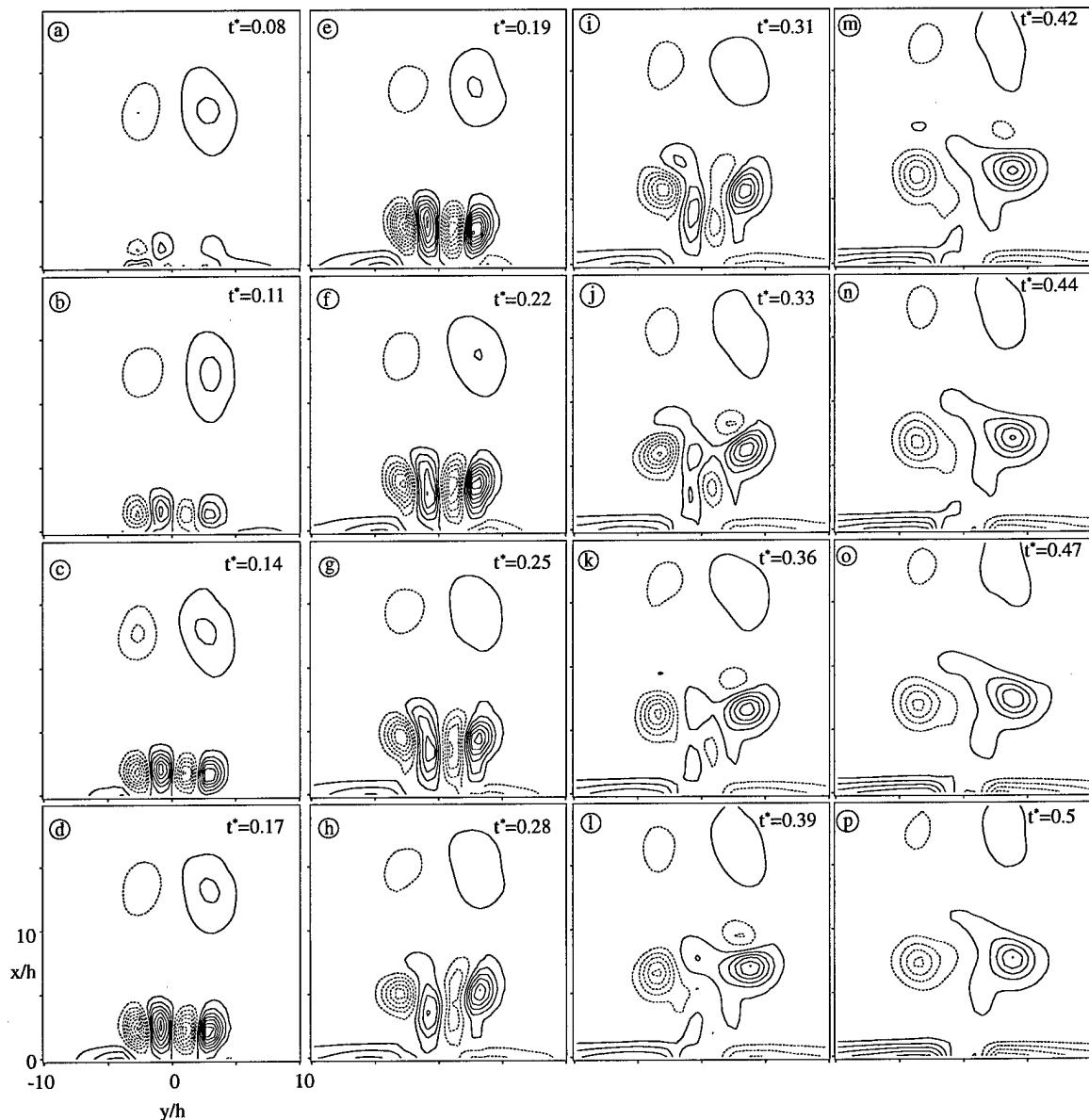
Figure II.15. Contours maps of the phase averaged spanwise vorticity, ω^*_z for $\theta=0°$. First contour at $\omega^*_z = \pm 0.071$, and increments are ± 0.0142.
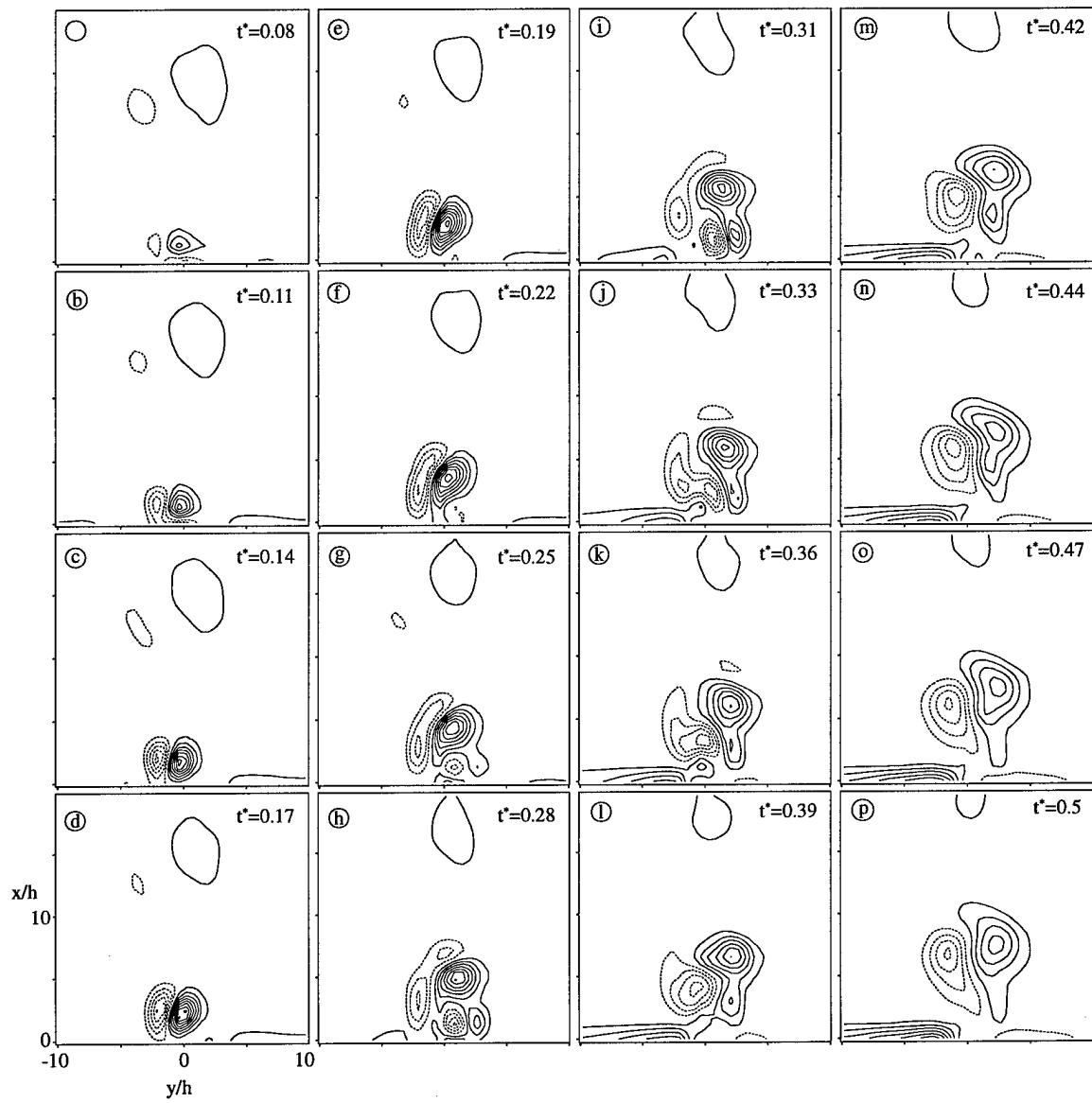
Figure II.16. As in Figure II.15 for θ=60°. First contour at $\omega^*_z = \pm 0.071$, and increments are ± 0.0142.
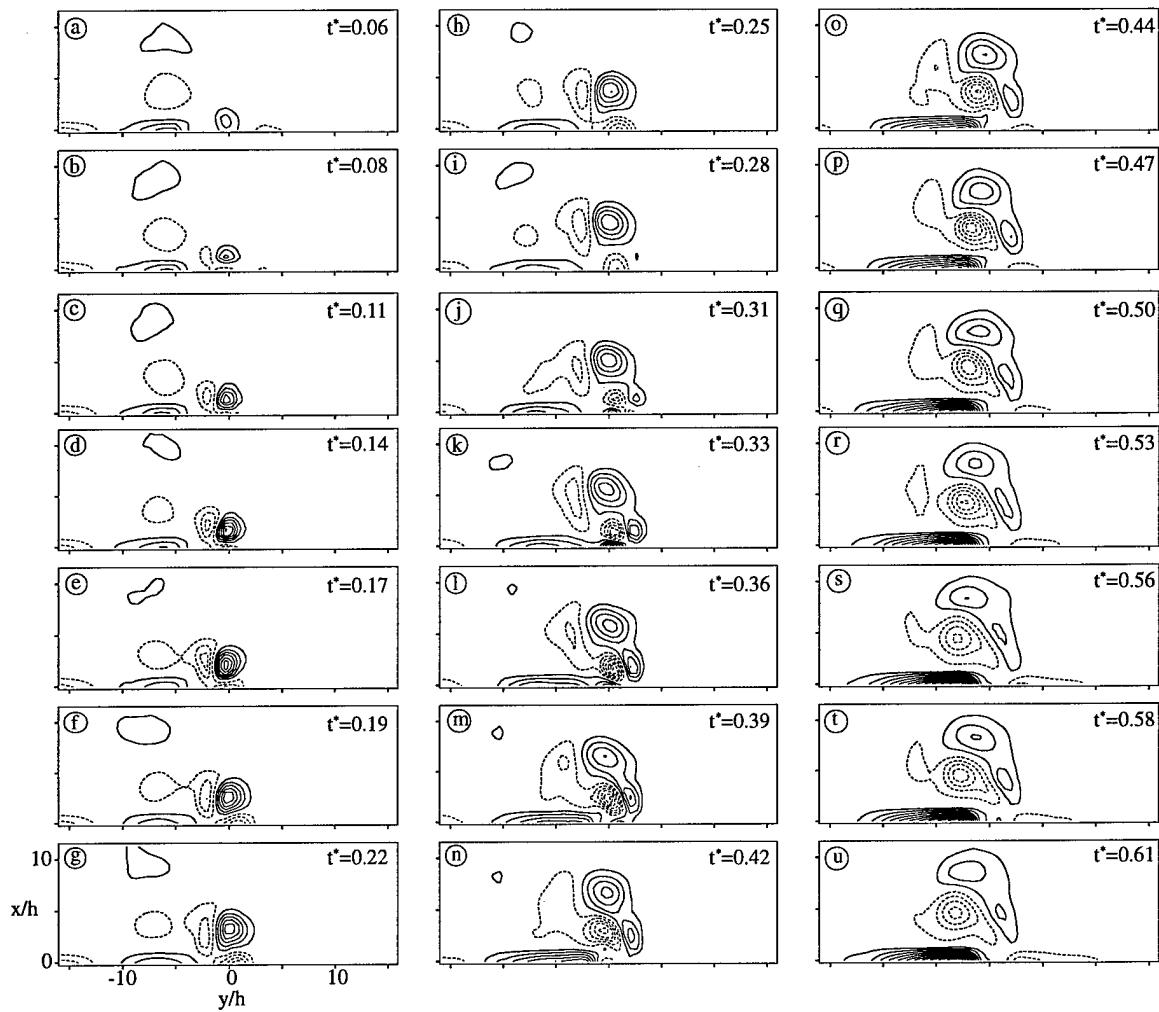
Figure II.17. As in Figure II.15 for $\theta=80°$. First contour at $\omega^{*}_{z}= \pm 0.071$, and increments are ± 0.0142.
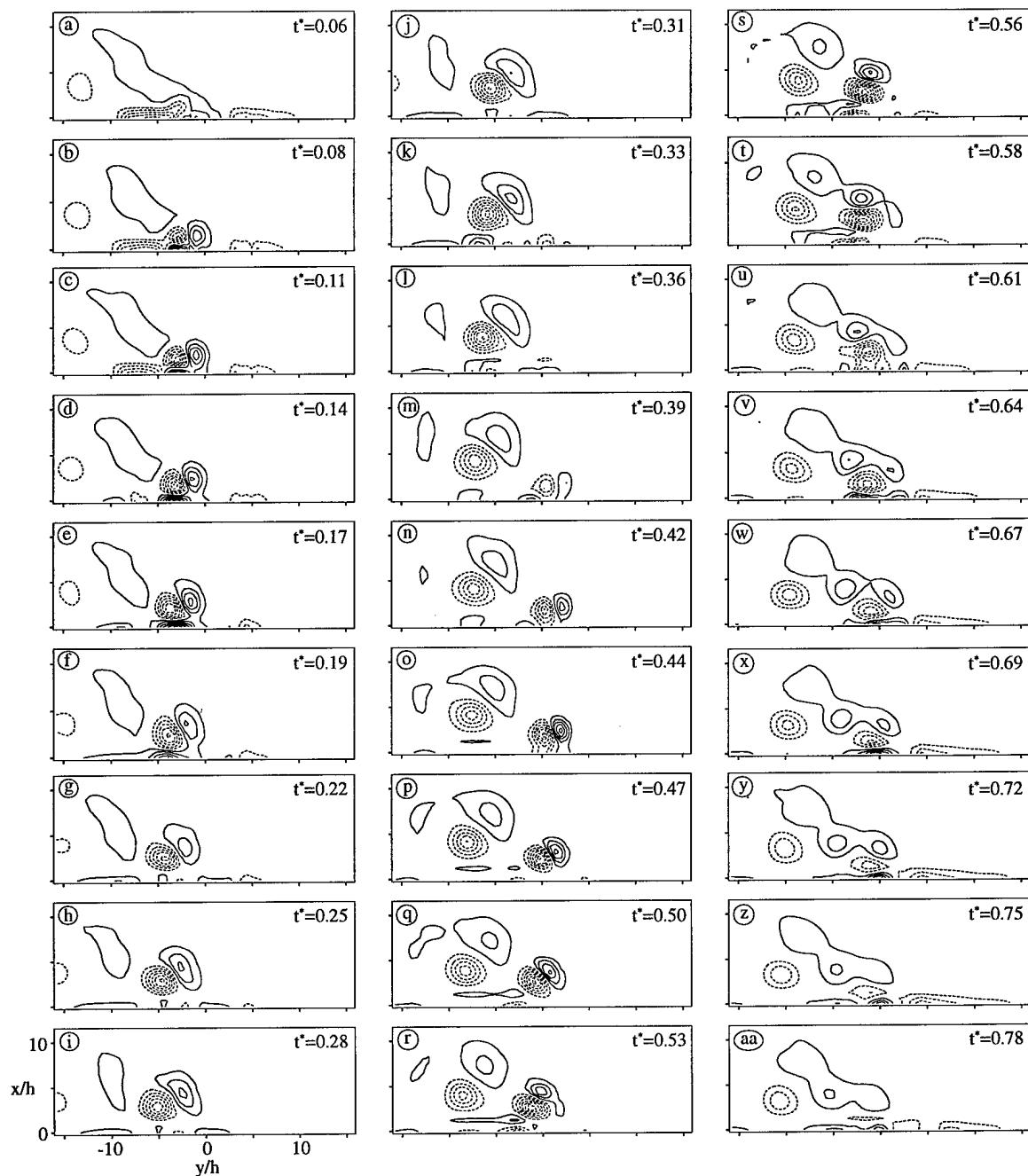
Figure II.18. As in Figure II.15 for θ=130°. First contour at $\omega^*_z = \pm 0.071$, and increments are ± 0.0142.

Finally, when $\theta = 130°$ (Figure II.18) the combined jet is vectored to the left along the wall (cf. Figure II.12). This is accompanied by the presence of negative vorticity on the left surface indicating boundary layer flow to the left. The vortex pair emerging out of L is actually entering a cross flow. L- is somewhat stronger than L+ and the pair begins to tilt to the left following its formation (Figure II.18c). It is interesting to note that the positive vortex becomes weaker as the tilting proceeds, presumably as a result of opposite shear in the cross flow. By the time R-R+ begins to emerge ($t^* = 0.361$, Figure II.18l), L-L+ is far enough removed and there is no direct interaction between the two successive pairs. Similar to the left pair, R- is stronger, causing this pair to tilt left also, and then convect toward L. Its proximity when the suction stroke of L begins allows R- to be re-entrained, while in higher θ cases, the entire pair is re-entrained.

II.4 Conclusions

The strong entrainment of ambient fluid that is induced near the flow orifice by the jet formation of synthetic jets is exploited for dynamic vectoring of adjacent jets by varying the amplitude or the relative phase of their driving waveforms. The direction of the ensuing merged jet is affected by the pressure field near the exit plane and by the interaction of the adjacent vortex pairs.

A comparison of velocity distributions in the near field of adjacent jets operating in phase and of a single jet suggests that the combined flow transports more fluid, the entrainment of ambient fluid toward the jet orifice is stronger, and that the combined jet spreads faster with streamwise distance. Measurements of spanwise vorticity show that during the formation of the combined jet, the adjacent (inner) vortices of the two vortex pairs cancel each other resulting in a single, larger pair that has a lower celerity than the vortex pair of a single jet at the same frequency and dimensionless stroke. Furthermore, vorticity levels within the boundary layers that are induced on the orifice plate by the entrained flow are considerably higher than for a single jet, indicating stronger entrainment on each side of the combined jet.

In the far field, the scaled velocity fields of the combined and single jets are very similar (as measured by the streamwise variation of the centerline velocity, jet width, or linear momentum) indicating similarity. However, the (scaled) volume flow rate of a jet pair in the far field is substantially larger than the corresponding flow rate of a single jet even though their rates of streamwise increase are similar. This is attributed to a large increase in entrainment in the near field due to vortex interactions (in the near field, the scaled volume flow rate of the adjacent jets is two times higher than for the single jet).

Vectoring of adjacent jets is investigated over a broad range of phase angles. When the phase angle is increased the combined jet begins to vector towards the jet that is leading in phase. For the present operating conditions it is found that there are three primary domains of phase angles. Below 60° the combined vectored jet remains above the surface of the orifice plate. When the phase angle is between 70° and 100°, the vectored jet forms a recirculating flow bubble near the surface and farther downstream is attached to the surface. When the phase angle exceeds 110° (but below 180°) the recirculating bubble disappears and the jet is completely attached to the surface.

Phase averaged vorticity measurements reveal some of the complex aspects of vortex interactions near the jet orifice. At relatively low phase angles, (below 20°), the inner vortices within the two pairs cancel each other. However, as the phase angle increases, the vortex pair of the jet that is leading in phase is subjected to an adverse pressure gradient (and a corresponding velocity field) that is induced by the suction cycle of the adjacent jet. As a result, the interaction between the adjacent vortex pairs shifts to merging of vortices of the same sign that also strongly affect the trajectory of the merged vortex pair. Beyond $\theta = 80°$, these interactions result in a vortex pair having an axis that is perpendicular to the exit plane, and an attached jet. When the phase angle increases beyond 120°, the successive vortex pairs do not merge and approximately follow the centerline of the combined jet.

Figure II.18

III. JET VECTORING WITH SYNTHETIC JETS

III.1 Introduction

Fluidic actuators employing control jets to affect a primary jet of the same fluid within an enclosed cavity have been studied since the late 1950's. These actuators perform a variety of "analog" (e.g., proportional fluidic amplifier) and "digital" (e.g., flip-flop) throttling and control functions in flow systems without moving mechanical parts (Joyce, 1983). In the "analog" actuator, the volume flow rate fraction of two opposite control jets leads to a proportional change in the volume flow rate of the primary stream out one of two corresponding output ports. The "digital" actuator is a bistable flow device in which the control jets and Coanda effect are used to direct the primary stream into one of two output ports. Although most of the fluidic technology has been restricted to enclosed cavities, some of these devices have also been used in free shear flows. Viets (1975) induced spontaneous oscillations in a free rectangular jet by exploiting the concept of a flip-flop actuator. More recently, Raman and Cornelius, 1995 used two such jets to impose time harmonic oscillations in a larger jet by direct impingement. The control jets were placed on opposite sides of the primary jet and could be operated in phase or out of phase with each other.

Jet vectoring without active actuation can also be achieved using Coanda effect, or the attachment of a wall jet to a curved surface which is an extension one of the nozzle walls (Newman, 1961). Although for a given jet momentum the effect is apparently limited by the characteristic radius of the curved surface, it has also been shown that controlled perturbations (and thus enhanced entrainment) of the shear layer of a jet adjacent to a solid boundary can lead to partial attachment of the jet to the surface. Koch (1990) used wall jets along in a circular diffuser to effect partial attachment and thus vectoring of a primary round jet. A counter current flow between an external collar (Coanda) surface and a primary jet has been used to effect thrust vectoring in low- and high-speed jets by Strykowski et al., 1996. The effect of suction at the downstream edge of a jet nozzle has also been investigated numerically by Lim and Redekopp (1997).

III.2 Apparatus and Measurements

A conventional rectangular jet emanating out of a 7.62 x 1.27 cm and 71cm long aluminum conduit is instrumented with a synthetic jet actuator on top of the exit plane having an orifice plate measuring 0.508 x 75 mm and mounted along the long side of the primary jet conduit as shown schematically in Figure III.1a-c. The air jet facility is described in detail in Wiltse & Glezer, 1993. The rectangular conduit is centrally mounted on the downstream endplate of a cylindrical plenum tube. No contraction is used, and an azimuthally uniform bleeding gap along the perimeter of the plenum tube (Figure III.1b) is adjusted until the velocity distribution across the plenum tube just upstream of the inlet of the conduit is approximately uniform. This minimizes secondary flow at the inlet and along the corners of the square conduit and, as a result, the turbulence level at the jet exit ($u'u'^{1/2} < 0.007U_{cl}$). In some cases, a step is added to the synthetic jet orifice (Figure III.1c). The conduit wall, which separates the synthetic jet from the primary jet is 1.8mm thick. The conduit is instrumented with 10 pressure taps along the center of the top and bottom walls which extend between $0.3 \leq x/H \leq 2.1$. The side walls of the primary jets are made of transparent Plexiglas to allow PIV measurements upstream of the exit plane. The primary jet is driven by an axial blower powered by a DC motor utilizing a closed loop controller, which maintains the rpm within 1%. In the present experiments, the primary jet centerline velocity is varied between 4 m/s and 33m/s. It is found that the flow in the jet conduit undergoes transition from laminar to turbulent when the centerline velocity is approximately 8m/s. PIV measurements of the cross stream velocity profiles at the exit plane are shown in Figure III.2, and show that the long conduit has lead to significant development of the profile. The transition to turbulent flow is evidenced by a fuller profile shape for centerline speeds above

8m/s. These measurements are used to determine the average streamwise velocity inside the conduit. When the flow inside the conduit is laminar, $U_{ave} = 0.72U_{cl}$ (in a fully developed laminar flow in a 2-D channel, $U_{ave} = 0.667U_{cl}$), and when the flow is turbulent, $U_{ave} = 0.86U_{cl}$. The Reynolds number in these experiments, based on the average velocity and H varies between 2450 and 24,000.

The actuator used in these experiments is essentially identical to the device used for the synthetic jet experiments. The orifice velocity (and thus Re_{Uo}) is calibrated against the cavity pressure of the synthetic jet using the same procedure as used for the adjacent jet. Whenever the orifice plate is removed and replaced (such as when the step size is changed), the calibration is repeated. For fixed frequency, Re_{Uo} is found to increase linearly with the cavity pressure fluctuations. Calibrations at a range of frequencies were also performed, and it was found that $Re_{Uo} \sim P_{rms}/f$.

These calibrations can be confirmed with phase-locked PIV data if the field of view contains the synthetic jet orifice. The cases described in Table II.1 below proved suitable. Rather than attempting to resolve the orifice velocity, the mismatch in the volume flow rate into and out of the measurement domain is calculated, and is taken to be the synthetic jet flow rate, which is in turn used to calculate Re_{Uo}. It was intended to fix Re_{Uo} at a value of 350 for the bulk of the cases in this study. However, examination of the high resolution data shows that although the synthetic jet centerline velocity is fixed in the calibrations, the average velocity increases significantly when steps are added, and Re_{Uo} does not remain constant as the primary jet velocity varies. The resultant value of Re_{Uo} for cases at f = 1120 Hz and several velocities are shown in Figure III.3 as a function of the step size. These data show that in addition to the effect of the step, increasing the primary jet speed degrades the synthetic jet performance. The amount of deviation from the target value due to primary jet velocity is much smaller than the step effect, and for this reason, it will often be assumed herein that the velocity remains constant at the average value for that step size. It was also determined that the resultant Re_{Uo} tended to decrease with driving frequency.

These measurements are made using largely DPIV. Theater fog was introduced at the blower inlet, and additional fog was introduced into entrainment regions (above and below the primary jet flow) which did not otherwise contain fog. Three different magnifications were used: 6.3μm/pixel, 21μm/pixel, and 37μm/pixel respectively. In each case, 64 data points were computed in the x and y direction, resulting in velocity fields that extend 0.46H, 1.56H, 2.75H respectively in both directions.

Case Name	U_{cl} (m/s)	U_{ave} (m/s)	s/h	Re_{Uo}	f (Hz)
AAD	7	5.16	0.00	314	1120
ABA	7	5.16	1.50	300	700
ABD	7	5.16	1.50	363	1120
ACB	7	5.16	2.35	406	720
ACD	7	5.16	2.35	432	1120
BBA	11	9.34	1.50	308	700
BAD	11	9.34	0.00	348	1120
CCB	13	11.08	2.35	392	720
DBC	16	14.01	1.50	300	900
EAD	17	14.89	0.00	336	1120
EBA	17	14.89	1.50	300	700
EBD	17	14.89	1.50	348	1120
ECB	17	14.89	2.35	372	720
ECD	17	14.89	2.35	403	1120
FAD	30	25.58	0.00	310	1120
FBD	30	25.58	1.50	325	1120
FCD	30	25.58	2.35	371	1120

Table II.1 High resolution phase-locked PIV data .

The high resolution cases allow for the determination of the synthetic jet Reynolds number as well as locations of stagnation points. It is also possible to calculate the flow rate through stream tubes bounded by the jet and the stagnation streamlines, which, as will be shown in Chapter IV, is vital to understanding jet vectoring. The high resolution cases are a subset of the mean data taken at lower resolution, and are summarized in Table II.1. A total of 17 zoomed in cases were measured and, each case is given an unique three-letter name, with the letters corresponding to the primary jet velocity, the step size and the forcing frequency, respectively.

The 21 μm/pixel magnification was chosen to provide sufficient magnification to resolve all mean effects inside of the channel, and to extend sufficiently upstream and downstream to capture the start and end of the vectoring effect. The data is used to calculate resultant forces using a control volume which is bounded by the channel walls, the exit plane, and the upstream end of the measurement domain (x/H = -0.83). When the vertical force is computed, the downstream end of the control volume is extended to include the step. Since none of these calculations required any unsteady data (it was confirmed that the unsteady terms of the control volume equations are insignificant) only mean data were taken. The data are averaged over 100-150 realizations, and therefore, especially in the turbulent cases, there is a relatively large (10%) experimental uncertainty on the mean velocity data, which exceeds known accuracy limitations of PIV.

Two component hot wire measurements are used when a high temporal resolution or a spatially large field is required. In the cases where x-wire measurements of the vectored flow are made, the probe is pitched so that its axis is in line with the mean flow, which served to keep the measurements within the ± 37° calibration range.

All PIV, hot wire, and pressure measurements are made on the spanwise centerline (z = 0). Several parameters are explored, including the primary jet velocity, step size, and frequency.

III.3 Results

Schlieren images of the unforced and forced primary jet are shown in Figure III.4a-b. The centerline velocity of the unforced jet is 7m/s, and the synthetic jet is operating at Re = 380, f = 1120Hz with a step s = 1.5h. It is evident that the flow within the conduit is laminar, and the Kelvin-Helmholtz instability of the primary jet shear layers leads to the formation of vortical structures that are symmetric about the jet centerline. The image of the forced flow shows that the primary jet is vectored toward the synthetic jet at a mean angle of 30□. The action of the actuator substantially increases the small scale motions within the primary jet, thus suggesting enhanced mixing in the jet shear layer. Direct excitation of dissipative scales within a square jet using cantilevered piezoelectric actuators was reported earlier by Wiltse and Glezer (1998). These authors show that as a result of the excitation, the dissipation within the forced segment of the jet shear layer increases by one to two orders of magnitude over a broad streamwise domain. Furthermore, direct excitation at high wave numbers enables coupling to both large- and small-scale motions. A similar effect takes place as a result of synthetic jet forcing, as confirmed by power spectra taken in the shear layer of the unforced jet, and in the upper (forced) and lower (unforced) shear layer of the forced jet shown in Figures III.5a-c. Note that for clarity, Figures III.5b and c are displaced two and four decades downward respectively. The operating frequency of the actuator (1120Hz) is over an order of magnitude higher than the natural unstable frequency band of the jet shear layer. The power spectra are measured at x/H = 3.15 and cross-stream coordinates corresponding to $U(y)/U_{cl} = 0.73$ within the forced and unforced shear layers along the long sides of the vectored jet (Figures III.5a and b, respectively) and the corresponding measurement within the unforced jet is shown for reference in Figure III.5c.
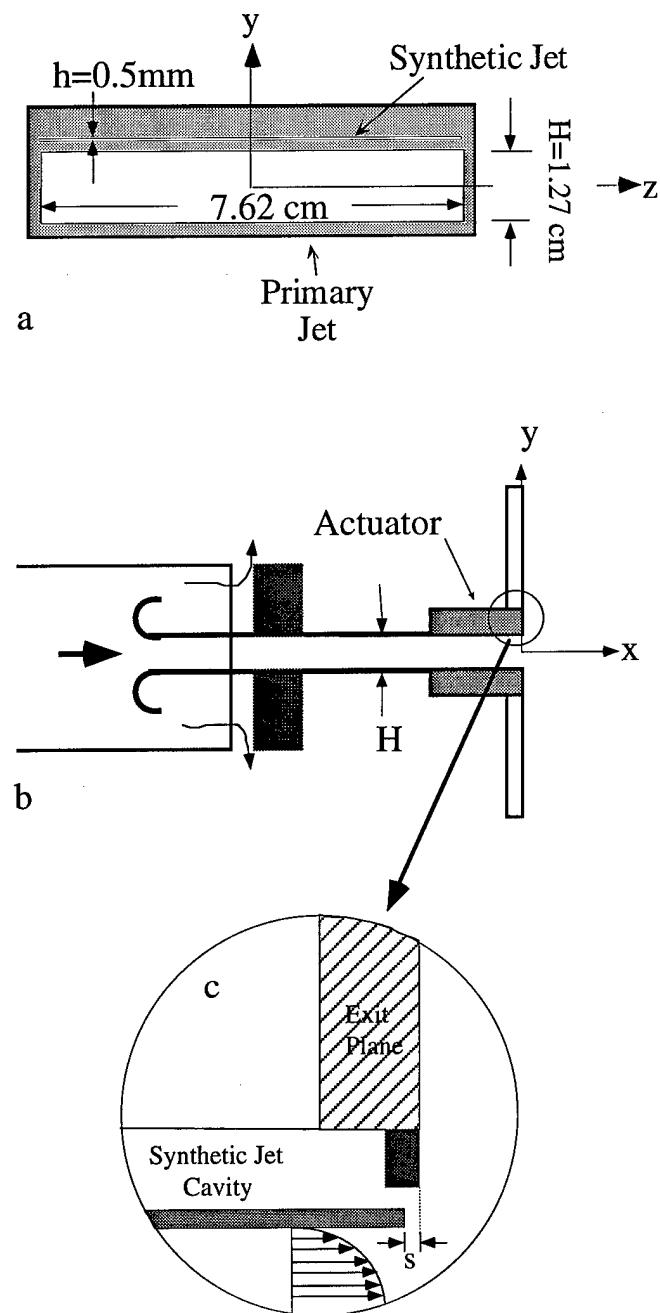
Figure III.1. Schematic of Primary Jet instrumented with a Synthetic Jet Actuator. (a) Exit (y-z) plane of primary jet and synthetic jet (b) side view (c) detail of synthetic jet.
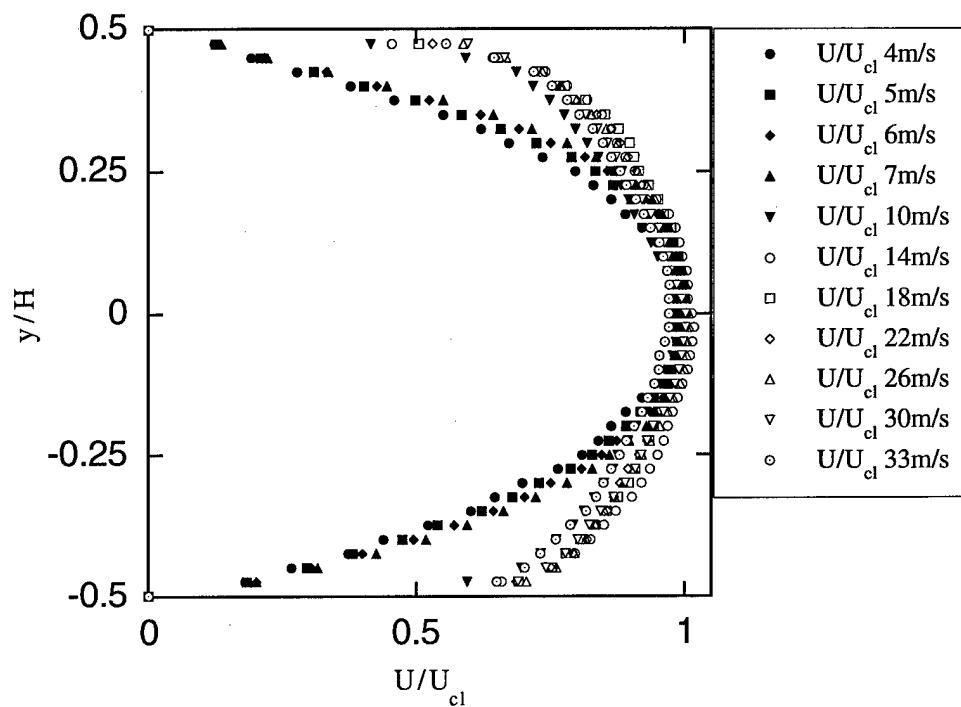
Figure III.2. Profiles of the streamwise component of velocity of the unforced primary jet.
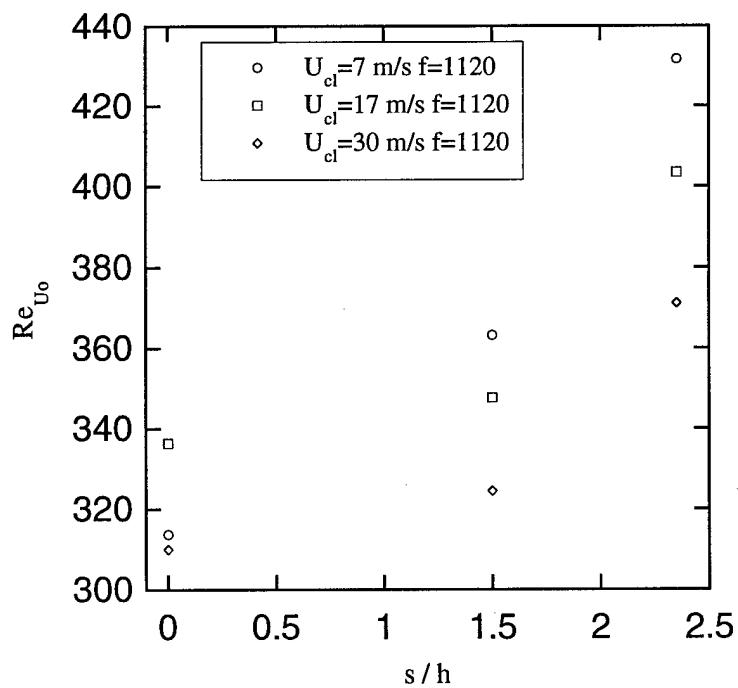

Figure III.3. Variation of synthetic jet Reynolds number with step size and primary jet centerline velocity.

The most unstable (K-H) frequency of the unforced jet and its higher harmonics are prominent in the spectrum of the unforced jet (Figure III.5c). By contrast, in the spectrum of the forced shear layer of the vectored jet the K-H instability is completely suppressed, small scale motions are enhanced over a broad range of wave numbers and it appears that an inertial sub-range is present with a spectral peak at the actuator frequency (Figure III.5a). While spectral components of the unstable K-H frequency of the unforced flow and its first harmonic are also present in the spectrum of the unforced shear layer of the vectored jet, the magnitude of these spectral components is considerably diminished compared to other spectral components within the same frequency band. There is also a substantial broad band increase in the magnitude of small-scale motions and a peak at the forcing frequency, suggesting that the forcing is transmitted through the core of the primary jet presumably by pressure fluctuations (similar results in the wake of a circular cylinder are reported by Amitay et al., 1998).

The proximity of the synthetic jet to the primary jet allows the two jets to interact such that during its suction stroke, the synthetic jet draws some of its fluid from the primary jet. This interaction results in the formation of a low pressure region between the two jets and the acceleration of the primary jet fluid near the upper conduit wall as shown schematically in Figure III.6). The pressure gradient leads to the turning of the flow inside of the conduit. The normal force on the top surface of the conduit balances the induced cross stream momentum of the primary jet.

III.3.1 The Mean Flow

Streamline maps of the forced mean flow for primary jet centerline velocities in the range $5 \leq U_{cl} \leq 27$ m/s within the streamwise and cross-stream domains $-0.22 < x/H < 2.53$ and $-0.81 < y/H < 1.94$ respectively are shown in Figures III.7a-g. The stream function is calculated from the PIV measurements within this domain by integrating the velocity field from the bottom right-hand corner of the measurement domain. This prevents the need to integrate across the physical boundaries, where data points are lost due to laser reflections. The synthetic jet is operated at $Re_{Uo} = 350$, $f = 1120$ Hz with a step $s = 1.5h$. These data are taken to demonstrate the overall character of the vectored jet, and cannot sufficiently resolve the details of the boundary layers or of the synthetic jet flow. For this reason, data near the surfaces are not included. With the synthetic jet input nominally unchanged (ignoring the $\pm$ 5% change with primary jet velocity, cf. Figure III.3), larger primary jet velocities result in smaller vector angles. The primary jet begins to turn upstream of the exit plane, and the change in angle is nearly completed at the exit plane, which can be seem most clearly in Figure III.7a. At 5m/s and 7m/s (Figure III.7a-b) the flow is separated from the lower conduit wall upstream of the exit plane (separation occurs if and only if the conduit flow is laminar). In all but the highest speed case, it appears that the upper shear layer of the primary jet is stretched in the cross-stream direction as a result of the forcing.

Some of the details of the mean flow inside the conduit and the near field are now investigated using PIV data acquired over a the domain $-0.83 \leq x/H \leq 0.75$ and $-0.6 \leq y/H \leq 0.98$. Mean profiles of the streamwise (U) and cross-stream (V) velocity components at the exit plane of the primary jet are shown in Figure III.8a and b for several primary jet (unforced) centerline velocities. In each of these cases, $Re_{Uo} = 350$, $s = 1.5h$, and $f = 1120$Hz. It is clear from Figure III.8a that at the lower speeds, the flow is separated at the lower wall of the conduit (although no appreciable reverse flow is measured). As noted above, following turbulent transition ($U_{cl} \approx 8$m/s), the flow does not separate, and the velocity near the lower wall resembles the unforced conduit flow. When the primary jet reaches an unforced centerline velocity of 30m/s, the effect of the forcing is virtually undetectable, and the streamwise velocity component appears to be symmetric about the $y = 0$. The cross stream velocity component (Figure III.8b) increases almost linearly toward the upper side of the conduit (past the separated region in the laminar cases) with the slope decreasing with primary jet speed.

The angle of the vectored flow is non-uniform across the jet exit, as shown in Figure III.9. The flow angle is largest near the upper conduit wall, and decreases monotonically toward the bottom side of conduit. Since the velocity magnitude within the separated region is small, the flow angle within this region is not included. Note that the vectoring angles at the exit plane are not the same as the final vectoring angles of the mean streamlines in Figure III.7, indicating that the flow continues to turn in the cross stream direction downstream of the exit plane. In Figure III.10, contours of the vector angle are plotted for the 7m/s case, which show that flow vectoring ends on a line which extends radially from the corner $x/H = 0$, $y/H = 1/2$, to $x/H = 1/2$, $y/H = 0$. This contour has a value of 28° and is marked on the Figure. Therefore, the vectoring is complete at the exit plane for the flow near the upper conduit wall, but the lower half of the jet continues to vector until $x/H = 1/2$. Ambient fluid being entrained into the primary jet shear layers undergoes a rapid change in flow angle, which is evidenced by the preponderance of contours above and below each of the primary jet shear layers.

Since the pressure at the exit plane is reduced due to the action of the synthetic jet, it is reasonable to expect that the flow rate through the conduit would increase when forcing is applied. The ratio of the volume flow rate of the forced flow, Q_f, to the unforced flow, Q_{uf}, is computed from the PIV data and plotted in Figure III.11 as a function of the primary jet Reynolds number for the unforced flow. Data from cases using three different step sizes (and thus three Re_{Uo} values) are shown, and $f = 1120$ Hz. At low speeds, when the channel flow is laminar, very little increase in flow rate is experienced. It has been shown above that in these cases, the flow is separated from the bottom wall of the conduit, and thus the flow area of the primary jet is reduced. This seems to balance the lowered exit plane pressure resulting in little change in flow rate. However, following the transition to turbulence, ($U_{ci} \approx 8$m/s), the flow occupies the entire height of the conduit, and the reduced exit plane pressure results in a marked increase in flow rate. The increase in flow rate becomes larger with step size, and peaks near 9% for the $s = 2.35h$ case. As the primary jet speed becomes large, Q_f decreases toward the unforced level.

PIV measurements upstream of the primary jet exit plane are used to compute the resultant forces on a control volume that is bounded by the conduit walls, the exit plane, and the upstream end of the measurement domain ($x/H = -0.83$). The streamwise momentum flux through a given streamwise station is

$$J(x) = \int_{-H/2}^{H/2} \rho U^2(x,y)\,dy.$$

As shown in Figure III.12, the increase in the primary jet flow rate is accompanied by an increase in its streamwise momentum flux at the exit plane. It is noteworthy that even though as much as half of the vectored momentum is in the cross-stream direction, the streamwise momentum also increases relative to the unforced case. Of particular note is the significant increase in the streamwise momentum flux for the laminar cases, even though the flow rate remained substantially unchanged. This increase (which is as high as 20% of the unforced value) is therefore entirely due to changes in the profile shape. The shape of the profiles in the conduit changes as the flow proceeds downstream, and as a result, the momentum flux also changes. Figure III.13 is a plot of the streamwise momentum flux as a function of streamwise position inside of the conduit for several primary jet velocities. The flux is normalized by the value at the inlet to the measurement domain. All data are from the case $s = 1.5h$, $f = 1120$, and $Re_{Uo} = 350$. In all cases, the flux peaks upstream of the exit plane, and then decreases. The momentum of the peak initially increases with primary jet speed, but decreases sharply following transition to turbulence within the duct. The momentum flux peak must indicates a pressure minimum at this location (upstream of the exit plane), and may be accompanied by a increase in the shear stress on the conduit walls, although the spatial resolution of the present data does not allow an estimate of the shear stress at the wall. For the lower speed turbulent cases (9m/s < U_{ci} < 16m/s), the momentum flux decreases to the magnitude at the control volume entrance, and at the higher speeds (U_{ci} > 16m/s) it decrease to below the level at the entrance.
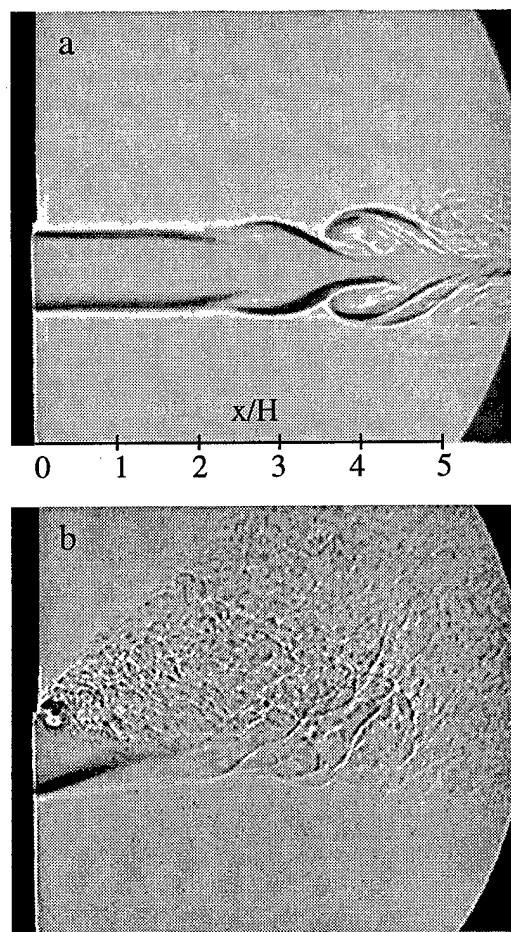
Figure III.4. Schlieren images of synthetic jet vectoring. (a) Primary jet unforced at U_{cl}=7m/s (b) Forced at Re_{U_o}=380, f=1120Hz with s=1.5h.
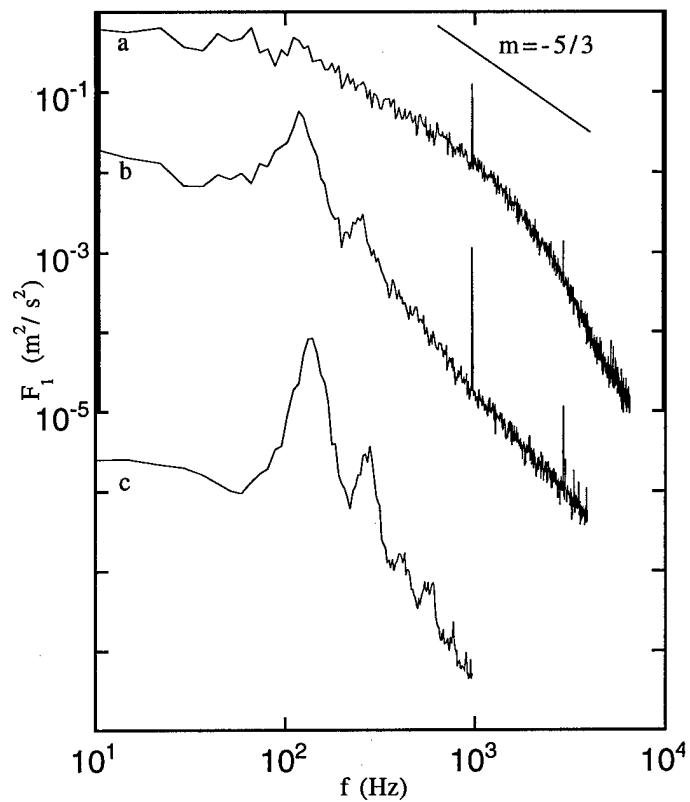
Figure III.5. Power spectra of the streamwise velocity measured at the cross stream locations corresponding to $U/U_{cl} = 0.73$ on the forced side of vectored jet (a), unforced side of vectored jet (b), unforced jet (c).
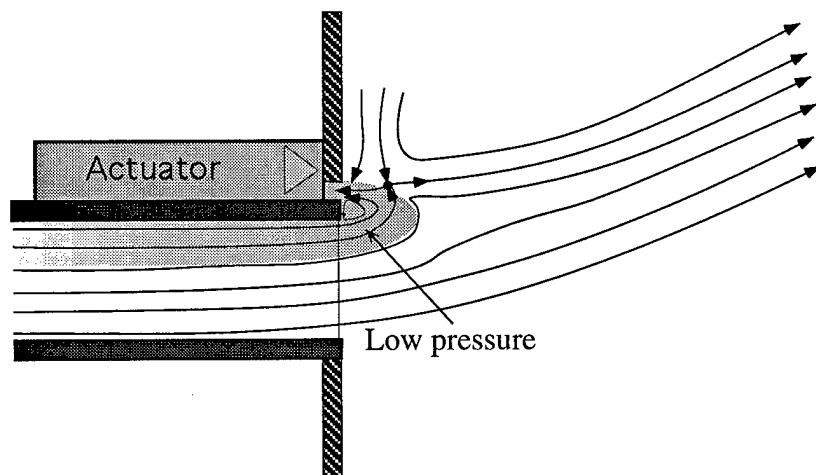

Figure III.6. Synthetic jet vectoring schematic.
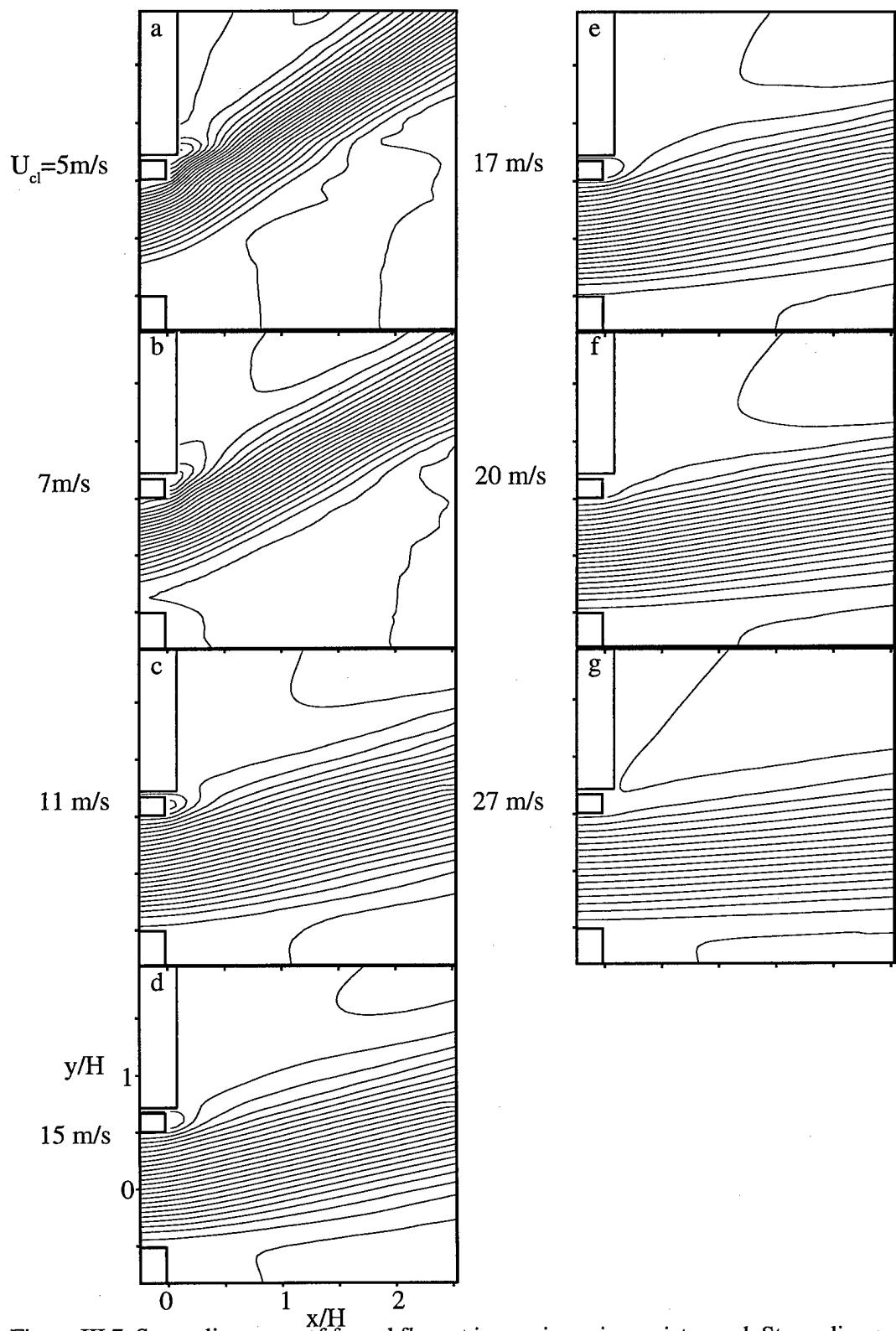
Figure III.7. Streamline maps of forced flow at increasing primary jet speed. Streamline spacing represents 5% of unforced flow rate.
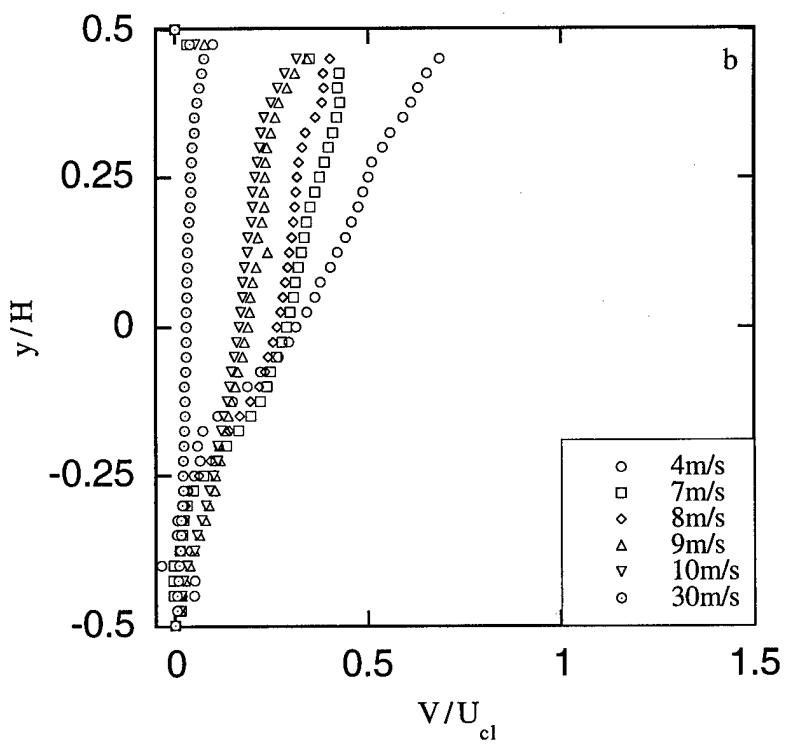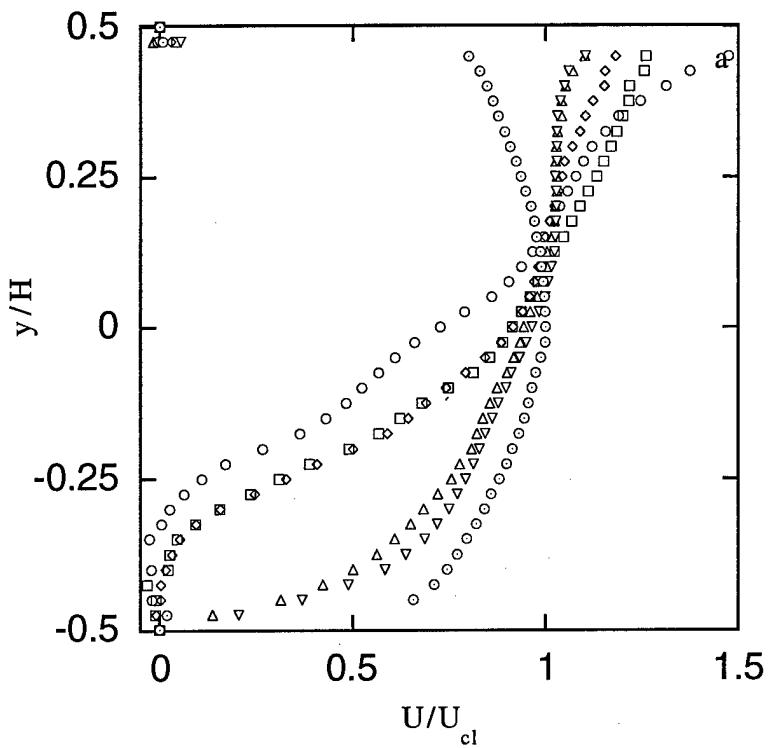
Figure III.8. Profiles of forced jet for Re_{Uo}=350, s/h=1.5, and f=1120Hz. (a) Streamwise component (b) cross-stream component.
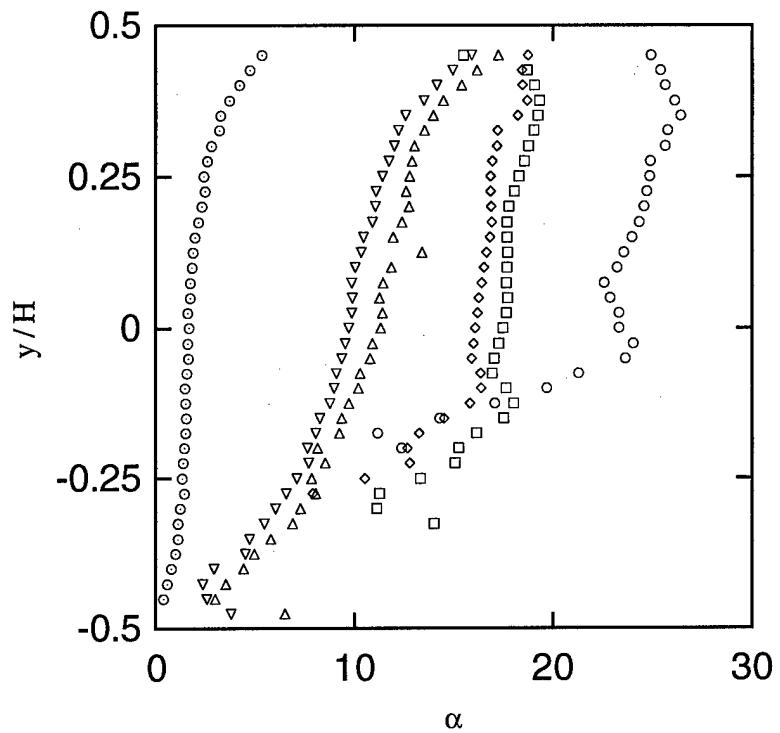
Figure III.9. Cross-stream variation of flow angle of forced jet at exit plane. Re_{U_o}=350, f=1120Hz, s/h=1.5. Symbols as in Figure IV.44.
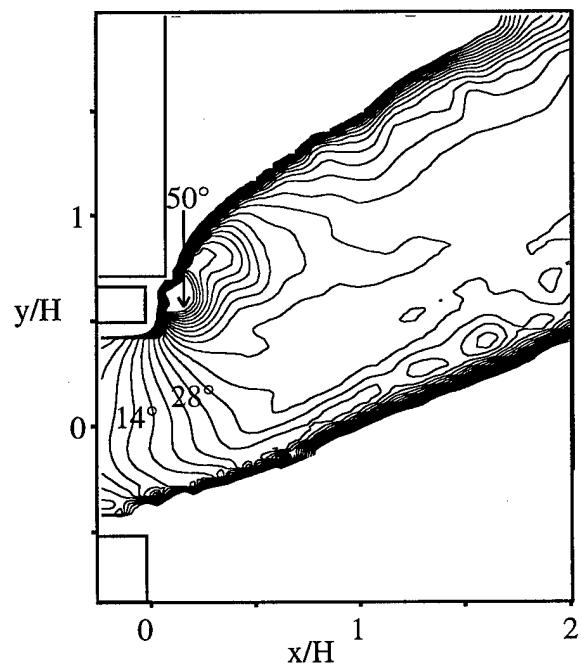
Figure III.10. Contour map of flow angle of vectored jet. U_{cl}=7m/s, f=1120Hz, s/h=1.5, starting contour and contour increment are 2°.
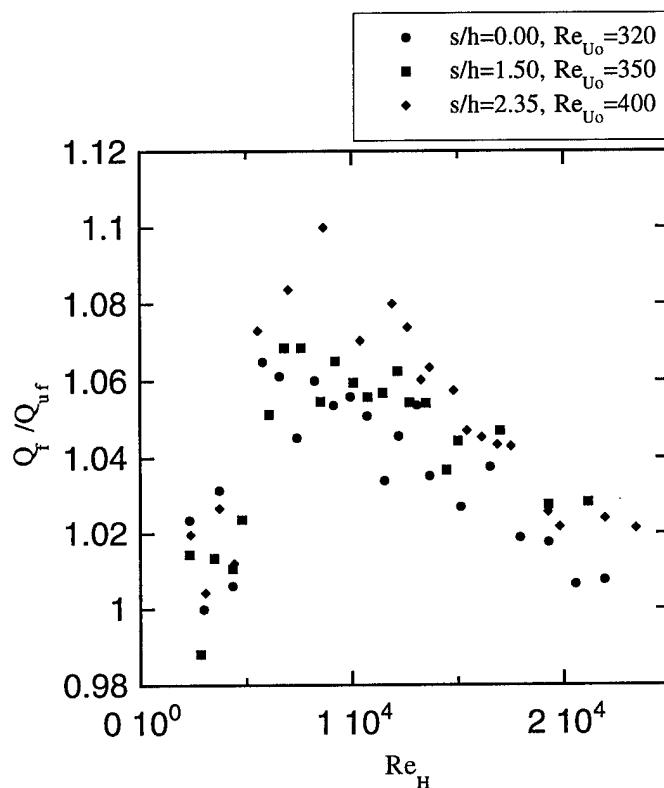
Figure III.11. Increase in primary jet conduit flow rate when forcing is applied, f=1120Hz.
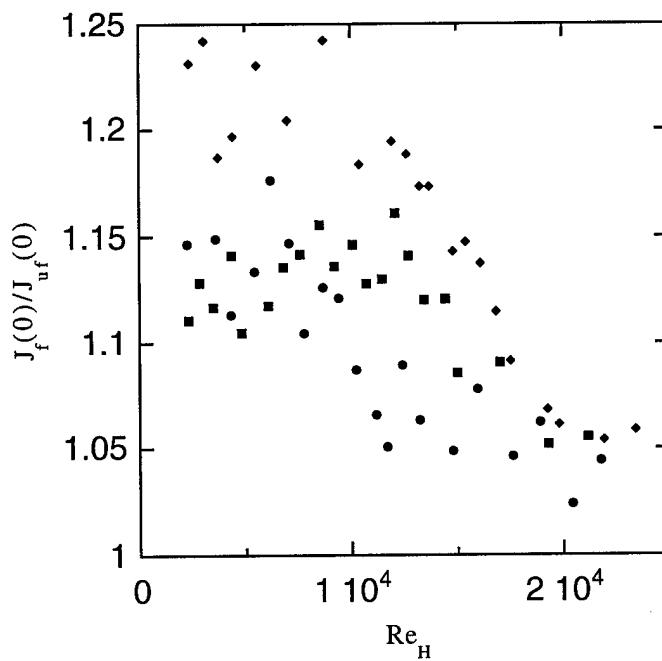


Figure III.12. Increase in exit plane streamwise momentum flux when forcing is applied, f=1120Hz. Symbols as in Figure IV.47.

The normal (cross stream) force on the jet conduit due to the vectoring of the primary jet is computed using the control volume approach described above, and the cross stream momentum flux at a given streamwise station is

$$J_y(x) = \int_{-H/2}^{H/2} \rho U(x,y) V(x,y) dy.$$

The static pressure along the upper and lower conduit surfaces is measured independently using the pressure taps. Figure III.14 shows the streamwise distributions of the resultant vertical force on the segment of the top and bottom surface that are bounded by the upstream extent of the data ($x/H \geq -3$) and by the downstream edge of a control volume having a variable streamwise length. The resulting normal force $F_y(x)$ is computed between $-3 \leq x/H \leq -0.5$ by the streamwise integration of the pressure difference on the upper and lower walls (closed symbols), and between $-0.82 \leq x/H \leq 0$ by computing the net flux of cross stream momentum using the PIV measurements (open symbols). It is clear that the resultant force increases with the primary jet velocity for these conditions (which will be further discussed with respect to Figure III.16). As can be seen from the pressure data, the effect of the vectoring is felt as far away as 2H upstream of the exit plane. However, these data also show that most of the contribution to the vectoring force occurs within $-H < x < 0$. The discrepancy between the force computed from the pressure distribution and the momentum flux is less than 5% of the maximum value. It is clear that the bulk of the vectoring force is acting very near the exit plane.

Figure III.15 shows the variation of the ratio of the vectoring force to the streamwise momentum flux with the average velocity of the primary jet. The data includes cases for three steps sizes with forcing at 1120 Hz, and an additional case with $s/h = 1.5$ and $f = 700$ Hz. The normalized vectoring force decreases with jet speed, and is generally higher when the effectiveness is increased by the addition of a step. The decrease is nearly linear in the 1120 Hz cases, with a distinct decrease in slope when the conduit flow becomes turbulent ($U_{ave} = 5.8$, $U_{cl} = 8$). For the lower frequency case, the decrease in the relative cross stream force continues at the same slope as the flow in the conduit undergoes transition.

In order to illustrate the dependence of the vectoring force on the synthetic jet parameters (frequency, orifice step size, and U_o) and the speed of the primary jet, the vectoring force on the nozzle is plotted dimensionally in Figure III.16. These data include three orifice step sizes ($s/h = 0$, 1.5, and 2.35), four frequencies (700, 720, 900, and 1120 Hz), and several synthetic jet Reynolds numbers. The frequencies were chosen to span the practical range of this actuator. These data show that: (a) in all cases, the vectoring force initially increases with primary jet speed, and in most cases reaches a maximum before decreasing, (b) The primary jet speed at which the vectoring force peaks increases with step size and decreases with frequency, and (c) an increase in Re_{Uo} results in an increase in the vectoring force, although the maximum force occurs at the same speed of the primary jet. In order to better to understand the physical phenomena behind these trends, several key cases, which correspond to the circled data points, are investigated in detail using high resolution PIV measurements. These data, which are taken phase locked to the synthetic jet forcing are summarized in Table III.1, and are discussed in detail below.

The effect of forcing on the primary jet downstream of the exit plane is measured using two component hot-wire anemometry for $U_{cl} = 7$m/s, $f = 1120$ Hz, and $s = 1.5h$. Cross stream distributions of the mean streamwise velocity component of the forced and unforced jets are measured at 11 streamwise stations, between $0.787 \leq x/H \leq 11.8$ and are plotted in similarity coordinates in Figure III.17. Since the characteristic cross-stream width (based on half the centerline velocity) of turbulent, two-dimensional jets increases linearly with downstream distance, the cross-stream (y) coordinate is normalized by the streamwise distance to the jet exit plane (x). Similar to measurements reported by other investigators (Gutmark and Wygnanski,

1976), the unforced jet (Figure III.18a) becomes self-similar for x/H > 6. It is noted that in similarity coordinates, the maximae of the streamwise velocity distributions occur at the same cross-stream coordinate for 2.46 ≤ x/H ≤ 11.8, indicating that the vectoring angle does not change appreciably within this domain. However, the cross stream spreading of the shear layers on each side of the forced jet is not symmetric, as is alluded to in Figure III.17b. This can be seen more clearly by considering the width of the vectored jet, which is commonly taken to be the cross stream location at which the streamwise velocity is equal to half the maximum value. In Figure III.18, the cross stream locations (one on either side of the jet) of the half-velocity points are plotted with respect to their downstream positions. It is clear that the forced side of the jet spreads linearly with x, while the spreading rate of the unforced side of the jet is smaller and grows like a fractional power of x through x/H = 8. It appears that for x/H > 8, the unforced shear layer begins to spread linearly with x. Note that at x/H = 10, the vectored jet is 2 times wider than the unforced jet.

The elapsed time required to reach the mean vectoring angle of the primary jet from the unforced state is determined by measuring the phase locked variation of the vectoring angle at the centerline of the primary jet using step amplitude modulated forcing. The orifice velocity of the synthetic jet in response to a step modulation of the driving signal input is shown in Figure III.19 for f = 1120 Hz and s/h = 1.5. The measurements are taken using a single hot wire sensor placed inside of the synthetic jet orifice, and the rectification of the measured velocity traces is removed. These data show that the amplitude of the velocity within the orifice of the synthetic jet reaches 85% of its final value within 2 cycles.

The time history of the angle of the velocity vector on the centerline of the primary jet is measured at the exit plane with two component (x-wire) anemometry and is shown in Figure III.20 for two primary jet velocities. In both cases, the actuation results in a monotonic increase in the vectoring angle which is also oscillating at the forcing frequency. The vectoring angle reaches an asymptotic mean level within 8 excitation cycles, however, the nominal amplitudes of the instantaneous oscillations at the actuation frequency are 3.5° and 3.0° for the U_{cl} = 7m/s and 15m/s respectively. When U_{cl} = 15m/s the conduit flow is turbulent, which results in instantaneous vectoring angle fluctuations which are not time periodic. The measurements of the vectoring angle are taken at primary jet centerline velocities ranging from 5 to 20m/s, and the characteristic vectoring time is determined using an exponential least squares fit to the data. The time constant and the asymptotic (mean) vectoring angle at each primary jet velocity are plotted in Figure III.21. The response time of the primary jet decreases linearly with the primary jet speed, and at large speeds, is approximately half the characteristic period of the synthetic jet. Note that the mean vectoring angle at the exit plane also decreases with primary jet speed, and that the slope changes when the conduit flow becomes turbulent.
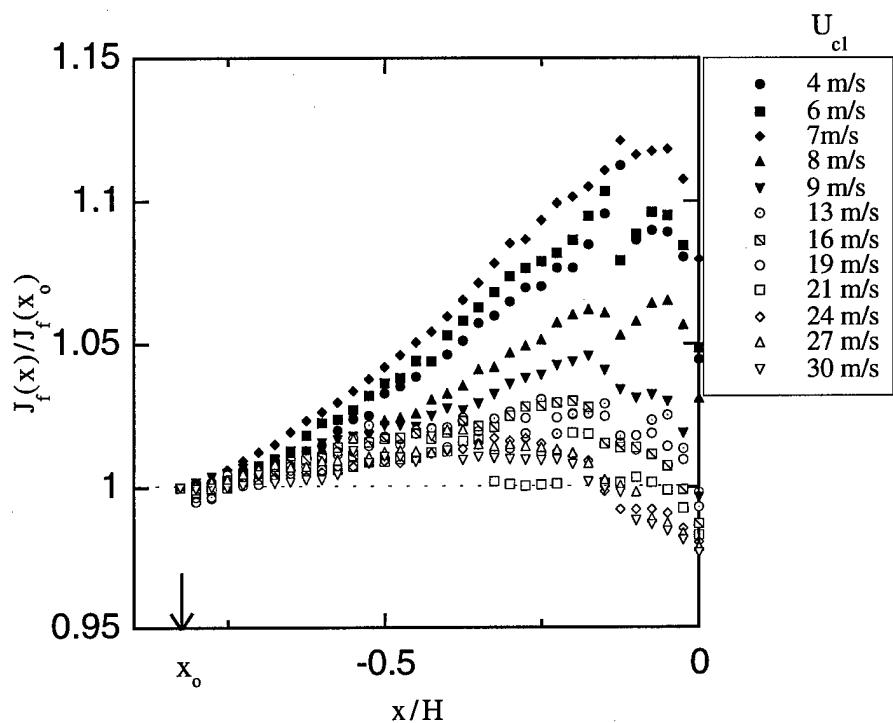
Figure III.13. Streamwise variation of streamwise momentum flux. $Re_{Uo}=350$, f=1120Hz, s/h=1.5. Values are normalized by the flux at the entrance to the measurement domain (x_o).
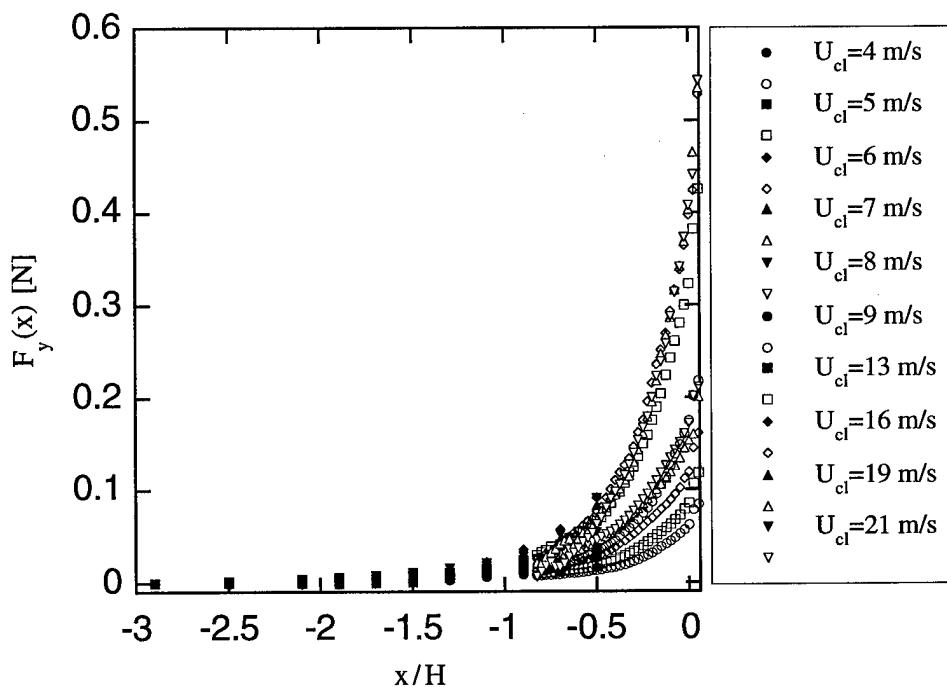

Figure I11.14. Streamwise variation of Vectoring Force. Closed symbols are pressure data, open are PIV data. $Re_{Uo}=350$, f=1120Hz, s/h=1.5.
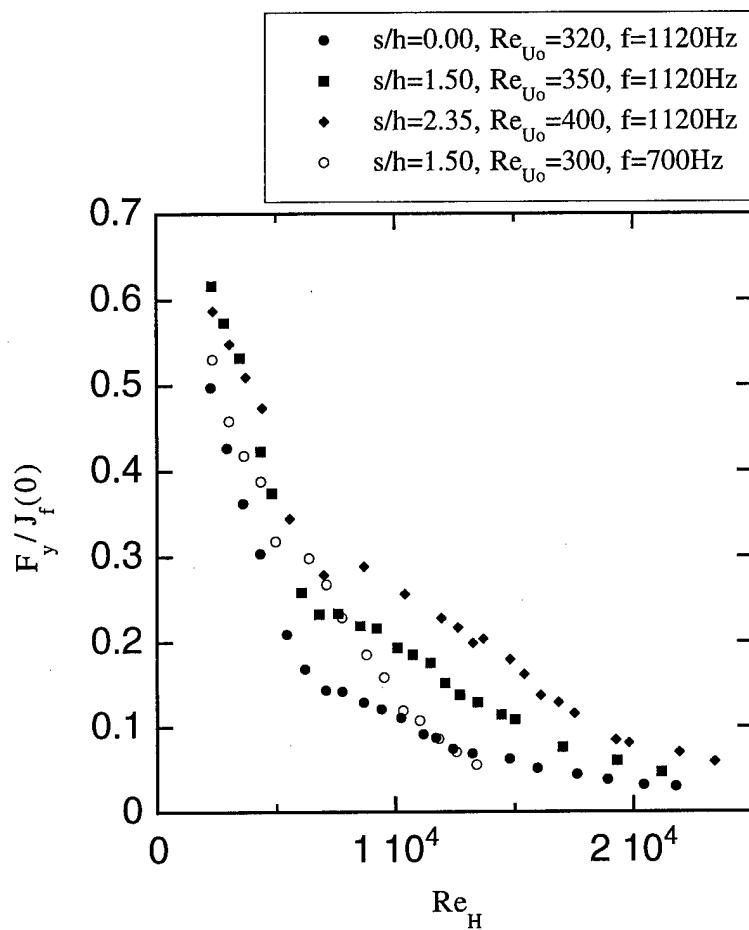
Figure III.15. Variation of vectoring force relative to the streamwise momentum flux with primary jet speed.
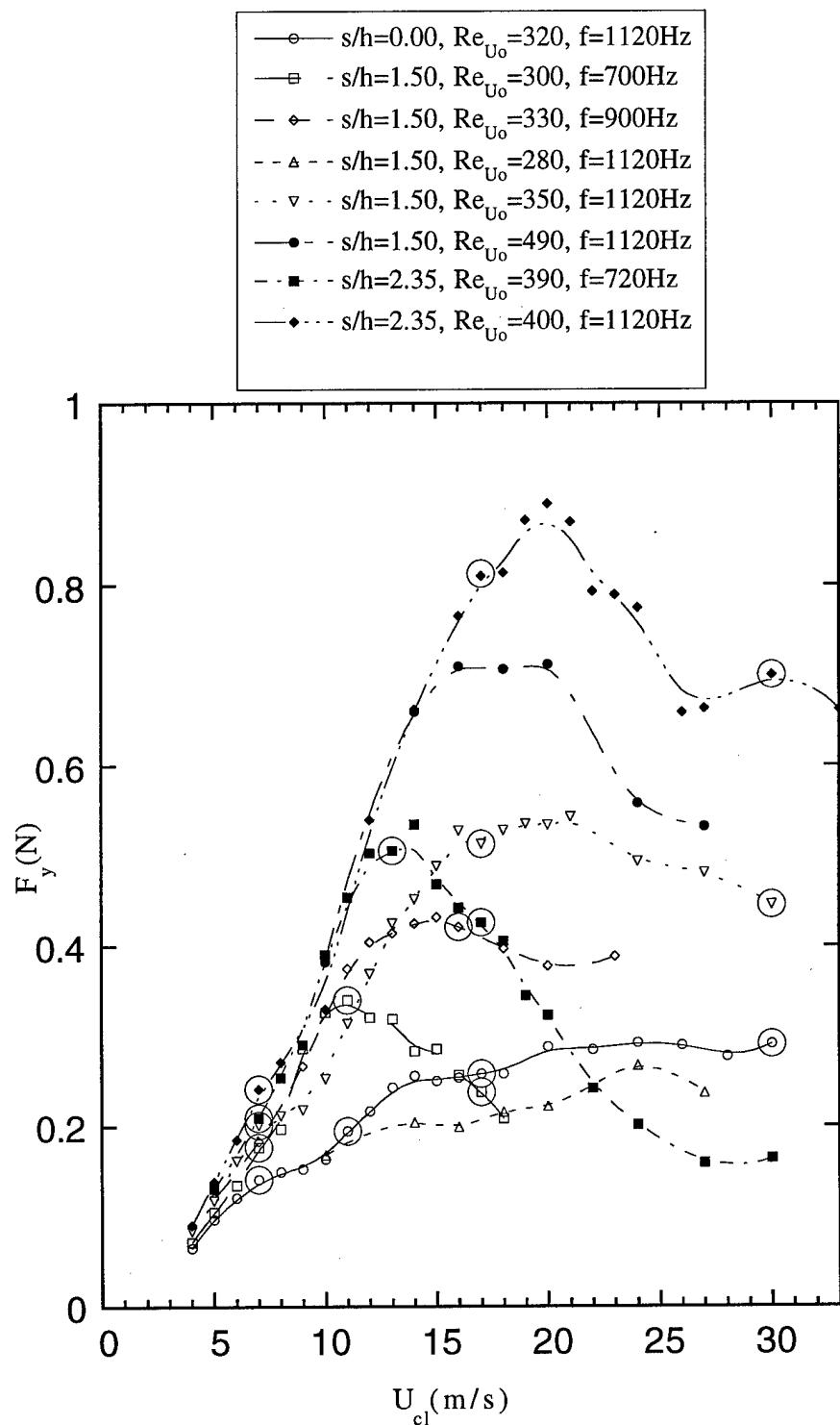
Figure III.16. Vectoring force as a function of the primary jet centerline velocity. Circled data points indicate that the high resolution phase-locked data summarized in Table III.1 was also taken for this case.
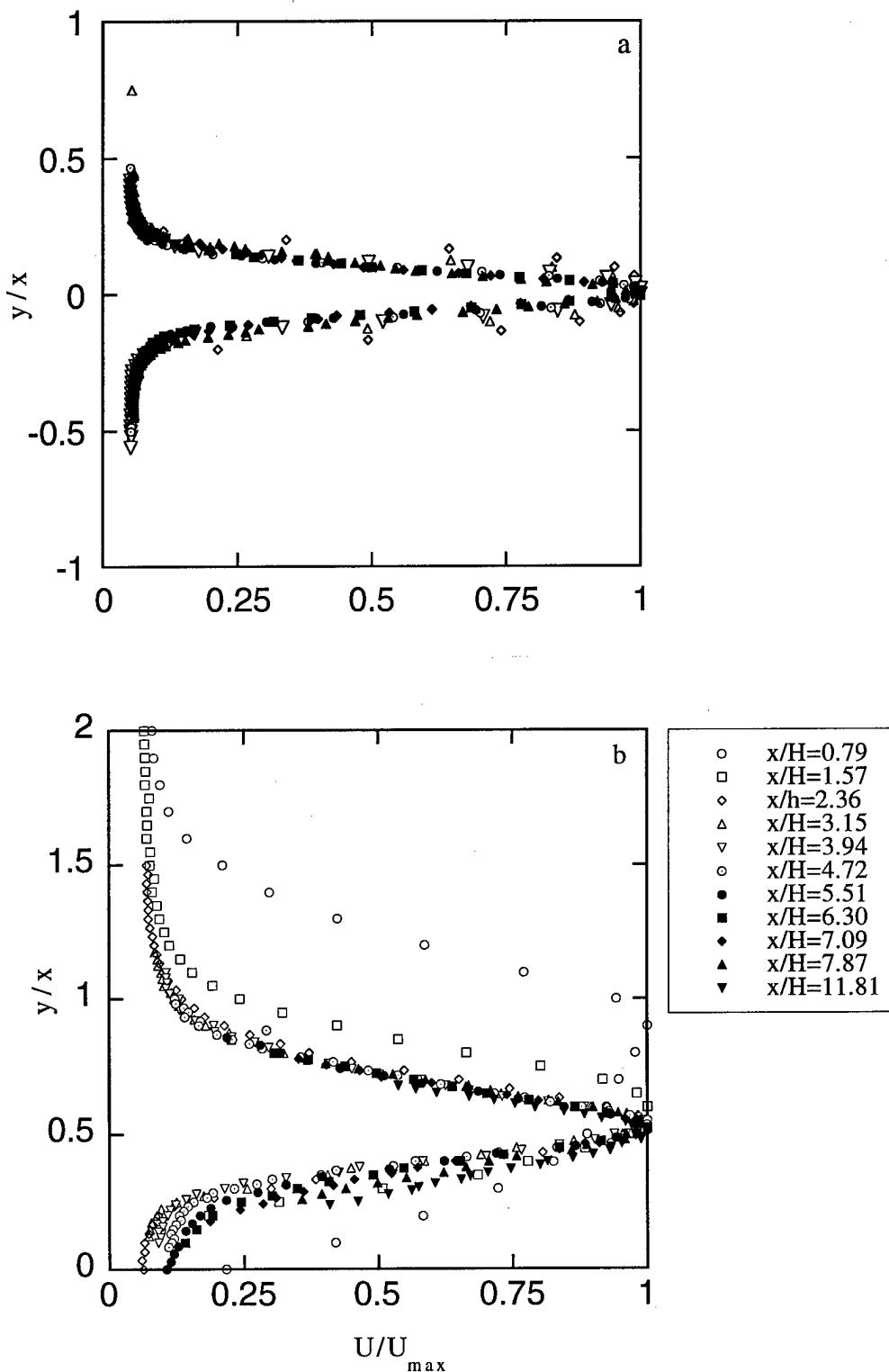
Figure III.17. Profiles of streamwise component of (a) unforced jet (b) forced jet. $Re_{Uo}=380$, f=1120Hz, s/h=1.5.
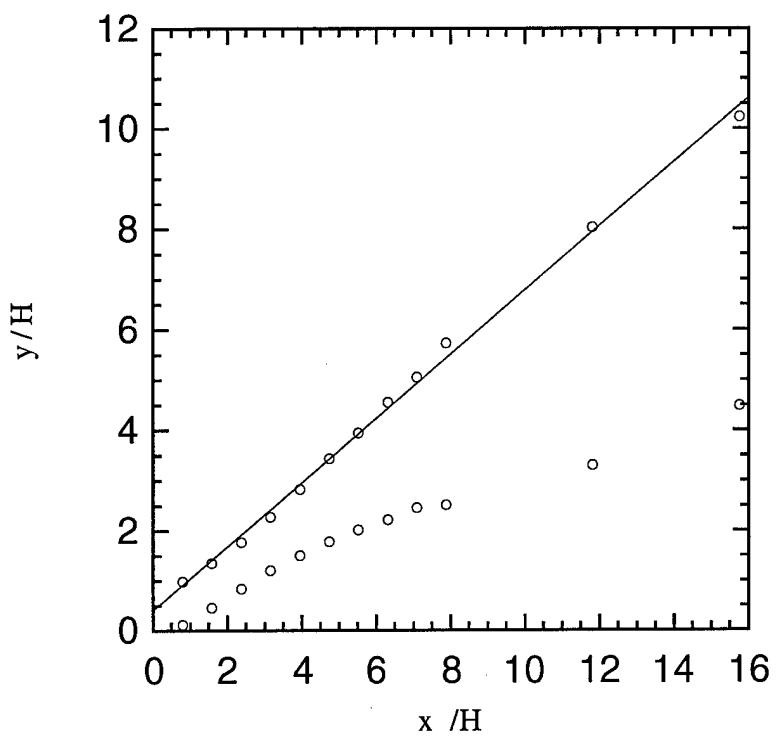
Figure III.18. Locations of the jet boundaries based on half the maximum velocity.
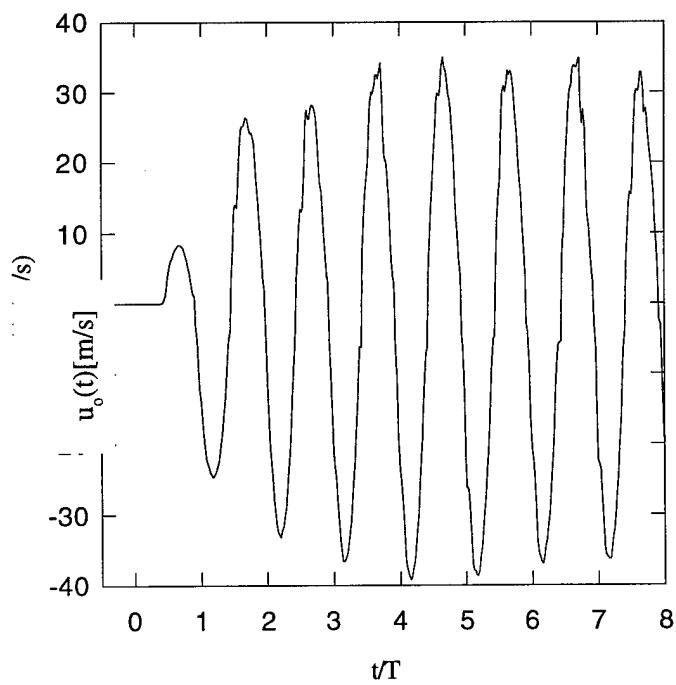
Figure III.19. Orifice velocity of synthetic jet activated impulsively at t/T=0.
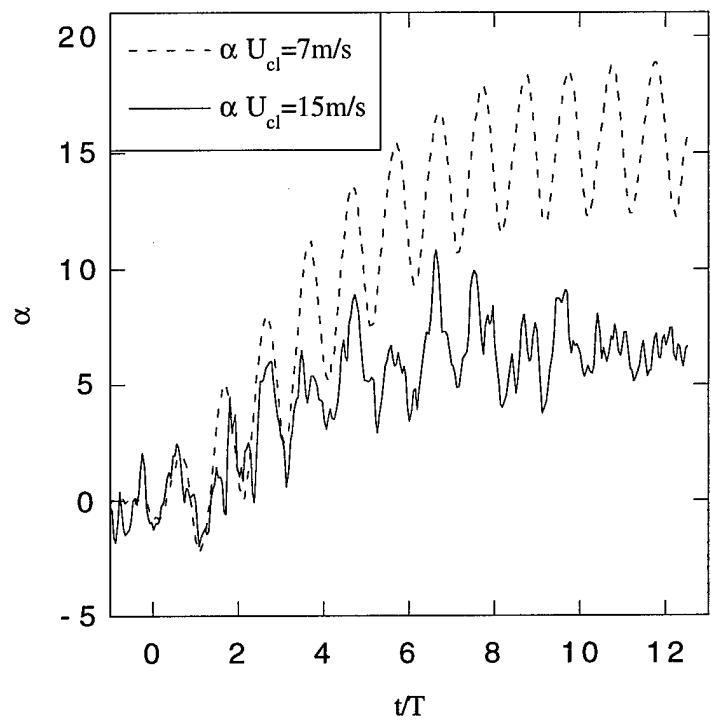
Figure III.20. Centerline flow angle at exit plane of the primary jet as synthetic jet is activated impulsively at t/T=0.
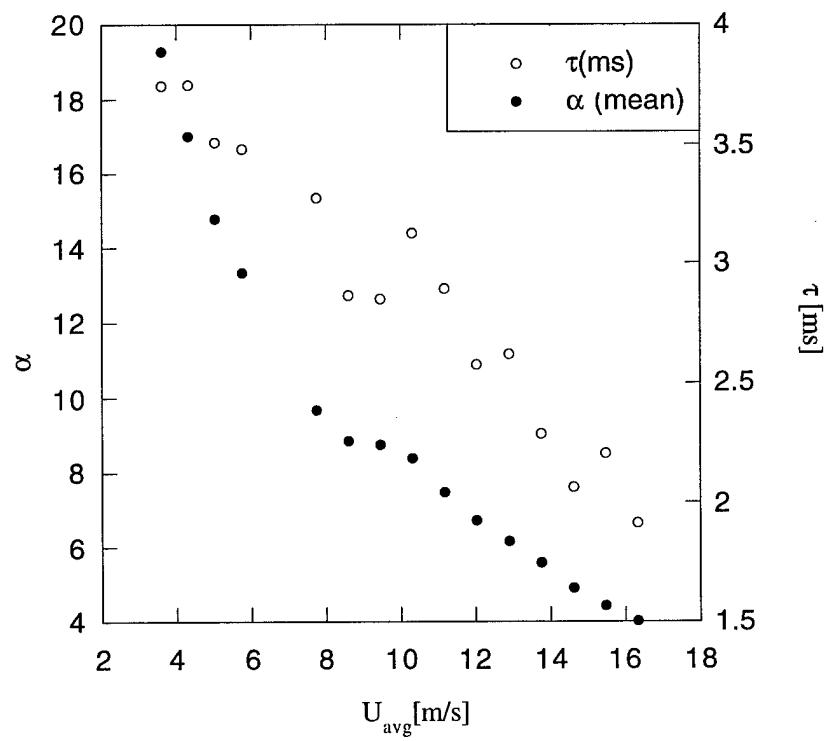
Figure III.21. Response time of the primary jet.

III.3.2 Unsteady Effects

As a prelude to the discussion of the interaction between the primary jet and the synthetic jet, it is instructive to consider the combination of a steady source and sink near the exit plane of the primary jet. If a steady sink is placed at the location of the synthetic jet orifice in this experiment, the sink flow would be drawn largely from the ambient, since the primary jet flow has momentum that is directed away from the sink, and the ambient is largely stagnant. A schematic of this situation is shown in Figure III.22a. It can be argued that as a result of the suction of some small amount of fluid from the primary jet, a stagnation point (saddle) would form between the sink and the primary jet exit plane. The location of this stagnation point depends on the volume flow rate of the primary jet fluid that is drawn into the sink. Because the sink would preferentially draw stagnant ambient fluid, it would have little effect on the primary jet. In fact, in a laboratory test the synthetic jet was replaced by a suction slot, and it was found that unless the suction flow rate was comparable to that of the primary jet, very little vectoring was achieved.

The addition of a steady source above the sink (Figure III.22b) leads to the addition of fluid above the sink with significant downstream momentum, and, although some of the sink flow is reversed and entrained, more primary jet fluid is entrained than without the source. The ratio between the volume flow rates drawn from the primary jet and from the source increases with the sink strength (since less sink flow will be entrained), and decrease with the primary jet velocity. This situation is analogous to the numerical work of Lim and Redekopp (1997) and Hammond and Redekopp (1998) in which suction is applied at the downstream end of the splitter plate in a shear layer, which results in vectoring of the combined flow in the near field. Since the shear layer in that study is infinite in the cross stream direction, the flow angle eventually returns to zero. However, in the hypothetical flow field depicted in Figure III.22b, the momentum of the source flow may be less than the primary jet, which allows for the vectored flow to remain so. As noted above, the synthetic jet may be thought of as an alternating source and sink. It was shown in §IV.1 that a stagnation point exists downstream of the synthetic jet orifice during the suction stroke, which limits the region from which it entrains. It will now be shown that this is also the case when the synthetic jet interacts with the primary jet, resulting is the entrainment of primary jet fluid during the suction stroke.

The unsteady interaction between the synthetic jet and the primary jet occurs within a small domain between the jets near the exit plane. In order to resolve the details of the flow structure within this domain, high magnification PIV images were obtained phase-locked to the actuator driving signal at 18 evenly spaced increments of the actuator cycle. These cases are summarized in Table II.1.

Some of the details of the interaction between the primary jet and the actuator are inferred from the phase-averaged streamline maps taken at 9 equally spaced increments in time for case AAD (1120 Hz, s/h = 0, and U_{cl} = 7m/s) shown in Figure III.23. The start of the blowing stroke of the synthetic jet is taken to be t/T = 0. The flow rate increment between adjacent streamlines is 1% of the unforced primary jet flow rate. Note that the data very near surfaces (within 0.014H) are distorted by surface reflections, and therefore data in this region are removed.

As is evident from the streamlines near the bottom right corner of each of the streamline maps, the direction of the primary jet flow outside of the interaction region remains relatively unchanged during the cycle of the synthetic jet. The time periodic oscillations in the vector angle have been discussed in connection to Figures III.20-21. At the start of the blowing stroke (Figure III.23a) a counter rotating vortex pair is formed as in the case of a synthetic jet in a quiescent medium. The axis of the pair is initially in line with the axis of the synthetic jet, but tilts toward the primary jet as it is convected downstream. The streamlines suggest that the lower (clockwise) half of the pair is more vigorous than the counter-clockwise half. This may be attributed to a distortion of the velocity profile within the synthetic jet orifice which yields higher

velocity near its bottom edge and thus the rollup of a stronger vortex. It should also be noted that the vorticity within the primary jet shear layer is of the opposite sine, and subsequently leads to the cancellation of this vortex farther downstream. The suction stroke of the actuator begins at t/T = 0.5, and results in the formation of a stagnation point downstream of the synthetic jet orifice (Figure III.23f). The stagnation point persists during the suction stroke, while moving in the positive cross stream direction. The trajectory of the stagnation point is discussed below in connection with Figure III.27. The stagnation streamlines divide the flow near the synthetic jet into four quadrants; namely, primary jet fluid that is drawn into the actuator, primary jet fluid which continues to move in the downstream direction, ambient fluid that is drawn into the synthetic jet, and ambient fluid that is advected along the primary jet. The rate at which primary jet fluid that is drawn into the primary jet is denoted as $Q_p(t)$.

Contour maps of dimensionless vorticity ($\omega_z^* = \omega_z / (U_o h)$) computed from the velocity data at the same points in phase are shown in Figure III.24. Contour levels start at $\omega^* = \pm 0.4$, and the contour increment is $\omega^* = 0.4$ (negative contours are dashed). At the beginning of the blowing stroke (Figure III.24a), fluid having ccw vorticity from the region close to the top surface of the conduit accumulates between the edge of the primary jet and the orifice of the synthetic jet. This fluid is drawn during the suction cycle of the synthetic jet and its accumulation leads to the formation of vorticity of the opposite sense in the wall boundary layer. The blowing cycle of the synthetic jet leads to the release of this vorticity concentration, which is then advected downstream as a free vortex (Figure III.24b). As for a synthetic jet in a quiescent surrounding, the blowing cycle results in the rollup of a counter rotating vortex pair. The rollup of the vortex pair is accompanied by the formation of vorticity of the opposite sense within the wall boundary layers on either side of the synthetic jet orifice (Figure III.24c-d). As noted above, at t/T = 0.33 (Figure III.24d), the ccw vortex of the pair is stronger, and as a result the axis of the pair tilts toward the primary jet as it convects downstream. It can also be seen in the vorticity plot that the rotational fluid of the ccw vortex of the pair is distributed over a much larger area than the cw vortex.

At the beginning of the suction stroke (t/T = 0.56, Figure III.24f), the synthetic jet ccw vortex is approximately 0.25H downstream from the exit plane and the suction motion along the exit plane is accompanied by vorticity of opposite sign on either side of the orifice. The magnitude of these vorticity concentrations increases as the suction stroke reaches its peak (Figure III.24h). It appears that the induced suction velocity near the surface between the primary jet and the synthetic jet is stronger than above the synthetic jet as is evidenced by the magnitude of vorticity concentrations there (which is larger that the vorticity magnitude within the primary jet itself).

The effect of a stepped orifice (s/h = 1.5, case ABD) on the interaction between the jets is shown in Figures III.25a-d using phase averaged streamlines and vorticity contour maps during the blowing and suction strokes. Compared to Figure III.24d, the vortex pair in Figure III.25a is more tilted toward the primary jet and the cw vortex is less diffused. The streamlines of the combined flow indicate a stronger vectoring effect than in the absence of the step. More importantly, it appears that during the suctions stroke, little fluid is drawn into the synthetic jet from above the step, and that the bulk of the synthetic jet fluid is drawn from the primary jet. As noted in connection with Figures III.11, 12 and 16, the stepped orifice leads to an increase in the volume flow rate and streamwise momentum flux of the primary jet as well as to an increase in the vectoring force, respectively.

The effect of the step size on the amount of fluid drawn from the primary jet is shown in Figures III.26a-c. The total volume flow rate into the synthetic jet, Q_{sj}, is determined by calculating the flow rate balance through the measurement domain, and is plotted along with $Q_p(t)$ for different step sizes. As discussed in §III, the Reynolds number of the synthetic jet increases with step size, and results in an increase in Q_{sj}. At the same time, the volume fraction of the synthetic jet flow that originates in the primary jet also increases with step size.

75
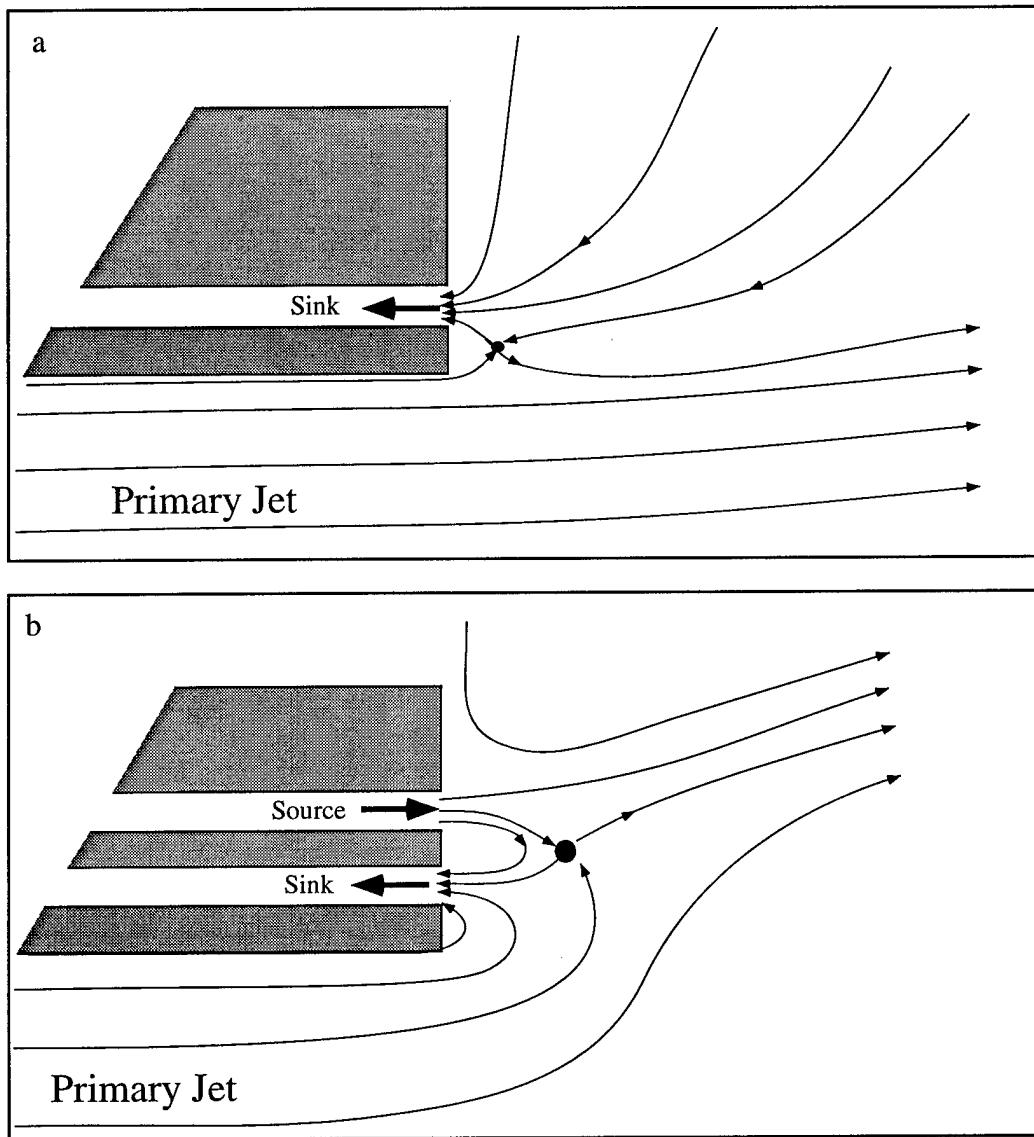
Figure III.22. Conjectured interaction between a jet and a (a) sink (b) source-sink combination.
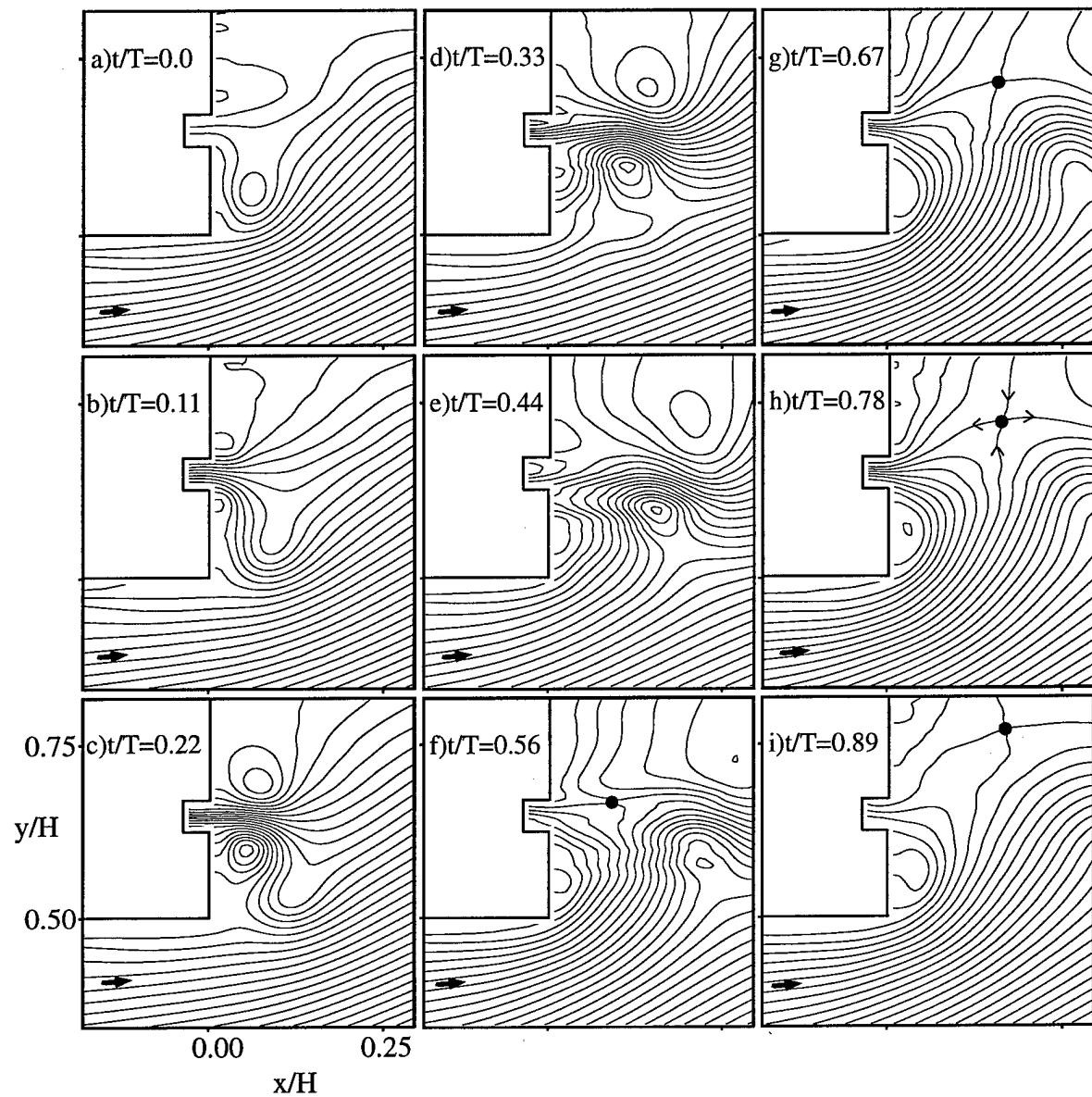
Figure III.23. Streamline maps of phase-locked velocity field near the synthetic jet at 9 equal increments of cycle. Streamfunction increment corresponds to 1% of total primary jet flow. Blowing stroke begins at t/T=0. Stagnation points are marked in (f)-(i). Case AAD (U_{cl}=7m/s, Re_{Uo}=314, f=1120, s/h=1.5).
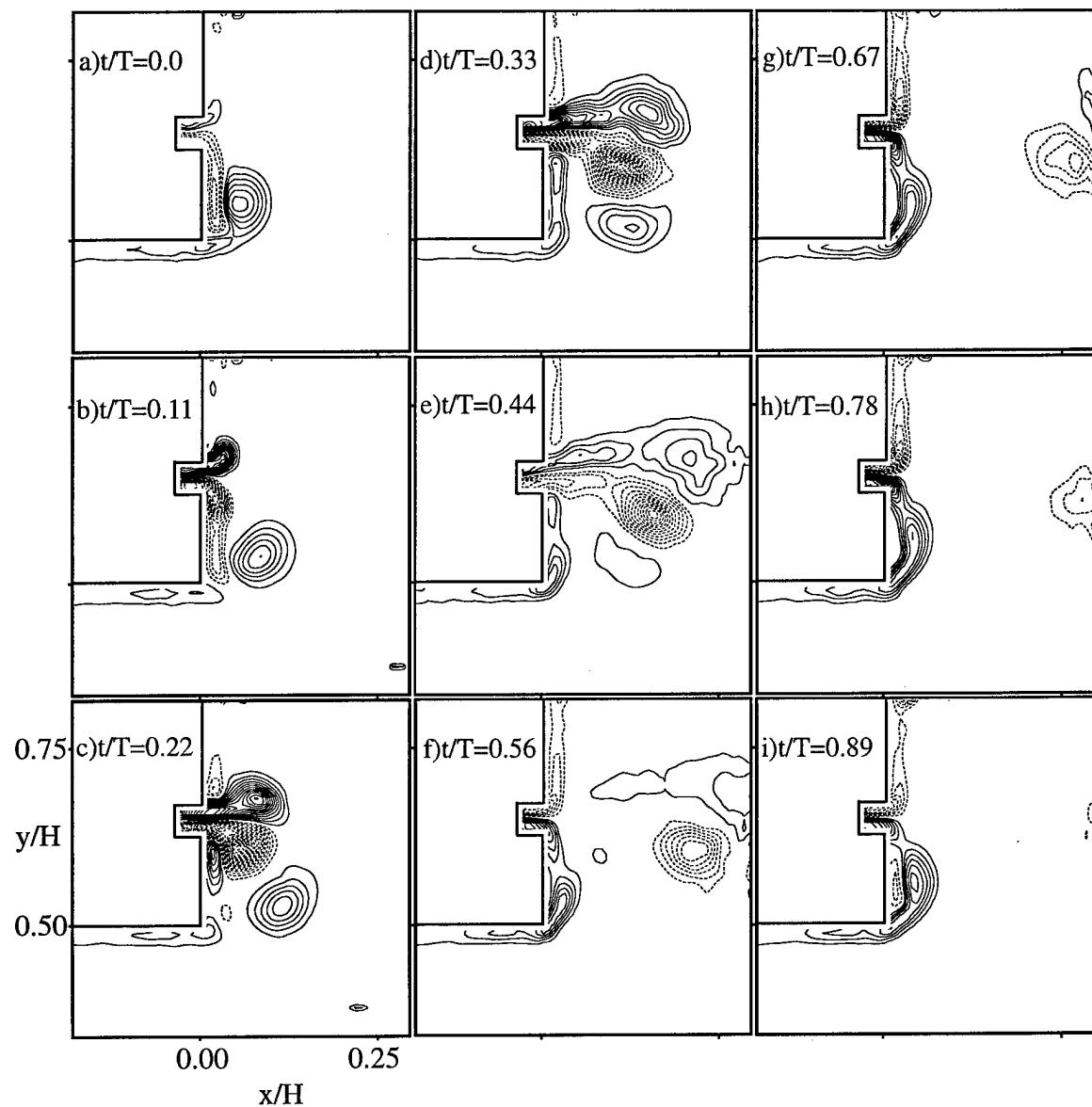
Figure III.24. Contours of dimensionless spanwise vorticity (ω'_z) in the interaction region for case AAD (U_c=7m/s, s/h=0, f=1120Hz, Re_{Uo}=314). The contour increment is 0.4, and negative contour levels are dashed.
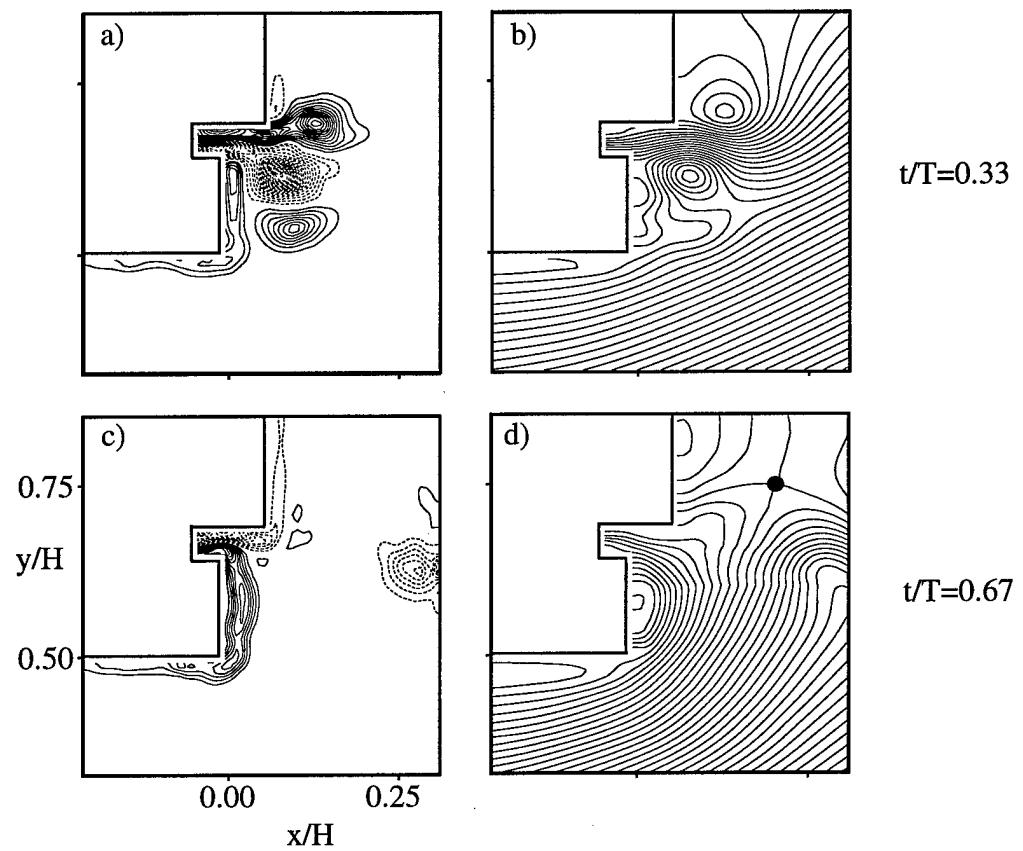
Figure III.25. Vorticity contours [(a) and (c)] and streamlines [(b) and (d)] and for case ABD (U_{cl}=7m/s, s/h=1.5, f=1120Hz, Re_{Uo}=363) during the blowing stoke [(a) and (b)] and suction stroke [(c) and (d)]. Increment in ω^*_z is 0.4, and streamline spacing corresponds to 1% of primary jet flow.
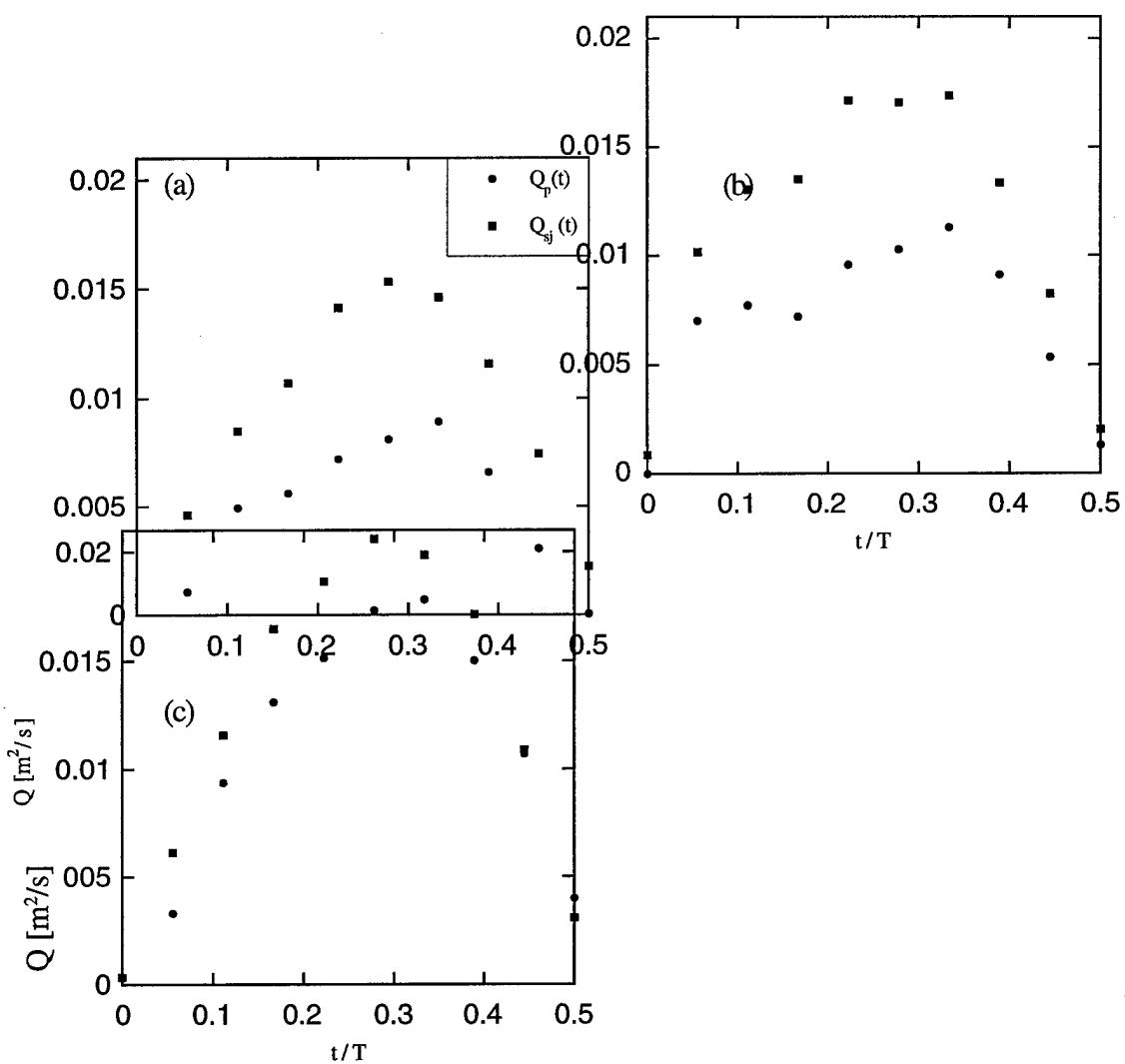
Figure III.26. Total flow rate into the synthetic jet (Q_{sj}) and flow rate of fluid originating in the primary jet (Q_p) for (a) s/h=0.0, (b) s/h=1.5, and (c) s/h=2.35. U_{cl}=7m/s, f=1120Hz.

It may be argued that one of the measures of the effectiveness of the synthetic jet is the position of the stagnation point that is induced during the suction stroke. An analogy is drawn to a sink in cross flow, for which the downstream distance between the sink and the stagnation point, r, is related to the free stream velocity and the sink flow rate, m, by

$$r = \frac{m}{2\pi U}.$$

In Figure III.27, the distance of the stagnation point from the synthetic jet orifice is plotted as a function of time for three different step sizes, and shows that lengthening the step brings the stagnation point closer to the synthetic jet orifice. A possible explanation for this behavior is that the larger step results in a larger vector angle, and in turn, a larger velocity magnitude in the vicinity of the synthetic jet "sink." In each case, r increases with the suction magnitude and reaches a maximum at $t/T = 0.75$, (in agreement with the behavior of a sink in a cross flow).

At a higher primary jet speed, the flow rate through the stream tube bounded by the upper conduit wall and the stagnation streamline is increased, and as a result, the volume of the circulating bubble that is formed between the actuator and the primary jet increases. This is shown in the streamline maps in Figures III.28a.1-4 for case DAD ($s/h = 0.0$, $U_{cl} = 17$m/s). Four equal time increments during the suction stroke are shown and the streamline spacing corresponds to 0.5% of the flow rate of the unforced primary jet. At the beginning of the suction stroke ($t/T = 0.556$) the behavior is similar to the case for $U_{cl} = 7$m/s (Figure III.23f). However, as the suction stroke proceeds, it is clear that only part of the fluid that enters the region bounded by the stagnation streamline is being drawn into the synthetic jet orifice. Therefore, a recirculation bubble forms between the synthetic jet and the primary jet, and grows until the suction ends. At this time, the bubble is released and propagates down stream (not shown). The net result is that the synthetic jet entrains less fluid from the primary jet than when the speed of the primary jet is lower (see Figure III.29).

As can be inferred from the data in Figure III.16, while the vectoring performance is similar for all step sizes and frequencies at low primary jet speeds, as the primary jet velocity increases, the vectoring performance becomes a more dependent on frequency and step size. Figures III.28b.1-4 shows the effect of the addition of a step ($s/h = 1.5$, case DBD). In this case, although the synthetic jet flow rate is similar, the step results in an increase in the portion of the synthetic jet flow that is drawn from the primary jet, which limits the size of the recirculation bubble. Simultaneously, the stagnation point moves closer to the synthetic jet because the primary jet is vectored more, and therefore the flow on which the sink acts during the suction stroke is moving faster. A further increase in the step size to 2.35h (case DCD, Figure III.28c.1 - 4) is not as dramatic as the change due to the addition of the smaller step. However, referring back to Figure III.16, this case has a considerably larger resultant force, which is due to the larger Re_{Uo} for that case (see Figure III.29c). The stagnation point trajectories for these three cases are shown in Figure III.30, and shows that as a result of the addition of the step, the stagnation point remains in the vicinity of the interaction region (at a very similar distance to the 7m/s cases in Figure III.27), and that an increase of s/h from 1.5 to 2.35 has very little effect.

It is shown that at the exit plane of the synthetic jet, the streamwise velocity is almost time harmonic with zero mean. The positive flow grows in amplitude and the negative flow ebbs while the mean velocity increases as the vortex pair rolls up and is advected downstream. The downstream distance over which this process occurs scales with the stroke length L_o. This effect is exploited with the aid of the step to alter the spatial symmetry of the inflow to the synthetic jet. If the frequency is reduced, L_o increases proportionally, and therefore, a longer step is required to achieve the same inflow asymmetry. Figure III.16 shows that the vertical force on the nozzle decreases dramatically at high speeds when the frequency is reduced. At $U_{cl} = 17$m/s and f = 700 Hz (case DBA) the streamlines during the start of suction stroke clearly show this loss of performance (Figure III.31, streamline spacing as in Figure III.28). The stagnation point initially forms farther downstream and moves faster out of the measurement

81

domain (compared with Figure III.28) while much more ambient fluid is entrained at the expense of the primary jet fluid.

The lower frequency (and thus longer L_o) in this case results in the development of the synthetic jet over a larger downstream distance. In particular, at lower frequency, each vortex pair from the synthetic jet is advected much farther downstream before the suction stroke begins which also effects the formation of the stagnation point. The difference in the relative convection speed of the pairs in cases DBA (700 Hz) and DBD (1120 Hz) are shown in Figure III.32, in which phase-locked contour maps of spanwise dimensionless (ω_z^*) vorticity are plotted for cases which are identical except for frequency. The cw vortex of the vortex pairs in the cases DBD and DBA (Figures III.32.1-2) is elongated compared to a corresponding cases at 7m/s (Figure III.24c). At the lower synthetic jet frequency (Figures III.32b.1-4), the remnants of the vortex pair, is convected out of the measurement domain faster than at 1120 Hz, where the pair is still visible at x/H = 0.2 when the suction stroke begins. This also affects the location of the stagnation point as shown in the stagnation point trajectories for the two cases in Figure III.33.

The effect of the step size and frequency on Q_p and Q_{sj} at U_{cl} = 17m/s are visible in Figure III.29. In each plot, $Q_{sj}(t)$ (which is related directly to Re_{Uo}) is also plotted for reference. The effect of a 1.5h step is seen by comparing Figure III.29a (s/h = 0) to Figure III.29b (s/h = 1.5). Clearly, a larger percentage of the total synthetic jet flow rate is drawn from the primary jet when the step is employed. Additional increase of the step to 2.35h results in an even larger fraction of the synthetic jet flow to be drawn from the primary jet. At lower frequency (700 Hz, Figure III.29d) a lower volume flow rate is drawn from the primary jet compared to a forcing at 1120 Hz (Figure III.29b).

Based on the data shown in Figures III.23-32, it appears that the vectoring is a strong function of the flow rate of fluid from the primary jet into the synthetic jet, and that this flow rate is a function of the primary jet speed, the step length, and the frequency of the synthetic jet. The dependence of the vectoring force on the volume flow rate that is drawn from the primary jet by the synthetic jet averaged during the suction stroke (denoted by Q_p) , is determined for each of the 17 high resolution phase locked cases summarized in Table II.1. Q_p is computed using the instantaneous (phase averaged) stream function. The difference between the magnitude of the stream function at the stagnation point and at the upper surface of the primary jet conduit is then defined as $Q_p(t)$ at that instant in time. These values averaged over the suction cycle are defined as Q_p.

To determine the dependence of the vectoring force on Q_p, it is assumed that the vectoring force depends only on the primary jet flow as characterized by U, H and ρ and on Q_p. It is conjectured that while Q_p is a function of s and f, the vectoring depends primarily on Q_p. On dimensional grounds, it is argued that

$$F = f(H, Q_p, U, \rho)$$

and thus

$$\frac{F}{\rho H U^2} = g\left(\frac{Q_p}{HU}\right) = g\left(\frac{Q_p}{Q}\right).$$

This relationship is plotted in Figure III.34, where each combination of step size and frequency is denoted by a different symbol. The good collapse of the data from the cases summarized in Table II.1 indeed suggests that the dimensionless vectoring force is primarily a function of the dimensionless volume fraction Q_p/Q, i.e. the ratio of the volume flow rate removed from the primary jet to the total primary jet volume flow rate. It is also necessary to determine the dependence of Q_p on the primary parameters that govern the performance of the synthetic jet to enable determination of the vectoring force directly from the synthetic jet parameters. If the synthetic jet parameters and the primary jet velocity can be related to Q_p, it will then be possible to relate them to the vectoring force.
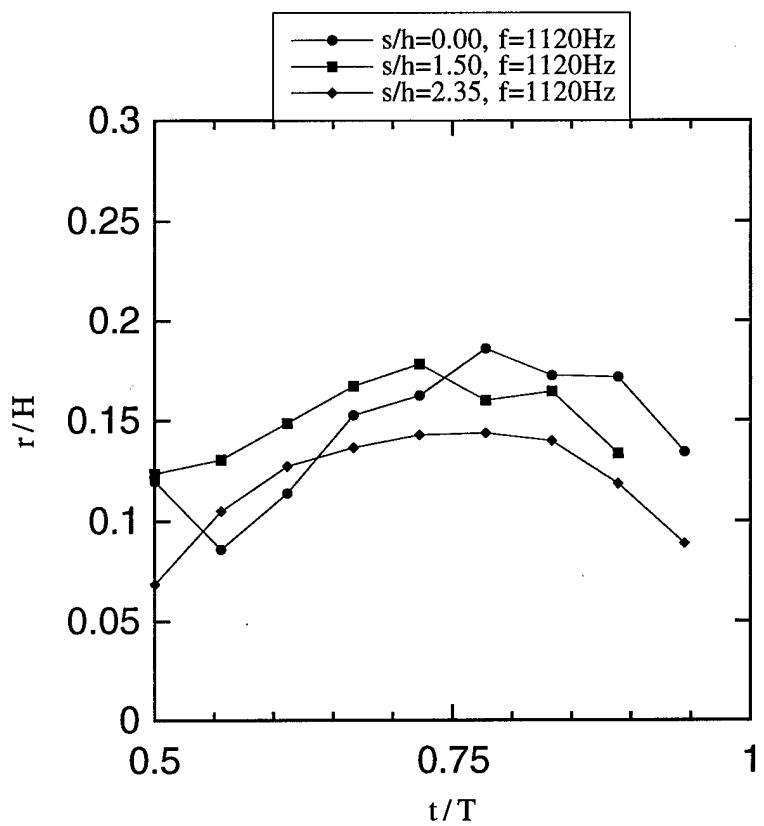
Figure III.27. Distance from the stagnation point to the synthetic jet orifice during the suction stroke for three cases at U_{cl}=7m/s and f=1120Hz.
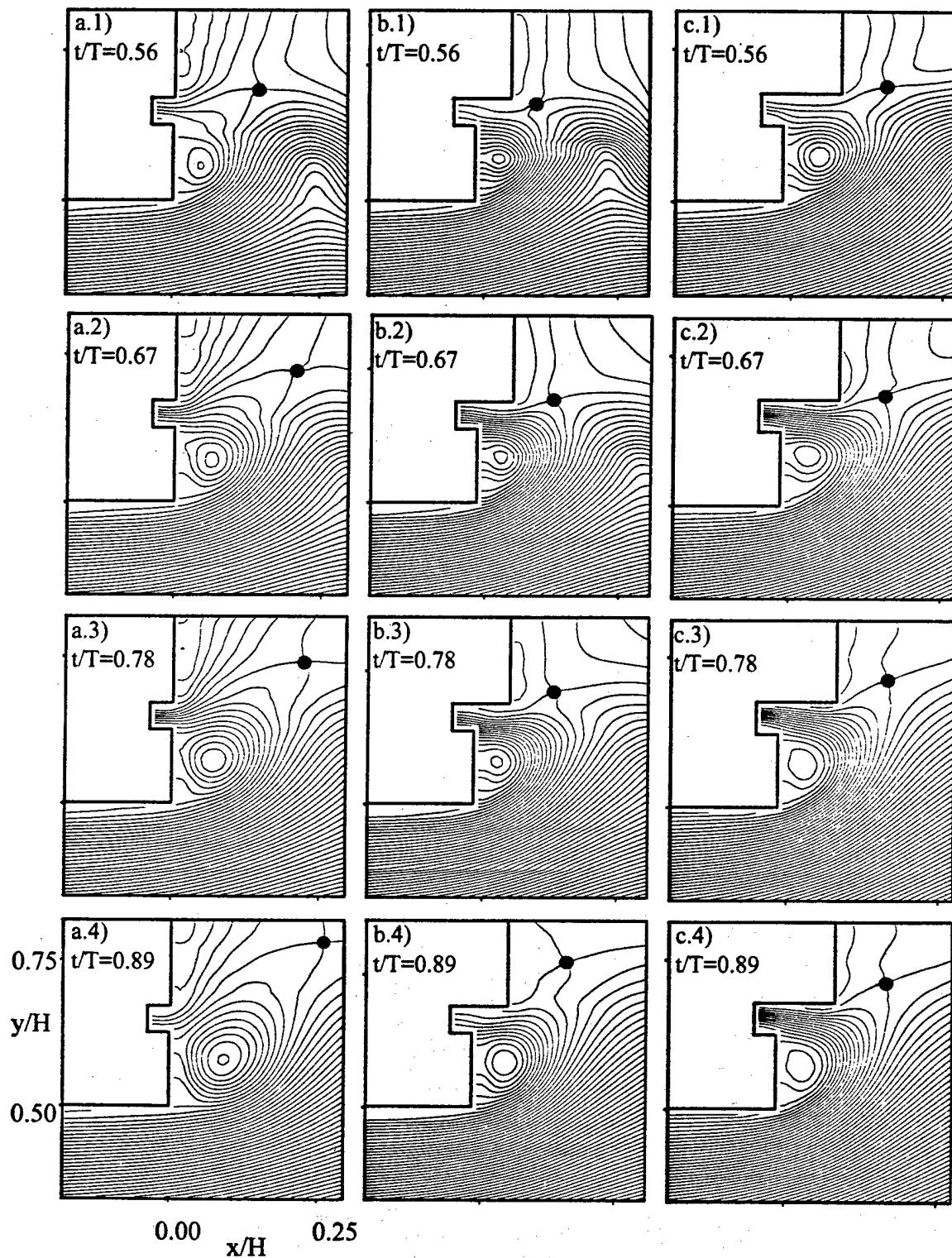
Figure III.28.Streamlines for U_{cl}=17m/s, f=1120Hz cases (a) EAD (s/h=0.0) (b)EBD (s/h=1.5) and (c) ECD (s/h=2.35). Streamline increment corresponds to 0.5% of primary jet flow rate.
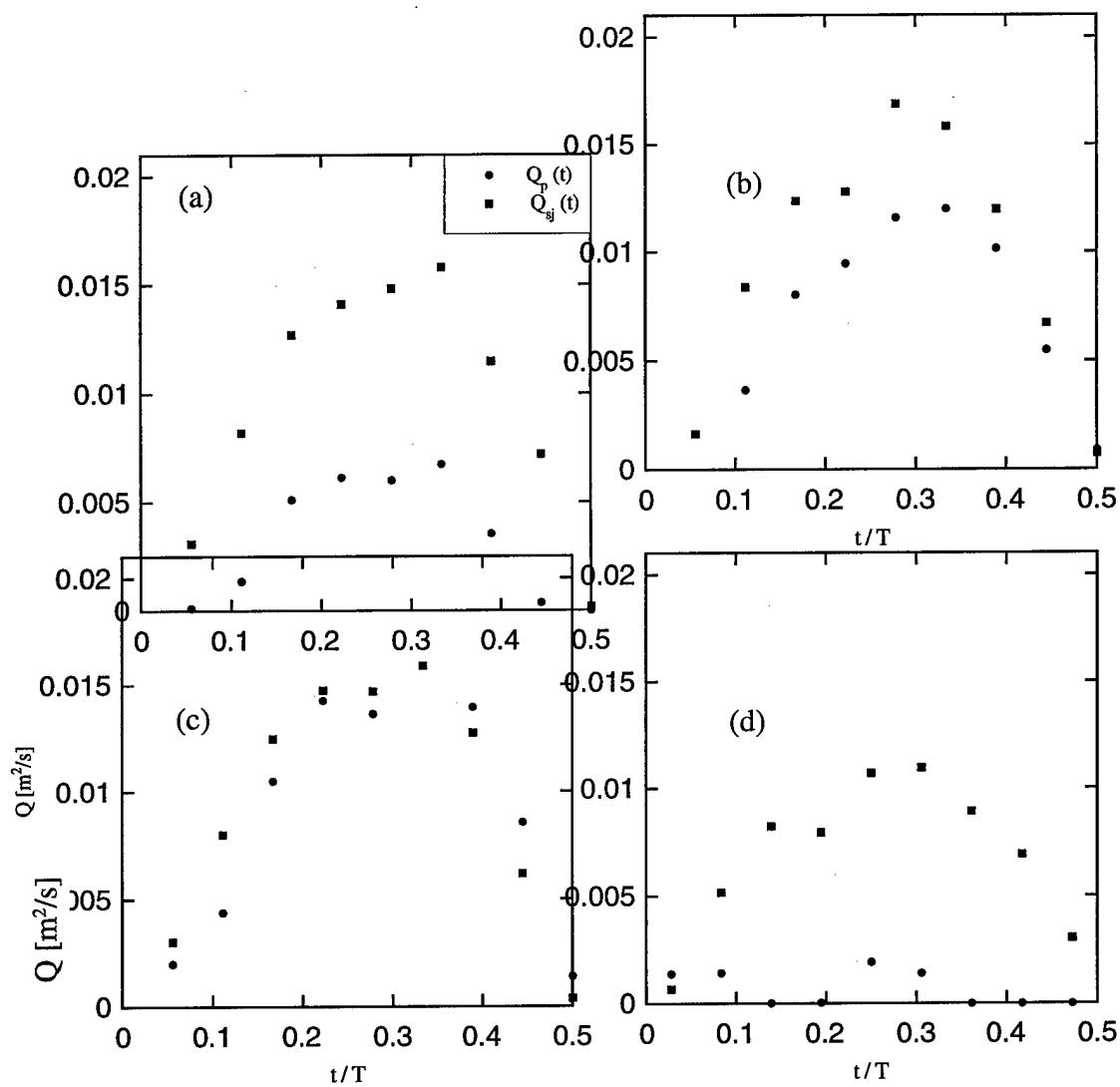
Figure III.29. Total flow rate into the synthetic jet (Q_{sj}) and flow rate of fluid originating in the primary jet (Q_p) for (a) s/h=0.0, f=1120Hz, (b) s/h=1.5, f=1120Hz, (c) s/h=2.35, f=1120Hz, and (d) s/h=1.5, f=700Hz. U_{cl}=17m/s.
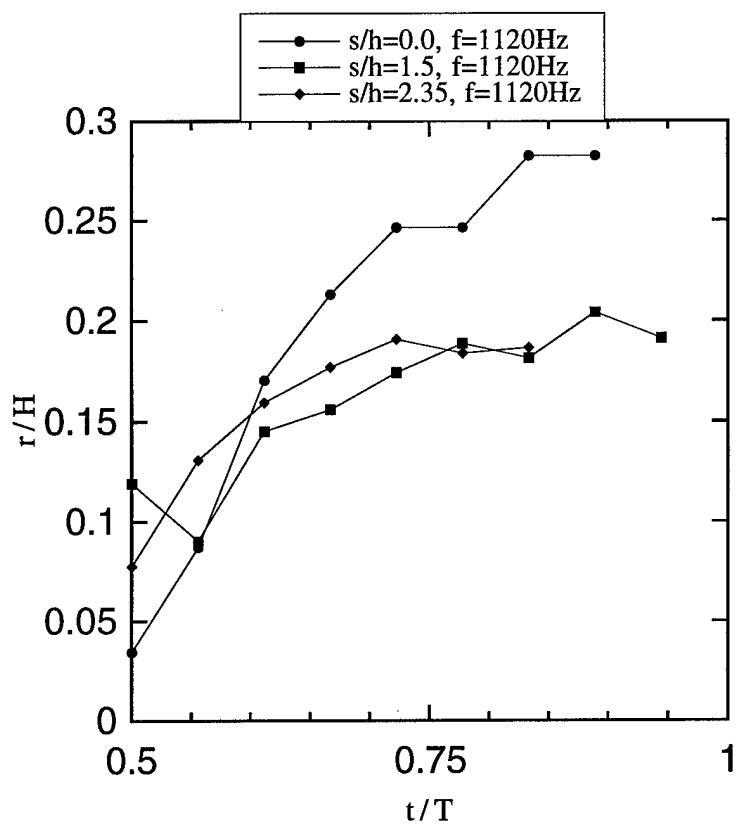
Figure III.30. Distance from the stagnation point to the synthetic jet orifice during the suction stroke for three cases at U_{cl}=17m/s and f=1120Hz.
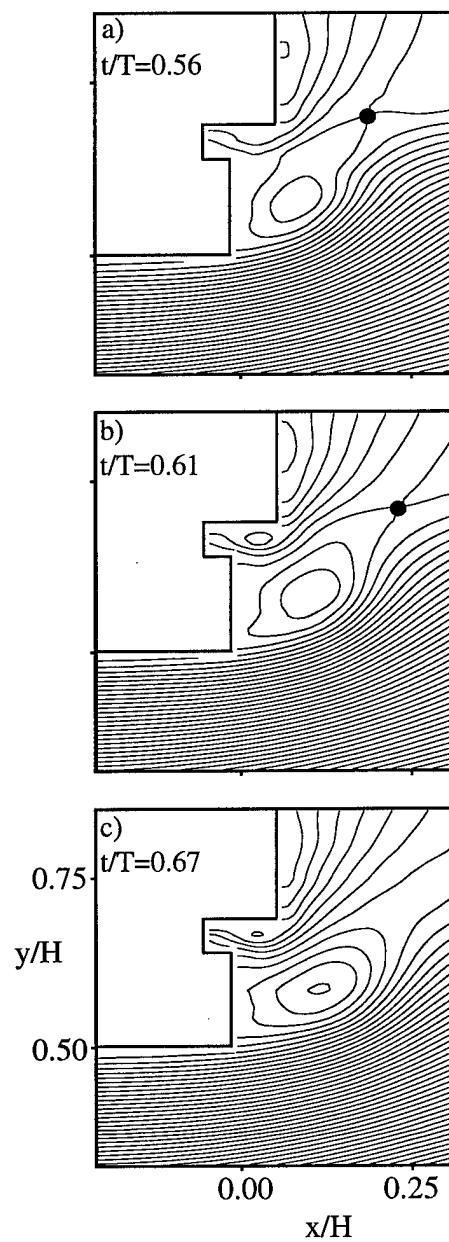
Figure III.31. Streamline maps for case EBA (U_{cl}=17m/s, s/h=1.5, f=700Hz, Re_{Uo}=300). Streamline spacing corresponds to 0.5% of primary jet flow rate.
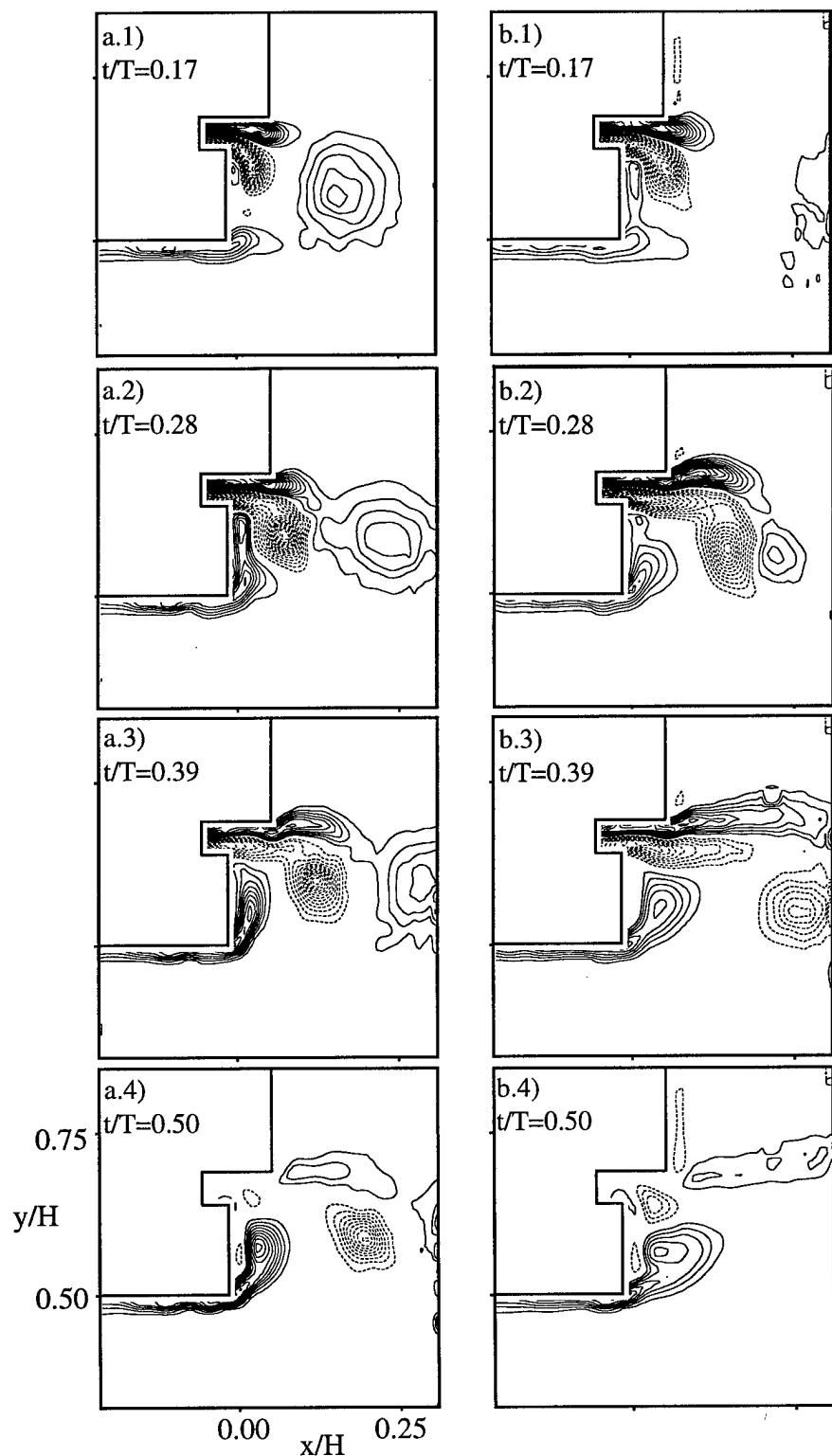
Figure III.32. Contours of ω^*_z for U_{cl}=17m/s, s/h=1.5 cases (a) EBD (f=1120Hz) and (b) EBA (700Hz). Contour increment is 0.4, and negative values are dashed.
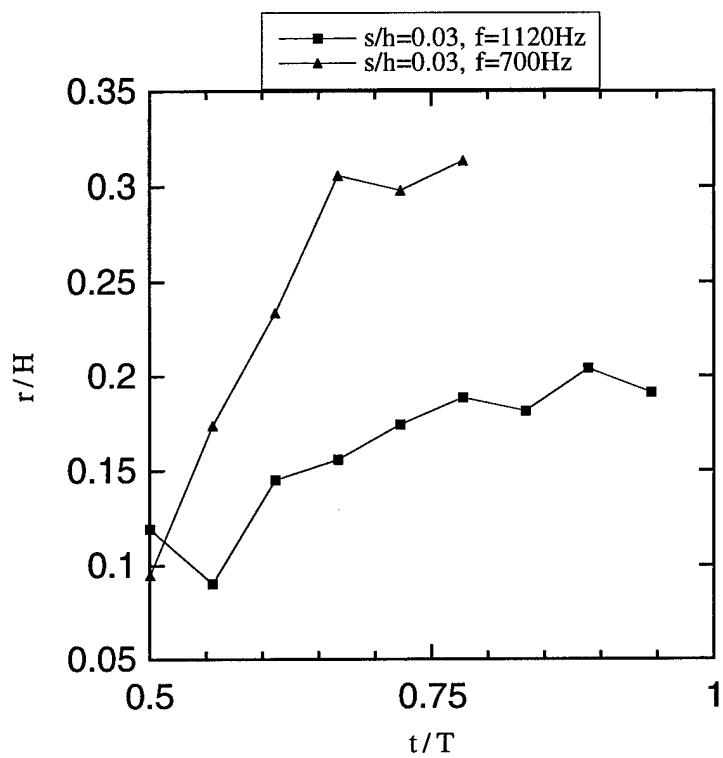
Figure III.33. Distance from the stagnation point to the synthetic jet orifice during the suction stroke for two cases at U_{cl}=17m/s and s/h=1.5.
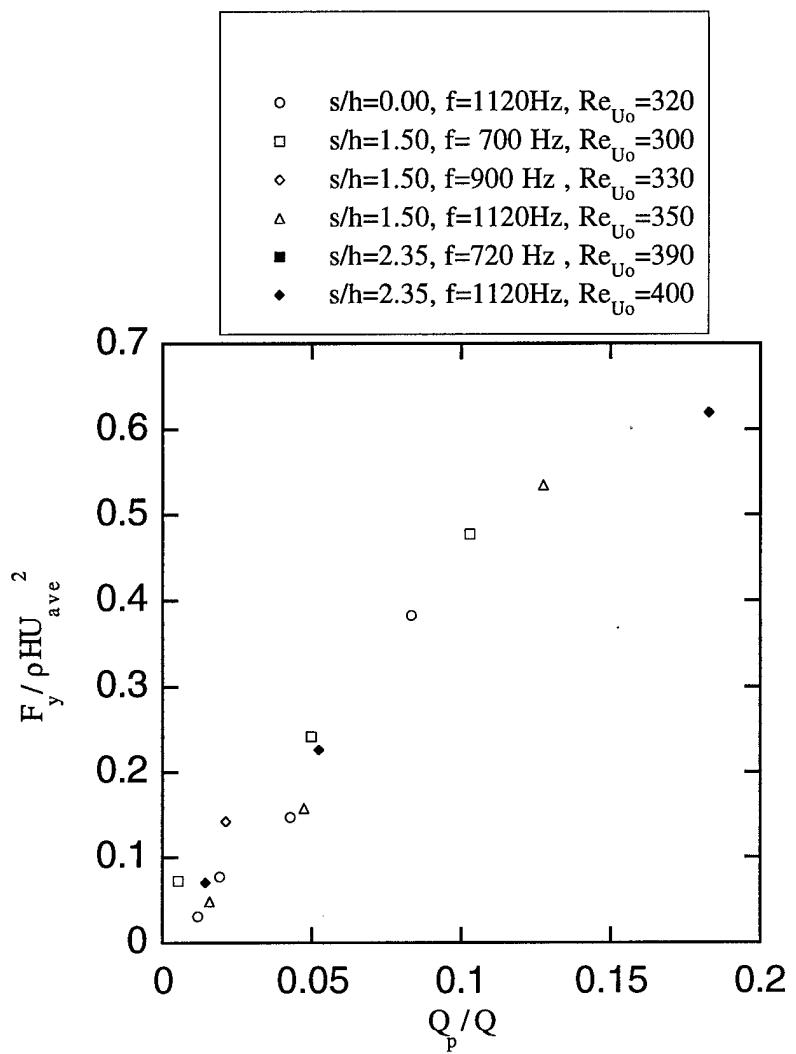
Figure III.34. Variation of the relative vectoring force with the volume flow rate ratio.

The dependence of Q_p/Q on a limited range of f, s/h, and U_{cl} is shown in Figures III.35a-c. Figure III.35a shows the variation of Q_p/Q with the centerline velocity of the primary jet for three sets of f and s/h. In each case, Q_p/Q decreases with U_{cl}. At f = 700 Hz and s/h = 1.5 Q_p/Q decreases more rapidly than the two cases at 1120 Hz. In Figure III.35b, it is shown that at fixed U_{cl} and s/h, Q_p/Q increases with frequency. Finally, Figure III.35c shows that Q_p/Q increases with the step length for two fixed values of U_{cl} and f. Note, however, that Q_p/Q is not zero as s/h→0. In fact, for U_{cl} = 7m/s, more than half of the synthetic jet flow is drawn from the primary jet. Recall from §IV.1 that a symmetric synthetic jet in a quiescent ambient entrains an equal amount of fluid from each side. The asymmetric geometry coupled with the primary jet flow serves to increase the entrainment from the primary jet side, and in some cases more than half of the synthetic jet fluid is drawn from the primary jet. It is conjectured that this is a result of the low pressure associated with the turning of the flow as it leaves the primary jet and enters the synthetic jet. A streamline map for the case AAD, (U_{cl} = 7m/s, Figure III.23) is reproduced in Figure III.36 for reference, and some relevant features are highlighted. Of particular note is the turing of the fluid near the conduit wall of the primary jet as it is drawn into the synthetic jet cavity during the suction stroke. In the present geometry, the radius of curvature of the streamlines scales with the thickness of the primary jet conduit, R. The centripetal acceleration of this fluid is balanced by a pressure gradient in the region between the synthetic jet and the primary jet.

$$\frac{\partial p}{\partial n} = -\frac{1}{\rho}\frac{V^2}{r}.$$

Where n is the direction normal to the streamline, V is the velocity magnitude along the streamline, and r varies between the conduit thickness, R, to the edge of the stagnation streamline as shown in Figure III.36. The present data show that at the exit plane, the magnitude of V is found to vary by less that 15% across this stream tube bounded by the conduit wall and the stagnation streamline, and that V scales with U_{ave}. It is therefore assumed that the thickness of the stream tube scales with $Q_p U_{ave}$. It is conjectured that this pressure gradient results in a pressure below the synthetic jet orifice which is lower than the region above the orifice, which will enhance Q_p. Therefore, Q_p increases both with the step size, and with the magnitude of the pressure in the region between the jets.

It has been shown that Q_p increases with step size since more flow is drawn from the primary jet. For a given Re_{Uo}, an increase in the frequency leads to a decrease in the stroke length (L_o) and therefore the synthetic jet to develops within a shorter downstream distance, and thus a shorter step is necessary to achieve the same Q_p. Increasing the primary jet speed results in a larger convection velocity of the synthetic jet fluid, and therefore has the same effect of increasing the stroke length (or decreasing the frequency). Based on this argument and the data of Figure III.35, it is conjectured that Q_p/Q is a function of the parameter s/λ, where λ = U_{ave}/f. However, as noted above, due to the low pressure associated with the turning of the primary jet flow towards the synthetic jet, Q_p/Q does not go to zero as s/h→0 suggesting that a "virtual origin" of s/λ is required, which, as shown in Figure III.35c, depends on the primary jet speed, and possibly the driving frequency. Therefore, a function of the modified parameter (s+s')/λ is sought, where -s'/λ is the value at which Q_p/Q goes to zero. The parameter s' may be thought of as a "negative step" at which $Q_p = 0$. It is likely that s' depends on the distance from the synthetic jet orifice to the edge of the primary jet, R, although the exact relationship is unknown. From the data reported here, a value of s' = 1.5h is found. As (s+s')/λ becomes large (i.e. as s/L_o becomes large and U_{ave} becomes small), it is expected that Q_p/Q asymptotically approaches unity. Furthermore, as (s+s')/λ becomes small (i.e. small s+s' or large U_{ave}), it is expected that Q_p/Q will approach zero. In Figure III.37, Q_p/Q is plotted as a function of (s+s')/λ, and for the range of these parameters generated for the cases summarized in Table II.1, there is a linear relationship. The largest value of Q_p/Q generated for these cases is less than 0.2, so it is not surprising that the expected asymptotic behavior is not manifested in the data.

91

This scaling does not account for the role of Re_{U_o}, which varies by 25% for the data in Figure III.37. It seems reasonable to expect that Q_p increase with Re_{U_o}, although the present data does not show such a trend indicating that in this range, Q_p depends only weakly on Re_{U_o}.

For the bulk of the data of this study, the value of Q_p is not known (Q_p is calculated only for the high resolution phase-locked data summarized in Table II.1 and cannot be determined from the mean data presented in Figure III.16). However, the value of Q_p for any case can be estimated by using the linear relationship between Q_p/Q and $(s+s')/\lambda$ shown in Figure III.37, making it possible to scale the data of Figure III.16. The normalized data for all cases are plotted in Figure III.38, and suggests that $F_y/\rho H U^2 \propto (Q_p/Q)^{1/2}$. The most obvious outlier is the low $Re_{U_o} = 280$ case indicating that the insensitivity to Re_{U_o} discussed in relation to Figure III.37 does not extend to very low values. It is also possible that the low value of U_o for this case may adversely affect the vortex rollup of the synthetic jet, and therefore alter the interaction with the primary jet.

III.4 Conclusions

A rectangular synthetic jet placed along the long side of a (primary) conventional rectangular jet such that the exit planes of the two jets coincide is used to vector the primary jet toward the actuator. The synthetic jet enhances small-scale motions within the interaction region between the two jets, and suppresses the Kelvin-Helmholtz instability in the forced shear layer of the primary jet. In addition, the flow rate and momentum flux vary along the conduit of the primary jet when forcing is applied.

The turning of the primary jet flow takes place largely within the jet conduit. When the conduit flow is laminar, the flow separates along the unforced side of the conduit wall upstream of the exit plane. Vectoring is achieved over nearly an order of magnitude in the primary jet velocity, and the vectoring angle decreases with the primary jet speed.

The jet is vectored due to a low pressure region that is induced by the synthetic jet near the exit plane when fluid is drawn from the primary jet into the synthetic jet. The turning of the flow is balanced by a normal force on the primary jet nozzle, which increases with primary jet speed and the volume flow of fluid removed from the primary jet, Q_p.

The addition of a small step along one side of the synthetic jet orifice leads to an increase in the volume flow rate that is drawn from the primary jet. At fixed Re_{U_o}, an increase in the frequency leads to a decrease in the stroke length (L_o) and therefore the synthetic jet develops within a shorter downstream distance, and thus requires a shorter step to achieve the same Q_p. An increase the primary jet speed results in a larger convection velocity of the synthetic jet fluid, and therefore is similar to an increase in the stroke length (or a decrease in frequency). The volume fraction Q_p/Q depends on the dimensionless step $(s+s')/\lambda$, where $\lambda = U_{ave}/f$ and s'/λ is the value at which Q_p/Q vanishes. It is likely that s' is related to the distance from the synthetic jet orifice to the edge of the primary jet, although the exact relationship is unknown.
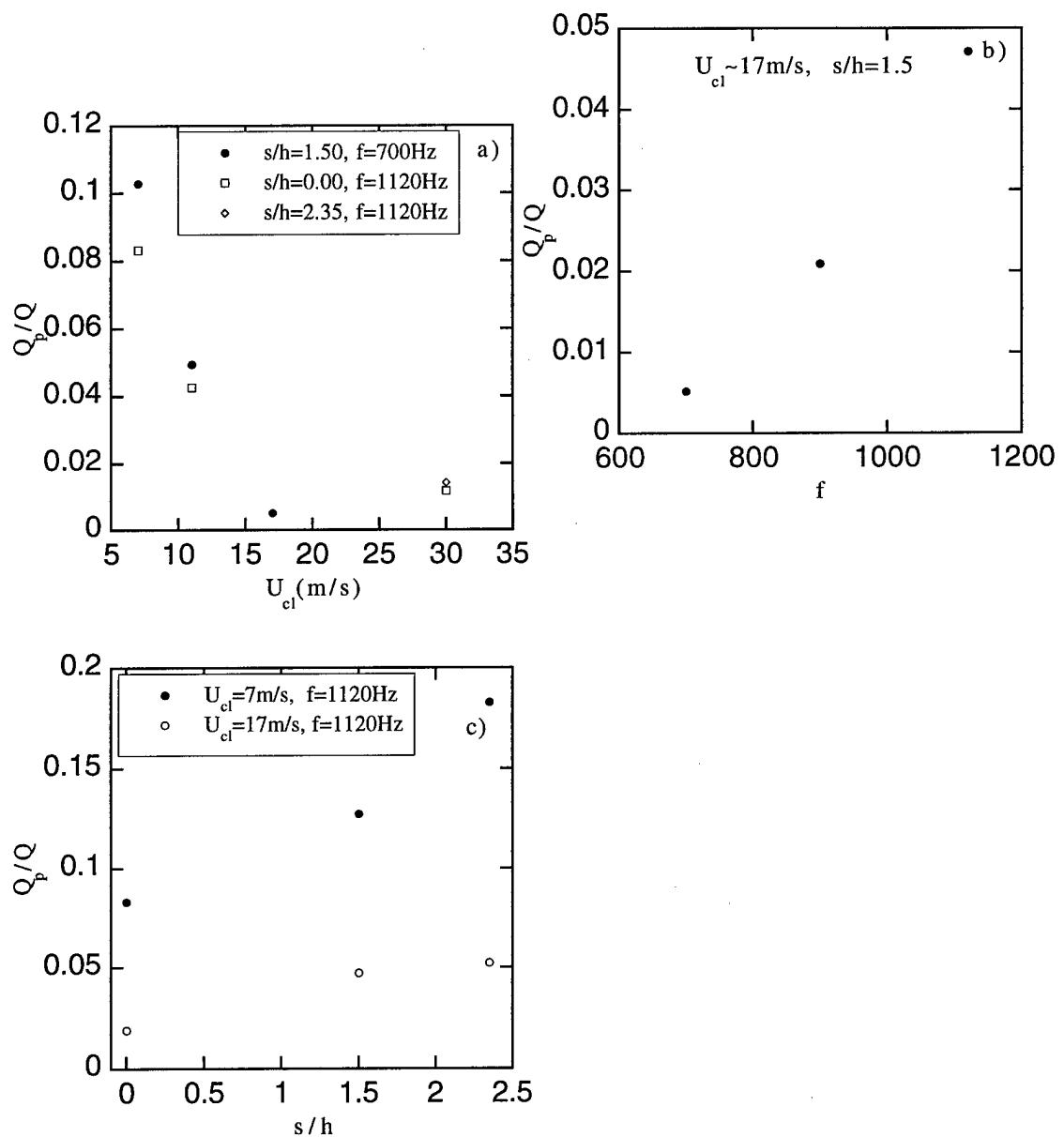
Figure III.35. Variation of the synthetic jet flow provided by the primary jet with (a) primary jet velocity (b) frequency and (c) step size.
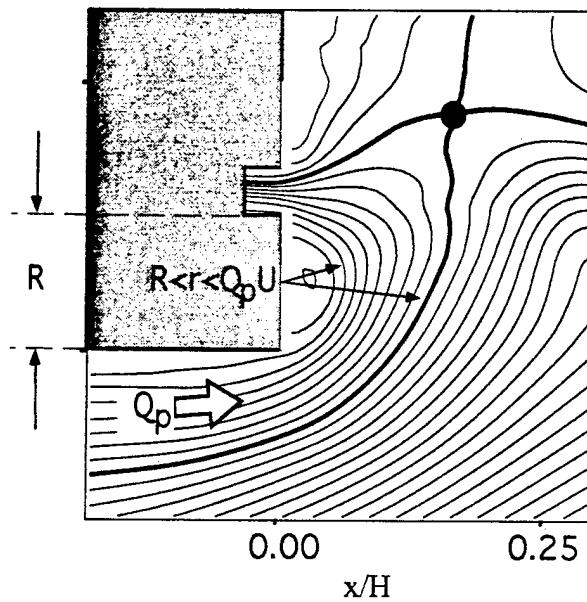
Figure III.36. Explanation of need for the parameter s'. Low pressure which results from the turning of the primary jet boundary layer at a radius that varies from R to Q_pU results in an increased tendency to entrain primary jet fluid rather than ambient fluid. For this reason, when s/h=0, as in the case pictured above (AAD), $Q_p>0.5$.
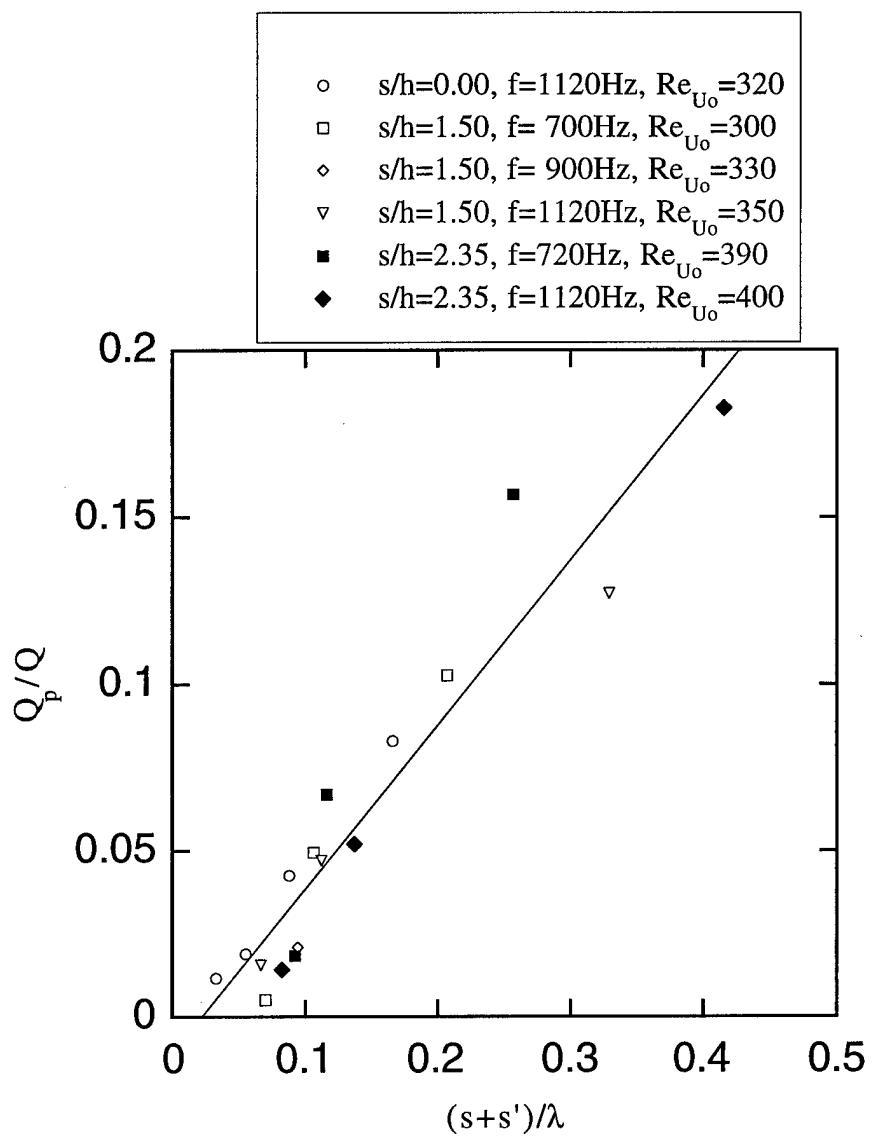
Figure III.37. Variation of the synthetic jet flow provided by the primary jet relative to the primary jet flow rate with the ratio of the modified step size to the wave length based on the driving frequency and the primary jet velocity.
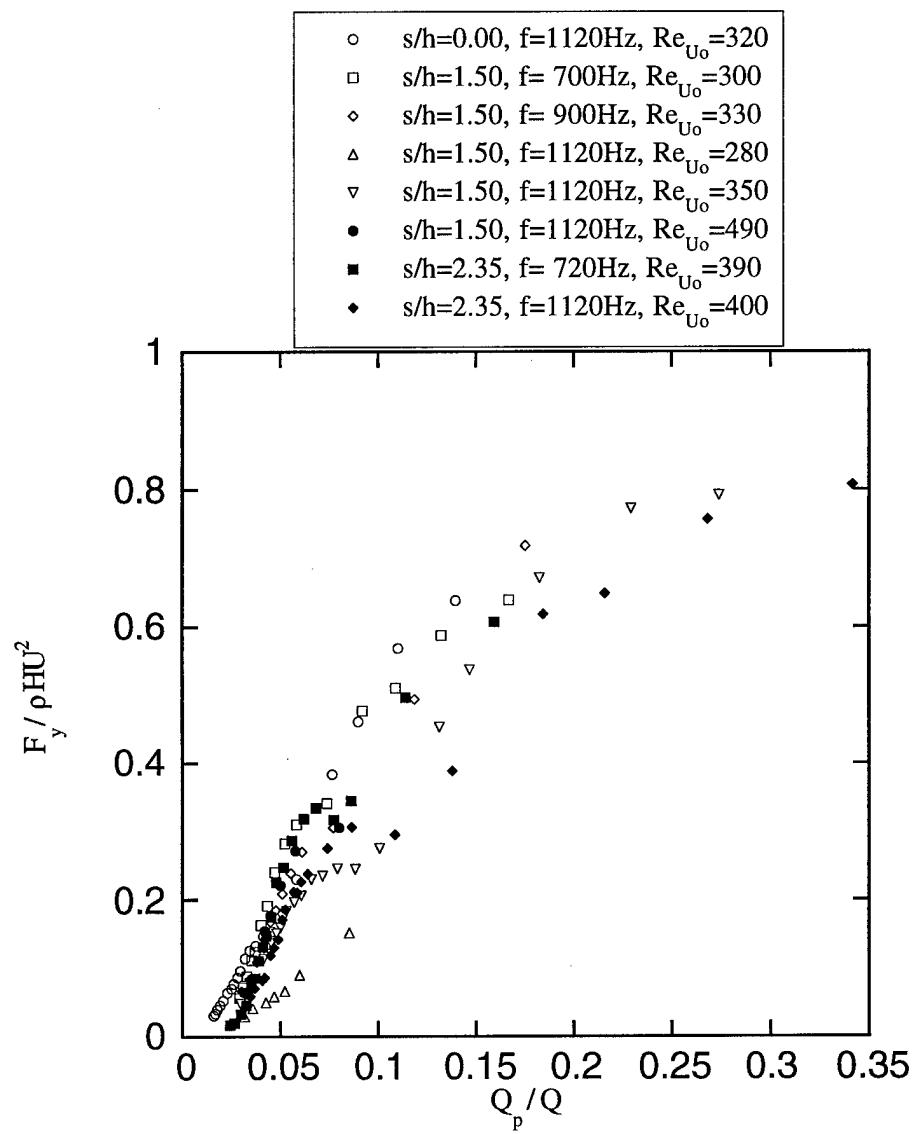
FigureIII.38. Variation of the relative vectoring force with flow rate ratio found by extrapolation of data from Figure III.37.

IV. AERODYNAMIC FLOW CONTROL ON AN UNCONVENTIONAL AIRFOIL

IV.1 Introduction

Active manipulation of separated flows over lifting surfaces at moderate and high angles of attack with the objective of improving the aerodynamic performance and extending their flight envelope by inducing complete or partial flow reattachment has been the focus of a number of investigations since the early eighties. Reattachment is normally effected by exploiting the receptivity of the separating shear layer to external excitation which affects the evolution of the ensuing vortical structures and their interactions with the flow boundary. Active flow control schemes that rely on the instability of the separating shear layer have employed a variety of actuation techniques including external (or global) acoustic excitation (e.g., Ahuja and Burrin, 1984 and Zaman, Bar-Sever and Mangalam, 1987), internal acoustic excitation applied through a small orifice in the surface of the airfoil (e.g., Huang et al., 1987 and Hsiao et al., 1990), surface-mounted vibrating mechanical flaps (Neuburger and Wygnanski, 1987 and Shepshelovich and Koss, 1990), and steady and unsteady blowing or bleeding (Williams et al., 1991, Seifert et al., 1996, Smith et al., 1998, Amitay et al., 1998 and Amitay et al., 1999).

Internal acoustic excitation (Huang et al., 1987) employs an acoustically driven cavity within the airfoil where controlled (normally time-harmonic) acoustic disturbance is emitted from a small rectangular orifice upstream of flow separation (typically near the leading edge of the airfoil). The work of Chang et al. (1992) confirmed earlier results of Hsiao et al. (1990) namely, that at low excitation levels, excitation applied at the unstable frequencies of the shear layer (St = 2) could lead to a 50% post-stall increase in lift. Similar coupling of the excitation input to the predominant instabilities of the separating shear layer was also employed in the experiments of Wygnanski and Seifert (1994) and Seifert et al. (1996) who used steady and unsteady jet blowing over a range of airfoils to achieve various degrees of separation control at a reduced frequency (that scales with the time of flight over the length of reattached flow) of order one. An important result of the work of Chang et al. (1992) was the demonstration that the application of acoustic excitation at levels that are somewhat higher than those of their baseline experiments resulted in effective control of separation over a broad range of excitation frequencies (up to St = 20) that far exceed the unstable frequency of the separating shear layer.

Smith et al. (1998) and Amitay et al. (1998, 1999) demonstrated the utility of synthetic (zero mass flux) jet actuators for the suppression of separation over an unconventional airfoil at moderate Reynolds numbers (up to 10^6) resulting in a dramatic increase in lift and decrease in pressure drag. The jets are typically operated at frequencies that are an order of magnitude higher than the shedding frequency of the airfoil [$F^+ \sim O(1)$] and because they are zero net mass flux in nature, their interaction with the cross flow leads to local modification of the apparent shape of the flow surface. Full or partial reattachment including the controlled formation of a closed separation bubble, can be controlled by the streamwise location and the strength of the jets. The excitation is effective over a broad streamwise domain that extends well upstream of where the flow separates in the absence of actuation and even downstream of the front stagnation point on the pressure side of the airfoil. The response of the flow to time-modulated control input was measured in the cross stream plane of the airfoil wake using jet formation frequencies that are either well above or of the same order as the natural shedding frequency [$F^+ \sim O(10)$ and $\sim O(1)$, respectively]. For both frequency ranges, the collapse of the separated flow region is associated with a strong momentary reduction in lift followed by a substantial increase in the mean lift. However, while at $F^+ \sim O(10)$ the shedding of organized vortical structures subsides following the initial transient, at $F^+ \sim O(1)$ actuation leads to a time-periodic shedding of a train of vortices (at the actuation frequency) that correspond to (peak to peak) lift coefficient fluctuations (at $F^+ = 0.95$) of up to 45% of the mean lift.

The sensitivity of the attached flow (and the restored lift) to the excitation frequency is also demonstrated in the numerical simulation of Donovan et al. (1998) who investigated flow reattachment over a NACA 0012 airfoil using unsteady zero mass flux blowing $F^+ = 1$. These simulations showed a 20% post-stall increase in lift at $\alpha = 22^0$. However, the reattachment was similar to a Coanda-like effect where the forced shear layer deflected towards the airfoil surface, and the time-periodic vortex shedding from the top surface of the airfoil, led to 20% oscillations in the lift coefficient. Similarly, the recent numerical simulations of Wu et al. (1998) reaffirmed that a separated flow can be effectively controlled by low-level periodic blowing/suction near the leading edge. The forcing modulates the evolution of vortical structures within the separated shear layer and promotes the formation of concentrated lifting vortices, which in turn interact with trailing-edge vortices and thereby alter the global stalled flow. In a certain range of post-stall angles of attack and forcing frequencies, the flow becomes periodic and is accompanied by a significant lift enhancement.

IV.2 Experimental Apparatus and Procedures

The experiments are conducted in an open return, low-speed wind tunnel having a square test section measuring 0.91m on the side, a maximum speed of 32m/sec and turbulence level less than 0.25%. The airfoil model is comprised of an aluminum leading edge circular cylinder mounted within an aerodynamic fairing constructed out of fiberglass and foam that is based on a uniformly stretched NACA four-digit series symmetric airfoil as shown schematically in Figure IV.1. The 62.2mm diameter cylinder spans the entire test section and can be rotated about its axis within the fairing and is tangent to the surface of the cylinder at the apexes of its cross-stream edges (i.e., +/-90°) where the airfoils has its maximum thickness. The chord of the combined cylinder-fairing airfoil is 25.4 cm, its thickness to chord ratio is 24% and its angle of attack, α, can be independently varied between -25° and 25°. The center section of the cylinder houses a pair of adjacent synthetic jet actuators each having a flush mounted rectangular orifice (the width is b = 0.5 mm and the length is 140 mm), such that the orifices are colinear with respect to the axis of the cylinder along their long dimension, and separated by 2.5mm. The performance of each jet is quantified in terms of the conventional momentum coefficient, C_μ. The center section of the cylinder is also instrumented with 47 pressure ports equally spaced around its circumference. Cross stream distributions of the streamwise and cross stream velocity components are measured in the wake of the airfoil using hot wire sensors having X-wire configuration that are mounted on a computer-controlled traversing mechanism.

IV.3 Results and Discussion

IV.3.1 Aerodynamic Performance

Distributions of the pressure measured along the surface ($\alpha = 0^0$, 5^0, 10^0, 15^0, 20^0 and 25^0) are shown in Figure IV.2a-f for the unforced (open symbols) and forced (solid symbols) flows. The jets are located at $\gamma = 60^0$ and the momentum coefficient ($C_\mu = 2U_j^2 2b/(U_0^2 c)$) is $1.8 \cdot 10^{-3}$ in the forced cases. At $\alpha = 0^0$ (Figure IV.2a) the unforced flow is attached over the entire airfoil surface with the exception of a small region near the point of maximum thickness ($x/c \approx 0.2$) where the strong adverse pressure gradient after the suction peak causes a local separation. Despite the limited spatial resolution of the pressure measurement there is some indication that the forcing reduces the extent of the separation bubble.

At angles of attack exceeding 5° (Figure IV.2b) the airfoil stalls without control. For $\alpha \le 15^0$ (Figures IV.2b-d) the forced flow becomes fully reattached and the pressure distribution exhibits a large suction peak near x/c = 0.1. A rapid pressure recovery occurs for 0.1 < x/c < 0.2 followed by a more gradual pressure recovery towards the trailing edge. Note that in the

absence of forcing at $\alpha = 5^0$ and 10^0 (Figures IV.2b and 2c, respectively), there are two regions where the pressure on the top (suction) surface is higher than on the bottom (pressure) surface. The first region in on the cylinder at $x/c < 0.062$ and $x/c < 0.055$ ($\alpha = 5^0$ and 10^0, respectively) and downstream of the separation at $x/c > 0.35$ and $x/c > 0.25$ ($\alpha = 5^0$ and 10^0, respectively). The application of forcing, for these two angles of attack, leads to flow reattachment and a lower pressure on the top except in a small section ($x/c > 0.65$ and 0.72 for $\alpha = 5^0$ and 10^0, respectively) near the trailing edge.

Forcing at $\alpha = 20^0$ (Figure IV.2e), results in a partial reattachment. The flow is attached through $x/c = 0.22$ but subsequently separates as a result of the strong adverse pressure gradient following the suction peak. For $\alpha = 25^0$ (Figure IV.2f), the C_p distribution is qualitatively similar to $\alpha = 20^0$ although the suction peak is lower. Note that the pressure distribution downstream of the separation is higher than the unforced flow contributing to increased lift and pressure drag. Nevertheless, the lift-to-drag ratio increases compared to the unforced case.

To assess the improvement in aerodynamic performance of the airfoil with control, the sectional coefficients of and pressure drag and the lift-to-drag ratio are computed by integrating the pressure distributions around the airfoil, and are plotted as a function of angle of attack in Figures IV.3a-c, respectively. These data confirm that in the absence of forcing the airfoil is stalled even at small angles of attack. With forcing ($\gamma = 60^0$, $C_\mu = 1.8 \cdot 10^{-3}$), the flow on the lifting surface of the airfoil is attached, and the lift coefficient increases approximately linearly with angle of attack as for conventional airfoils. Flow reattachment also results in reduced pressure drag coefficient, and exhibits the characteristic parabolic dependence on α of conventional airfoils. At high angles of attack ($\alpha = 25^0$), the lift curve has yet to exhibit the downturn characteristic of stall, but the rapidly increasing drag (exceeding the drag coefficient on the unforced airfoil at $\alpha = 25^0$) and the shape of the pressure distributions suggest that stall is imminent although not necessarily occurring in the same sense as on the unforced airfoil. In general, the synthetic jet forcing increases lift, reduces pressure drag increases the lift-to-pressure drag ratio (Figure IV.3c) and increases the stall margin by controlling separation at high angles of attack.

To explore the influence of the azimuthal location and strength of the control jets on the flow control effectiveness, surface pressure measurements are repeated with different values of C_μ and γ. Figures IV.4a and 4b show the lift-to-pressure drag ratio as a function of γ and C_μ, respectively, for $\alpha = 15^0$. The effect of jets' location is assessed in Figure IV.4a by fixing C_μ and varying γ. For $\gamma < 0^0$ ($C_\mu = 1.8 \cdot 10^{-3}$), there is little effect on the separation. Increasing γ beyond 0^0 increases L/D_p to a maximum at $\gamma = 30^0$, and further increase in γ leads to a modest drop in L/D_p. Figure IV.4b shows the effect of actuator performance on the L/D_p at different azimuthal locations, γ. Proportional control is obtained when $\gamma = 30^0$. These data also show that as the actuators are placed closer to the separation, the less power required to effect (provided of course that the location of separation is known in advance). When the jets are placed at $\gamma = 60^0$, their effectiveness is independent of C_μ up to $C_\mu = 2 \cdot 10^{-4}$.

IV.3.2 Transient Response to Pulsed Reattachment ($F^+ \sim O(10)$, $O(1)$)

In what follows, two cases of dynamic reattachment following a pulsed amplitude modulation of the actuator (control) input for which the frequencies of the excitation signal, F^+, are $O(1)$ and $O(10)$. The modulation is synchronized with the actuator driving signal such that the leading edge of the modulating waveform coincides with a zero crossing of the actuator signal and continues for 0.5 sec. Using x-wire anemometry, the transient of the flow resulting from the pulsed excitation is measured in detail across the wake at $x/c = 2$. The airfoil is placed at an angle of attack of 17.5^0, the actuators are located at an angle of 60^0 (with respect to the

incoming flow), the momentum coefficient is $2.3 \cdot 10^{-3}$ and the free stream velocity is 18.5 m/s (Re_c = 310,000).

The transient effects of pulsed modulation are captured in gray scale raster plots of the phase-averaged cross-stream distributions of the streamwise (a) and cross-stream (b) velocity components (Figure IV.5). The jet actuators are driven at F^+ = 10 and the flow is unforced before and after the modulation is applied (marked with "up" and "down" arrows on the time scale). Corresponding time-averaged cross-stream velocity distributions of the unforced (open symbols) and forced (solids symbols) flow are shown for reference on the right hand side of each phase plot. The flow transient associated with the onset of the modulation is sensed at the measurement station at t/T = 100 (approximately 25 actuator periods after the modulation is effected). The flow reattachment on the airfoil is marked by strong fluctuations in the streamwise and cross-stream velocity components that are felt across the entire wake and at some instances even beyond the cross-stream measurement domain. Following the initial transient, the wake becomes substantially narrower, the streamwise velocity deficit is substantially reduced, and the center of the wake is shifted downwards (as is evident in the time-averaged cross-stream velocity distributions on the right hand side of the Figure). The reattachment is also accompanied by a pronounced increase in cross-stream velocity component in the negative y direction (Figure IV.5b). Similar to the flow transient that is associated with the onset of the modulation, the arrival of the transient, induced by its trailing edge at the measurement station (t/T = 462) is again felt across the entire wake, although the strength of this velocity transient appears to be considerable weaker ostensibly as a result of small variations in the progression of the ensuing flow separation. The wake is first shifted farther downward (i.e., in the negative y direction) before gradually relaxing to the unforced state.

The corresponding phase-averaged cross-stream distributions of the spanwise vorticity are computed from the streamwise and cross-stream velocity distributions and are shown in Figure IV.6 (the time-averaged cross-stream vorticity distribution for the separated (open symbols) and attached (solid symbols) flows are shown on the right hand side of the Figure). When the flow is separated (i.e., before and after the pulse modulated excitation is applied), the vorticity distribution in the wake is comprised of a train of vortical structures of alternating sign (clockwise vorticity is taken to be negative) having a nominal passage frequency of 50 Hz. Nevertheless, the total vorticity flux across the wake during one period of the (unforced) shedding frequency is approximately zero. As was shown by Smith et al., 1998, the actuation leads to flow reattachment and the establishment of a higher (positive) lift force on the airfoil, which must be accompanied by a change in the vorticity flux and a net increase in circulation associated with positive (counter-clockwise) vorticity. However, following the reattachment, a strong clockwise vortex indicating *a reduction in lift* is initially advected past the measurement station followed closely by a stronger counter-clockwise vortex indicating the re-establishment of lift. These two large vortices are followed by a series of smaller vortices of alternating signs and diminishing strength. It appears that the reduced wake of the attached airfoil ultimately reaches a state of symmetric vorticity distribution as can be seen for t/T > 300 in Figure IV.6. When the (pulse modulation) control is turned off, the flow separates again and the airfoil loses its lift. This reduction in lift is accompanied by a decrease in circulation and the shedding of negative (clockwise) vorticity. However, immediately following the termination of the control, a counter-clockwise vortex indicating *a momentary increase in lift* is advected past the measurement station before the separated vorticity field is established.

As noted by Amitay et al., 1998, the time rate of change in circulation is given by the vorticity flux

$$\frac{d\Gamma}{dt} = \int_{-\infty}^{\infty} U\Omega_z \, dy$$

The phase-averaged vorticity flux and incremental change in the circulation with respect to the

100

unforced case are estimated (not accounting for contributions of the fluctuating components) from the phase-averaged cross-stream distributions of the streamwise velocity and spanwise vorticity, and are shown in Figures IV.7a and 7b, respectively. The vorticity flux in the separated flow (Figure IV.7a) oscillates about a zero mean during the passage of counter-rotating wake vortices, which corresponds to a lift force of alternating sign. The application of pulsed modulation results in a sharp positive peak (0.3), which corresponds to the passage of a clockwise vortex shed from the top surface of the airfoil. The positive peak is followed by a negative peak (with a peak level of -0.27) that is associated with the passage of a counter-clockwise vortex corresponding to the re-establishment of lift. Subsequently, the vorticity flux changes sign two more times before reaching low-level oscillations about zero.
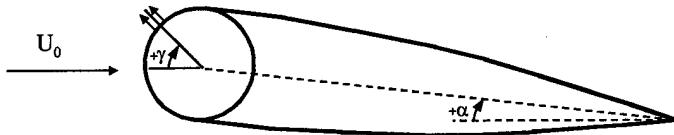
Figure IV.1. Airfoil model.

When the flow reattaches, the increment in the circulation $\Delta\Gamma$ (Figure IV.7b) initially diminishes to a value of -0.6 and then recovers to a value of 0.45 with the shedding of the second counter-clockwise vortex. It appears that the shedding of the "starting vortex" causes partial trailing edge separation, which is manifested by the shedding of another (weaker) clockwise vortex followed by a train of vortices of alternating signs (see cartoon). The circulation (and lift coefficient) ultimately converges to its attached value, which is in good agreement with the lift coefficient obtained from the pressure measurements. When the control is turned off the circulation initially increases before settling to the unforced stalled level, which is similar to the transient variation of lift during dynamic stall.

In the measurements described above, the reduced frequency of the actuator jets is $F^+ = 10$. Previous work on airfoil separation control emphasizes primarily actuation frequencies that were typically of the same order as the natural shedding frequency of the airfoil (i.e., $F^+ \sim O(1)$) regardless of the choice of actuators. In order to demonstrate the effect of the forcing frequency on the velocity distribution in the airfoil wake and the corresponding variation in lift that are associated with the suppression of separation, a series of experiments are conducted in which the synthetic jets are driven at 71 Hz which corresponds to $F^+ = 0.95$.

To begin with, the pressure coefficient distributions around the airfoil when the flow is forced at $F^+ = 0.95$ (gray symbols), $F^+ = 10$ (black symbols) and in the absence of forcing (solid line) are shown in Figure IV.8. For $F^+ = 10$ the pressure distribution exhibits a large suction peak near the leading edge on the suction side of the airfoil followed by a rapid recovery of the pressure towards the trailing edge. When low frequency forcing ($F^+ = 0.95$) is used the pressure distribution exhibits a smaller and sharper suction peak near the leading edge, and as a results the contribution of this peak to the lift is smaller than for the high frequency forcing. Downstream of the suction peak the pressure difference in pressure coefficient between the suction and pressure sides is larger than for high frequency forcing resulting in a larger contribution to the lift but also larger contribution to drag. Consequently, the lift-to-pressure drag ratio, which for the unforced case is 1.05, increases to 2.53 and 3.59 for low and high frequency forcing, respectively.
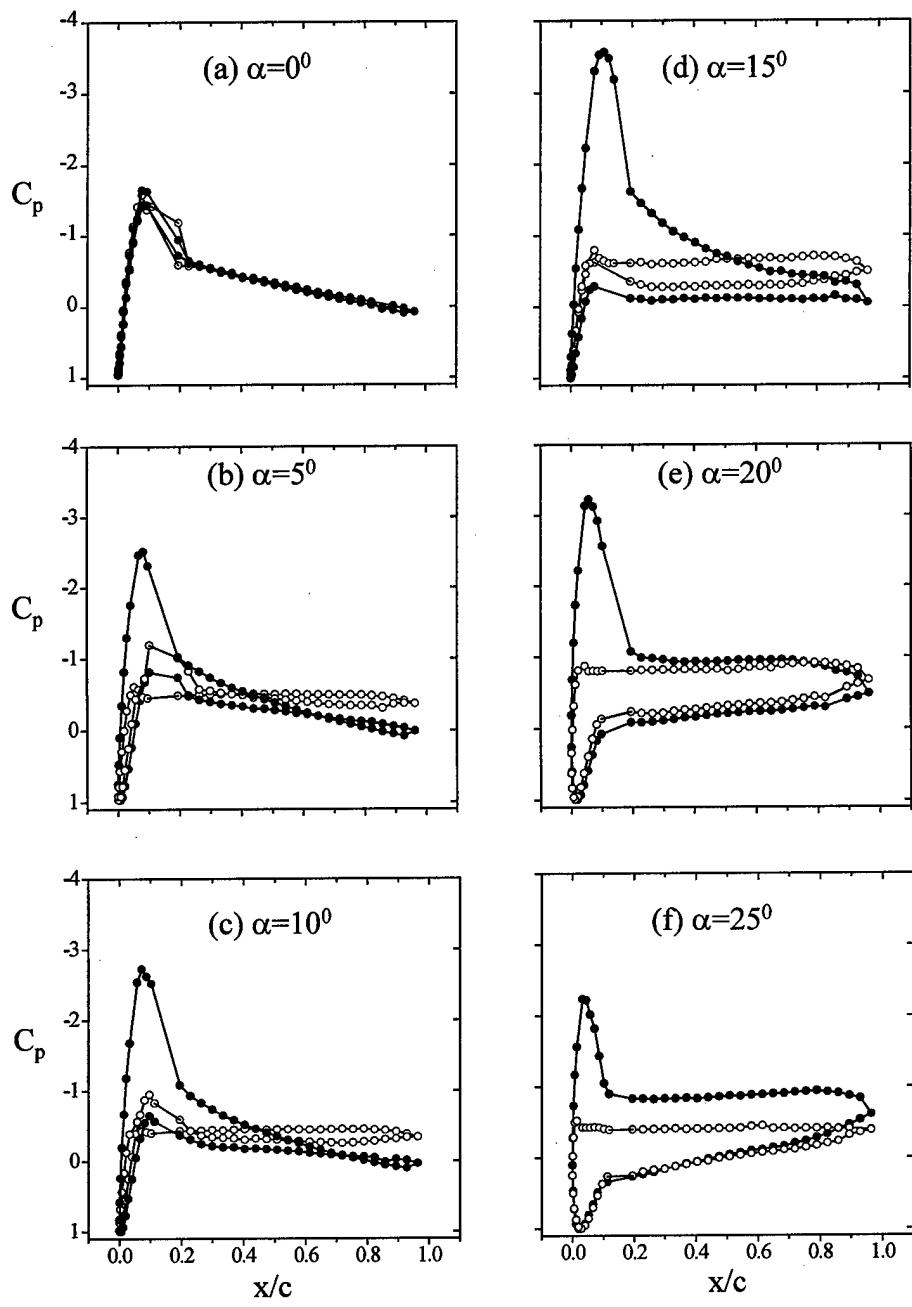
Figure IV.2. C_p distribution around the airfoil at different α. (—o—) Unforced, (—•—) forced.
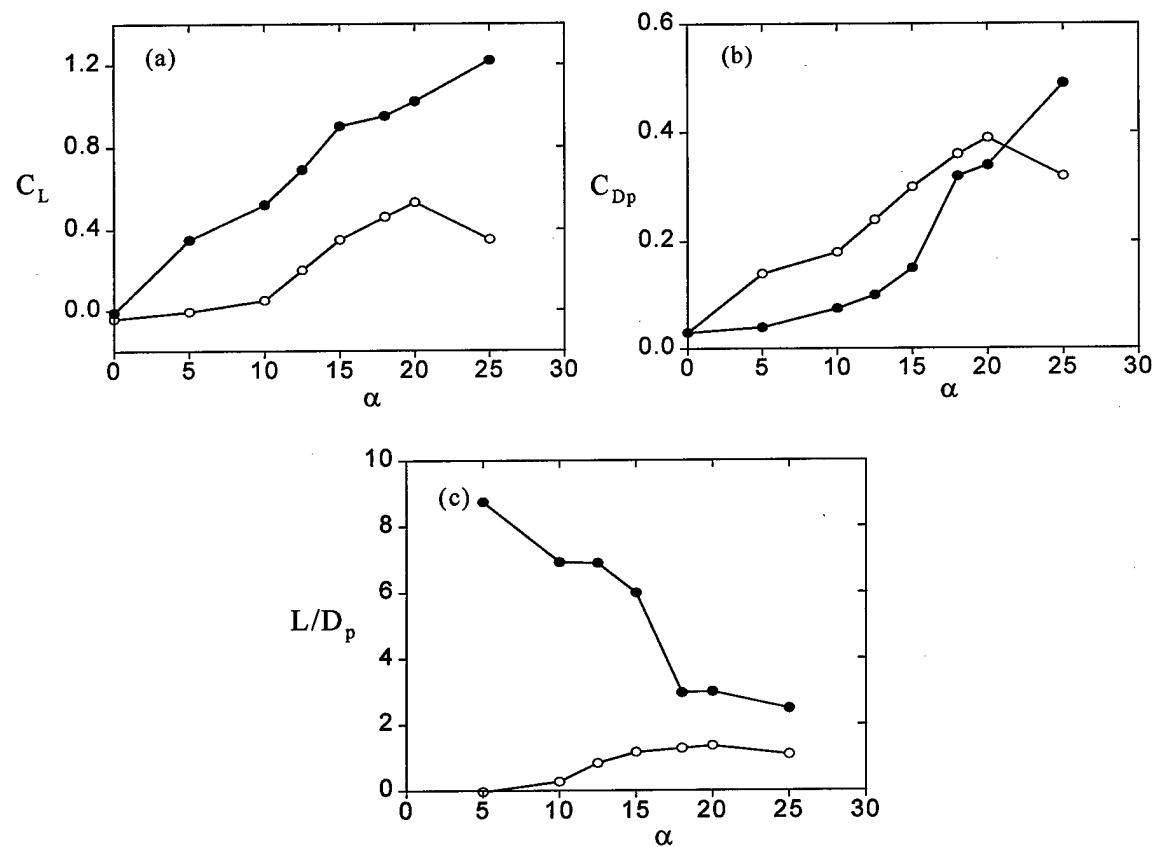
Figure IV.3. C_L, C_{Dp} and L/D_p as a function of α. (—o—) Unforced, (—•—) forced.
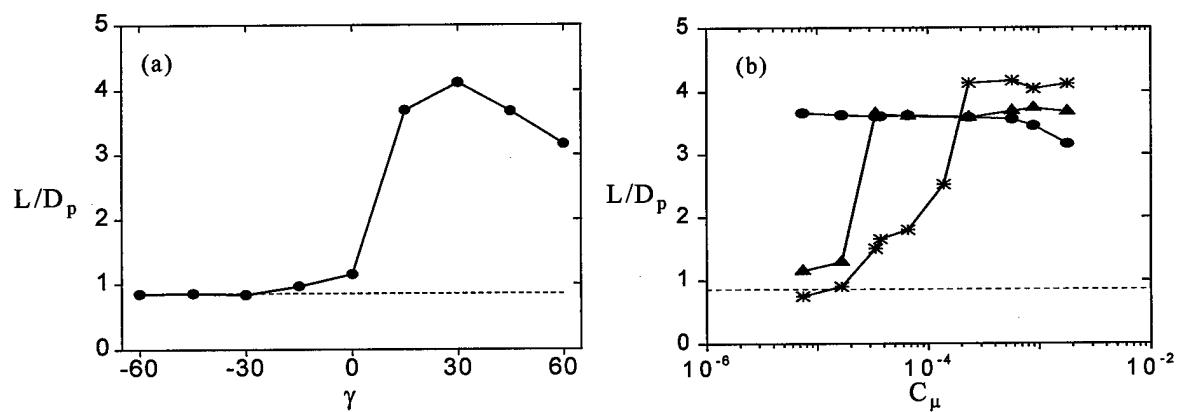
Figure IV.4. The effect of γ (a) and C_μ (b) on the lift-to pressure drag ratio. (—*—) $\gamma = 30^0$, (—▲—) $\gamma = 45^0$, (—•—) $\gamma = 60^0$.
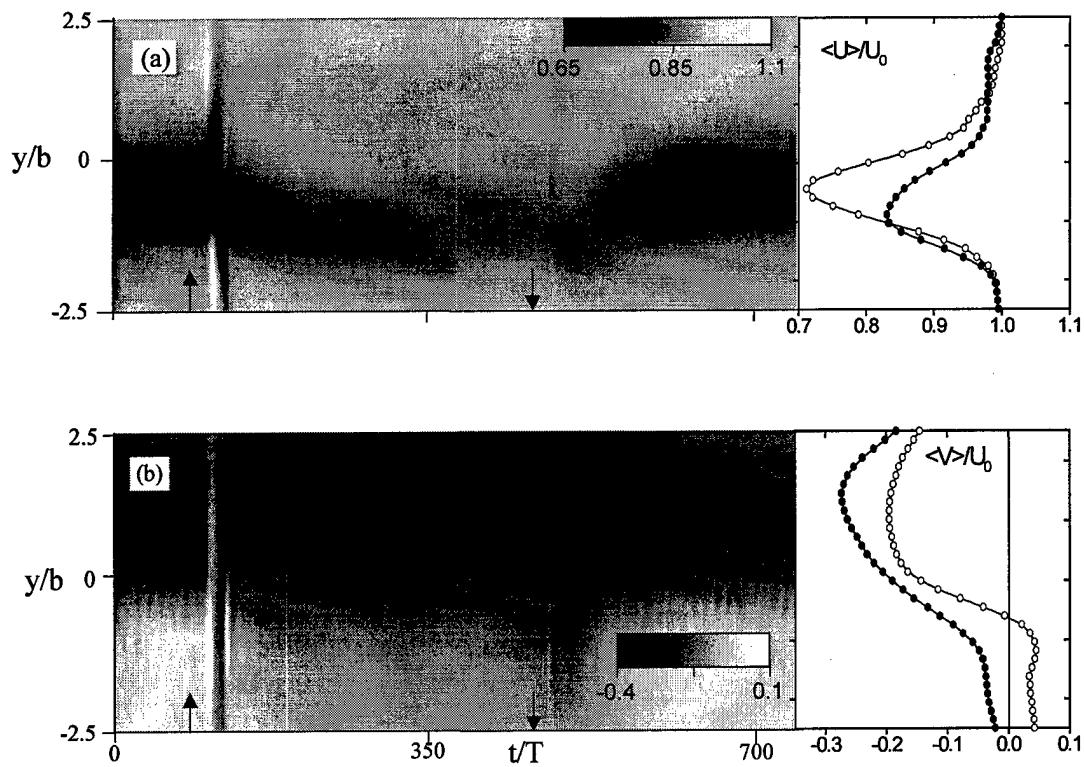
Figure IV.5. Phase-averaged gray scale raster plots of the cross-stream distributions of the streamwise and cross-stream velocity components along with the corresponding time-averaged velocity profiles; $F^+=10$.
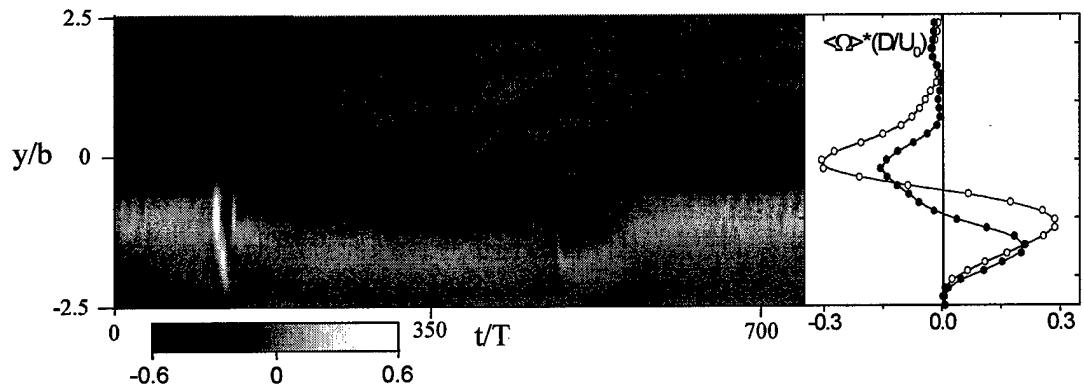
Figure IV.6. Phase-averaged gray scale raster plot of the cross-stream distribution of the spanwise vorticity along with the corresponding time-averaged spanwise vorticity; $F^+=10$.

Similar to Figures IV.5a and IV.5b Figures IV.9a and IV.9b show gray scale raster plots of the phase-averaged cross-stream distributions of <U> and <V>, respectively, when pulsed modulation excitation is applied with $F^+ = 0.95$. The corresponding time-averaged cross-stream velocity distributions (with and without the modulated excitation) are also shown for reference on the right hand side of each plot. The initial transient following the application of the pulse modulated control is very similar to the measurements shown in Figure IV.6 ($F^+ = 10$), where reattachment is marked by strong fluctuations of both velocity components. However, as is evident from Figure IV.9 there is a fundamental difference between the velocity fields of the reattached flows for $F^+ = 0.95$ and 10 after the initial transient subside. When the flow is forced at a reduced (dimensionless) frequency of order one, the velocity field across the wake continues to oscillate at the forcing frequency as long as the control signal is applied and when the flow is presumably attached.

These oscillations are also apparent in the phase-averaged cross-stream distributions of the spanwise vorticity for $F^+ = 0.95$ (Figure IV.10, which also includes the time-averaged cross-stream vorticity distributions). As for the high frequency forcing (Figure IV.6), the transient immediately following the reattachment is associated with the appearance of a strong clockwise vortex indicating an initial reduction in lift. The lift begins to increase with the appearance of a stronger counter-clockwise vortex. However, in contrast to the reattachment at the higher reduced frequency in which the shedding of organized vortical structures appears to subside following the transient, the reattachment at a reduced frequency of order one appears to be accompanied by the coherent shedding of a train of strong vortices at the driving frequency. The flow transients associated with the termination of the pulse modulation and the subsequent relaxation of the wake are similar to the corresponding transients at the higher forcing frequency suggesting that the separation processes in both cases are similar. These data suggest that when the flow is forced at a low reduced frequency, which is of the same order of the natural shedding frequency to which the separated flow is inherently receptive, the control input is amplified and the reattachment is manifested by passage of the shear layer vortices along the surface of the airfoil. However, when the actuation frequency is high enough, the interaction of the jets with the flow occurs at a smaller length scale, which leads to local modification of the apparent shape of the airfoil, and suppresses the shedding of large scale vortices.

Using the phase-averaged cross-stream distributions of the streamwise velocity and spanwise vorticity, the phase-averaged increment (relative to the unforced flow) in the circulation is estimated and shown in Figure IV.11 ($F^+ = 0.95$ and 10 are shown using gray and black curves, respectively). When the flow reattachment begins, $-\Delta\Gamma$ exhibits a similar transient at both control frequencies (i.e., a negative peak followed by a positive peak). However, while for high frequency forcing the lift coefficient ultimately reaches a steady level, low frequency forcing results in oscillations of $-\Delta\Gamma$ at the forcing frequency with peak to peak fluctuations of up to 45% of the mean level for the attached flow.

The flow mechanisms associated with the two forcing frequencies are demonstrated in a sequence of smoke visualization images in Figures. IV.12a-c (the separated flow, in the absence of control, is shown for reference in Figure IV.12a). The smoke is injected in a sheet at center span and is illuminated using a pulsed laser. The field of view is restricted to a small domain measuring $0.1 < x/c < 0.5$ above the airfoil (shown schematically in the insert in Figure IV.12a). When the control jets are operated at $F^+ \sim O(10)$ (Figure IV.12b), the flow is attached to the airfoil and the visualization shows several coherent vortical structures at the operating frequency of the jets. It is noted however, that these vortices quickly lose their identity and vanish well before they reach the trailing edge of the airfoil (Honohan and Glezer, 1999). When the actuation frequency is $F^+ \sim O(1)$ (Figure IV.12c), the reattachment is characterized by the formation of large vortical structures that scale with the chord of the airfoil and persist well beyond the trailing edge of the airfoil. It appears that because the formation frequency of these

vortices couples with the natural shedding frequency of the airfoil, they are actually enhanced with downstream distance as might be predicted by stability theory. It is the formation and shedding of these vortical structures that leads to time-periodic variation in lift.

The spectral contents of the wake under the two forcing conditions is measured at $x/c = 2$ on the lower side of the wake at a cross-stream elevation where the streamwise velocity deficit is half the maximum deficit (Figure IV.13). In this Figure, the light gray curve corresponds to the unforced flow and the gray and black curves correspond to low and high frequency forcing, respectively. The velocity spectrum of the unforced flow includes a strong spectral peak at the (natural) shedding frequency (50 Hz) and begins to decay at higher frequencies ($f > 100$ Hz). When the flow is forced at $F^+ \sim O(1)$, the magnitude of the spectral components across the entire spectrum is reduced compared to the unforced flow, presumably as a result of the unsteady reattachment on the top surface of the airfoil. Similar to the unforced flow, the spectra exhibit a spectral peak at the forcing frequency, which is larger than the corresponding peak at the unforced flow, confirming the persistence of vortical structures at the forcing frequency after the disappearance of the reattachment transients. When high frequency forcing is applied, the turbulent kinetic energy throughout the entire spectrum is significantly reduced and there is no discernible peak that corresponds to the passage frequency of organized coherent structures. This indicates that there is a substantial difference in the nature of flow reattachment on the top surface of the airfoil.

$$\frac{d\Gamma}{dt} = \int\limits_{-\infty}^{\infty} \Omega_Z \cdot U dy$$
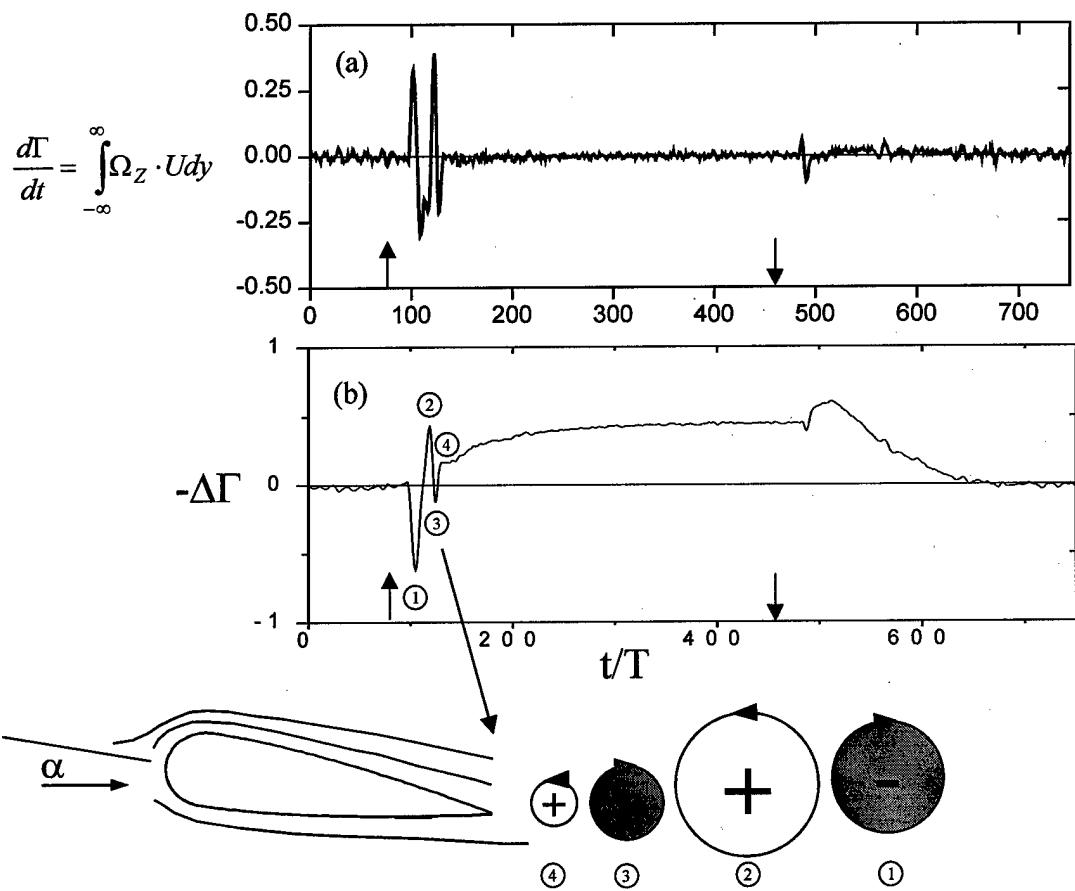
Figure IV.7. Phase-averaged vorticity flux (a) and lift coefficient increment (b) for α =17.5° and γ = 60°. F^+ = 10.
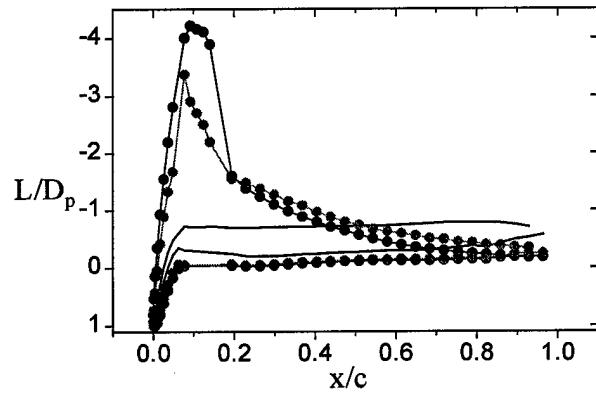
Figure IV.8. Pressure coefficient distributions around the airfoil. (———) unforced, (—•—) F^+=0.95, (—•—) F^+=10.

107
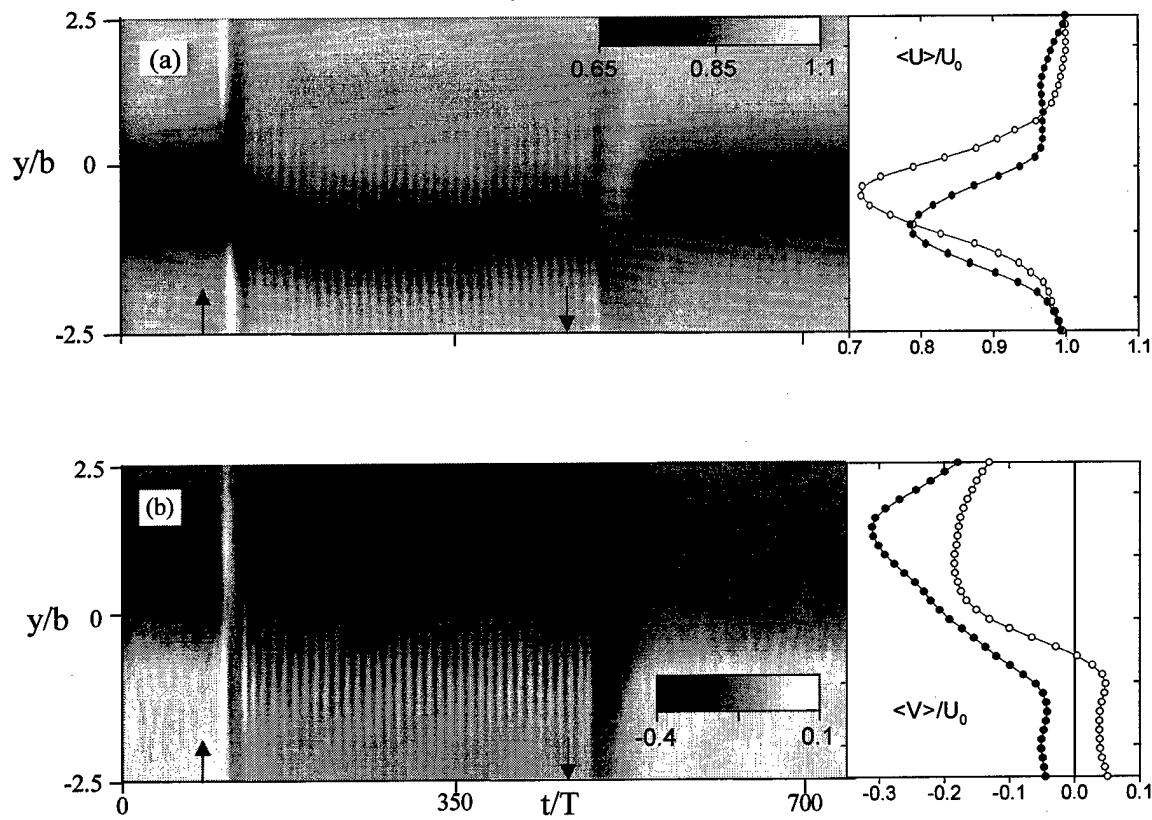
Figure IV.9. Phase-averaged gray scale raster plots of the cross-stream distributions of the streamwise and cross-stream velocity components along with the corresponding time-averaged velocity profiles; $F^+=0.95$.
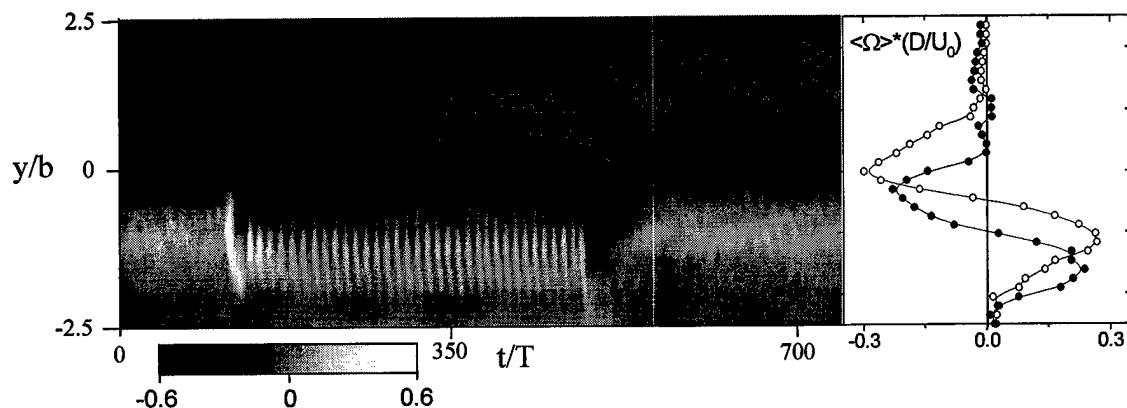
Figure IV.10. Phase-averaged gray scale raster plot of the cross-stream distribution of the spanwise vorticity along with the corresponding time-averaged spanwise vorticity; $F^+=0.95$
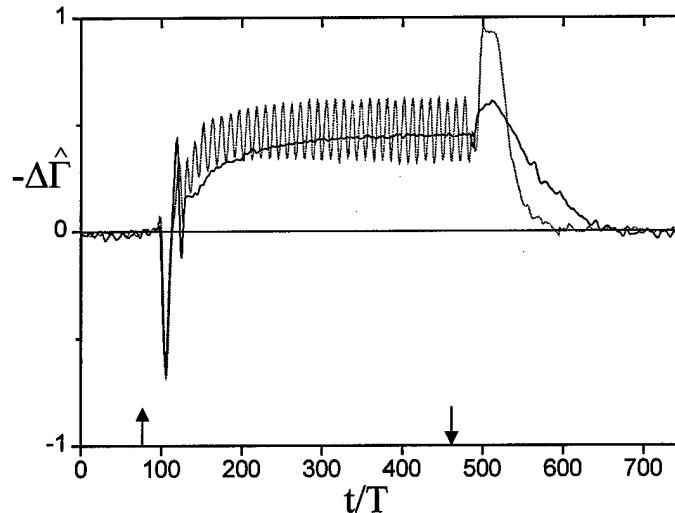
Figure IV.11. Phase-averaged circulation increment for $\alpha = 17.5^0$, $\gamma = 60^0$ and $F^+ = 0.95$ (gray), and 10 (black).
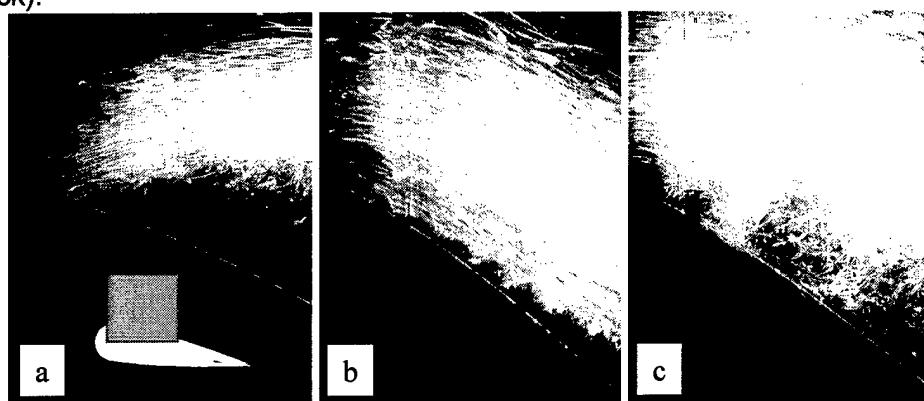
Figure IV.12. Smoke flow visualization, (a) unforced, (b) $F^+ \sim O(10)$ and (c) $F^+ \sim O(1)$.
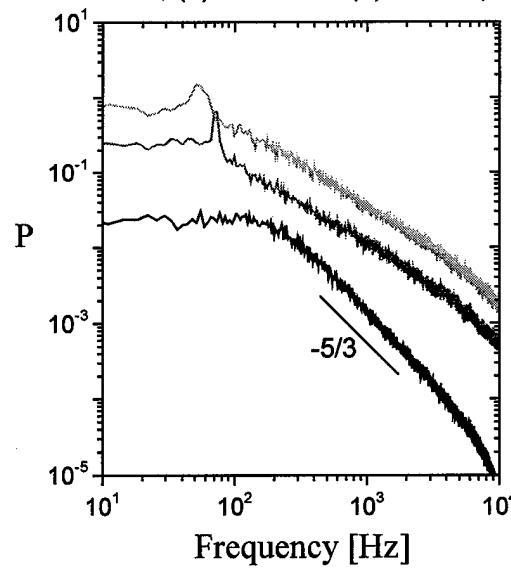
Figure IV.13. Power spectra measured at x/c = 2 at $\alpha = 17.5°$ and $\gamma = 60°$. (———) unforced, (———) $F^+ = 0.95$, (———) $F^+ = 10$.

109

IV.3.3 Variation of the Forcing Frequency

In order to further demonstrate the effect of the forcing frequency on the dynamics of the flow reattachment, the synthetic jets are driven at six frequencies corresponding to F^+ = 0.95, 2.05, 3.4, 10, 14.7 and 20 (71Hz, 148Hz, 246Hz, 740Hz, 1088Hz and 1480Hz, respectively). Actuation at F^+ = 0.95, 2.05 and 3.4 is effected using two speakers mounted at opposite ends of the cylinder. The high frequency forcing is obtained using the drivers described in Section II that are mounted within the cylinder cavity. Note that at high frequencies the performance of the speakers is significantly reduced due to three-dimensional acoustic effects and the appearance of standing waves within the cavity of the cylinder. Measurements of the velocity at the orifice using a single hot-wire sensor (not shown here) reveal that when the speakers are used at high frequencies, there is a significant degradation in jets performance in the presence of cross flow.

Figure IV.14a shows distributions of pressure coefficient around the airfoil at F^+ = 0.95 (circles), 2.05 (stars) and 3.4 (triangles), while Figure IV.14b shows the pressure distributions at F^+ =10 (circles), 14.7 (stars) and 20 (triangles). The pressure distribution for the unforced flow (solid line) is also shown for comparison. Forcing at low frequencies (Figure IV.14a) results in a very sharp suction peak around x/c = 0.075, which corresponds to the location of the separation in the unforced case. Concomitantly, the degree of pressure recovery towards the trailing edge is reduced with increasing control frequency, leading to an increase in pressure-drag. However, forcing pressure distributions for $F^+ \geq$ 10, Figure IV.14b (which is more than an order of magnitude higher than the shedding frequency, F^+ = 0.7), exhibit larger and wider suction peak and consequently a larger increase in the lift coefficient. Following the suction peak the pressure difference between the suction and pressure sides is smaller than at corresponding stations for the low frequency forcing resulting in a lower pressure drag. Moreover, while for low forcing frequencies (Figure IV.14a) the pressure distribution varies with the forcing frequency, at high forcing frequencies (Figure IV.14b) the pressure distribution is almost invariant.

Integration of the pressure distributions around the airfoil yields the coefficients of lift and pressure-drag, as well as the lift-to-drag ratio for different reduced frequencies (Figure IV.15). Two distinct domains are immediately apparent. In the first domain (I), where the forcing frequencies are of the same order of the shedding frequency ($F^+ < 4$) L/D_p decreases with increasing forcing frequency, as also expected from stability considerations of the separated shear layer. The second domain (marked as II on the Figure), the forcing frequency is more than an order of magnitude higher than the shedding frequency ($F^+ \geq$ 10) and the lift-to pressure drag is considerably higher and appears to be independent of the forcing frequency.

To further explore the difference between the two frequency regimes, the flow response to step amplitude modulation of the control input is investigated at the different forcing frequencies. The time dependence of the phase-averaged incremental change in the circulation with respect to the unforced flow is computed in the same way as for Figure IV.7 and is shown in Figures IV.16a-d for F^+ = 0.95, 2.05, 3.4 and 10, respectively. In all the cases the time-averaged circulation reaches the same value following the transients. However, at F^+ = 0.95, 2.05 (Figures IV.16a and b, respectively) the circulation oscillates at the forcing frequency with peak-to-peak fluctuations that decrease from 45% to 7%, respectively, of the mean circulation coefficient of the attached flow. When the forcing frequency is increased to F^+ = 3.4 and 10 (Figures IV.16c and d) there are no oscillations at the driving frequency, and as shown in Figure IV.15 there is a nominal increase of ~35% in lift–to-pressure drag ratio compared to the low frequencies.
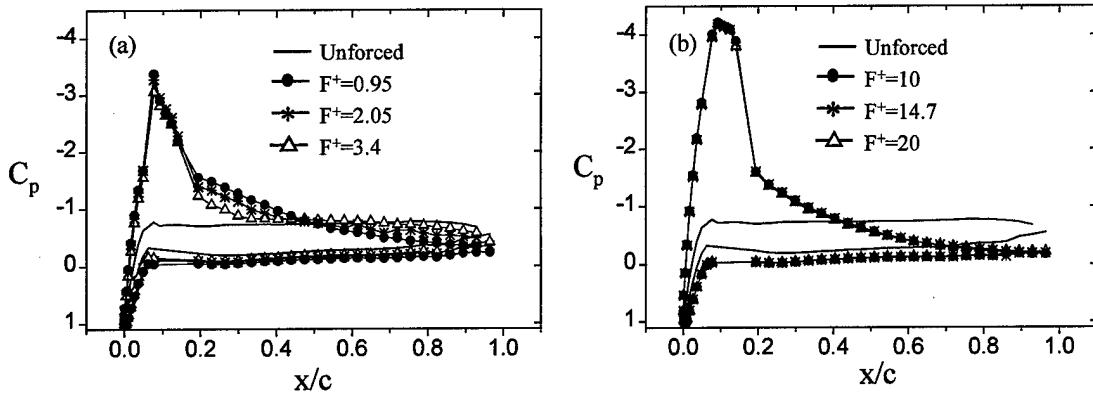
**Figure IV.14.** C_p distributions at $\alpha = 17.5°$ and $\gamma = 60°$. (a) $F^+ \sim O(1)$ and (b) $F^+ \sim O(10)$.
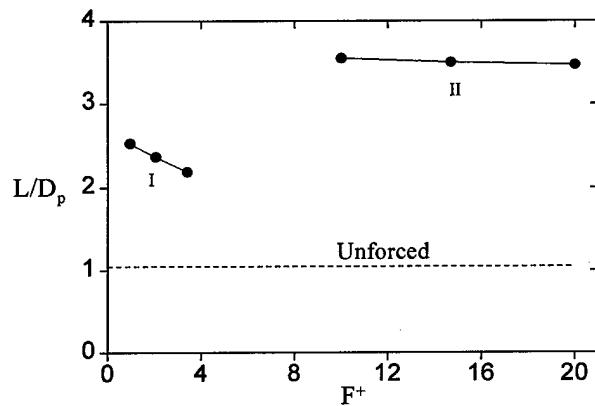

**Figure IV.15.** The effect of the forcing frequency on the lift-to-pressure drag ratio.
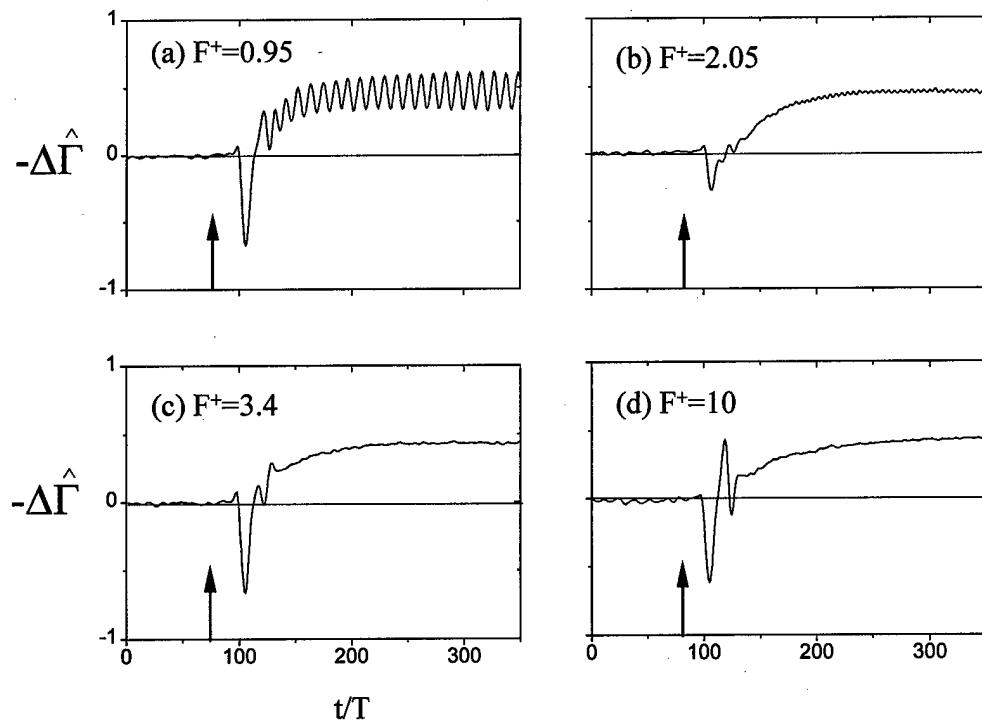
Figure IV.16. Phase-averaged lift coefficient increment for $\alpha = 17.5°$ and $\gamma = 60°$ at different F^+.

111

IV.4 Conclusions

The present work reports wind tunnel experiments on the control of separated flow over an unconventional airfoil using synthetic jet actuators operating at frequencies that are either an order of magnitude higher or of the same order of the characteristic shedding frequency of the airfoil. The tests are conducted at $Re_c = 310,000$, and, in the absence of control, the flow separates at angles of attack exceeding 5^0. When control is applied, the flow is completely attached to the surface up to an angle of attack of 20^0 and partially attached for higher angles of attack. Flow reattachment using synthetic jet forcing leads to an increase in lift and reduction of pressure drag (i.e., an increase of the lift-to-pressure drag ratio) and increase in the stall margin by controlling separation at high angles of attack.

An investigation of the dependence of flow control effectiveness on the actuators location (measured by γ) and on their momentum flux (measured by C_μ) shows that the maximum effect is obtained at $\gamma = 30^0$ and $C_\mu = 1.8\,10^{-3}$, and further increase in γ leads to a modest drop in L/D_p. At this position of the jets ($\gamma = 30^0$) there is a range of C_μ where proportional control can be realized. When the jets are placed closer to the separation point, L/D_p becomes independent of C_μ and a given level of L/D_p can be sustained at levels of C_μ as low as $2\,10^{-4}$.

One of the primary focuses of the present work is the dynamics of controlled flow reattachment and separation effected by synthetic jet actuators. Flow reattachment and the establishment of a higher (positive) lift force on the airfoil is accompanied by a net increase in circulation associated with positive vorticity. Measurements of the vorticity flux within the wake of the airfoil phase locked to pulse modulated excitation has shown that the reattachment begins with the shedding of a strong clockwise vortex that results in *a reduction in lift* is advected past the measurement station followed closely by the shedding of a stronger counter-clockwise vortex that accompanies the re-establishment of lift. When the pulsed modulation is terminated (i.e., control is turned off), the flow separates again and the airfoil loses its lift. This reduction in lift is normally accompanied by shedding of negative (clockwise) vorticity. However, immediately following the termination of the control, in a manner similar to dynamic stall, a counter-clockwise vortex indicating *a momentary increase in lift* is shed and advected past the measurement station before the lift diminishes to a fully separated flow.

Phase locked measurements of the vorticity flux in the wake of the airfoil have also demonstrated that when the actuation frequency is higher than the natural shedding frequency of the airfoil (i.e., $F^+ \sim O(10)$ and higher) the lift force associated with the reattached flow is nominally invariant with time. However, at low actuation frequencies that are of the same order of the shedding frequency (i.e., $F^+ \sim O(1)$), the (quasi) steady lift force (following the transients associated with the reattachment) oscillates at the forcing frequency with peak to peak variations that are as high as 45% of the mean lift. These oscillations are accompanied by the shedding of a train of strong vortices that persists as long as the control input is applied. The flow transients associated with the beginning and termination of the pulse modulated excitation of the low frequency excitation are quite similar to the transients at the high forcing frequency.

In order to further demonstrate the effect of the forcing frequency, the synthetic jets are driven *at fixed $C_\square = 2.3\,10^{-3}$* over a range of frequencies corresponding to F^+ between 0.95 and 20. The dependence of the lift-to-pressure drag ratio on F^+ shows two distinct domains. The first domain is characterized by forcing frequencies that are of the same order of the shedding frequency ($F^+ < 4$), in which L/D_p decreases with the forcing frequency, as might be predicted by the stability theory. The second domain characterized by forcing frequencies that are at least an order of magnitude higher than the shedding frequency (e.g., $F^+ \geq 10$). Within this domain L/D_p is nominally 35% higher than the level within the low frequency domain and is virtually invariant with the forcing frequency.

112

Phase-locked measurements using step modulation excitation demonstrate that the oscillations amplitude of the (quasi) steady lift of the attached flow at low excitation frequencies decreases with increasing F^+ (from 45% down to 7% at $F^+ = 2.05$). These oscillations are completely suppressed at high forcing frequencies which, as noted above, results in higher L/D_p.

The spectral contents of the wake under the two forcing conditions is measured in the near wake ($x/c = 2$) on the lower side of the wake at a cross-stream elevation where the streamwise velocity deficit is half the maximum deficit. The velocity spectrum of the unforced flow includes a strong spectral peak at the (natural) shedding frequency (50 Hz) and begins to decay at higher frequencies ($f > 100$ Hz). When the flow is forced at $F^+ \sim O(1)$, the magnitude of the spectral components across the entire spectrum is reduced compared to the unforced flow, presumably as a result of the unsteady reattachment on the top surface of the airfoil. Similar to the unforced flow, the spectra exhibit a spectral peak at the forcing frequency confirming the persistence of vortical structures at the forcing frequency after the disappearance of the reattachment transients. When high frequency forcing is applied, the turbulent kinetic energy throughout the entire spectrum is significantly reduced and there is no discernible peak that corresponds to the passage frequency of organized coherent structures. This indicates that there is a substantial difference in the nature of flow reattachment on the top surface of the airfoil. It is remarkable that high frequency forcing leads not only to the appearance of a featureless spectrum but also to the emergence of a spectral band having a −5/3 slope indicating enhanced dissipation.

V. AERODYNAMIC FLOW CONTROL ON A 2-D CYLINDER

V.1 Introduction

The receptivity of separated shear flows in aerodynamic applications to the introduction of controlled disturbances into the surface boundary layer just upstream of the separation has been exploited to effect partial or even complete reattachment in nominally 2-D and axisymmetric flow configurations (e.g., Huang, Maestrello & Bryant, 1987, Hsiao, Liu, & Shyu, 1990, Sigurdson & Roshko, 1985, and Kiya, Shimizu & Mochizuki, 1997). Flow excitation has been effected using a variety of techniques including both external and internal acoustic excitation (e.g., Ahuja & Burrin, 1984, Huang, Maestrello & Bryant, 1987), vibrating flaps (e.g., Neuberger & Wygnanski, 1987), unsteady bleeding or blowing (e.g., Sigurdson & Roshko, 1985, Williams, Acharya, Bernhardt & Yang, 1991, Hsiao et al., 1990 and Seifert, Bachar, Wygnanski, Koss & Shepshelovich, 1993), vibrating surfaces (Pal & Sinha, 1997), and more recently zero mass flux synthetic jets (Amitay, Honohan, Trautman and Glezer, 1997). These investigation have shown that varying degrees of flow reattachment can lead to substantial modifications of surface pressure (and ostensibly shear stress) distributions and consequently to alteration of the overall lift and drag.

Although the interest in control of separation for aerodynamic applications has been primarily focused on 2- and 3-D airfoils, some control strategies have been investigated in the nominally two-dimensional flow around a circular cylinder (e.g., Williams et al., 1991, Hsiao et al., 1990 and Pal & Sinha, 1997). This simple geometry is particularly attractive because the base flow has been extensively studied and documented over a broad range of Reynolds numbers. Furthermore, the evolution of flow separation with Reynolds number over the cylinder is reasonably well understood as outlined, for example, in a review article by Roshko & Fiszdon, 1969. In particular, these authors note that for $Re < 2 \cdot 10^5$, the onset of transition to turbulence typically occurs in the free shear layer downstream of the separation point uncoupled from the vortex shedding, and it progresses upstream towards the separation point with increasing Reynolds number. In the critical regime the separation is still laminar and is followed closely by transition, reattachment and subsequently by turbulent separation on the back of the cylinder. This separation-reattachment bubble allows the boundary layer to withstand higher than normal pressure rise and thus the separation point on the cylinder moves farther downstream and the base pressure increases. As the cylinder Reynolds number increases beyond $3.5 \cdot 10^6$, the separation-reattachment bubble disappears and transition to turbulence begins to move upstream of the separation point.

In the earlier experiments of Amitay et al., 1997, the lift and drag forces on a circular cylinder were significantly altered by the formation of small closed recirculating flow regimes near the surface over a range of azimuthal locations between the front and rear stagnation points using synthetic (i.e., zero mass flux) jet actuators (Smith and Glezer, 1997). The actuators induce a local "transpiring" recirculation bubble, which acts as a "virtual surface" and displaces local streamlines well outside the undisturbed boundary layer. As a result, the pressure coefficient on the surface of the cylinder decreases substantially *both upstream and downstream* of the actuator suggesting that the potential flow outside of the surface boundary layer is moving faster than the unforced flow. Depending on the azimuthal location of the actuators, the lift and drag coefficients of the cylinder increase and decrease, respectively. Similar modifications of the surface pressure distribution were also reported by Williams et al., 1991, Hsiao et al., 1990, and Pal & Sinha, 1997. In particular, the work of Hsiao et al., 1990, (using internal acoustic excitation) has demonstrated that these effects are not limited to a narrow spectral band around an unstable frequency (i.e., $St \approx O(1)$) but persist over a broad range of Strouhal numbers up to about 12. In a related more recent paper Chang, Hsiao & Shyu, 1992 have demonstrated a substantial improvement of the stall characteristics of an NACA 63-018 airfoil by acoustic excitation (applied at 0.012c) at Strouhal numbers up to 20.

114

The present work focuses on the modification of the global aerodynamic forces on a 2-D cylinder model using surface fluidic actuators based on synthetic jet technology. Because synthetic jets are zero-mass-flux and are synthesized from the working fluid in the flow system in which they are embedded, their interaction with a cross flow results in formation of closed recirculation regions and in a modification of the surface pressure distribution which also affects flow separation. The work is conducted in a low-speed wind tunnel and cylinder Reynolds numbers up to 131,000 are realized. Section II describes the experimental apparatus. In Section III we discuss surface pressure measurements, velocity measurements in the near wake, and the response of the lift force and of the near wake to a transient change in the control input. The conclusions are presented in Section IV.

V.2 Experimental Apparatus

The present experiments are conducted in an open return, low-speed wind tunnel having a square test section measuring 0.91 m on the side. The maximum speed is 32 m/sec and the turbulence level is less than 0.25%. The cylinder model is constructed out of aluminum, its diameter is D = 6.22 cm and it spans the entire test section. The present experiments were performed at Re_D = 31,000, 75,500, and 131,000. The center section of the cylinder is equipped with 47 pressure ports equally spaced around its circumference. The static pressure around the circumference of the cylinder is measured using a 48-channel Scanivalve switch and a MKS pressure transducer. Distributions of the streamwise and cross-stream velocity components are measured using a miniature x-wire probe mounted on a computer-controlled traversing mechanism. A 200 MHz laboratory computer is used for experiment control and data acquisition. The center section of the cylinder is also instrumented with a pair of adjacent plane synthetic jet actuators each having an orifice width b = 0.5 mm and spaced 2.5 mm apart along the long side (140 mm) of their orifices. The jet orifices are flush with the external surface of the cylinder and colinear with respect to its axis (Figure V.1). The performance of the two jets is quantified in terms of the conventional dimensionless momentum coefficient

$$C_\mu = \frac{2\rho_j U_j^2 2b}{\rho_0 U_0^2 D}$$

Where ρ, and ρ_0 are the densities and of the jet and the free stream fluids, respectively, U_0 is the free stream velocity and U_j is the cross-stream averaged jet velocity measured at 1mm (i.e., x/b = 2) downstream of the orifice. The cylinder can be rotated about its axis so that the angle between the jets and the direction of the free stream can be varied.

The operation of synthetic jet actuators is described in detail in an earlier paper of Smith and Glezer (1997). Nominally round (or plane) turbulent air (or liquid) jets are synthesized by a train of vortex rings (or two-dimensional vortex pairs). The vortices are formed at the edge of an orifice of an otherwise sealed cavity by the motion of a small diaphragm that is mounted on a cavity wall and is driven at resonance by piezoelectric actuators. During the forward motion of the diaphragm, fluid is ejected from the cavity forming a vortex pair that is advected away under its own self-induced velocity. When the diaphragm begins to move away from the cavity, the vortex is sufficiently removed and is thus unaffected by the ambient fluid that is drawn into the cavity. Although, during each cycle the net mass flux out of the cavity is zero, each vortex pair has a finite hydrodynamic impulse. In the present experiments, two parallel synthetic jets are used to form a larger jet having a prescribed distribution of linear momentum. The operating frequency of the jet is 740 Hz and thus the Strouhal numbers at Re_D = 31,000, 75,500, and 131,000 are 6.1, 2.6, and 1.5, respectively.

V.3 Results

V.3.1 Pressure Measurements

Azimuthal distributions of the pressure coefficient $C_p(\theta)$ on the surface of the cylinder for the unforced and forced flow taken from the data of Amitay et al.[10] ($Re_D = 75,500$ and $C\mu = 6\cdot10^{-4}$) at several actuator angles γ (each marked with a dashed line) are shown for reference in Figures V.2a-f. When the jets are directed upstream (i.e., $\gamma=0^0$ Figure V.2a), the azimuthal pressure distribution is almost unchanged (although there is a slight decrease in pressure near the minimum at $\theta \approx \pm68^0$) suggesting that the momentum coefficient is too low (the global effect of the jet near the front stagnation point scales with the momentum coefficient). However, the effect of the jets on the pressure distribution becomes substantially more pronounced as γ is increased. In fact, when $\gamma = 45^0$ (Figure V.2b), there is already a global change in $C_p(\theta)$ around most of the circumference of the cylinder. The pressure coefficient decreases *both* upstream and downstream of the actuator relative to the unforced flow between the front stagnation point and $\theta \approx 120^0$ (where the flow appears to separate) with a minimum around $\theta \approx 75^0$ indicating a non-zero lift force (see Figure V.4a below). It appears that the lower static pressure upstream and downstream of the synthetic jet pair is induced by the strong suction towards the jet orifice (Smith and Glezer[12]). Of particular note is the almost uniform increase in the base pressure of the cylinder between the top and bottom separation points indicating a decrease in pressure drag (see Figure V.4b below). When $\gamma = 90^0$ (Figure 2c), there is further decrease in surface pressure on the top surface of the cylinder and the separation point appears to move downstream to $\theta \approx 125^0$, but the base pressure is not as low as for $\gamma = 45^0$ and thus there is a lesser reduction in pressure drag (see Figure V.4b). It is noted that asymmetric pressure distributions similar to Figure V.2c have been observed in an unforced cylinder flow at Reynolds numbers of the order $0.36\cdot10^6$ (Shih, Wang, Coles, and Roshko, 1993) when turbulent reattachment occurs on one side of the cylinder but not on the other, resulting in drag and lift coefficients were 0.5 and 1.6, respectively. At this Reynolds number the flow apparently tends to be bi-stable and may even exhibit hysteresis (Schewe, 1993).

The static pressure between the front stagnation point and the separation point continues to decrease (relative to the unforced flow) as γ is increased. When $\gamma = 100^0$, the pressure minimum at $\theta \approx 85^0$ almost reaches the potential flow value of -3). The most prominent feature in the pressure distribution when $\gamma > 90^0$ (Figures V.2d-f) is the appearance of a local minimum in the static pressure on the *unforced* (lower) half of the cylinder upstream of the separation point which offsets the increase in lift. When $\gamma = 110^0$ (Figure 2e), the two pressure minima and the rest of the pressure distributions on the top and bottom surfaces are almost symmetric indicating that at this actuator angle the lift is approximately zero. As γ is further increased to 120^0 (Figure V.2f), the pressure distribution upstream of the actuator on the forced side is almost indistinguishable from the pressure distribution of the unforced flow and the jets appear to affect only the base region and the opposite (bottom) half of the cylinder, indicating a reversal in the direction of the lift force.

Based on flow visualization experiments (Amitay et al., 1997) it is conjectured that the pressure distribution on the forced (top) half of the cylinder results from two competing effects. While the change in the curvature of the forced flow leads to an increase in the local base pressure, the suction flow towards the actuators from the bottom surface causes a decrease in the static pressure on the unforced side. This effect diminishes as γ increases over 130^0 (not shown).

The azimuthal variation in the pressure distribution $\Delta C_p(\theta)$ (relative to the unforced flow) as a result of the flow modification induced by the jet is measured for $Re_D = 31,000$, $75,500$, and $131,000$ (Figure V.3) for a jet placed at $\gamma = 60^0$ while keeping the momentum coefficient $C\mu$

116

invariant ($C_\mu = 10^{-4}$). The magnitude of the peak decrease in the pressure coefficient on the top surface of the cylinder upstream of the separation clearly increases with Reynolds number (as does the lift). As can be seen from Figure V.2, the crossover between the pressure distributions of the unforced and forced flows normally corresponds to the point of separation, and thus the data in Figure V.3 suggest that the separation point moves up to $\theta = 140^\circ$ when the Reynolds number increases. The corresponding lift coefficient for the three Reynolds numbers are 0.32, 0.46, and 0.93. In this range of Reynolds numbers the base pressure of the cylinder normally decreases with increasing Reynolds number (e.g., Roshko and Fiszdon, 1969). As seen in Figure V.3, in all three cases while the base pressure of the forced flow is greater than in the unforced flow, the magnitude of the increase in base pressure diminishes somewhat as the Reynolds number increases. The corresponding fractional decrease in the drag coefficient for each of the Reynolds numbers is 0.07, 0.20, and 0.085.

The variation of the lift coefficients C_L and of the normalized increment in (pressure) drag $\hat{C}_D$ ($\hat{C}_D = C_{D_{forced}} / C_{D_{unforced}} - 1$) with azimuthal jet position are shown in Figures V.4a and V.4b, respectively. These data are taken at $Re_D = 75,000$ at two actuation frequencies 740 Hz (St = 2.6) and 1300 Hz (St = 4.5) and, in addition, at $Re_D = 131,000$ at 740 Hz (St = 4.5). As is evident from these data, the distributions of C_L and $\hat{C}_D$ are qualitatively independent of the actuation frequency. At both frequencies, $\hat{C}_D$ decreases (i.e., there is a decrease in drag) while C_L increases with γ. At $Re_D = 75,000$, the maximum lift coefficient is approximately 0.54 while at $Re_D = 131,000$, the lift coefficient reaches a maximum of 0.93. As the lift force reverses its direction for $\gamma > 100^\circ$, $\hat{C}_D$ increases (i.e., there is an increase in the drag force). The lift force vanishes at $\gamma = 135^\circ$ for both Reynolds numbers and actuator frequencies, and the largest reversed lift force is 0.93 for $Re_D = 131,000$. It is also noted that the local minimum in drag for the nominal range $60^\circ < \gamma < 110^\circ$ is probably associated with the protrusion of the jets into the free stream and an increase in frontal blockage of the cylinder.

V.3.2 Velocity Measurements

The modification of the aerodynamic forces on the cylinder is accompanied by substantial changes in the structure of its wake which are studied using hot wire anemometry in the near wake for $Re_D = 75,500$, $C_\mu = 6 \cdot 10^{-4}$ and jet angle $\gamma = 60^\circ$.

The cross stream distributions of the time-averaged streamwise and cross stream velocity components and of the spanwise vorticity are shown in Figures V.5a-c, respectively (the distributions of the unforced flow are plotted using open symbols). For the unforced case, the cross stream distributions of both velocity components as well as of the vorticity are reasonably symmetric about the cylinder's centerline (y/D=0), indicating that the lift coefficient is nearly zero. As can be seen in Figure V.5a, when the flow is forced, the establishment of lift on the cylinder and the reduction in its drag are accompanied by a downward displacement of the wake (opposite to the direction of the lift force) and a smaller velocity deficit. Furthermore, the cross-stream velocity in the forced flow exhibits an offset which corresponds to a downward motion in the potential flow above the wake. The forcing also results in a smaller concentration of mean vorticity on both sides of the wake with a slight asymmetry top and bottom [the peak vorticity on the top side (i.e., the forced side) is somewhat lower than at the bottom]. Nevertheless it can be shown that the vorticity flux on either side of the wake (i.e., the flux of positive and negative vorticity) is the same as for the unforced flow (the net vorticity flux across the wake is zero in either case).

117
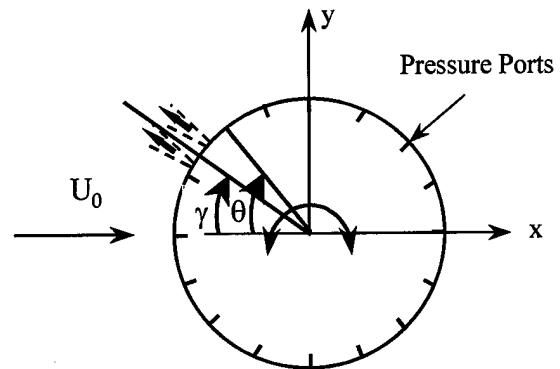
**Figure V.1.** Schematic diagram of the cylinder model.
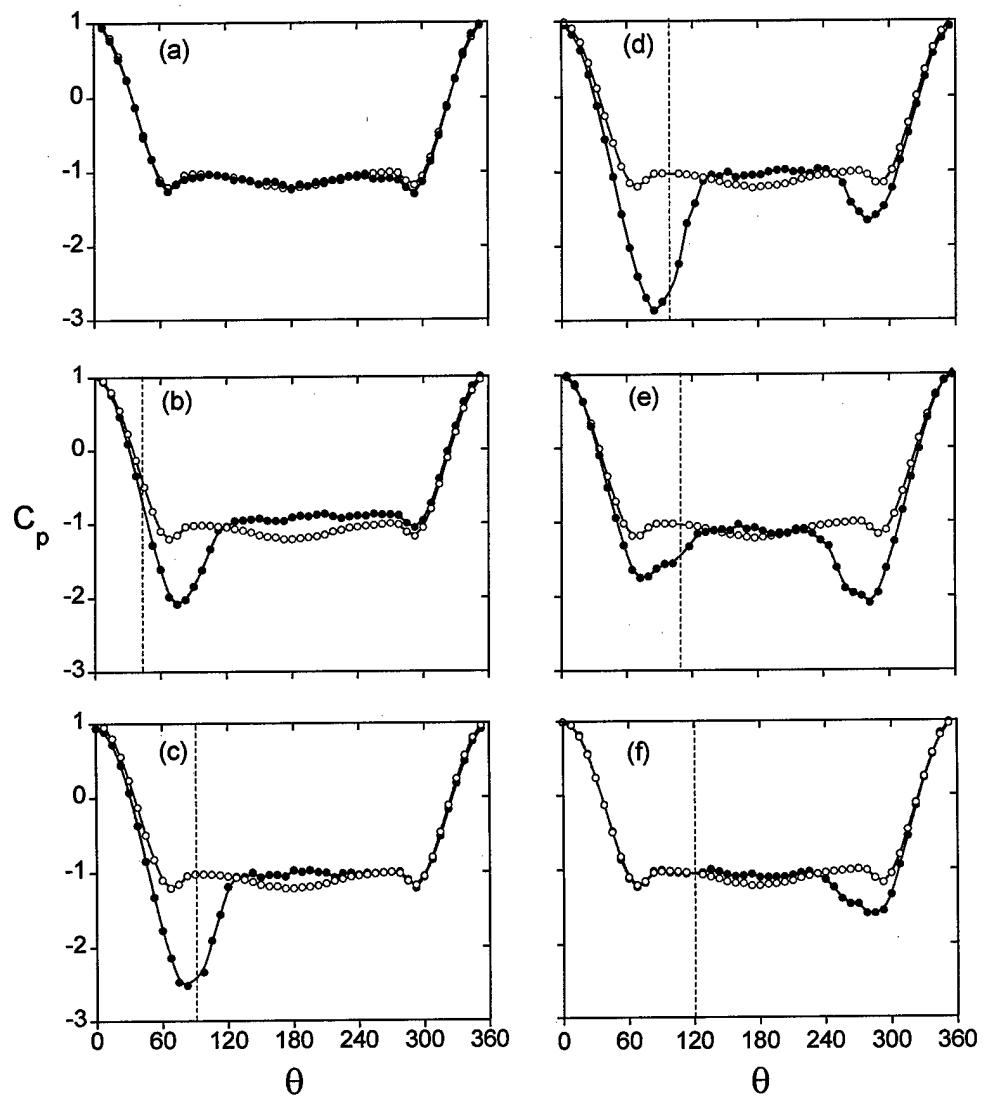
Figure V.2. Azimuthal variations of $C_p(\theta)$ at Re_D=75,500 (—○—) unforced and (—●—) forced.
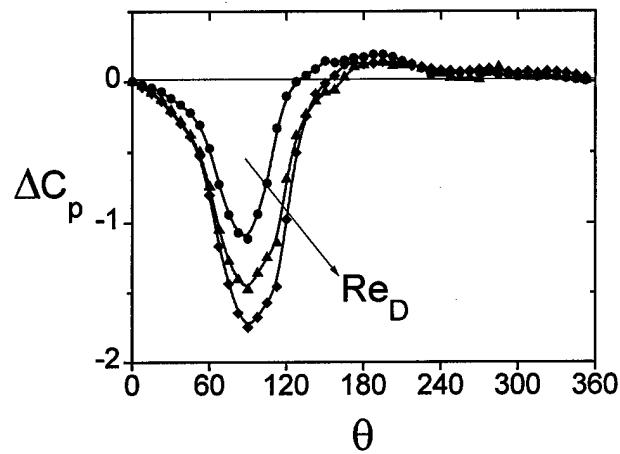
Figure V.3. Azimuthal variations of $\Delta C_p(\theta)$ at different Reynolds numbers.
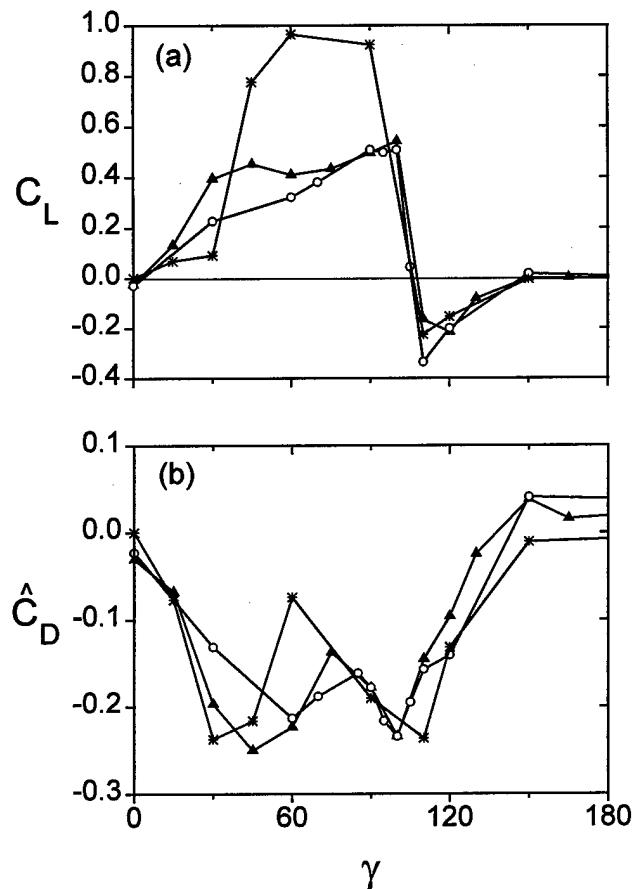
Figure V.4. Variations of C_L and $\hat{C}_D$ with jet angle. (—○—) Re_D=75,500, St = 2.6, (—▲—) Re_D=75,500, St = 4.5 and (—✳—) Re_D=131,000, St = 1.49.

The corresponding cross-stream distributions of the rms velocity fluctuations u', v' and of the Reynolds stress u'v' are shown in Figures V.6a-c, respectively. As for the velocity distributions in Figure V.5, the turbulent fluctuations in the unforced wake are nominally symmetric about the cylinder's centerline. When the flow is forced, all three turbulent quantities are substantially reduced across the entire (displaced) wake. This diminution is ostensibly the result of enhanced dissipation that is effected by direct coupling of the excitation to the small scale motions within the wake. Similar behavior was observed by Wiltse and Glezer (1997) in which they focused on direct excitation of the small scales within the dissipation range of a free shear flow. As shown in Figure V.7a below, the excitation frequency of the jets is within the dissipation range of the wake flow and substantially higher than the natural shedding frequency.

Note that the distribution of the Reynolds stress in the forced flow is not symmetric about the center of the wake and appears to be higher on the (upper) forced side. Nevertheless, u'v' is still smaller on both sides of the wake compared to the unforced flow.

Power spectra of the streamwise velocity measured at x/D=1 and 3 on both sides of the wake at cross stream elevations where the streamwise velocity deficit is half the maximum deficit are shown in Figures V.7a and b, respectively. In these figures the gray curves correspond to the unforced flow and the velocity spectra measured at the upper half of the wake are shifted vertically by two decades. The spectra of the unforced flow at x/D = 1 are dominated by a spectral peak at the (natural) shedding frequency (50 Hz) with a number of broader peaks at the higher harmonics. At x/D = 3, the spectral peak at the shedding frequency is larger and the magnitudes of the spectral components at its higher harmonics are substantially reduced. It is also noteworthy that the slope of the unforced spectra at the high frequencies which is almost - 5/3 at x/D = 1, increases somewhat with downstream distance. When the flow is forced, the spectrum on the upper (forced) side of the wake is dominated by the spectral peak at the forcing frequency (740 Hz) and the spectral peak at the shedding frequency is significantly attenuated. In fact, there appears to be a reduction in spectral contents of all frequencies below the forcing frequency suggesting enhanced transfer of energy from the large- to small-scale motions with the wake. This reduction in spectral content of the large scales is accompanied by an increase in the power content of the smaller scales at frequencies above the forcing frequency. On the bottom (unforced) side of the wake, the shedding frequency increases to 80 Hz as a result of the reduction in the cross stream extent of the wake (although the magnitude of the spectral peak at this frequency is smaller than in the unforced flow). More importantly, this spectral distribution indicates that the turbulent kinetic energy on the bottom side of the wake is reduced throughout the entire spectrum compared to the unforced flow. At x/D = 3, the spectra of the forced flow include a spectral component at the higher shedding frequency (80 Hz) on both sides of the wake, where on the bottom (unforced) side there is also an additional smaller peak at the shedding frequency of the unforced flow. Furthermore, the turbulent kinetic energy throughout the entire spectrum of the forced flow is reduced on both sides of the wake, suggesting that direct forcing of the small scales increases the dissipation.

The effectiveness of the actuator jets when the flow about the cylinder is deliberately modified by a surface trip was investigated by Amitay et al. (1997) by placing two spanwise aluminum tubes (1mm in diameter) on the surface of the central section of the cylinder at $\theta = \pm 35°$. The resulting azimuthal distribution of the pressure coefficient are reproduced for reference in Figure V.8. The pressure distribution of the tripped flow (open symbols) on the top and bottom surfaces of the cylinder is reasonably symmetric. Compared to the unforced flow (solid curve), the separation point of the tripped (but unforced) flow moves from $\theta = 85°$ to $120°$ as the cross-stream width of the wake decreases and the base pressure of the cylinder increases (accompanied by a decrease in pressure drag) which indicates turbulent separation and is similar to the pressure distribution at a higher Reynolds number (Roshko & Fiszden, 1969). When the jets are activated (solid symbols) at $\gamma = 110°$ (with tripping in place), there is a substantial decrease in

120

the static pressure upstream and downstream of the actuators which is evident as far upstream as $\theta = 30^0$. Furthermore, as a result of the change in the curvature of the external flow, the separation point moves to $\theta = 140^0$. Note, however, that in the presence of the trip, the effect of the activation on the bottom half of the cylinder is smaller than for the smooth (i.e., untripped) cylinder.

Cross stream distributions of the mean streamwise velocity, Reynolds stress, and the spanwise vorticity measured at x/D = 3 in the presence of the trip for the unforced flow (open symbols) and forced flow (solid symbols) are shown in Figures V.9a-c (the data for the smooth cylinder is also shown for reference using a solid curve). The cross stream velocity distribution in the presence of the trip (unforced, Figure V.9a) is nearly symmetric about y/D = 0 (the minor asymmetry is probably owing to slight differences in the azimuthal position of the trip cylinders) and shows a reduction in the velocity deficit which is commensurate with the reduction in the cross stream width of the wake. When the flow is forced the velocity deficit is substantially reduced which indicates further reduction in the cross stream width of the wake, and the wake is displaced in a downward opposite to the direction of the (lift) force on the cylinder. Of particular note is the effect of the jets on the Reynolds stress (Figure V.9b). In the presence of the trip, the Reynolds stress of the unforced flow is significantly higher than for the smooth cylinder across the entire wake, which is consistent with turbulent separation. However, the Reynolds stress of the forced flow is substantially lower (even lower than the Reynolds stress in the wake of the smooth cylinder) as a result of enhanced small-scale dissipation. As shown in Figure V.9c, in the presence of the trip, positive and negative mean vorticity concentrations on the top and bottom sides of the wake are smaller than in the wake of the smooth cylinder ostensibly as a result of the cross stream width of the wake and an increase in the shedding frequency. The further reduction in corresponding vorticity concentrations in the forced flow indicate a further increase in the shedding frequency along with the increase in lift and reduction in drag.

Power spectra of the streamwise velocity measured at x/D=1 and 3 on both sides of the wake (similar to Figures V.7a and b) are shown in Figures V.10a and b, respectively for the smooth cylinder, and for the unforced and forced flow in the presence of the trip. At x/D = 1 (Figure V.10a) the spectra on both sides of the wake in the presence of the trip are very similar to the spectra of the unforced flow except that the shedding frequency increases to 65 Hz and there is a decrease in the spectral content of frequencies below 200 Hz. Farther downstream (x/D = 3, Figure V.10b), the magnitude of the spectral peak at the shedding frequency increases (relative to the unforced flow) and there is a decrease in the total turbulent kinetic energy across the entire spectrum. When the flow is forced, the shedding frequency increases to 85 Hz although the magnitude of the spectral peak at the shedding frequency on the forced side of the wake is substantially lower than in the unforced case. Furthermore, the spectrum of the forced flow includes a peak at the actuation frequency along with two side bands corresponding at the shedding frequency indicating the effect of the forcing on the separating shear layer at downstream of the cylinder. The spectral peak at the actuation frequency is absent in spectra of the forced flow at x/D = 3 (Figure V.10b). The turbulent kinetic energy is considerably lower compared to the unforced flow (with the trip in place) particularly at the low end of the spectrum. It is noteworthy that while the effect of the forcing on the low frequencies is almost symmetric on both sides of the wake, the reduction in the turbulent kinetic energy at high frequencies is greater on the upper (forced) side of the wake.
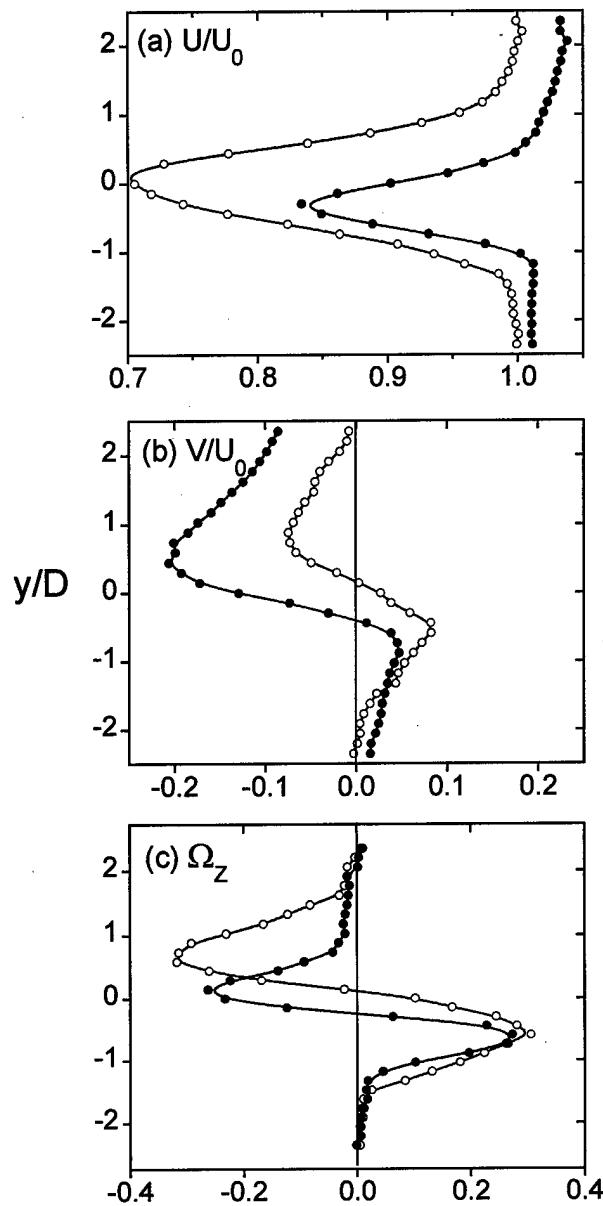
Figure V.5. The cross stream distributions of (a) the streamwise, (b) the cross stream velocity and (c) the spanwise vorticity. (—o—) unforced and (—●—) forced.

Figure V.6: The cross stream distributions of the fluctuating (a) streamwise, (b) cross stream velocity and (c) Reynolds stress. (—o—) unforced and (—●—) forced.
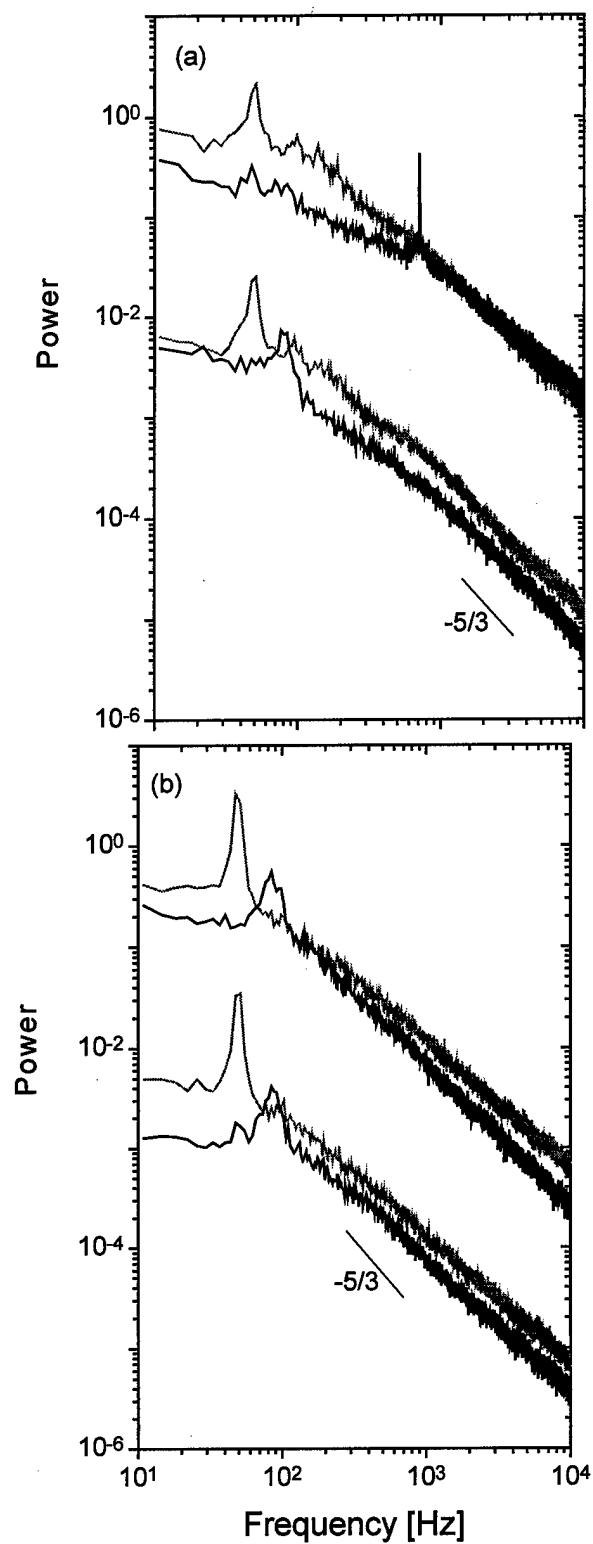
Figure V.7. Power spectra measured at (a) x/D=1 and (b) x/D=3. The gray and black lines represent the unforced and forced cases.
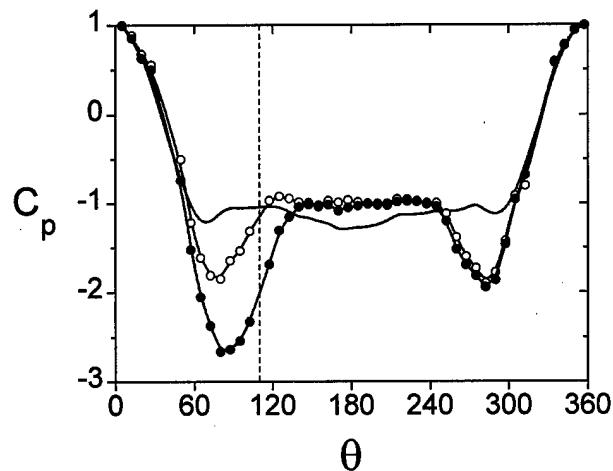
Figure V.8. Azimuthal pressure distribution $C_p(\theta)$ with boundary layer tripping. (—○—) unforced, (—●—) forced and (——) base case.
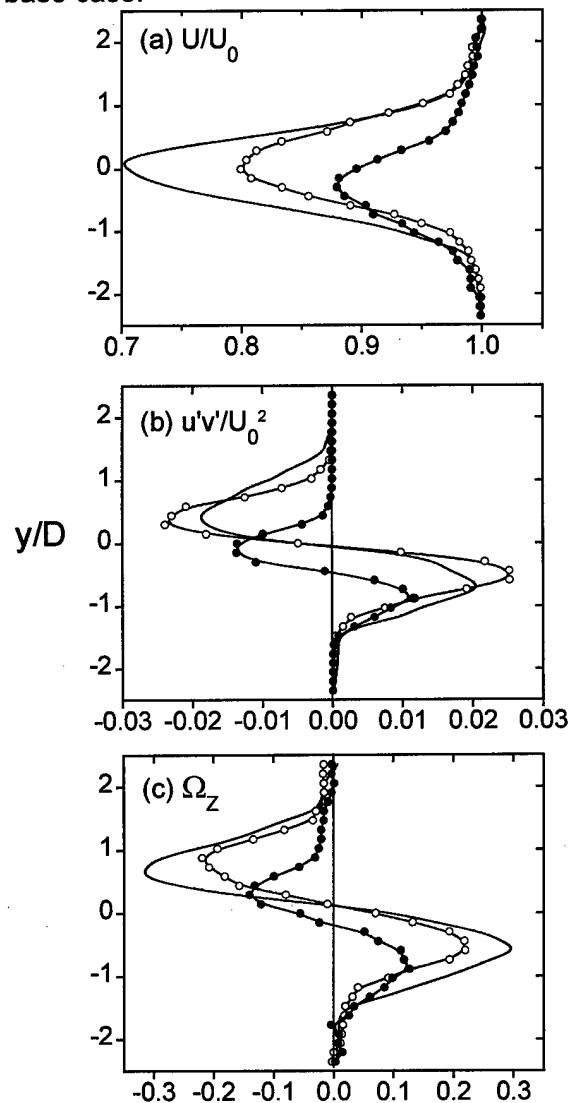
Figure V.9. Cross-stream distribution of the normalized (a) streamwise velocity, (b) Reynolds stress and (c) spanwise vorticity. (—○—) unforced, (—●—) forced and (——) base case..

125
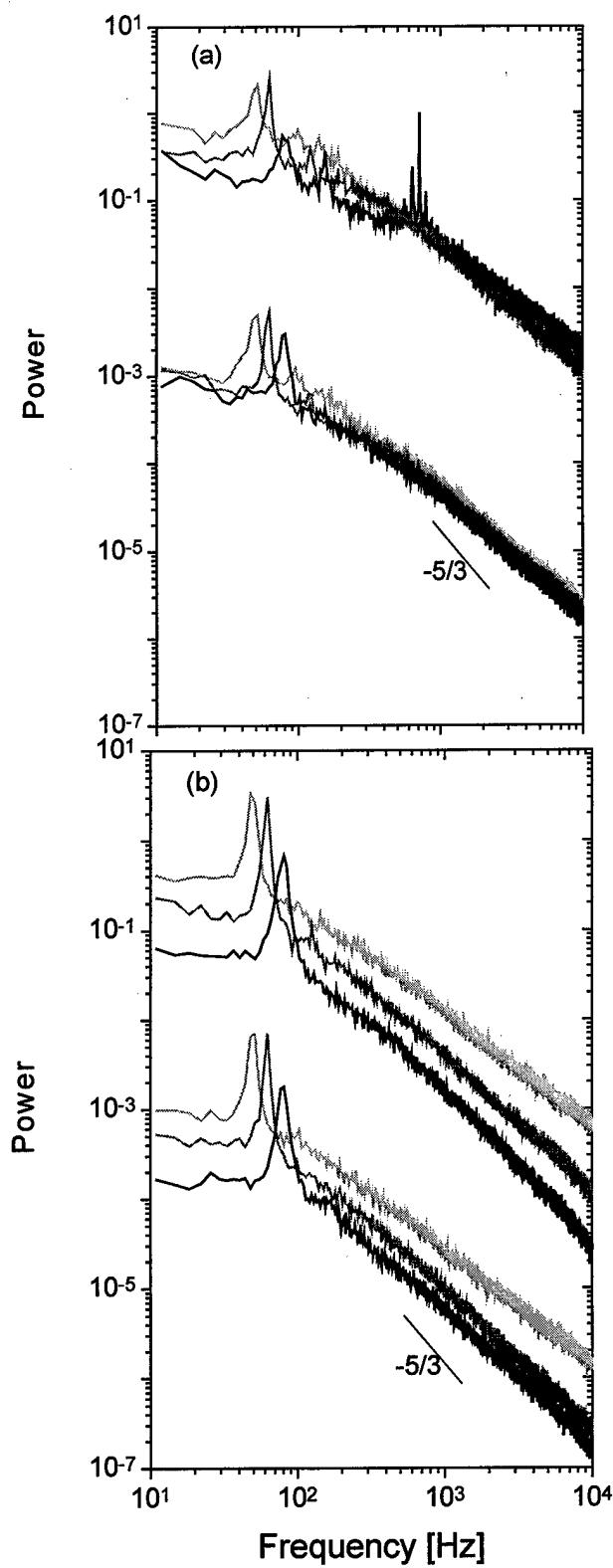
Figure V.10. Power spectra measured at (a) x/D=1 and (b) x/D=3. The light gray, the gray and the black lines represent the unforced smooth, unforced tripped and forced tripped cases.

126

V.3.3 Transient Response to Pulsed Excitation

In this section we discuss the transient response of the flow about the cylinder to pulsed excitation and, in particular, the transient effect on the velocity field and the evolution of the vortical structures in the wake, and on the corresponding time-dependent lift force on the cylinder.

The response of the synthetic jet (issuing into a quiescent medium) to pulsed (hat-shaped) amplitude modulation of the driving signal can assessed from measurements of the centerline streamwise velocity at the jet exit plane (Figure V.11). Each data set consists of 150 successive realizations, where each realization starts 71T before the beginning of the pulse, the duration of the pulse is 284T long and the sampling continues 275T following the termination of the pulse (T is the period of the actuator frequency). The modulation is synchronized to the actuator's driving signal so that the leading and trailing edges of the modulating pulse (marked with arrows) coincide with zero crossing of the driving signal. At the exit plane the synthetic jet responds to the modulating pulse within a fraction of T (approximately 1msec) and the apparent frequency doubling of the measured signal results from sensor rectification.

The transient response of the flow to pulsed excitation is measured in detail across the wake of the cylinder at x/D=3 using x-wire anemometry, where the measurements are taken phase-locked to the modulating pulse. Color raster plots of the phase averaged cross-stream distributions of the streamwise and cross-stream velocity components are shown in Figures V.12a and b, respectively. The corresponding time averaged cross-stream velocity distributions (i.e., in the presence and absence of the modulated excitation) are shown for reference on the right hand side of each plot. The phase-averaged unforced flow (i.e., before the actuator is pulsed) is nominally symmetric about the wake centerline and exhibit only relatively weak oscillations at the passage frequency (50 Hz) of the wake vortices because there is no clear phase reference between these vortices and modulation frequency.

After the beginning of the pulse (as marked with an arrow on the time scale), there is a time lag of approximately 10T before the flow transient reaches the measurement station. It is noteworthy that the appearance of the transient is marked by the presence of several strong oscillation cycles that are felt across the entire wake and have a nominal frequency of 50 Hz (i.e., close to the "natural" shedding frequency of the cylinder). These oscillations appear to be more coherent (i.e., phase-locked) than the nominal oscillations that are associated with the passage of the wake vortices before the arrival of the pulse suggesting that they are triggered by and phase locked to the pulse itself. Following the transient associated with the arrival of the leading edge of the pulse, the wake becomes substantially narrower, the streamwise velocity deficit is substantially reduced, and the center of the wake (as marked by the peak of the velocity deficit) is shifted downward by y/D = 0.3 (this is also evident from cross stream distributions of the time-averaged velocity on the right hand side of Figure V.12a). Note also the increase in the downward (i.e., negative) cross-stream velocity component above the wake region which offsets the normally antisymmetric distribution within the wake.

Similar to the transient that is associated with the arrival of the leading edge of the pulse at the measurement station, the arrival of the its trailing edge again triggers strong oscillations of the velocity field at approximately the "natural" shedding frequency of the cylinder. There is a fundamental difference however between the response of the wake flow to the leading and trailing edges of the pulse in that it appears that at the trailing edge the oscillations persist (i.e., remain phase-locked to the pulse) much longer (approximately 220T) than during the passage of the leading edge. Ultimately, the wake returns to its original (unforced state).

It appears that the broad spectral contents associated with the leading and trailing edges of the pulse trigger or lock vortex shedding at the natural frequency of the cylinder. It is remarkable, however that the shedding (or the oscillations) are damped much more rapidly following the transient associated with the activation of the jets compared to the transient associated with its termination. It is conjectured that the difference between the two scenarios is that when the jets are turned off, the oscillations of the flow about the cylinder (and thus in the wake) decay to the unforced state through "natural" damping which comes from wall shear stress and the motion of the separation regions on the top and bottom surfaces. However, when the jet is active its interaction with the cross flow about the cylinder and the introduction of small scale motions into the surface boundary layer (which increase the Reynolds stresses) provides additional damping.

Phase-averaged cross stream distributions of the spanwise vorticity are computed from the velocity distributions in Figures V.12a and b and are shown in Figure V.13 using color contour plots (the time-averaged cross-stream distributions in the presence and absence of the jets are also plotted in on the right hand side). Also included in Figure V.13 are two insets that show expanded time scales (each 110T wide) of the vorticity distributions during the passage of the leading and trailing edges of the pulse. When the flow is unforced, the vorticity distribution in the wake is comprised of a train of alternating vortical structures of opposite sense at the upper and lower cross stream halves of the wake (counter-clockwise vorticity as in the top half is taken to be negative). The phase-averaged vortical structures in the unforced flow are somewhat "blurred" because there is no clear phase reference between these vortices and modulation frequency. Nevertheless, the total vorticity across the wake during one period of the (unforced) shedding frequency is approximately zero. As shown in Figures V.12a and b the arrival of the leading and trailing edges of the pulse are associated with strong oscillations of the wake flow which correspond to the passage of coherent vortical structures at the natural shedding frequency. These vortices are clearly visible in the two insets.

As shown in §V.3.1, forcing with the jets leads to a positive lift force on the cylinder which must be accompanied by a transient change in the vorticity flux with a net transient increase in circulation associated with positive (clockwise) vorticity. Following the application of the pulse, a strong clockwise vortex is advected past the measurement station and is followed by a series of four counter rotating vortices before the wake reaches its final (limit) state where the cross section of the vortices is substantially smaller (commensurate with the decrease in the cross stream width of the wake) as the shedding frequency increases from 50 to 80 Hz. Similarly, a longer train of counter rotating vortices is advected past the measurement station at the natural shedding frequency following the trailing edge of the pulse. It is expected that the decrease in lift force is accompanied by net change in the vorticity flux and a decrease in circulation.

The time rate of change in circulation is given by the vorticity flux

$$\frac{d\Gamma}{dt} = \int_{-\infty}^{\infty} U\Omega_z dy$$

and thus the incremental lift coefficient of the cylinder (computed relative to the lift at time t = 0) can be computed from

$$C_L = -2\frac{\Gamma}{U_0 D} \quad .$$

The phase-averaged vorticity flux and lift coefficients are estimated (not accounting for contributions of the fluctuating components) using the phase averaged cross-stream distributions of the streamwise velocity and spanwise vorticity and are shown in Figures V.14a and b, respectively. It is expected that the net vorticity flux over one period of the shedding frequency be zero before the flow is forced and after the transients that are associated with the pulsed modulation and the establishment or removal of the lift force subside. As shown in

Figure V.14a, the vorticity flux in the unforced flow oscillates with the passage of counter-rotating wake vortices corresponding to a lift force of alternating sign. When pulsed modulation is applied, the vorticity flux has a sharp negative peak (-0.21) which corresponds to the passage of a clockwise vortex that is shed from the lower half of the cylinder. This is followed by a positive peak (where the amplitude reaches a maximum value of 0.21) that is associated with the passage of a counterclockwise vortex, which is shed from the top surface of the cylinder. Subsequently, then, the vorticity flux changes its sign two more times at the shedding frequency before reaching low-level oscillations about zero. When the pulse is terminated (i.e., the jets are turned off), the vorticity flux first develops a negative peak which is followed by a series of larger peaks of alternating signs where the maximum positive and negative values are 0.37 and -0.3, respectively followed by a slow decay. The lift coefficient of the unforced flow is nominally zero (Figure V.14b). When pulsed modulation is applied, C_L has an overshoot to a value of 0.59 and subsequently within 20T approaches the steady value of 0.39. When the jets are turned off C_L oscillates around a zero mean between 0.6 and -0.38 and within 250T decays back to zero.
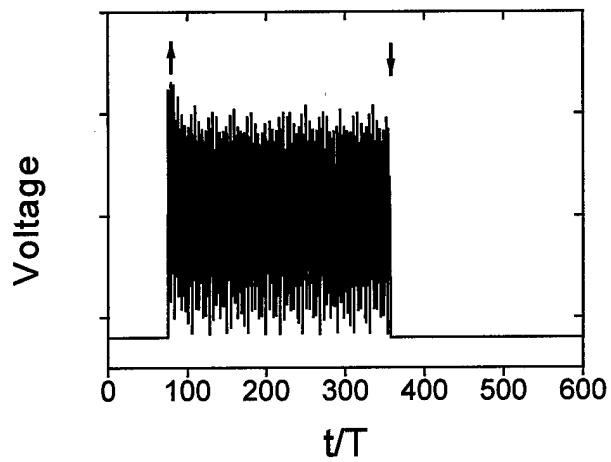
**Figure V.11.** The response of the synthetic jet to a pulsed amplitude modulation at the jet exit plane.
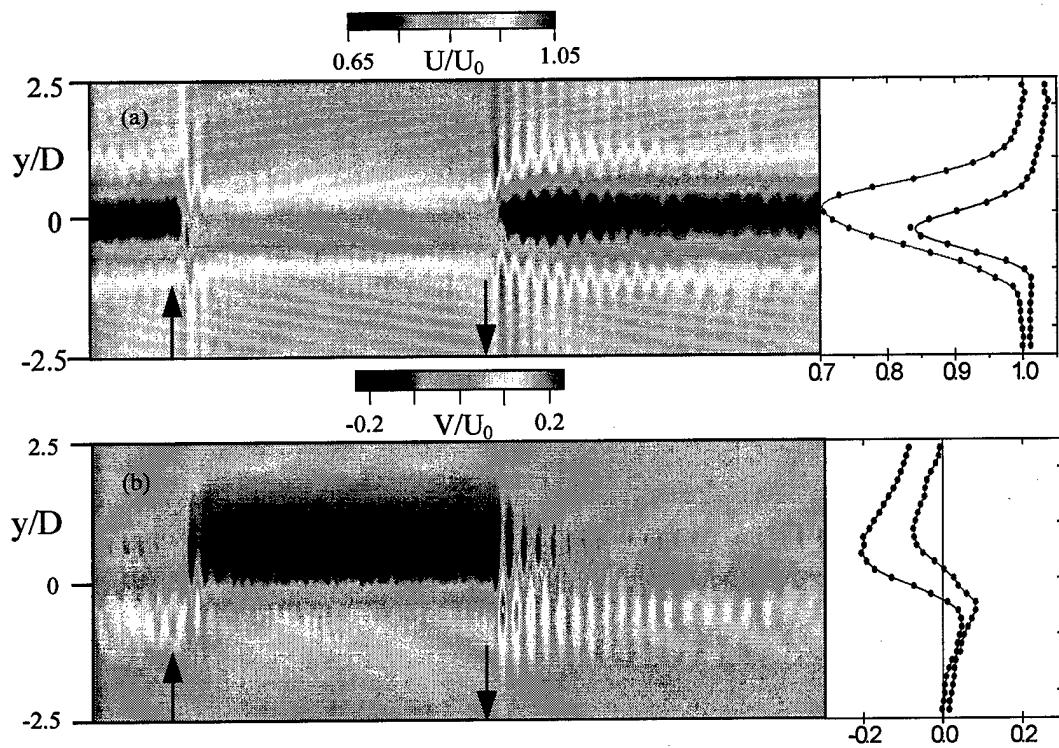
Figure 12: The transient response of the (a) streamwise and (b) cross stream velocity.
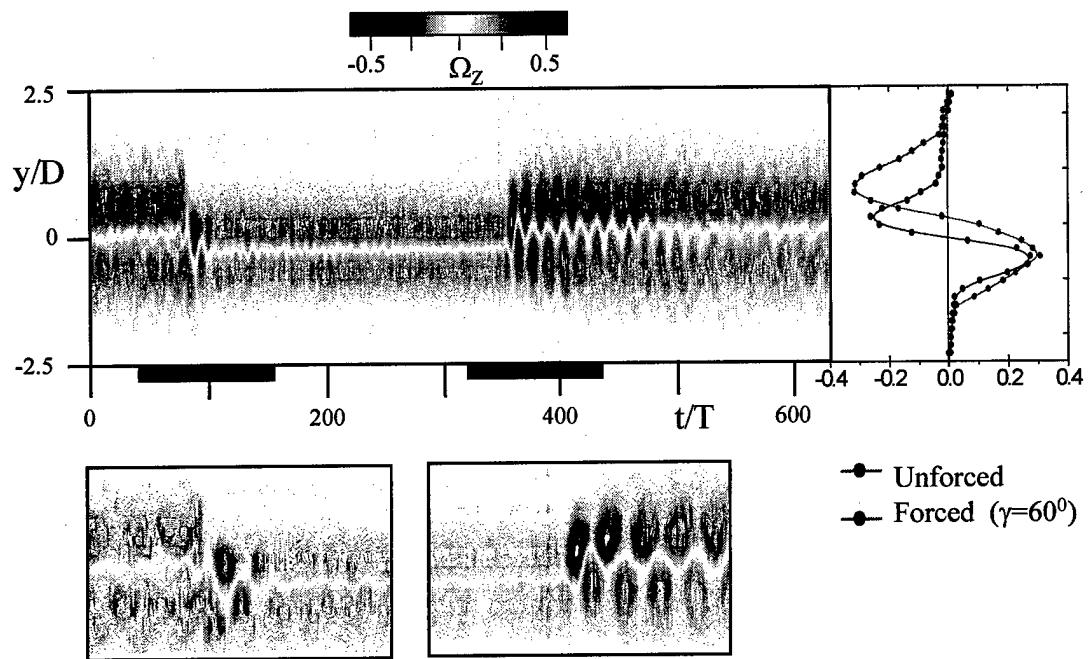
Figure 13: The transient response of the spanwise vorticity.

130
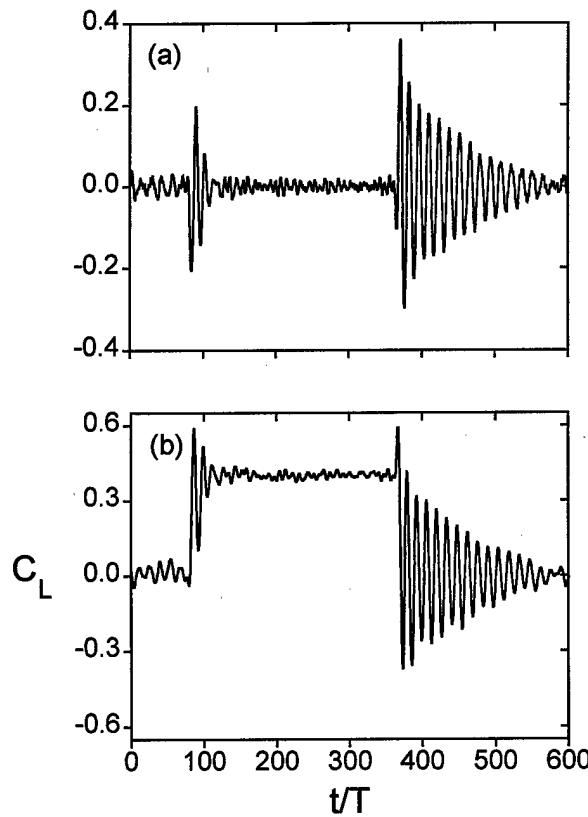
Figure V.14. The time response of the phase-averaged (a) vorticity flux and (b) lift coefficient.

V.4 Conclusions

The modification of the of global aerodynamic forces on a 2-D cylinder model using surface fluidic actuators based on synthetic jets technology are investigated experimentally in wind tunnel experiments at cylinder Reynolds numbers up to 131,000. The actuators induce a local "transpirating" recirculation bubble, which acts as a "virtual surface" and displaces local streamlines well outside the undisturbed boundary layer. As a result, the pressure coefficient on the surface of the cylinder decreases substantially *both upstream and downstream* of the actuator indicating that the potential flow outside of the surface boundary layer is moving faster than the unforced flow. Depending on the azimuthal location of the actuators, the lift and drag coefficients of the cylinder increase and decrease, respectively by effecting asymmetric pressure distributions. Such distributions are similar to bi-stable pressure distributions which in the unforced flow are only observed within a narrow range of Reynolds numbers an order of magnitude higher. Furthermore, the separation location on the back of the cylinder can be manipulated in a manner that is similar to the separation-reattachment bubble (and subsequently turbulent separation) in the "critical" Reynolds number regime of the unforced flow up to $ReD \approx 3.5 \cdot 10^6$. It is also found that the pressure distribution on the cylinder can be modified even in the presence of trip cylinders well upstream of the actuator jets. The modification of the aerodynamic forces on the cylinder is accompanied by substantial changes in the structure of its wake which are studied using hot wire anemometry. The establishment of lift on the cylinder and the reduction in its drag are accompanied by a downward displacement of the wake associated with a cross-stream velocity (opposite to the direction of the lift force) and a smaller streamwise velocity deficit. In the absence of flow transients, the vorticity flux on either side of the wake (i.e., the flux of positive and negative vorticity) is the same as for the unforced flow (the net vorticity flux across the wake is zero in either case). The changes in the mean flow are accompanied by a reduction in cross-stream distributions of the rms velocity fluctuations u', v' and of the Reynolds stress u'v' across the entire wake. This diminution is ostensibly the result

131

of enhanced dissipation that is effected by direct coupling of the excitation to the small scale motions within the wake. Furthermore, the reduction in the cross-stream width of the wake is accompanied by an increase in the shedding frequency of the large scale wake vortices. The response of the lift force and of the wake flow to a transient change in the control input are also investigated using pulsed amplitude modulation. The transient response of the flow is measured in detail across the wake using phase-locked x-wire anemometry and is marked by the presence of several strong oscillation cycles at the natural shedding frequency that are felt across the entire wake and are triggered by the change in the control input. However, there is a fundamental difference between the response of the time-dependent lift force (estimated from the phase-averaged vorticity flux) and of the wake flow to a "low-to-high" and "high-to-low" transitions of the control input. It appears that the damping associated with the latter transition is lower and that the flow oscillations persist much longer than during the "low-to-high" transition before the lift force and the wake asymptote to their final state. It is conjectured that the difference between the two scenarios is that when the jets are turned off, the oscillations of the flow about the cylinder (and thus in the wake) decay to the unforced state through "natural" damping which comes from wall shear stress and the motion of the separation regions on the top and bottom surfaces. However, when the jet is active, its interaction with the cross flow about the cylinder and the introduction of small scale motions into the surface boundary layer (which increase the Reynolds stresses) provides additional damping.

REFERENCES

Ahuja, K. K. and Burrin, R. H., 1984, "Control of flow separation by sound", AIAA Paper 84-2298.

Amitay, M., Kibens, V., Parekh, D. E. and Glezer, A., 1999, "Flow Reattachment Dynamics over a Thick Airfoil Controlled by Synthetic Jet Actuators", AIAA Paper 99-1001.

Amitay, M. Honohan, A. Trautman, M.and Glezer, A, "Modification of the aerodynamic characteristics of bluff bodies using fluidic actuators," 28th AIAA Fluid Dynamics Conference #97-2004 (1997).

Amitay, M. Smith, B. L. and Glezer , A., "Aerodynamic Flow Vectoring using Synthetic Jet Technology." 36th AIAA Aerospace Sciences Meeting #98-0208 (1998).

Andres, J.M. and Ingard, U., "Acoustic streaming at high Reynolds numbers," *J. Acous. Soc. Am.*, **25**, pg. 928 (1953).

Auerbach, D., "Experiments on the trajectory and circulation of the starting vortex," *J. Fluid Mech.*, **183**, pg. 185 (1987).

Bernal, L.P. and Roshko, A., "Streamwise vortex structure in plane mixing layers," *J. Fluid Mech.*, **170**, pg. 499 (1986).

Bradbury, L.J.S., "The Structure of a self-preserving turbulent plane jet," *J. Fluid Mech.*, **23**, pg. 31 (1965).

Bremhorst and K. and Hollis, P. G, "Velocity Field of an Axisymmetric Pulsed, Subsonic Air Jet," *AIAA J.*, **28**, pg. 2043 (1990).

Chang, R. C., Hsiao, F.-B., and Shyu, R.-N., 1992, "Forcing level effects of internal acoustic excitation on the improvement of airfoil performance", J. of Aircraft, 29(5), 823-829.

Davidson, B.J. and Riley, N., "Jets induced by oscillatory motion," *J. Fluid Mech.* ,**53**, pg. 287 (1972).

Didden, N., "Untersuchung laminarer instabiler Ringwirbel mittels Laser-Doppler-Anemometrie," Dissertation, University of Göttingen; also Mitt. MPI und AVA, Göttingen , Nr. 64 (1977).

Didden, N., "On the formation of vortex rings: rolling-up and production of circulation," *Z. Angew. Math. Phys.*, **30**, pg. 101 (1979).

Donovan, J.F. Kral, L.D. and Cary, A.W., "Active flow control applied to an airfoil," AIAA 35th Aerospace Sciences Meeting #98-0210 (1998).

Everitt, K.W. and Robins, A.G., "The development and structure of turbulent plane jets," *J. Fluid Mech.*, **88**, pg. 563 (1978).

Gharib, M. Rambod, E. and Shariff, K., "A universal time scale for vor1tex ring formation," *J. Fluid. Mech.* **360**, pg. 121, (1998).

Gilarranz, J.L. Yue, X. and Rediniotis, O.K. "PIV measurements and modeling of synthetic jet actuators for flow control," ASME #FEDSM98-5087 (1998).

Glezer, A., "The formation of vortex rings," *Phys. Fluids* , **31**, pg. 3532 (1988).

Glezer, A. and Coles, D., "An experimental study of a turbulent vortex ring," *J. Fluid Mech.*, **211**, pg. 243 (1990).

Gutmark, E. and Ho, Chih-Ming. "Preffered modes and the spreading rates of jets," *Phys. Fluids.*, **26**, pg. 2932 (1983).

Gutmark, E. and Wygnanski, I., "The planar turbulent jet," *J. Fluid Mech.*, **73**, pg. 465 (1976).

Hammond, D.A. and Redekopp, L.G., "Global Dynamics of Symmetric and Asymmetric Wakes," *J. Fluid Mech.* **331**, pg. 231 (1997).

Heskestad, G., "Hot-wire measurements in a plane turbulent jet," *ASME J. Appl. Mech.*, **32**, pg. 721 (1965).

Honohan, A. M., and Glezer, A., 1998, "The interaction of a synthetic jet with a crossflow", 51st Annual meeting, American Physical Society, Division of Fluid Dynamics, November 22-24, Philadelphia, Pennsylvania.

Hsiao, F.-B., Liu, C.-F., and Shyu, J.-Y., 1990, "Control of wall-separated flow by internal acoustic excitation", AIAA Journal, 28(8), 1440-1446.

Huang, L. S., Maestrello, L. and Bryant, T. D., 1987, "Separation control over an airfoil at high angles of attack by sound emanating from the surface", AIAA Paper 87-1261.

133

Ingard, U. and Labate, S., "Acoustic circulation effects and the nonlinear impedance of orifices," *J. Acoust. Soc. Am.*, **22**, pg. 211 (1950).

James, R.D. Jacobs, J.W. and Glezer, A., "A round turbulent jet produced by an oscillating diaphragm," *Phys. Fluids* , **8**, pg. 2484 (1996).

Joyce , J.W. "Fluidics—Basic component and applications," Special Report HDL-SR-83-9, (1983).

Kiya M., Shimizu M. and Mochizuki O. "Sinusoidal Forcing of a Turbulent Separation Bubble", *J. Fluid Mech.*, Vol. 342, pp. 119-139, 1997.

Koch , C.R., "Closed Loop Control of a Round Jet/Diffuser in Transitory Stall," PhD. Thesis, Stanford University, (1990).

Kotsovinos, N.E. and Angelidis, P.B., "The momentum flux in turbulent submerged jets," *J. Fluid Mech.*, 229, pg. 453 (1991).

Kovasznay, L.S.G. Fujita, H. and Lee, R. L., "Unsteady turbulent puffs," *Adv. Geophys.*, **18B**, pg. 253 (1973).

Kral, L.D. Donovan, J.F. Cain, A.B. and Cary, A.W., "Numerical simulation of synthetic jet actuators," AIAA 28th Fluid Dynamics Conference #97-1824 (1997).

Krothapalli, A. Baganoff, D. and Karamcheti, K., "On the mixing of a rectangular jet," *J. Fluid Mech.*, **107**, pg. 201 (1981).

Lebedeva, I.V., "Experimental study of acoustic streaming in the vicinity of orifices," *Sov. Phys. Acoust.*, **26**, pg. 331 (1980).

Lee, M. and Reynolds, W.C., "Bifrucating and blooming jets," Stanford report TF-22 (1985).

LePera, S. and Vandsburger, U. "Coupled Multiple Jet Excitation." 35th AIAA Aerospace Sciences Meeting #97-0075 (1997).

Lighthill, M. J., "Acoustic Streaming," *J. Sound Vib.*, **61**, pg. 391 (1978).

Lim, D. and Redekopp, L.G., "Aerodynamic Flow Vectoring of 2-D Co-flowing Jets," AIAA 35th Aerospace Sciences Meeting, Reno, NV, #97-0214 (1997).

Lueptow, R.M. Breuer, K.S. and Haritonidis, J.H., "Computer-aided calibration of X-probes using a look-up table," *Exp. Fluids*, **6**, pg 115 (1988).

Mednikov, E.P. and Novitskii, B.G., "Experimental study of intense acoustic streaming," *Sov. Phys. Acoust.*, **21**, pg. 152 (1975).

Meissner, A., "Uber piezo-elektrische Kristalle bei Hoch-frequenz." *Z.tech. Physik.*, **7**, 1926.

Neuburger, D. and Wygnanski, I., 1987, "The use of a vibrating ribbon to delay separation on two dimensional airfoils", TR-88-0004.

Newman, B. G. "The Deflexion of Plane Jets by Adjacent Boundaries-Coanda Effect," *Boundary Layer and Flow Control* **1**, edited by Lachmann, G. V. pg. 232 (1961).

Nyborg, W. L., "Acoustic Streaming Due to Attenuated Plane Waves," *J. Acoust. Soc. Am.* **25**, #68, (1953).

Nygaard, K.J. and Glezer, A., "Evolution of Streamwise Vortices and the generation of Small-Scale Motions in a Plane Mixing Layer," *J. Fluid Mech.*, **231**, pg. 257 (1991).

Pal D. and Sinha K. "Controlling an Unsteady Separating Boundary Layer on a Cylinder with an active Compliant Wall", AIAA Paper 97-0212, 35th Aerospace Sciences meeting, Reno, NV, 1997.

Raman, G. and Cornelius, D., "Jet Mixing Control Using Excitation from Miniature Oscillating Jets," *AIAA J.* **33**, #2, pg. 365 (1995).

Riley, N. and Wibrow, M. F., "The flow induced by the torsional oscillations of an elliptic cylinder," *J. Fluid Mech.* , **290**, pg. 279 (1995).

Rizzetta, D.P. Visbal, M.R. and Stanek, M.J. "Numerical investigation of synthetic jet flowfields," AIAA 29th Fluid Dynamics Conference #98-2910 (1998).

Roberts, F. A., "Effects of a periodic disturbance on structure and mixing in turbulent shear layers and wakes," PhD Thesis California Institute of Technology (1985).

Roshko A. and Fiszdon W. "On the Persistence of Transition in the Near Wake". Problems of Hydrodynamics and Continuum Mechanics. Soc. Industrial and Appl. Math., Philadelphia, 1969.

Savas, O. and Coles, D., "Coherence measurements in synthetic turbulent boundary layers," *J. Fluid Mech.*, **160**, pg. 421 (1985).

Schneider, P., "Sekundarwirbelbildung bei Ringwirbeln und in Freistrahlen," *Z. Flugwiss. Weltraumforsch*, **4**, pg. 307 (1980).

Seifert, A., Darabi, A., and Wygnanski, I., 1996, "Delay of airfoil stall by periodic excitation", J. of Aircraft, *33*(4), 691-698.

Shepshelovich, M. and Koss, D., 1990, "Active flow control on low Reynolds number airfoils", AIAA Paper 90-3039-CP, 28th AIAA Aerospace Sciences Mtg., NV.

Sigurdson L.S. and Roshko A. "Controlled Unsteady Excitation of a Reattaching Flow", AIAA Paper 85-00552, 1985.

Smith, B.L. and Glezer, A., "Vectoring and small-scale motions effected in free shear flows using synthetic jet actuators," AIAA 35th Aerospace Sciences Meeting #97-0213 (1997).

Smith, B.L. and Glezer, A., "The formation and evolution of synthetic jets," *Phys. Fluids*, **10**, #9, pg. 2281 (1998).

Smith, D. R., Amitay, M., Kibens, K., Parekh, D. E. and Glezer, A., 1998, "Modification of lifting body aerodynamics using synthetic jet actuators", AIAA Paper 98-0209.

Strykowski, P.J. Krothapalli, A. and Forliti D.J., "Counterflow Thrust Vectoring of Supersonic Jets," AIAA 34th Aerospace Sciences Meeting, Reno, NV #96-0115, (1996).

Stuart, J. T., "Double boundary layers in oscillatory viscous flow," *J. Fluid Mech.*, **24**, 1966.

Van der Hegge Zijnen, B.G., "Measurements of the velocity distribution in a plane turbulent jet of air," *App. Sci. Res.* Sec. A, **7**, pg. 256 (1958).

Van Dyke, M., *Album of Fluid Motion*, The Parabolic Press, Stanford, California (1982).

Viets, H. "Flip-Flop Jet Nozzle," *AIAA J.* **13**, #10, pg. 1375 (1975).

Westerveldt, P.J., " The Theory of Steady Rotational Flow Generated by a Sound Field," *J. Acoustic Soc. Am.* **25**, #60, (1953).

Williams, D. R., Acharya, M., Bernhardt, J. and Yang, P.-M., 1991, "The mechanism of flow control on a cylinder with the unsteady bleed technique", AIAA Paper 91-0039.

Williamson, C.H.K., "Three-dimensional aspects and transition of the wake of a circular cylinder," in *Turbulent Shear Flows* 7, Springer Verlag Berlin Heidelberg (1991).

Wiltse, J.M. and Glezer, A. "Manipulation of free shear flows using piezoelectric actuators," *J. Fluid Mech.* **249**, 1993.

Wiltse, J.M., and Glezer, A. "Direct Excitation of Small-Scale Motions in Free Shear Flows," *Phys. Fluids* **10** #8 pg. 2026 (1998).

Wu, J.-Z., Lu, X.-Y., Denny, A.G., Fan, M. and Wu, J.-M., 1998, "Post-stall control on an airfoil by local unsteady forcing", J. of Fluid Mech., vol. 371, 21-58.

Wygnanski, I. And Seifert, A., "The control of separation by periodic oscillations", AIAA Paper 94-2608.

Zaman, K. B. M. Q., Bar-sever, A., and Mangalam, S. M., 1987, "Effect of acoustic excitation on the flow over a low-Re airfoil", J. of Fluid Mech., *182*, 127-148.